Examination of Drone Localization Performance with Commercially Available Embedded GPS Sensors

Gokul Nathan

A thesis

submitted in partial fulfillment of the

requirements for the degree of

Master of Science in Electrical Engineering

University of Washington

2024

Committee:

Sep Makhsous

Akshay Gadre

Alex Mamishev

Jai Jaisimha

Program Authorized to Offer Degree:

Department of Electrical Engineering

University of Washington

Abstract

Examination of Drone Localization Performance with Commercially Available Embedded GPS Sensors

Gokul Nathan

Chair of the Supervisory Committee:
Sep Makhsous
Electrical and Computer Engineering

With the commercial drone market worth 24 billion USD and project to grow, accurate 3D localization in urban air mobility is critical. Existing GPS systems in these environments are plagued by multipath propagation and signal obstruction, resulting in typical urban GPS errors ranging from 15 to 100 meters, far below the precision needed for safe operations. Using a combination of experimental testing and data-driven modeling, this study quantitatively demonstrates that a composite machine learning approach using commercially available embedded GPS sensors, incorporating a Windowed Inverse Variance Weighted Filter combined with LSTM Recurrent Neural Networks, can significantly reduce localization errors. Testing across varied urban settings, GPS sensors improved location accuracy by up to 47% compared to conventional filter methods in literature, with the model effectively reducing the average error in urban environments to less than 1.8 meters. Dynamic Accuracy Index (DAI), a metric quantifying the balance between positional accuracy and data processing speed, is introduced. The experimental results reveal our system's proficiency, particularly evident in its DAI of 0.18 meter/Hz, surpassing

other conventional filter methods operating at approximately 1 Hz with a DAI of 5.11 meter/Hz and proposed filter + neural network methods presented in the literature with DAI of 2.17. The findings affirm the potential of using recurrent neural network-based machine learning algorithms in enhancing GPS localization systems, presenting a viable pathway for integrating these technologies into commercial UAV operations. This contribution is not only pivotal for the advancement of urban air mobility but also enhances the safety and operational efficiency of UAVs in complex environments.

TABLE OF CONTENTS

LIST OF FIGURES

LIST OF TABLES

LIST OF ABBREVIATIONS

Abbreviations	Explanation
AAM	Advanced Air Mobility
AGL	Above Ground Level
CNS	Communications, Navigation, and Surveillance
DGPS	Differential Global Positioning System
DNN	Deep Neural Network
DSP	Digital Signal Processing
EGNOS	European Geostationary Navigation Overlay Service
FAA	Federal Aviation Administration
GDOP	Geometric Dilution of Precision
GIS	Geographic Information System
HDOP	Horizontal Dilution of Precision
ICAO	International Civil Aviation Organization
ILS	Instrument Landing System
IMU	Inertial Measurement Unit
LIDAR	Light Detection and Ranging
LNA	Low Noise Amplifier
ML	Machine Learning
MAE	Mean Absolute Error
MSE	Mean Squared Error
MSAS	Multifunctional Satellite Augmentation System
NMEA	National Marine Electronics Association
NSF	National Science Foundation
PDOP	Position Dilution of Precision
PBN	Performance-Based Navigation
PPP	Precise Point Positioning
PRN	Pseudorandom Noise
RDC	Remote Data Collector
RFI	Radio Frequency Interference
RNAV	Area Navigation
RMSE	Root Mean Square Error
RNN	Recurrent Neural Network
RTK	Real-Time Kinematic
SBAS	Satellite-Based Augmentation System
TAMS	Traffic Aware Strategic Air Mobility
UAV	Unmanned Aerial Vehicle
UART	Universal Asynchronous Receiver-Transmitter
VHF	Very High Frequency
VOR	VHF Omnidirectional Range
WAAS	Wide Area Augmentation System
XFF	Expansive Flight Framework

ACKNOWLEDGEMENTS

I am profoundly grateful to a host of individuals whose support was invaluable in the completion of this thesis.

Firstly, I would like to extend my deepest gratitude to my advisor, Professor Sep Makhsous, whose expert guidance, unwavering support, and insightful critiques have been instrumental in shaping both the direction and success of this research. His patience and mentorship have been paramount throughout this challenging journey. I am also thankful to the members of my thesis committee, Assistant Professor Akshay Gadre, Professor Alexander V. Mamishev, and Affiliate Professor Jai Jaisimha, for their invaluable feedback and rigorous scrutiny, which significantly contributed to refining my work.

Special thanks go to my colleagues and friends at the University of Washington's SEAL Robotics Lab, especially Sanda Thang, Rachel Samson, and Brandon Ha, who contributed to the research and experimental work presented in this thesis. Specifically, Rachel Samson helped me with the figures presented in Chapters 1 and 2. My figures won't be half as good without her help. I would like to add special acknowledgment to Alperen Cuci, who contributed significantly to the work presented in Annex A. He helped formalize my handwritten equations, gave much needed structure to my mathematical writings. I would also like to acknowledge the contributions to the engineering work presented in this thesis by Jon Wick, Mathew Garcia, Matthew Le, Haodong Zhao, Morris Huang, and Ethan J. Aroco.

My appreciation also extends to the technical staff and administrative personnel of the department, whose assistance with logistical and bureaucratic hurdles allowed me to focus on my research.

DEDICATION

I owe a tremendous debt of gratitude to my family for their love, moral support, and endless patience through the many long hours that went into this thesis. Their belief in my capabilities continues to inspire me and drives my pursuit of excellence.

CHAPTER 1. INTRODUCTION

In recent years, the concept of Urban Air Mobility (UAM), a key component of the Federal Aviation Authority's (FAA) broader Advanced Air Mobility (AAM) initiative [1], has gained significant attention and investment due to advancements in automation and electric propulsion technology [2], [3]. One focus of the AAM initiative is creating and implementing autonomous drones, aiming to enhance last-mile delivery systems [4]. Precise localization is essential for autonomous vehicles (AVs), where accurate positioning is key for effective navigation and situational awareness relative to the surroundings and other entities [5], [6]. Precise localization is even more crucial for Unmanned Aerial Vehicles (UAVs) due to their three-dimensional operating environment and the complexity of the aerial traffic coordination [7]. The work studied in this thesis is motivated by the technological challenges and economic opportunities surrounding the implementation of AAM in urban environments.

1.1 PROBLEM MOTIVATION

Currently, the Global Position System (GPS) is the most used technology for the outdoor localization of drones [8], [9]. While GPS has transformed object trajectory and motion tracking in terrestrial applications, there remain challenges to its capabilities and reliability in complex urban environments [10]–[13], specifically in novel aerospace applications [11], [14]–[17]. This challenge stems from the intrinsic limitations of current GPS systems [18]–[23], which are primarily designed for 2D positional accuracy [16], [24]–[27], which prove inadequate for the demands of 3D urban navigation [26], [28]–[30] amidst complex aerial and urban landscapes. To effectively utilize GPS for 3D localization and extend existing 2D techniques that improve GPS performance in urban environments, it's essential to tackle the challenges associated with signal obfuscation, signal masking, and multipath errors [31]–[33] prevalent in dense urban environments. This thesis focuses on refining GPS-based position estimation through machine learning algorithms that utilize standard NMEA data from existing GPS receivers without requiring hardware modifications.

An accurate 3D localization system can contribute positively to the peripheral technological challenges inherent in AAM operations [34]–[37]:

- A precise localization system ensures that drones from different manufacturers can operate within the same airspace without interference, facilitating seamless integration and coordination.

- Localization technologies that require lower power consumption can extend the operational range of drones by reducing the energy burden of navigation systems and optimize for efficient pathfinding.

Addressing these technological challenges is essential for unlocking the full potential of UAM operations. UAM operations can reduce a package cost by up to 60% compared to conventional delivery methods if techno-economic challenges are solved [38]. A significant portion of costs are due to technological, safety, and efficiency limitations, approximately 13.5 USD for lightweight payloads [34] to 60.0 USD for heavier payloads [38]–[40]. Consequently, there's a need for a low-cost, low-power, interoperable sensor system capable of highly accurate localization [41] for UAVs. This research seeks to identify the performance specifications for a UAV localization system tailored for Urban Air Mobility (UAM), assess the capabilities of current consumer-grade GPS units, and introduce and evaluate a novel, low-power, hardware-embedded GPS system enhanced with a composite machine learning algorithm. The goal is to deliver a high-speed, highly accurate, low-power localization solution that effectively addresses the unique challenges of UAVs navigating densely populated urban landscapes.

1.2 OVERVIEW OF CURRENT DRONE LOCALIZATION TECHNOLOGIES

Drones utilize multiple data sources to ascertain their positions within an environment. This section provides a background on the choice of available localizations sensors, focusing on vision, Inertial Measurement Units (IMUs), and GPS sensors.

1.2.1 *Capabilities and challenges with vision localization technology*

Vision localization technology uses cameras and computer vision algorithms to determine a drone's position by analyzing visual features from the surrounding environment. It excels in environments with distinct visual markers, offering precise positioning, with visual odometry techniques achieving sub-meter accuracy [42] in ideal conditions [43].

However, the technology requires intensive computation for image processing, which can strain the limited processing capabilities of UAVs, increase power consumption, and impact system efficiency. Additionally, vision systems may perform poorly in low-light or visually sparse settings and raise privacy concerns in populated areas due to their surveillance capabilities [44]–[47].

1.2.2 *Capabilities and challenges with inertial measurement units for localizations*

IMUs are sensor systems commonly used for drone localization. IMUs typically consist of a combination of accelerometers and gyroscopes, sometimes complemented with magnetometers, that measure specific force, angular rate, and magnetic field strength. By integrating these measurements over time, IMUs estimate the drone's position and orientation relative to a known starting point. One of the primary advantages of IMUs is their high update rate and responsiveness, making them suitable for real-time applications such as drone navigation. IMUs can provide continuous motion measurements, enabling rapid updates to the drone's position and orientation. Additionally, IMUs are relatively lightweight and compact, making them ideal for integration into small unmanned aerial vehicles. IMUs have had success in the automotive industry, enhancing autonomous vehicle navigation and stability for features like electronic stability control and lane-keeping assistance [48]–[50].

IMUs, however, have significant limitations that can impact their accuracy and reliability. One challenge is sensor drift, where small errors in sensor measurements accumulate over time, leading to gradual inaccuracies in position estimation. This drift is particularly problematic in long-duration flights, where even minor errors can result in significant deviations from the intended path. Furthermore, IMUs alone cannot provide absolute positioning information and are susceptible to cumulative errors over time. IMUs often require periodic recalibration or integration with other sensor modalities, such as GPS or visual odometry, to mitigate drift.

1.2.3 *Capabilities and challenges of using GPS for drone localizations*

The Global Positioning System (GPS) is a satellite-based navigation system widely used for localization. GPS operates on the principle of trilateration, where the position of a receiver can be determined by measuring its distance from multiple satellites.

There are several reasons for prioritizing GPS technology in drone localization systems. Firstly, GPS is widely adopted and integrated into micro consumer drones, providing a proven and reliable solution for navigation. Features such as auto landing and subject orbit flight heavily rely on GPS positioning to function accurately [51], [52]. Secondly, GPS offers global coverage, allowing drones to navigate seamlessly across different geographic regions without the need for additional infrastructure. This universality makes GPS an attractive choice for drone applications requiring mobility and versatility. In contrast to alternative localization technologies such as cameras or inertial measurement units (IMUs), GPS is the primary focus of this thesis due to its cost-effectiveness, simplicity of implementation, and superior reliability. Given the considerations, GPS emerges as the preferred choice, offering lower computational demands, absence of drift, and robust performance, aligning closely with the objectives of this research endeavor.

To comprehend the specifications required for a localization system of UAM drones, it's crucial to examine how the FAA's concept of operations, current rules, and considerations influence the deployment of drones.

1.3 DESIGN FUNCTIONALITY REQUIREMENTS FOR AUTONOMOUS DRONE OPERATIONS

The operational landscape for drones is heavily influenced by airspace regulations set forth by the International Civil Aviation Organization (ICAO) and the FAA, which categorizes airspace into distinct classes [53]. UAM drones predominantly operate within Class G airspace, extending from the surface to around 400 feet above ground level (AGL) in the US. This altitude limitation is a crucial safety measure aimed at minimizing the risk of mid-air collisions and maintaining airspace integrity near airports and other airways. UAVs must comply with stringent requirements to uphold airspace safety and established aviation regulations. The following sections delve into the considerations that shape UAM airspace and their collective impact on the advancing localization demand for drones.

1.3.1 *Safety considerations influencing drone operations*

FAA has emphasized the critical importance of risk mitigation strategies [54] to facilitate the safe, widespread adoption of drone technology in urban environments. Safety in UAM is predicated on the twin objectives of reducing the severity of potential accidents and minimizing the likelihood of their occurrence.

Urban environments present numerous challenges, such as obstacles, weather, and turbulence, that necessitate robust localization systems for effective collision avoidance. Studies suggest segmenting urban airspace into Obstacle and Free Space zones to facilitate navigation and maintain safe separation from hazards [55], [56]. Weather and turbulence effects can further constrain free space, emphasizing the need for precise navigation [57]–[59]. Further, to minimize the probability of mid-air collisions, drones need to be aware of their position and simultaneously model other drones as obstacles to avoid. To this effect, drones must maintain constant separation from each other and the obstacle space [60].

Traditional Air Traffic Management systems (TAMS) impose a standard separation of 5 nautical miles or 2 minutes between aircraft [61], a regulation that is impractical for drones [6]. Various approaches have been proposed in the literature to address this challenge [62]–[64]. These methods dictate stringent accuracy and operational frequency demands on the localization subsystem. Specifically, the localization system must provide high precision and high-frequency updates to safely manage drone movements within tight separation constraints and dynamic flight conditions. Equation (1) summarizes the relationship between the precision of the localization system, the separation distance between aircraft, and the dynamic nature of their movement [65], [66].

$$\left\lfloor \frac{Loc_{\text{prec}}}{2} \right\rfloor \leq \lfloor \text{Sep} \rfloor \text{ and } \lfloor \text{Sep} \rfloor \geq \lceil \max(ASB, |Dyn_{\text{dist}}|) \tag{1}$$

where Loc_{prec} represents the max precision error of the localization system, Sep denotes the separation distance between aircraft and ASB is a parameter representing a safety margin. Dyn_{dist} represents the minimum dynamic distance between aircraft during flight as required by the airspace rules. Equation (1) mathematically defines the required precision as half the minimum

separation distance, ensuring that drones maintain safe navigation within designated air corridors and minimize collision risks. Drone traffic flow dynamics significantly impact the minimum positional resolution required for the localization system [67]–[69]. Based on equation (1), a minimum altitude resolution of 12.5 ft is needed to satisfy the constraints placed on UAVs in [67], [68].

1.3.2 *Social considerations influencing drone operations*

Urban Air Mobility (UAM) often takes place at lower altitudes and near residential zones, heightening community concerns about airspace development [70]–[72]. Privacy issues significantly influence drone operation requirements, including weight, power consumption, noise, speed, and operational duration [73]. To safeguard privacy, the use of high-resolution cameras is restricted, as they cannot identify human-sized targets from distances under 42 meters [74], affecting the effectiveness of visual-based navigation strategies. Moreover, transmitting GPS-tagged images for navigation risks privacy breaches. Therefore, drone localization systems should focus on using onboard sensors and computing to ensure precise and reliable navigation without infringing on privacy.

1.3.3 *CNS considerations influencing drone operations*

To facilitate autonomous drone operations, critical operational requirements pertaining to communication, navigation, and surveillance (CNS) systems need to be addressed [67]. UAV communication infrastructure significantly influences localization due to reliance on unencrypted frequencies, which are susceptible to interference and have limited range [54], [67]. Advanced signal processing within the communication subsystem is crucial for managing signal variability, which can alter by up to 45 dB in the signal-to-noise ratio [75]. Given the vulnerabilities of UAV communication systems, it's critical that processing and computing for localization occur directly on the UAV. Utilizing onboard systems mitigates the latency and reliability issues associated with remote data processing, ensuring real-time decision-making and enhancing the effectiveness of navigation and communication in varied environments. This approach bolsters the overall safety and reliability of UAV operations.

1.3.4 *Scalability and compatibility*

To effectively manage diverse air vehicle types within Urban Air Mobility (UAM), it's vital for the localization subsystem to be scalable and compatible across various drone platforms. Limited scalability can lead to challenges such as poor adaptation to different UAV configurations and dynamic operating environments, reducing accuracy and operational efficacy. Thus, it's essential to develop localization algorithms and infrastructure that are not only adaptable to various UAV setups and environmental conditions but also capable of handling high traffic volumes and complex urban settings in real-time. Prioritizing scalability ensures that the localization system supports a broad range of drone models and operational demands, facilitating safe and efficient UAM operations.

Table 1-1. Impact of UAM operations on GPS localization system

Functional Requirement	Impact on GPS Localization subsystem
Safety	Requires high-speed, accurate localization to ensure UAVs navigate safely without collisions. GPS data must be precisely monitored and corrected in real-time to adapt to dynamic urban environments and maintain flight within safe pathways
Social	GPS localization must respect privacy considerations, ensuring data collection avoids sensitive areas. Systems should prioritize low-power, high-accuracy GPS solutions that minimize the intrusion into private spaces while navigating urban landscapes. Localization systems must ensure accuracy without intruding on private spaces.
CNS	Depends on robust performance to overcome communication disruptions and ensure reliable operation. Advanced GPS systems need to process signals effectively, especially in urban settings where interference is common.
Scalability	Scalable GPS systems are crucial for adapting to diverse drone types and operational demands. These systems should offer flexibility in deployment for different UAV configurations and ensure that GPS data remains accurate and reliable across varying scales of urban air traffic.

This section outlined various requirements for autonomous drone operations, including reliability, robustness, scalability, adaptability, separation, and integration. The current UAM Concept of Operations (Con-Ops) [1], [54], [67] satisfies these requirements by requiring drones to fly within prescribed air corridors while accounting for uncertainties in their positions.

1.4 INFLUENCE OF DRONE OPERATIONS ON TECHNICAL REQUIREMENTS FOR LOCALIZATION SYSTEM

This section explores how the functionality requirements in the previous section influence the technical requirements of the localization system.

1.4.1 *GPS systems in urban locations*

GPS technology, vital for drone navigation, faces challenges in urban environments from obstructions like tall buildings, leading to signal blockage and multipath issues, reducing accuracy and reliability [76]–[78]. This impacts critical applications such as emergency response and drone delivery, where precise positioning under 3 meters is necessary [6]. Despite advances in GNSS hardware, antenna designs, signal processing, sensor fusion, and ML techniques[79]–[83], significant gaps remain in GPS localization effectiveness in urban areas [84]. Filter methods can't handle multiple faults simultaneously seen in urban environments [85], statistical methods can't handle situations with limited GPS data [84], [86], and simple neural network models struggle with absolute positioning and dynamic multi-path conditions [87]–[89]. With drone operating predominantly in less complex rural and suburban settings [41], [90], [91], urban-specific algorithm development is essential for safe navigation in urban areas.

This research evaluates GPS systems per ICAO guidelines, focusing exclusively on GPS due to its approval for aerospace use [92]. The minimum evaluation benchmarks include FAA standards for 15 ft accuracy 95% of the time [93] and ICAO's PBN 0.3 accuracy requirement for all flight phases [94]. The thesis adopts stricter standards for its analysis.

This study focuses on single-frequency GPS receivers due to their affordability and wide application. While less costly than multi-frequency models, single-frequency units typically offer similar tracking resolution, albeit with a slower position acquisition rate. Multi-frequency receivers, despite faster acquisition and a 95% reduction in initialization time[95]–[98], require more power and are far more costlier[99]. This investigation assesses single-frequency receivers' suitability for precise, rapid positioning tasks.

1.4.2 *Multiple sensors localization challenges*

The current research paradigm, widely embraced in both commercial and military aviation, endorses the use of multiple GPS receivers to address coverage issues in larger aircraft [16], [17], [100]–[104]. Extending this approach to drone applications, we aim to explore the variability between low-power sensors with limited computational capabilities. This investigation also aligns with the prevalent trend in commercially available flight controllers that accept independent primary and secondary GPS receivers [105]. The study also seeks to investigate whether the fused performance of these sensors can result in a low-power system equipped with low-power external antennas capable of achieving performance levels comparable to larger GPS acquisition units that consume at least an order of magnitude more power [106].

1.4.3 *Machine learning integration*

Certain machine learning algorithms have improved localization accuracy by dynamically integrating data from sensors, environmental conditions, and historical data in other environments and applications [80], [107]–[111]. The study will investigate advanced neural network models to determine if they can effectively adapt to complex urban terrains and infrastructures, enhancing localization performance for high-speed, accurate, and low-power aerospace applications.

1.4.4 *Embedded localization system*

Efficient resource utilization is critical in embedded localization systems on drones, where power, weight, and size are major constraints. The project uses commercially available sensors and microcontrollers (COTS) to avoid the need for new sensor development, focusing on optimizing these components for low power consumption and minimal weight. Real-time processing on embedded systems ensures immediate localization updates, crucial for dynamic urban environments. Techniques like duty cycling and data compression further reduce power usage, extending drone operational endurance. Standardized interfaces ensure these localization modules easily integrate into various drone platforms, enhancing system interoperability and allowing for scalability across different operational needs. To ensure compatibility with the energy constraints typical of drone platforms, the power budget for the localization system is limited to around 15 Watts [112].

1.5 MINIMAL TECHNICAL REQUIREMENTS FOR DRONE LOCALIZATION SYSTEM

The advancement of drone technology has led to increasingly stringent requirements for their operation, driving the need for minimal operating specifications to ensure safe and efficient performance. These specifications encompass a range of scientific and engineering challenges that must be addressed to meet the demands of diverse applications and operational environments. The functional design requirements for drone localization necessitate the following technical specifications, which are presented in Table 1-2.

Table 1-2. Functional, operational, and technical requirements for localization sub-system to satisfy autonomous UAM drone operations

Functional Requirement	Operational Requirement Summary	Technical Requirement
Safety	High-Speed Localization	Update rate of at least 10 Hz; latency under 50 milliseconds
	Precise Localization Capability	Accuracy under 3 m horizontally; under 12.5 ft vertically in urban conditions 95.5% of time
Social	Accurate Localization Capability	Accuracy under 3 m horizontally; under 12.5 ft vertically
	Preserve Privacy	Onboard processing of GPS
CNS	Develop for Airborne Applications	Antenna placement to enhance signal and reduce noise; onboard processing of GPS signals
		Firm-real time operation
Scalability	Low Power Localization System	Power consumption under 15 Watts; compatible across various drone platforms
		Scalability to adapt to different UAV configurations and operational demands

1.5.1 *Operational frequency considerations for embedded systems*

Operational frequency is crucial in embedded systems for drones, requiring a balance between processing speed and power efficiency. The system must process data in real time while conserving energy for longer flight times. It's important to minimize delay to respond quickly to changing conditions, although higher frequencies can introduce errors and increase power consumption. The GPS localization system must update its position based on satellite signals at a frequency of at least 10 Hz. The effective update rate of a standard GPS receiver used in drones currently is about 1 Hz [113]–[115]. However, additional signal treatment, such as mean value or low pass filtering, may be necessary, thus decreasing the effective update rate further [113].

1.5.1.1 Delay and latency

Max delay refers to the maximum allowable latency between input commands or sensor measurements and the corresponding output actions or responses from the drone. Minimizing max delay is essential for maintaining responsiveness and agility in drone operations, especially in scenarios requiring precise maneuvering or interaction with dynamic environments. Engineering challenges associated with reducing max delay include optimizing control algorithms, minimizing sensor fusion latency, and enhancing communication protocols. The targeted maximum delay acceptable for a localization system is to be under 50 milliseconds for consecutive measurements of locations [116].

1.5.2 *Power consumption considerations for embedded systems*

Power consumption is a critical consideration in drone controller design, as it directly impacts flight endurance, payload capacity, and overall mission capabilities. Minimizing power consumption while maximizing performance is a significant engineering challenge that requires careful optimization of hardware components, firmware algorithms, and operational strategies. The localization subsystem uses varying watts of power, depending on the technology used to perform localization. The key parameter to optimize is the meter-watt per frequency. The metric measures how accurate weighted average offset errors the system can localize at a given power and how little power It consumes. The lower the value, the better the performance of the system.

A good target for a GPS-based localization system is 3 meters or less, at 10 Hz or better, while consuming less than 10 W.

1.6 RESEARCH QUESTIONS

This thesis addresses the limitations of GPS systems as highlighted in previous studies (Section 1.1) by incorporating machine learning techniques to enhance GPS localization performance in challenging urban environments, specifically for Urban Air Mobility (UAM) applications. The central aim is concisely summarized as the following statement:

To enable GPS based, high-accuracy localization of UAVs operating in urban environments.

The objective is accomplished through a two-step approach:

1. Development of a hardware GPS Data Acquisition (DAQ) System: Tailored specifically for drones, this system not only collects GPS data during flight for testing but is also capable of processing this data onboard using the algorithms developed in this thesis.

2. Optimization of Machine Learning Techniques for Drones: Using machine learning, this thesis aims to identify and correct GPS localization errors while operating on flight class hardware.

1.7 PROJECT OUTLINE

To address the key inquiry, this project's scope and objectives, the comprehensive exploration extends across three pivotal domains: Theoretical Design, Functional Design, and Experimental Work. Figure 1-1 demonstrates this scope in a visual format.

Theoretical Design segment: An investigation into the theoretical underpinnings of GPS, flight dynamics and leveraging machine learning algorithms. This involves a detailed examination of GPS operational principles, including signal propagation, error sources, and mitigation techniques, underpinned by the mathematical foundations that support the application of advanced machine learning models, notably Long Short-Term Memory (LSTM) and Recurrent Neural Networks (RNN), aimed at rectifying inaccuracies inherent in GPS data.

Functional Design: This section studies engineering specifics required to realize the theoretical concepts. It encompasses the development of an embedded system architecture tailored for drone platforms, ensuring the system's expansibility and adaptability. The design also involves a custom GPS Data Acquisition (DAQ) system, optimized to facilitate precise and efficient data gathering essential for machine learning model training and validation. Work is also carried on generating efficient machine learning architecture for GPS error correction.

Experimental Design: This section transitions from theory to practice, employing a structured approach to validate the theoretical models and system designs. This includes a series of meticulously planned tests ranging from static to dynamic, ground to hover, each designed to rigorously assess the performance of the GPS machine learning enhancements in real-world conditions. Moreover, this phase incorporates ML Training, aimed at refining the algorithms based on the empirical data gathered, thus ensuring the models' robustness and reliability.

Future Work: There is a huge commercial demand and a large technical problem that needs to be solved for the effective implementation of UAMs and AAMs. Commercialization prospects of this technology are explored through further Flight studies, NSF I-CORP program, and integration of XFF. The larger technical problem of effective urban navigation for aerospace vehicles is explored as part of the author’s future research endeavors. This includes using flight data to develop novel error correction algorithms and generative AI applications. Further development efforts of an extension of the hardware architecture and R-sensors.

1.7.1 *Organization of chapters*

This thesis is systematically organized into nine chapters, each focusing on distinct aspects of integrating GPS and machine learning to enhance drone navigation accuracy and reliability. This structured approach facilitates a comprehensive exploration of the subject matter, from foundational principles and theoretical designs to practical implementations and future directions.

Chapter 1 sets the stage for the thesis by outlining the motivation behind the research, which includes addressing the technological challenge of extending GPS capabilities to 3D localization for UAM. It lays out the design, functionality, and technical requirements for a drone localization system built upon GPS technology.

Chapter 2 delves into the Global Positioning System (GPS) and provides an overview of its operating principles. Additionally, it explores the NMEA standard, signal characteristics, and the architecture and types of GPS receivers, concluding with an examination of the various sources of errors in GPS systems and new opportunities in the field of GPS localization.

Chapter 3 focuses on the Theoretical Design of ML Algorithms. It highlights the application of machine learning in GPS studies and provides an overview of the proposed algorithm IRNN-DNN. It concludes with the details of the algorithm's implementation.

Chapter 4 outlines the Functional Design of the GPS DAQ System and Drone Platform, emphasizing the development of an embedded system architecture tailored for drone navigation and a customized DAQ (PATHFINDER) for efficient data collection and processing.

Chapter 5 presents the Experimental Design, describing the methodology and setup for conducting various tests to evaluate the performance of the GPS and machine learning enhancements in real-world scenarios. This includes the selection of testing locations, mounting GPS on drones, and analyzing errors in different phases of flight.

Chapter 6 discusses the results of testing the PATHFINDER system and offers insights into the performance of GPS sensors within the design ML framework.

Chapter 7 highlights Performance Enhancement through Neural Networks, exploring the classification of environments using machine learning and the application of LSTM RNN neural networks on static GPS data to enhance navigational accuracy.

Chapter 8 concludes with Limitations, Conclusions, and Future Work, reflecting on the challenges encountered, the achievements of the project, and potential future research directions that could further advance the field of drone navigation technology.

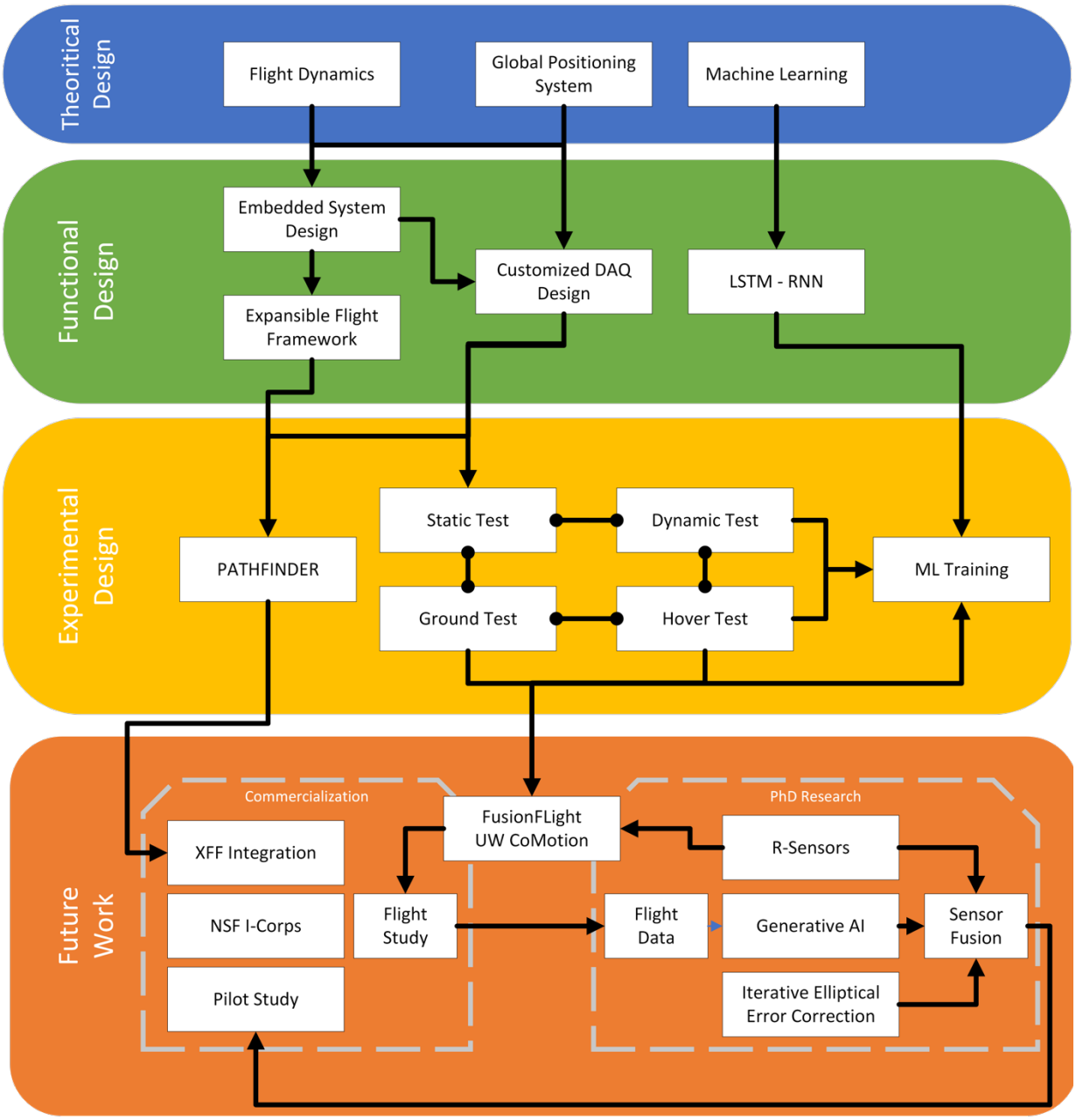

Figure 1-1. A visual outline of the thesis document.

CHAPTER 2. BACKGROUND ON GLOBAL POSITIONING SYSTEM

In this chapter, a background exploration of the Global Positioning System (GPS) is provided, delving into its operational principles and components. The chapter aims to elucidate how these attributes influence the performance of drone GPS localization in urban environments.

2.1 GPS OPERATING PRINCIPLES

In this subsection, the operating principles of the Global Positioning System (GPS) are explored, including discussions on its various segments and the trilateration method used for determining position.

2.1.1 *Space segment*

The space segment of the GPS encompasses a constellation of 31 active GPS satellites orbiting the Earth [117]. Each GPS satellite is equipped with highly accurate atomic clocks. The satellites continuously transmit signals towards the Earth's surface in various frequency bands. These signals contain encoded data, including the satellite's unique identifier, ephemeris data (position and velocity information), precise timing information (satellite clock time), and health status indicators. The primary signal is the L1 band, operating at a frequency of 1575.42 MHz, while additional signals are transmitted on the L2 and L5 bands at frequencies of 1227.60 MHz and 1176.45 MHz, respectively.

Different codes are modulated onto these carrier frequencies to facilitate signal reception and processing by GPS receivers. The Coarse/Acquisition (C/A) code is a low-accuracy code available to civilian users, providing positioning accuracy within approximately 10-20 meters in ideal conditions [17], [118], [119]. In contrast, the Precise (P) code is a high-accuracy code reserved for military use, offering a centimeter-level positioning accuracy [120].

The civilian GPS signal comprises three main components - a carrier, navigation data, and spreading code, encoded within the GPS L1 C/A signal [121]. The carrier is a sinusoidal signal defining the frequency band for broadcasting the GPS signal, with the GPS L1 C/A. GPS codes

are generated and transmitted using complex modulation schemes and encoding techniques. They are produced onboard GPS satellites using precise timing references from atomic clocks.

The navigation data is a binary-coded message containing crucial information about the GPS satellite, such as its ephemeris, clock parameters, and health status, transmitted at a slow rate of 50 bits per second for the L1 C/A signal [121]. Errors or inconsistencies in the navigation data can lead to inaccuracies in determining the receiver's position.

The Spreading code is a high-frequency, periodic binary sequence transmitted at 1.023 MHz for the L1 C/A signal. This code sequence is a pseudorandom noise (PRN) code and is unique to each GPS satellite. Because it is unique to each satellite, the PRN also serves as an identifier for the GPS satellite, e.g., satellite PRN 12 refers to the GPS satellite broadcasting its signal with the 12^{th} PRN code defined in the interface specification [122]. Spreading codes are also designed to minimize correlation with phase-shifted versions of the signals. This helps minimize impact of signal reflections, which can occur when the GPS signals bounce off objects such as buildings or terrain before reaching the receiver.

2.1.2 *Control segment*

The control segment of the GPS system plays a crucial role in ensuring the accuracy of satellite positions and clock synchronization [123]. The first step in the process involves determining the precise orbits of the GPS satellites. Ground stations track the signals transmitted by the satellites and measure the time it takes for the signals to reach them. By analyzing these measurements from multiple stations, the control segment can triangulate the position of each satellite and calculate its orbit with high accuracy.

In addition to orbit determination, the control segment ensures that the atomic clocks onboard the satellites are synchronized. The clocks aboard the satellites can experience slight deviations. The control segment computes orbit and clock error corrections. Once the corrections are calculated, they are transmitted to the GPS satellites using ground-based uplink stations. These correction signals are modulated onto the carrier signal broadcast by the satellites and transmitted back to Earth. The correction signals contain information about the orbit and clock corrections for

each satellite. In this study, the assumption is made that the received GPS signals incorporate corrections transmitted by the control segment.

2.1.3 *User segment*

The user segment in the Global Positioning System (GPS) comprises the GPS receivers and devices utilized by end-users to obtain positioning and timing information. The primary function of the user segment is to receive and process the signals transmitted by the GPS satellites to determine the user's precise location, velocity, and time. Chapter 2.3 discusses in more detail the different types of GPS receiver and their role in GPS localization system(s). The following sub-section (2.1.3.1) discusses the operating principles in detail.

In the context of this thesis research, the performance characteristics of the user segment, including accuracy, precision, speed, and power consumption, directly impact the effectiveness of GPS localization in urban environments for drones [124]. The central challenge in GPS localization for drones lies in reconciling the competing demands of accuracy, speed, power consumption, and cost. Each requirement presents its own set of priorities: achieving higher accuracy or faster localization typically comes at the expense of increased costs and power consumption. Conversely, efforts to minimize power consumption and costs often result in sacrifices in accuracy and localization speed. However, the essential task for UAVs is to fulfill all four criteria simultaneously. This juxtaposition of priorities creates a significant obstacle for UAV localization systems, particularly in urban environments where precise localization is paramount.

2.1.3.1 Trilateration method

A GPS receiver works on the trilateration principle [125] to determine the precise location of the receiver on Earth's surface. Trilateration involves calculating the intersection point of spheres centered at known positions (satellites) with radii equal to the measured distances between the satellites and the receiver. This method leverages the travel time of signals transmitted by the satellites to the receiver. The mathematical formulation of trilateration begins with expressing the distances between the receiver and each satellite in terms of their coordinates and the speed of light. Let (x_i, y_i, z_i) denote the coordinates of the $i-th$ satellite, and t_i represent the travel time

of the signal from the $i-th$ satellite to the receiver. The distance, R_i, between the receiver and the $i-th$ satellite, can be expressed as:

$$R_i = c \cdot t_i \tag{2}$$

where c is the speed of light. The position of the receiver (x, y, z) can then be calculated by solving a system of nonlinear equations [123], [126], [127], typically formulated as:

$$\begin{aligned}
(x - x_1)^2 + (y - y_1)^2 + (z - z_1)^2 &= c^2 \cdot (t_1 - d)^2 \\
(x - x_2)^2 + (y - y_2)^2 + (z - z_2)^2 &= c^2 \cdot (t_2 - d)^2 \\
(x - x_3)^2 + (y - y_3)^2 + (z - z_3)^2 &= c^2 \cdot (t_3 - d)^2 \\
&\vdots \\
(x - x_n)^2 + (y - y_n)^2 + (z - z_n)^2 &= c^2 \cdot (t_n - d)^2
\end{aligned} \tag{3}$$

where (x_k, y_k, z_k) denote the coordinates of the k − th satellite, and t_k represent the travel time of the signal from the k − th satellite to the receiver. The term, d, represents the difference in time between the receiver's clock and the satellite's clock, which needs to be estimated along with the receiver's position. Iterative algorithms [17] are essential for refining initial estimates, $(x_{est}, y_{est}, z_{est})$ [123], [128], [129], of (x, y, z) until a satisfactory level of accuracy is achieved.

The synchronization of satellite signals is a crucial aspect of GPS accuracy. Satellites equipped with atomic clocks transmit signals at precisely known times, all of which are synchronized with each other and with Coordinated Universal Time (UTC). Conversely, the clock in the receiver is not synchronized with UTC, leading to a discrepancy, denoted as Δt_{0_n}, where the receiver's clock can be ahead (Δt_{0_n}>0) or behind (Δt_{0_n} <0). This discrepancy results in an error in the measurement of the signal's transit time and, consequently, the calculated distance (R_n) to the satellite. The measured distance, affected by this time error, is referred to as the pseudo-range (PSR).

$$t_n = \Delta t_n - \Delta t_{0_n} \tag{4}$$

$$PSR_n \;=\; R_n \;+ \mathrm{c} \cdot \Delta t_{0_n} \tag{5}$$

Consequently, a minimum of four satellites is needed for a good positional estimate. The prominent method for solving this set of equations is the Gauss-Newton method. Mathematically, denoting the nonlinear equations in (3) as $\boldsymbol{f}(\boldsymbol{X})$, where $\mathbf{X}$ is the vector of unknowns, $(\mathrm{x}, \mathrm{y}, \mathrm{z}, \mathrm{d})$ gives:

$$f(\boldsymbol{X}) \;=\; f(\boldsymbol{X_{est}}) \;+\; f'(\boldsymbol{X})\,(\boldsymbol{X} - \boldsymbol{X_{est}}) \tag{6}$$

where $\boldsymbol{X_{est}}$ is the initial estimate of the of the solution $(x_{est}, y_{est}, z_{est}, \Delta t_0)$. From (2), (3), (5), and (6):

$$\begin{aligned} PSR \;=\; \sqrt{(x_{\,est} - x_1)^2 \;+\; (y_{est} - y_1)^2 \;+\; (z_{est} - z_1)^2} \;+\; \frac{\partial R_n}{\partial x}\Delta x \\ +\; \frac{\partial R_n}{\partial y}\Delta y + \frac{\partial R_n}{\partial z}\Delta z \;+\; \mathrm{c} \cdot \Delta t_{0_n} \end{aligned} \tag{7}$$

where $\Delta x, \Delta y, \Delta z$ are the unknown errors in the final estimated position.

$$(x, y, z) - \;(x_{est}, y_{est}, z_{est}) \;=\; (\Delta x, \Delta y, \Delta z) \tag{8}$$

Reorganizing terms and generating a set of linear transformation equations [127], we get

$$\begin{bmatrix} PSR_1 \;-\; R_1 \\ PSR_1 \;-\; R_1 \\ PSR_1 \;-\; R_1 \\ \vdots \\ PSR_k \;-\; R_k \end{bmatrix} = \begin{bmatrix} \frac{x_{est_1} - x_1}{R_1} & \frac{y_{est_1} - y_1}{R_1} & \frac{z_{est_1} - z_1}{R_1} & c \\ \frac{x_{est_2} - x_2}{R_2} & \frac{y_{est_2} - y_2}{R_2} & \frac{z_{est_2} - z_2}{R_2} & c \\ \frac{x_{est_3} - x_3}{R_3} & \frac{y_{est_3} - y_3}{R_3} & \frac{z_{est_3} - z_3}{R_3} & c \\ \vdots & \vdots & \vdots & \vdots \\ \frac{x_{est_1} - x_1}{R_k} & \frac{y_{est_1} - y_1}{R_k} & \frac{z_{est_1} - z_1}{R_k} & c \end{bmatrix} \cdot \begin{bmatrix} \Delta x \\ \Delta y \\ \Delta z \\ \Delta t_0 \end{bmatrix}; \; for \; k \;\geq 4 \tag{9}$$

$$\begin{bmatrix}\Delta x\\ \Delta y\\ \Delta z\\ \Delta t_0\end{bmatrix} = \begin{bmatrix}\frac{x_{est_1}-x_1}{R_1} & \frac{y_{est_1}-y_1}{R_1} & \frac{z_{est_1}-z_1}{R_1} & c\\ \frac{x_{est_2}-x_2}{R_2} & \frac{y_{est_2}-y_2}{R_2} & \frac{z_{est_2}-z_2}{R_2} & c\\ \frac{x_{est_3}-x_3}{R_3} & \frac{y_{est_3}-y_3}{R_3} & \frac{z_{est_3}-z_3}{R_3} & c\\ \vdots & \vdots & \vdots & \vdots\\ \frac{x_{est_1}-x_1}{R_k} & \frac{y_{est_1}-y_1}{R_k} & \frac{z_{est_1}-z_1}{R_k} & c\end{bmatrix}^{-1} \cdot \begin{bmatrix}PSR_1 - R_1\\ PSR_1 - R_1\\ PSR_1 - R_1\\ \vdots\\ PSR_k - R_k\end{bmatrix}; \; for\; k \geq 4 \tag{10}$$

$$\begin{bmatrix}\Delta x\\ \Delta y\\ \Delta z\\ \Delta t_0\end{bmatrix} = \boldsymbol{W}_{GPS}{}^{-1} \cdot \boldsymbol{X}_{GPS};\; for\; k \geq 4 \tag{11}$$

Equation (10) is also in the form of the standard machine learning equation.

2.1.4 *Expected GPS performance*

On average, GPS Navigation System Error (NSE) is generally uniform everywhere in the U.S. GPS paths and profiles can be straight, curved, or any 3-D trajectory the aircraft can follow. This means that systemic errors studied in one location will be similar to those in another location, and the actual flying of the drone will have a low impact on the system error. Consequently, additional errors are situational, and it is these additional errors that need to be studied and improved upon [130]. Vertical GPS errors are at least 50% greater than horizontal errors in-situ [113]. Under optimal conditions, the GPS-based localization system can achieve accuracy with a lateral position error of less than 1 meter. However, in more challenging operational environments, such as dense urban areas or areas with significant obstructions, horizontal accuracy may degrade, resulting in errors in the order of hundreds of meters [131]. Moreover, vertical accuracy, as highlighted in various studies [113], [132], [133], tends to exhibit greater errors, typically exceeding 2 meters under ideal conditions and surpassing 100s of meters when operating under cover or in environments with limited satellite visibility. Consequently, for the GPS localization system, both the vertical and horizontal positions estimates need to be improved upon.

2.2 NMEA STANDARD

Pseudorange (PSR) measurements offer crucial raw distance estimates between the receiver and satellites, providing insights into GPS system performance. In addition to these measurements, the National Marine Electronics Association (NMEA) data standard [134] provides a standardized messaging format that conveys supplementary information beyond PSR data. NMEA messages encapsulate details about the receiver's position, velocity, time, and satellite data, enriched by metadata and status indicators. This additional information enhances the understanding of GPS system operation and performance.

The inclusion of a section on the NMEA standard within the thesis holds significant importance, as it aligns with the objective of developing a hardware-software model aimed at improving processed GPS data. Unlike studies focused on manipulating raw PSR data [14], [110], [135], [136], the iRNN-DNN approach prioritizes the utilization of NMEA data as a standardized and readily accessible alternative based on prior related work [137]–[141]. Leveraging NMEA messages ensures compatibility and interoperability across diverse GPS devices and enhances readability compared to traditional PSR codes.

The use of NMEA data instead of pseudorange (PSR) in our PATHFINDER system is primarily driven by regulatory, economic, and technical advantages. Firstly, NMEA data meets Federal Aviation Administration (FAA) standards, simplifying certification by adhering to established safety and operational guidelines. This standardization expedites regulatory approvals and ensures system compliance with strict safety protocols.

Economically, NMEA's standardized format boosts interoperability across different GPS devices, significantly lowering development costs and enhancing system scalability for broader deployment. This standardization aids not only in cost reduction but also improves system robustness across varied operational contexts

Technically, NMEA data enriches localization with additional parameters such as velocity and satellite information, which complements PSR measurements without compromising their integrity. This approach maintains the PSR signal's integrity while augmenting it with valuable data, enhancing overall GPS accuracy and reliability. The integration of NMEA thus supports a

more robust and flexible localization system design, offering substantial improvements in GPS performance for UAV applications.

2.2.1 *NMEA data format*

NMEA provides a structured and uniform way of conveying information between different devices. At the core of the NMEA standard are data sentences, which are formatted strings of characters containing specific types of information. These sentences are designed to convey different types of data relevant to navigation, positioning, and other marine-related parameters. Each sentence has a unique identifier and a defined structure, making it easy for receiving devices to parse and interpret the information.

Among the commonly used NMEA sentences are the GGA (Global Positioning System Fix Data), RMC (Recommended Minimum Navigation Information), and GSV (Satellites in View) sentences. The GGA sentence, for example, provides essential details about the current GPS fix, including latitude, longitude, altitude, and fix quality. The RMC sentence includes important navigation information such as time, date, speed over ground, and course over ground. The GSV sentence, on the other hand, offers insights into the satellites that are currently in view of the receiver, including their IDs, elevation angles, azimuths, and signal strengths.

Table 2-1. NMEA message types and descriptions.

NMEA Message	Description	Relevance to Study	Example Values
GGA	Global Positioning System Fix Data: Provides essential fix information such as latitude, longitude, altitude, and fix quality.	HIGH.	$GPGGA,123519,...
GLL	Geographic Position – Latitude/Longitude: Provides latitude and longitude data.	NOT USED. DUPLICATION OF INFORMATION	$GPGLL,4916.45,N,...
GSA	GPS DOP and Active Satellites: Provides details about the Dilution of Precision (DOP) and the satellites being used for navigation.	HIGH. Essential for assessing GPS quality.	$GPGSA,A,3,...
GSV	Satellites in View: Provides information about the satellites that are currently in view, including their IDs, elevation angles, azimuths, and signal strengths.	HIGH. Used to understand satellite geometry	$GPGSV,2,1,...
RMC	Recommended Minimum Navigation Information: Includes time, date, speed over ground, course over ground, and other essential navigation data.	HIGH. Used for navigation data integration	$GPRMC,081836,A,...
VTG	Track Made Good and Ground Speed: Provides information about the track made good (course) and ground speed.	NOT USED	$GPVTG,054.7,T,...
GRS	GPS Range Residuals: Provides information about the residuals in the range measurements used by the GPS receiver.	MEDIUM. Used for GPS monitoring.	$GPGRS,024603,...
GST	GPS Pseudorange Noise Statistics: Provides statistics about the pseudorange noise of the GPS signals.	LOW. Secondary fallback source of data	$GPGST,024603,...
ZDA	Time and Date: Provides information about the current time and date in UTC format.	NOT USED. DUPLICATION OF INFORMATION	$GPZDA,201530.00,...
HDT	Heading, True: Provides the true heading of the vessel or vehicle.	NOT USED. DUPLICATION OF INFORMATION	$GPHDT,101.2,T,...

Messages of interest to the study are highlighted in green; the pale orange messages are not used for ML training but are collected to monitor the GPS performance in-situ. Definitions of messages were adopted from [134], [142] and generative LLMs were used to create dummy example sentences.

2.2.2 *Signal characteristics analysis*

In GPS navigation, understanding the signal characteristics extracted from NMEA processed data is crucial for assessing the quality and reliability of position information. This section focuses on key parameters such as signal strength, satellite visibility, and dilution of precision (DOP) values to evaluate the overall performance of the GPS system.

Signal strength, often measured in decibels (dB), indicates the power level of the GPS signals received by the receiver. A higher signal strength typically correlates with better reception quality and more accurate positioning. Analyzing signal strength variations over time and across different satellite channels provides insights into signal stability and potential interference issues. Low signal strength may result in degraded positioning accuracy, especially in environments with obstructions or signal blockages.

Satellite visibility refers to the number of satellites detected and tracked by the GPS receiver at any given time. A higher number of visible satellites generally leads to improved positioning accuracy and reliability. By analyzing satellite visibility data, users can assess the availability of sufficient satellite signals for accurate positioning calculations. Variations in satellite visibility may occur due to factors such as satellite orbits, atmospheric conditions, and terrain obstacles. Understanding satellite visibility patterns helps users anticipate potential signal loss or degradation in specific geographic areas or environmental conditions.

Dilution of Precision (DOP) is a factor significantly affecting the positional accuracy achievable with GPS technology. The precision of location determination via GPS is influenced by two main aspects: the intrinsic accuracy of pseudo-range measurements and the spatial distribution of the satellites in view. Figure 2-1 illustrates the influence of satellite position on DOP The impact of these factors on positional accuracy is quantitatively expressed through various DOP values, a set of scalar measures that describe the geometric strength of the satellite configuration in relation to the receiver's location [127]. Various Dilution of DOP designations are employed, including GDOP, which assesses 3-D spatial positioning and time deviation; PDOP, which gauges 3-D spatial positioning; VDOP, evaluates the vertical positioning accuracy; and HDOP, which evaluates horizontal positioning on a plane. The accuracy of any measurement is proportionately dependent on the DOP value. This means that if the DOP value doubles, the error

in determining a position increase by a factor of two [127]. Lower DOP values indicate better geometric conditions for accurate positioning, while higher DOP values suggest increased uncertainty and reduced accuracy. Analyzing DOP values allows users to assess the geometric integrity of satellite constellations and identify optimal positioning opportunities.

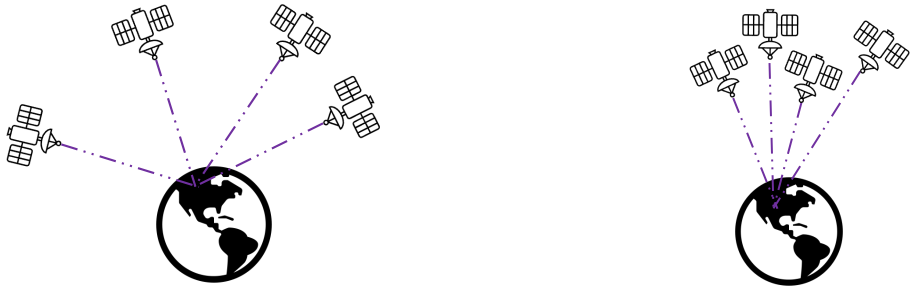

(a) (b)

Figure 2-1. PDOP is interpretable as the inverse value of the tetrahedral volume formed by all the satellites in view of the receiver. a) The larger the volume, i.e., the more spread out the satellite positions are, the lower the PDOP value. b) Narrow spread in the satellite position leads to higher PDOP values and lower precision in the GPS solution. Adapted from [127]

By monitoring DOP variations during navigation, drone localization systems can anticipate potential accuracy fluctuations and make informed decisions regarding data usage and reliability. Interpreting signal quality indicators derived from NMEA processed data involves assessing the relationship between signal characteristics and positioning accuracy. Strong signal strength, consistent satellite visibility, and low DOP values generally indicate favorable conditions for accurate GPS positioning. Conversely, weak signal strength, intermittent satellite visibility, and high DOP values may compromise positioning accuracy and reliability.

2.3 GPS RECEIVERS

GPS receivers consist of several key hardware components [143], including antennas to receive the GPS signals, radio frequency (RF) front-end circuitry to amplify and filter the incoming signals, digital signal processing (DSP) units to demodulate and decode the signals, and a computation unit to calculate the user's position based on the information received from multiple satellites. While this thesis does not delve into the design of GPS receiver components, these components affect the performance of GPS receivers and, by extension, the accuracy and reliability of drone navigation in urban environments.

2.3.1 *Grades of GPS receivers*

GPS receivers are categorized into different grades based on their accuracy, precision, and intended applications [144], [145]. These grades range from high-precision survey-grade receivers to consumer-grade devices commonly found in smartphones and navigation systems.

2.3.1.1 Survey-grade GPS receivers

Survey-grade GPS receivers offer the highest GPS precision and accuracy, engineered for professional surveying and geodetic applications where centimeter-level accuracy is needed. These devices have advanced features such as real-time kinematic (RTK) positioning and carrier-phase measurements, enabling high precision in position determination. For example, Trimble's Geo 7 series and 6000 series are survey-grade GPS receivers known for their high accuracy and extensive features. However, these accuracy metrics are measured and guaranteed only in stationary applications. Additionally, Survey-grade receivers typically have high computational demands to process complex algorithms for accurate positioning, which results in significant power consumption.

Despite their exceptional performance in stationary surveying tasks, survey-grade receivers are unsuitable for drone UAM operations and aerospace applications due to their high-power consumption (20W for a GPS unit, with an additional 5-45 W depending on the antenna used) and computational demands. Additionally, the advanced features optimized for stationary surveying tasks may not align with the dynamic requirements of aerial operations. This unsuitability is further discussed in section 2.5 These GPS receivers are expensive. Trimble's Geo 7X series costs approximately 6666 USD [146] and the 6000 series costs 1800 USD [147]. This high cost offers a poor performance-to-price ratio compared to mapping and consumer-grade receivers for UAM applications.

2.3.1.2 Mapping-grade GPS receivers

Mapping-grade GPS receivers are tailored for applications such as mapping, Geographic Information Systems (GIS), and land surveying, offering moderate accuracy and precision. These devices, like Trimble Juno series, come equipped with features like data logging, post-processing capabilities, and compatibility with GIS software packages.

However, mapping-grade receivers typically operate at frequencies below 1 Hz, resulting in a limited update rate that may lead to delayed or less accurate position fixes. For instance, the Trimble's mapping receivers operate at frequencies ranging from 0.1 to 0.5 Hz, impacting their suitability for dynamic aerial operations. Moreover, mapping-grade receivers often have moderate power requirements compared to survey-grade units, consuming approximately 10 to 25 watts nominally [148]. This makes them more energy-efficient but still may not meet the demands of drone UAM operations and aerospace applications that require rapid and precise positioning.

Cost-wise, mapping-grade GPS receivers vary widely, with prices typically starting at $2500 and ranging up to $6000 [148]. They offer real-time horizontal precision ranging from 2 - 10m, corrected horizontal network accuracy of 0.5 - 5m, and post-processed horizontal network accuracy of 0.3 - 15m [145], [148]. While they offer moderate accuracy and precision suitable for mapping and surveying tasks, their limited update rate and moderate power consumption limit their suitability for dynamic UAM operations.

2.3.1.3 Consumer/recreational-grade GPS receivers

Consumer-grade GPS receivers are characterized by their lower cost and accuracy than survey-grade and mapping-grade counterparts. Widely integrated into consumer electronics such as smartphones, handheld GPS devices, and automotive navigation systems, these receivers offer convenience and accessibility for general navigation purposes. Models like Garmin's 76 and 60 series fall into this category. Neo-6M and MTK3999 are devices that integrate the entire receiver architecture in a single-chip solution. The receivers cost anywhere from 10 to 250 USD.

Consumer-grade units typically operate with lower power consumption [145], on the order of 18-25 mW [149], making them suitable for various consumer applications. Due to their affordability and accessibility, consumer-grade GPS receivers are ideal for drone UAM applications. However, further research and development are needed to enhance their accuracy and precision [150] for aerospace use. This thesis contributes positively to the ongoing efforts in this regard by addressing key challenges and proposing potential solutions for integrating consumer-grade GPS technology into drone UAM systems.

2.4 ERROR IN GPS SYSTEMS

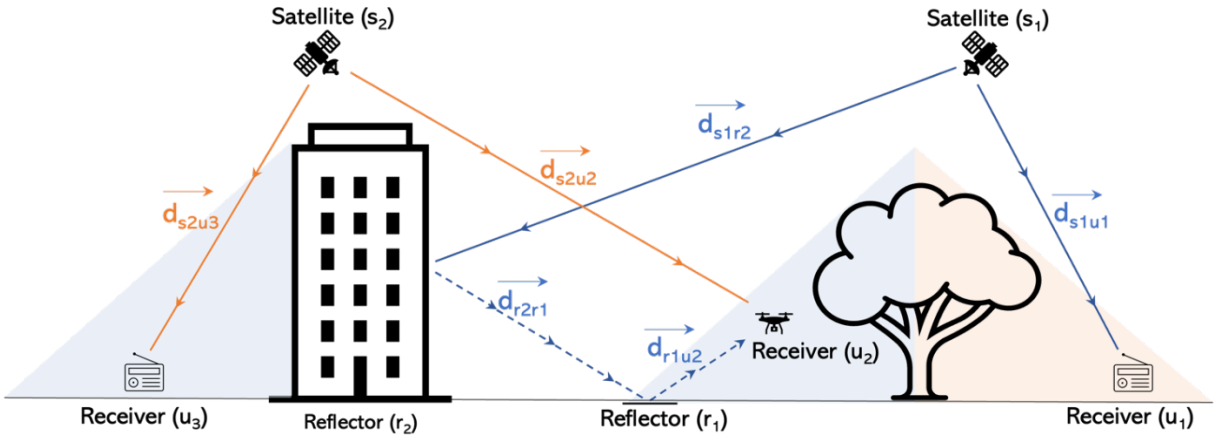

Figure 2-2. Illustration of GPS signal propagation paths demonstrating direct and multipath effects, where signals reflect off surfaces or are obstructed by obstacles, leading to potential reception delays and accuracy degradation in GPS receivers. Receivers U_3 and U_2 are in the shadow of satellite S_1. Receiver U_1 is in the shadow of satellite S_2. Receiver U_2 can only receive a reflected signal from satellite S1, contributing to longer propagation time and, consequently, a longer pseudo-range measurement.

The implications of the error outlined in Table 2-2 on drone localization systems are significant, particularly in safety-critical applications such as urban drone navigation. The errors include effects from the ionosphere, satellite clocks, ephemeris data, troposphere, receiver measurements, and multi-path interference. The unfiltered total RMS value of these errors is calculated to be 5.3 meters, which reduces to 5.1 meters after filtering, a meager 3.77% improvement. Consequently, simple filtering methods are insufficient to reduce the error magnitude. Even though the GPS receiver exhibits error rates relatively close to the 3m requirement, this is under ideal test conditions with a very well-calibrated and high-end survey-grade GPS receiver. Additionally, the cumulative effect of these errors can result in substantial deviations in position accuracy. Given the nature of these errors, they are not constant and vary substantially. In urban environments, where signal obstructions, multipath interference, and dense structures are prevalent, the observed error values tend to increase. This phenomenon can be attributed to factors such as signal blockage by tall buildings, reflections causing multipath effects, and increased signal attenuation, Figure 2-2, due to environmental conditions. These challenges are explored in the subsequent sections.

Table 2-2. Impact of different errors on average GPS receiver in ideal conditions[127]

Sources of Error	Magnitude of Error (meters)
Effects of Ionosphere	4
Satellite clocks	2.1
Ephemeris data	2.1
Troposphere impact	0.7
Receiver Measurements	0.5
Multi-path	
Unfiltered $total_{RMS}$ Value	5.3
filtered $total_{RMS}$ Value	5.1
Vertical error (68.3%) VDOP=2.5	12.8
Vertical error (95.5%) VDOP=2.5	25.6
Horizontal error (68.3%) VDOP=2.5	10.2
Horizontal error (95.5%) VDOP=2.5	20.4

Measurements conducted by the US Federal Aviation Administration over a 24-hour duration, it has been observed that in 95% of instances, the horizontal error remains below 7.4 meters, while the vertical error stays under 9.0 meters. The row highlighted in green is the major focus of this study. Row in yellow are studied in connection to their impact on experimental design but are not considered during algorithm optimization

Table 2-2 highlights specific errors of interest, with multipath errors making the most significant contribution. Given the necessity for high precision in aerospace applications, the magnitudes of these errors, at 12.8 and 10.2 meters, exceed the desired accuracy level by an order of magnitude, underscoring the criticality of addressing multipath interference. The 2nd order of significance doubles this error to 25.6 and 20.4, respectively. Moreover, signal masking emerges as another pivotal error source, particularly challenging in urban environments due to obstructed lines of sight to satellites. While multipath errors can be mitigated with access to signals from multiple satellites, urban signal masking presents a more complex problem. The exploration also extends to the utilization of multiple GPS receivers, necessitating an examination of consistency across these devices. Thus, multipath and signal masking stand out as significant factors warranting focused attention in this thesis. Other concerns, such as Low Signal-to-Noise Ratio (SNR), Ephemeris errors, and Carrier Wave degradation, although relevant, are not the primary emphasis of this research. The following sub-sections, 2.4.1 to 2.4.4 orders the sources in order of interest to this thesis.

2.4.1 *Signal masking*

One of the primary challenges in GPS signal reception is signal masking, occurring when obstacles such as buildings, trees, or terrain obstruct the line of sight between the GPS receiver and the satellites, leading to partial or complete signal loss and causing inaccuracies in position calculations [125], [151]–[153]. As depicted in Figure 2-2, receivers u_1 and u_3 are masked from receiving signals from satellites s_2 and s_1, respectively. For equation (11), With N satellites, we have N constraint equations for solving $\boldsymbol{W}_{GPS}$. For $N \geq 5$, the system is overdetermined. This leads to a narrower solution space for the iterative method, such as Newton's method, reducing the search area and allowing for faster convergence to a solution. The precision of the position estimation is improved with more signals. The additional constraints from the extra satellites help refine the solution, resulting in reduced positional uncertainty. This is reflected in lower Dilution of Precision (DOP) values, indicating better positioning accuracy. Additionally, the impact of clock mismatches between the receiver and satellites is mitigated with more signals. Clock errors introduce inaccuracies in the measured time differences between the receiver and satellites, affecting the calculated distances and, consequently, the position estimation. However, with a larger number of satellites, the effect of individual clock errors is averaged out, reducing their impact on the final position solution. Consequently, with signal masking, the receivers have fewer reference signals to perform trilateration, leading to imprecise and inaccurate positioning.

2.4.2 *Multipath interference*

Multipath interference arises when GPS signals bounce off surfaces, leading to multiple signal paths reaching the receiver, introducing errors by causing signal delay or phase shifts, especially problematic in urban environments with numerous reflective surfaces [154]. In Figure 2-2, the receiver u_2 receives a direct, $\overrightarrow{d_{s_2u_2}}$, signal from s_2. However, u_2 also receives a reflected signal from s_1, $\overrightarrow{d_{s_2r_2}} \rightarrow \overrightarrow{d_{r_2r_1}} \rightarrow \overrightarrow{d_{r_1u_2}}$, $\overrightarrow{d_{s_2r_2}}$ is the path from satellite s_2 to a primary reflector r_2, $\overrightarrow{d_{r_2r_1}}$is the path from primary to a secondary reflector, r_1, (s) and $\overrightarrow{d_{r1u2}}$ is the path from the secondary reflector to receiver.

$$\overrightarrow{d_{s_2r_2}} + \overrightarrow{d_{r_2r_1}} + \overrightarrow{d_{r_1u_2}} \geq \overrightarrow{d_{s_1u_2}} \tag{12}$$

By triangle inequality, as shown in (12) where $\overrightarrow{d_{s_1u_2}}$ is most direct path a signal can take from satellite s_1 to receiver r_2, the reflected path is longer, and consequently takes a longer time to reach the receiver. From (24), the effects of this delay are immediately apparent in terms of the larger error bounds and imprecise position estimates.

2.4.3 *Receiver and hardware variability*

GPS receivers may have inherent sensor variations due to factors such as manufacturing tolerances or temperature fluctuations, which introduce systematic errors that affect the consistency of GPS measurements [155]. Variations in GPS receiver components can introduce biases that affect measurement accuracy, requiring calibration and correction for a reliable GPS positioning [156]. The physical placement and orientation of GPS sensors within a device or system can significantly impact measurement accuracy, with misalignment or suboptimal sensor placement introducing errors, especially in applications where precise orientation matters [156]. Incorrect sensor orientation can cause drones to misinterpret trajectory, leading to deviations from intended flight paths, compromised operational efficiency, and increased risk of collisions or lost drones. These errors not only compromise the precision and reliability of positioning but also affect the overall performance and safety of drone operations.

2.4.4 *Receiver noise and interference*

Global Navigation Satellite System (GNSS) signals are inherently weak when they reach the Earth's surface. This low-power characteristic makes them highly susceptible to Radio Frequency Interference (RFI), posing a significant challenge to receiver performance. RFI can originate from various sources, including natural phenomena, man-made electronic devices, and communication systems. The impact of RFI is a severe degradation of receiver sensitivity and accuracy, leading to increased errors in positioning and timing measurements [157]–[159]. For drone localization systems, the implications of RFI extend beyond mere inconvenience. The precision of drone navigation and the safety of its operations are directly compromised by interference, potentially resulting in navigational inaccuracies, loss of signal lock, and even system failure.

2.5 OPPORTUNITIES FOR RESEARCH

Section 2.5.1 explores the limitations of existing GPS mitigation techniques and the potential for innovative solutions in the field. Recent research has suggested using advanced machine learning models, such as graph-based neural networks [111], convolutional neural networks (CNNs) [160], [161], and ML-augmented particle filters [162]–[164], primarily developed for automotive applications, enhances GPS accuracy and reliability in urban areas. In response to these developments, this thesis proposes an adapted approach that employs a filter-enhanced composite neural network, integrating recurrent neural networks (RNNs) with a subsequent deep neural network (DNN) layer. This combination aims to leverage the strengths of each model to improve GPS signal processing and accuracy significantly. Section 7.2 will delve into the rationale behind selecting this specific model configuration, discussing how it addresses the shortcomings of existing technologies and its suitability for drone localization in dense urban settings.

2.5.1 *Unsuitability of existing mitigation techniques*

Existing mitigation techniques for improving GPS positioning accuracy include Differential GPS (DGPS), Real-Time Kinematic (RTK) corrections, and Precise Point Positioning (PPP) techniques. These methods aim to enhance the reliability and precision of GPS-based localization systems in various applications. Despite the advancements offered by these techniques in various domains, they are unsuitable for a GPS-based localization system for drones due to several limitations. This section will elucidate why these correction techniques are unsuitable for UAM operations.

2.5.1.1 Differential GPS (DGPS)

Differential GPS (DGPS) methodologies leverage reference station networks and satellite-based augmentation systems (SBAS) like WAAS, EGNOS, and MSAS to refine GPS positioning accuracy [165], [166]. DGPS achieves this by juxtaposing measurements from reference stations with those from the receiver, enabling corrections for factors such as atmospheric delays and satellite clock inaccuracies [167, p. 33].

One significant challenge for DGPS in drone and aerospace applications is the limited coverage of reference station networks and SBAS, particularly in remote or sparsely populated areas where drone operations may be conducted. This limitation becomes more pronounced in urban environments, where signal blockage from tall buildings and structures can further reduce coverage, leading to intermittent or unreliable correction signals. DGPS heavily relies on ground-based infrastructure [167], posing challenges in scenarios where access to reference stations is restricted or unavailable. In urban operations, where airspace may be congested and ground access limited, relying solely on ground-based correction signals may not be practical. Moreover, DGPS requires a clear line of sight between the receiver and reference stations to ensure accurate corrections [168], making it less effective in environments with obstructed visibility. Effective DGPS implementation necessitates the use of specialized receivers capable of processing correction data from reference stations or SBAS. These receivers often cost more than standard GPS receivers [169], adding to the overall expenses of drone and aerospace operations. While DGPS offers significant improvements in GPS positioning accuracy through correction techniques for large aircraft operations near airports, limitations such as coverage constraints, reliance on ground infrastructure, and requiring specialized and costly receivers challenge its suitability for drone operations.

2.5.1.2 Real-Time Kinematic (RTK) correction

Real-time kinematic (RTK) correction methods involve transmitting correction data from a base station to the receiver in real time, enabling centimeter-level positioning accuracy. RTK offers potentially significant advantages for achieving high-precision positioning in real-time applications.

RTK correction relies on a direct line of sight between the base station and the receiver [170], [171]. In urban environments maintaining a clear line of sight is challenging. Signal obstruction from buildings and structures can degrade the quality of correction signals, leading to intermittent or unreliable corrections and affecting the overall accuracy of drone positioning. The effective range of RTK correction signals is inherently limited [170], determined by factors such as signal frequency and atmospheric conditions [172]. These limitations make RTK less suitable for applications where drones may operate beyond the range of the base station, such as long-range

delivery missions. In scenarios where drones need to cover expansive areas or operate in remote locations with sparse ground infrastructure, maintaining continuous RTK corrections becomes impractical, limiting its utility for drone applications. Achieving reliable RTK correction coverage requires deploying multiple base stations strategically throughout the operating environment to ensure adequate signal coverage. This necessitates substantial infrastructure investment, including the purchase, installation, and maintenance of base stations, increasing the overall cost of implementing RTK correction for drone operations. Additionally, ongoing operational costs, such as subscription fees for RTK correction services or network maintenance, can further contribute to the overall cost of using RTK for drone navigation. These cost considerations pose significant challenges, particularly for drone operators in UAM applications, where cost-effectiveness and scalability are critical factors.

2.5.1.3 Precise Point Positioning (PPP)

PPP techniques represent a sophisticated approach to achieving highly accurate positioning without the need for ground-based reference stations. PPP relies on precise satellite orbit and clock correction data from specialized service providers [173], [174]. By utilizing this correction data, PPP algorithms can calculate the drone's position with a high level of accuracy, often in the sub-1-centimeter range [175], depending on various factors such as satellite geometry and signal quality. One of the key advantages of PPP is its ability to provide accurate positioning globally, without the need for infrastructure deployment or reliance on nearby reference stations.

PPP typically requires a longer convergence time [173]. Convergence time refers to the duration it takes for the PPP algorithm to compute a reliable position solution with a specified level of accuracy. In dynamic environments such as urban areas, where drones may need to adjust their position and orientation to navigate safely rapidly, the longer convergence time of PPP can pose challenges. Delays in obtaining accurate position updates may result in suboptimal navigation performance and potentially compromise the safety of drone operations. The availability and geometry of satellites visible to the receiver heavily influences the performance of PPP. In urban environments characterized by tall buildings, narrow streets, and dense foliage, the visibility of satellites may be obstructed or limited, leading to degraded positioning accuracy, potentially worser than conventional GPS [175], [176]. Additionally, the geometry of satellite constellations

can vary depending on the receiver's location and the time of day, further impacting the reliability of PPP solutions. In scenarios where satellite visibility is restricted or compromised, PPP may struggle to maintain accurate positioning, making it less suitable for precision drone operations in urban environments.

2.5.1.4 Satellite-Based Augmentation Systems (SBAS)

SBAS, including systems like WAAS [166], enhance GPS accuracy through corrections transmitted by geostationary satellites [177] . These systems improve position accuracy by providing corrections for GPS signal errors caused by ionospheric disturbances, timing, and satellite orbit errors. SBAS is particularly effective in open skies where the line of sight to the geostationary satellites is unobstructed [178].

The effectiveness of SBAS is significantly reduced in urban settings where high-rise buildings and dense infrastructures frequently obstruct the line of sight to the satellites. Such obstructions not only hinder the reception of the GPS signals but also the SBAS correction signals, leading to delays and inaccuracies in the corrected data. Additionally, the urban canyon effect, where signals reflect off buildings causing multipath errors, exacerbates the challenge, as SBAS systems are not designed to handle such complex signal distortions. The reliance on ground stations for generating corrections also adds to operational costs and limits the feasibility of expanding SBAS coverage, particularly in regions lacking the necessary infrastructure [179]. Consequently, while SBAS provides notable improvements in open areas, its limitations in urban scenarios may lead to unreliable positioning for drones, potentially compromising navigational accuracy and operational safety.

2.6 EMPLOYING NEURAL NETWORKS TO AUGMENT DRONE LOCALIZATION

The advancement of UAV localization systems has greatly benefited from the incorporation of Machine Learning (ML) and Deep Learning (DL) techniques [180]. ML and DL algorithms excel in recognizing patterns and data-driven decision-making, which are essential characteristics for UAV navigation. These computational methodologies have shown unparalleled capabilities in handling complex, non-linear problems, making them ideal for improving the precision and efficiency of the UAV navigation [181], [182]. The rationale behind the applicability of ANN and

DNN [80], [183] in this domain is anchored on several foundational aspects that align with UAV operations. Existing prior art establishes the validity of using machine learning to augment GPS systems [80], [181], [184]–[186].

Deep learning neural network (DNN) models extend upon the principles of ML by incorporating multiple layers of transformations, enabling them to capture intricate patterns within data. Mathematically, a single layer in a deep neural network [187] is represented as:

$$\boldsymbol{h}^{(l)} = g(\boldsymbol{W}^{(l)} * \boldsymbol{h}^{(l-1)} * \boldsymbol{b}^{(l)}) \tag{13}$$

where $\boldsymbol{h}^{(l)}$ is the activation of layer *l*, $\boldsymbol{W}^{(l)}$ and $\boldsymbol{b}^{(l)}$ are the weight matrix and bias vector of layer *l* respectively, and *g* is the activation function. This formulation can be applied to UAV GPS data by interpreting the weight matrix W, as analogous to the rotation matrix R (refer to page 204), with the bias vector $\vec{b}$ adjusting for offsets akin to calibration corrections in sensor data:

$$\vec{a}_N = g * (R * \vec{a}_B + b) \tag{14}$$

where g is an activation function introducing non-linearity, essential for modeling complex behaviors. In the context of GPS error correction, the equation can be extended to account for error propagation and correction mechanisms.

$$\overrightarrow{gps}_c = g * (R_W * \overrightarrow{gps}_u + b) \tag{15}$$

The vector $\overrightarrow{\mathrm{gps}}_{\mathrm{c}}$represents the corrected GPS data, while $\overrightarrow{\mathrm{gps}}_{\mathrm{u}}$denotes the raw GPS measurements. By applying the transformation R_{W} to the raw measurements $\overrightarrow{\mathrm{gps}}_{\mathrm{u}}$ potential errors inherent in the GPS data, such as drift or noise, can be mitigated or compensated for. The bias vector *b* allows for additional adjustments to account for systematic errors or biases in the sensor measurements. Equation (15) informs us that any ML algorithm we propose must have a regression layer as the last layer before the output. Furthermore, the activation function *g* introduces non-linearity into the correction process, which is essential for modeling the complex relationship

between the raw GPS measurements and the corrected data. This non-linearity enables the correction algorithm to adapt to varying environmental conditions and sensor characteristics, thereby improving the accuracy and reliability of the corrected GPS data. By treating the correction process as a transformation operation, errors in the raw GPS measurements can be effectively identified and corrected, leading to more accurate and reliable positioning information for UAVs and other applications. Overall, this formulation provides a systematic approach to GPS error correction by leveraging principles from neural network architectures.

However, there is a notable gap in exploring the potential of Recurrent Neural Networks (RNNs), particularly Long Short-Term Memory (LSTM) and RNN, for localization accuracy correction and multi-path mitigation [80]. Despite the demonstrated promise of LSTM in examining time-series aerospace telemetry data, including GPS, [141], [185], the availability of public time-series aerospace GPS data remains insufficient [80], [186], posing significant challenges to research. GPS systems inherently use temporal data in their function, and use of correction methodologies like RTK establishes the validity of using historical time and motion data to augment GPS. An analysis of research publications spanning from 2000 to 2021, as depicted in Figure 2-3, delineates the distribution of papers across different architectures. Among the 125 total academic. papers examined in [80], only a fraction of these papers, accounting for 19 out of 75, delve into the potential applications of LSTM and/or RNN in the context of Global Navigation Satellite System (GNSS) error correction operations, underscoring a glaring gap in exploration within aerospace navigation research. Other deep learning architectures have been employed to fuse temporal sensor data [188], enhancing the accuracy of state estimation over time [189]. By leveraging deep learning, aerospace navigation systems can achieve robust performance in dynamic environments, where traditional fusion methods may struggle to capture intricate relationships between sensor measurements. Considering these observations, there exists a significant opportunity for research to delve into the potential of RNNs, particularly LSTM variants, in addressing GPS localization accuracy correction and multi-path mitigation challenges within aerospace navigation.

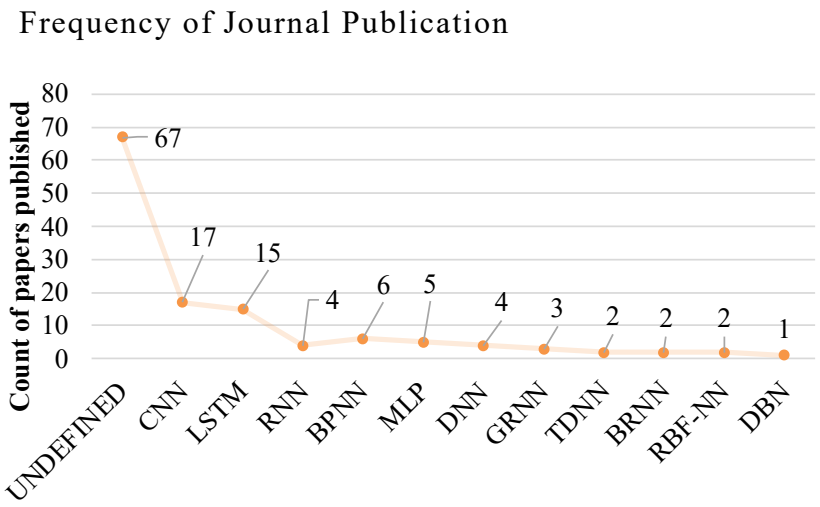

Figure 2-3. Frequency distribution of methods favored for publication in research papers. Data sourced from [80]

2.7 CHAPTER SUMMARY

This chapter provided an overview of the basic operating principles of GPS, including the mechanics of trilateration and its significance in localization. We discussed the impact of receiver quality on localization accuracy and explored the utility of NMEA data for enhancing GPS precision. Additionally, the chapter addressed the key errors of interest for drone localization—signal masking, multipath, and receiver variance errors—detailing their implications for urban drone navigation. We also evaluated various GPS positioning augmenting systems, noting their limitations for drone applications in urban settings. The unsuitability of these systems for drones underscored the necessity for innovative solutions. In response, we proposed the integration of machine learning. ML methods have significantly advanced the field of localization. This evolution has been particularly evident in the application of Artificial Neural Networks (ANNs) and Deep Learning (DL) techniques. We also advance the notion of using LSTM networks in the correction process. The subsequent Chapter 3 delves into the design and development of the proposed ML algorithm.

CHAPTER 3. THEORETICAL DESIGN OF ML ALGORITHM

This chapter introduces the theoretical underpinnings and the design strategy of the machine learning (ML) algorithm tailored for GPS localization improvement, particularly focusing on addressing the challenges of localization accuracy and multi-path error correction in aerospace applications. It outlines the algorithm's conceptual framework, emphasizing its application within MATLAB for both development and evaluative purposes.

3.1 ALGORITHM OVERVIEW

The GPS correction algorithm developed in this thesis, illustrated in Figure 3-1, is an integrated approach to enhancing GPS sensor data accuracy through a multi-stage correction process. It represents a fusion of temporal dynamics modeling using Long Short-Term Memory (LSTM) networks—a variant of Recurrent Neural Networks (RNN)—with Deep Neural Networks (DNN) for comprehensive noise and error correction in GPS sensor data. The algorithm is designed to address both immediate, high-frequency errors and more persistent, long-term inaccuracies that GPS sensors encounter in various operational environments.

The raw data undergoes preliminary filtering using a Windowed Inverse Variance Weighted Correction filter to reduce noise, dynamically adjusted based on the environment classified by an upstream classifier. This classifier dictates the initial correction by assessing the GPS data collection environment, affecting subsequent correction stages, and refining the process for various operational contexts. The corrected data is then flattened, normalized based on predictor characteristics, and fed into an LSTM, which predicts altitude, angular, and offset errors. Subsequently, these predictions are processed through a Deep Neural Network (DNN) model that works on integrating the temporal predicted errors with the data-driven error prediction. An error correction module then uses the inverse of the haversine process (see equation (27)) to generate a corrected set of coordinates. The refined GPS dataset is then compared against a ground truth GPS to confirm accuracy. The final algorithm does this automatically to monitor the model’s confidence. However, for the purpose of this thesis, this comparator is not implemented. The user performed the comparison manually and tuned available parameters to optimize performance.

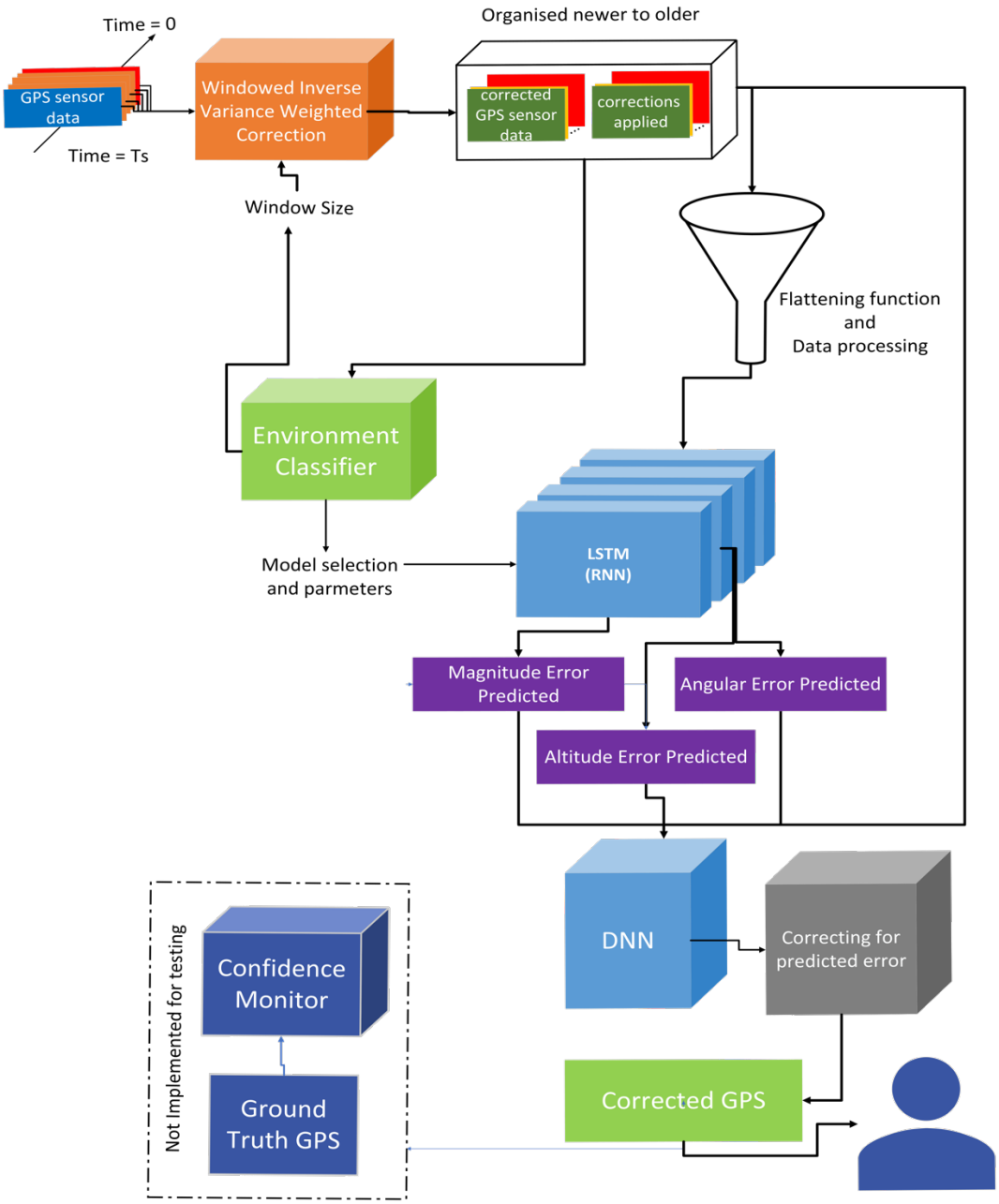

Figure 3-1. Composite IRNN-DNN Framework for GPS Sensor Data Correction. This flowchart illustrates a multi-tiered approach to refining GPS data, starting with raw input processed by an inverse variance weighted filter and categorized by environmental context. The data is then advanced through LSTM (RNN) and DNN stages for temporal and non-sequential error correction, culminating in a GPS output closely matching the ground truth. Each algorithmic component, from the initial filtering to the composite error prediction, is integral to the model's capacity to deliver precise navigational data.

The LSTM model, a specialized form of RNN depicted in the subsequent stage of Figure 3-1, captures the temporal dynamics of the GPS errors. It specifically addresses errors with a

temporal component, such as periodic interference from multi-path effects or signal dropouts. The model's ability to process time-series data makes it ideally suited for anticipating and correcting short-term, high-frequency errors that are temporally correlated. In conjunction with the LSTM, a DNN model is employed to composite the output and handle non-sequential errors. The DNN accounts for sensor-specific noise that might be positional, temporal, or computational in nature. It also tackles DC offsets and other environmental noise that is not accounted for by the LSTM. In the following sections, each of these sub-components of the algorithm is further discussed.

3.2 WINDOWED INVERSE VARIANCE WEIGHTED CORRECTION

The windowed inverse variance filter algorithm, also referred to as the inverse variance filter in the thesis, is rooted in the fundamental concept of statistical weighting, where the reliability of each measurement is determined by its variance [190]. By inversely weighting measurements based on their variance, the algorithm assigns greater importance to more accurate and less variable data points while downplaying the influence of noisy or uncertain measurements. This approach ensures that the final corrected values are more representative of the true underlying data distribution. Accordingly, when estimating a parameter from a set of measurements, those with lower variance (i.e., higher precision) should contribute more to the estimation process, as they provide more reliable information. Conversely, measurements with higher variance (i.e., lower precision) should be assigned less weight, as they are more likely to be influenced by random noise or systematic errors.

The inverse variance filter constitutes a pivotal component within the algorithmic framework, designed to rectify sensor measurements by leveraging the principles of inverse variance weighting. Unlike conventional approaches that consider all historical samples from t=0 [190] or only apply the filter to the current value [191]–[194], the proposed method employs a dynamic window of values denoted as $\boldsymbol{W}$ characterized by a predetermined size $\boldsymbol{m}$. Within this window, the variance of sensor measurements for each parameter is meticulously analyzed to discern trends and fluctuations. The sensor measurements at time, t, for all sensors, $\boldsymbol{S}^t$, is represented as:

$$\boldsymbol{S}^t = \{s_1^t, s_2^t, s_3^t, s_4^t, s_5^t, \dots\} \tag{16}$$

$$s_n^t = \{{}_n^t s_1, {}_n^t s_2, {}_n^t s_3, \dots, {}_n^t s_k\}^T \tag{17}$$

$$\tilde{\boldsymbol{S}}^t = \boldsymbol{S}^t + C_k^t \tag{18}$$

where parameters of an individual sensor n at time t, the measurements across all parameters k are denoted in column vector as, s_n^t. The corrected sensor measurements, $\tilde{\boldsymbol{S}}^t$, are obtained by adding the correction C_k^t to $\boldsymbol{S}^t$. Then for each parameter j within sensor i, calculate the variance σ_{ij}^2 over the window $\boldsymbol{W}$ as in(19).

$$\sigma_{ij}^2 = \frac{1}{m-1} \sum_{k=t-m}^{t-1} \left(S_{ij}^k - \mu_{ij}\right)^2 \tag{19}$$

$$\mu_{ij} = \frac{1}{m} \sum_{k=t-m}^{t-1} S_{ij}^k \tag{20}$$

where μ_{ij} is the mean value of parameter j in sensor i over the window $\boldsymbol{W}$ calculated as shown in (20). The weight w_{ij} for each parameter in sensor is inversely proportional to the variance is:

$$w_{ij} = \frac{1}{\sigma_{ij}^2 + \epsilon} \tag{21}$$

where ϵ is a small constant added to prevent division by zero in the case of zero variance. The deviation, ΔS_{ij}^t, of the current measurement from its mean is given by (22).

$$\Delta S_{ij}^{t} = S_{ij}^{t} - \mu_{ij} \tag{22}$$

$$C_{ij} = w_{ij} \times \Delta S_{ij}^{t} \tag{23}$$

where C_{ij} correction term applied to each measurement. Following the correction process, the corrections matrix applied C_k^t and the corresponding corrected data $\tilde{\boldsymbol{S}}^t$ are concatenated to form a unified dataset. This concatenated dataset is then passed on to the subsequent stages of the algorithm for further processing and analysis. The inverse variance filter algorithm is designed to be scalable, accommodating variations in the number of sensors and parameters. The algorithm's scalability is attributed to its modular structure, enabling seamless integration of additional sensors or parameters without necessitating substantial modifications to the underlying framework.

3.3 NEURAL NETWORK

In this thesis, we introduce an Integrated Recurrent Neural Network-Deep Neural Network (IRNN-DNN) model, for the correction of GPS data by harnessing temporal dynamics and mitigating environmental noise effects. This model is specifically designed to improve GPS performance when hovering. This model is paramount to the correction algorithm, intricately capturing high-frequency fluctuations and compensating for the persistent errors associated with GPS signals.

3.3.1.1 Neural network design

The IRNN-DNN model processes inputs within a structured three-dimensional matrix, denoted as $\mathcal{M}$, which encapsulates multi-sensor time-series data. This matrix is formally defined as:

$$\mathcal{M} \in \mathbb{R}^{NxPxW} \tag{24}$$

where N represents the number of GPS sensors on the drone (with N = 5 in our scenario), P signifies the number of monitored parameters per GPS system (with $P = 11$ as the designated key parameters in this study), and W is the window size corresponding to the number of sequential

data points considered for each parameter (with $W = 25$ chosen for initial training and testing purposes). Each element m_{npw} corresponds to a specific value of the p^{th} parameter of the n^{th} sensor at time $w * t_s$ from the current sample time.

$$\mathcal{M}^{NxPX1} = [\tilde{\boldsymbol{S}}^{1} \quad \boldsymbol{C^1}] \tag{25}$$

The selection of $W = 25$ is predicated on preliminary observations indicating that a 2.5-second window typically includes sufficient data to observe counteracting error signals in an urban environment. By examining contiguous 2.5-second intervals of GPS data, the model proposed can recognize and assimilate the sporadic nature of GPS errors. This duration has been empirically observed to encompass the periodic characteristics of the error signals, allowing for capturing both immediate and delayed error effects. The LSTM by considering the multiple 2.5 seconds windows, can predict the larger periodic error contributions, The validation of this choice is an integral part of the thesis and warrants a dedicated investigation. Section 6.2 examines this choice of window size. In the final algorithm implementation, this parameter can be autotuned by the model during batch training and validation tests. The preliminary selection is based on visual inspection of error signals across various environments, with the justification that it captures an adequate representation of the underlying error dynamics. Following convention, the input to the IRNN-DNN can be represented by the following equation:

$$\mathbf{X} = \mathcal{F}(\boldsymbol{\mathcal{M}}) \tag{26}$$

where $\mathcal{F}(.)$ is a flattening function, transforming the 3D sensor data matrix into a 2D matrix suitable for neural network processing. This transformation, while appearing simple, is crucial in aligning the data for the learning apparatus. The architecture of the neural network comprises layers that specialize in interpreting these sequences. The recurrent layers are specifically designed to discern the temporal correlation within **X**, the flattened input matrix to the neural network. The preprocessing stage converts this 3D matrix into a 2D format by flattening it into a shape of 250 columns and 11 rows in our study. The flattening function is also important for compatibility with MATLAB, where the data will be processed, and the model trained. Figure 3-2 illustrates the

IRNN-DNN model architecture being designed and implemented in MATLAB, commencing with the input of corrected GPS data and associated corrections derived from the inverse variance weighted filter. This input, encapsulated within a three-dimensional matrix, undergoes a transformation via a Flatten Layer, rendering it into a format conducive to LSTM analysis. A critical aspect of the preprocessing step is scaling the some of the raw NMEA data but not others. Latitude, longitude, and altitude components are transformed to the NEU frame. This transformation normalizes the positional data, but not the raw NMEA components describing the quality of the fix. The raw, scalable NMEA signal quality indicators act as predictors and are normalized based on their theoretical maximum values. Non-scalable parameters, like antenna status, are sent to the ML training without any normalization. The NEU frame represents a local tangent plane where positions are described relative to a local reference point, effectively mitigating geospatial biases. This is crucial for normalizing these components without tying the model's learning capacity to any specific geographical location.

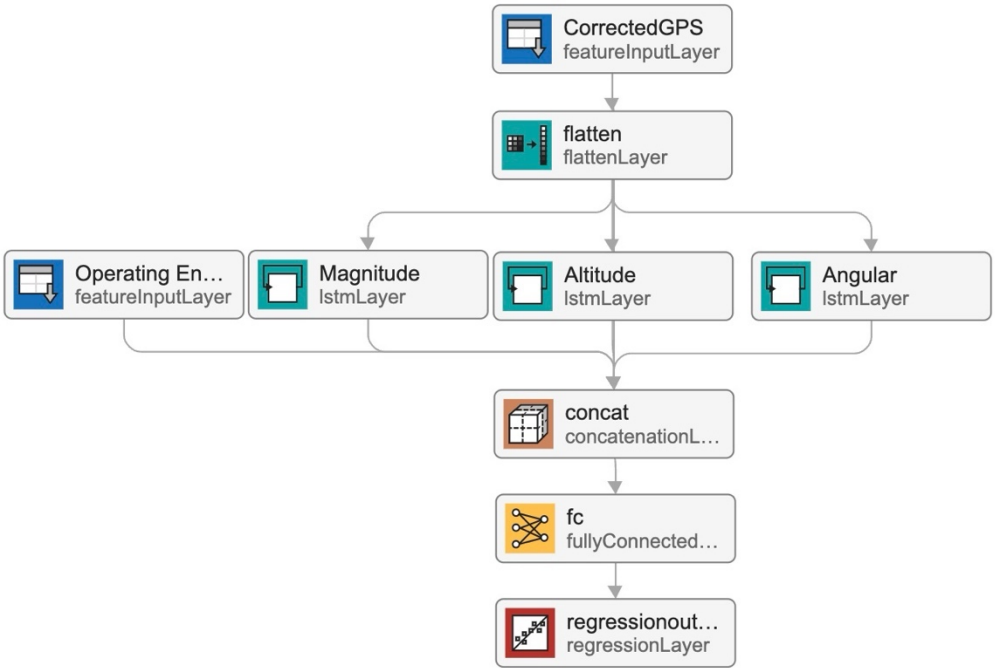

Figure 3-2. Schematic of the Enhanced IRNN-DNN Model for GPS Data Correction. This diagram depicts the neural network architecture implemented in MATLAB, illustrating the sequential process from time-series GPS data input to the final error prediction, showcasing the synergy between LSTM processing, environmental context integration, and dense network prediction for predicting errors in a GPS sensor.

The LSTM's capacity for information retention across intervals is critical for pinpointing error sequences inherent to GPS signals. Each LSTM module is dedicated to detecting and analyzing specific types of errors—altitude, angular, and magnitude—across all the data streams. These LSTM layers effectively identify temporal anomalies and errors which are essential for correcting transient and frequent disturbances typical in urban GPS data. Concurrently, the Feature Input Layer processes output from the environmental classifier, which includes locational labels and confidence predictions. This data is then concatenated with the LSTM outputs, enriching the model with contextual environmental information. The Concatenation Layer fuses the LSTM outputs with the environmental context, passing this integrated data to the Dense Neural Network (DNN) structure. This is shown in Figure 3-2 as a fully connected deep layer that synthesizes the temporal and contextual features into a unified feature set. The final stage of the IRNN-DNN model is marked by a Regression Layer, where the high-dimensional feature space is distilled into cumulative correction to the GPS estimates. This layer outputs continuous values that signify the model's best estimation of the GPS errors at the sample time of the system. The output is configured to predict three values of residual magnitude error, angular error, and residual altitude, as described in Figure 5-8. Utilizing standard pre-built modules in MATLAB, the IRNN-DNN model's development and testing phases are expedited, emphasizing the operational validation of the model. The IRNN-DNN model's MATLAB implementation signifies a considered balance between leveraging existing neural network frameworks and innovating within those narrow confines, as a proof of strategy that the specific combination of a windowed inverse variance filter with an LSTM and DNN ML model can serve effective predictors of errors in complex urban environments in real time. This balance allows for validating the model's conceptual integrity and the practical refinement necessary for real-world GPS data correction applications.

3.4 COMBINED ALGORITHM IMPLEMENTATION

The schematic provided in Figure 3-3 forms the basis for the algorithm's implementation on a drone platform for testing. It leverages a microcontroller for the initial acquisition and parsing of GPS data. A dedicated data collection unit interfaces with GPS sensors, funneling NMEA messages to the embedded flight computer at a rate of 10 Hz. The sensor employs a co-processor to perform the trilateration calculations discussed in section 2.1.3.1. Upon reception, the microcontroller undertakes the critical task of parsing the NMEA data. It systematically extracts

pertinent parameters and structures the data into a format primed for advanced processing. This transformation is vital for aligning the incoming data stream with the algorithm's requirements. Additionally, both raw and parsed data, alongside auxiliary information such as pseudorange and residuals, are archived in the local storage for subsequent analysis. Once parsed, the data is temporarily stored in volatile memory within the microcontroller, providing a buffer for the subsequent transmission and processing stages. This intermediate storage is necessary to manage data flow and prevent loss during high-frequency collection periods, where the sensor may send data at a rate higher than 10 Hz. This approach not only preserves data integrity but also furnishes a rich dataset for potential future examination. The performance and capabilities of the chosen microcontroller are of paramount importance, with a comprehensive performance review slated for the following chapter.

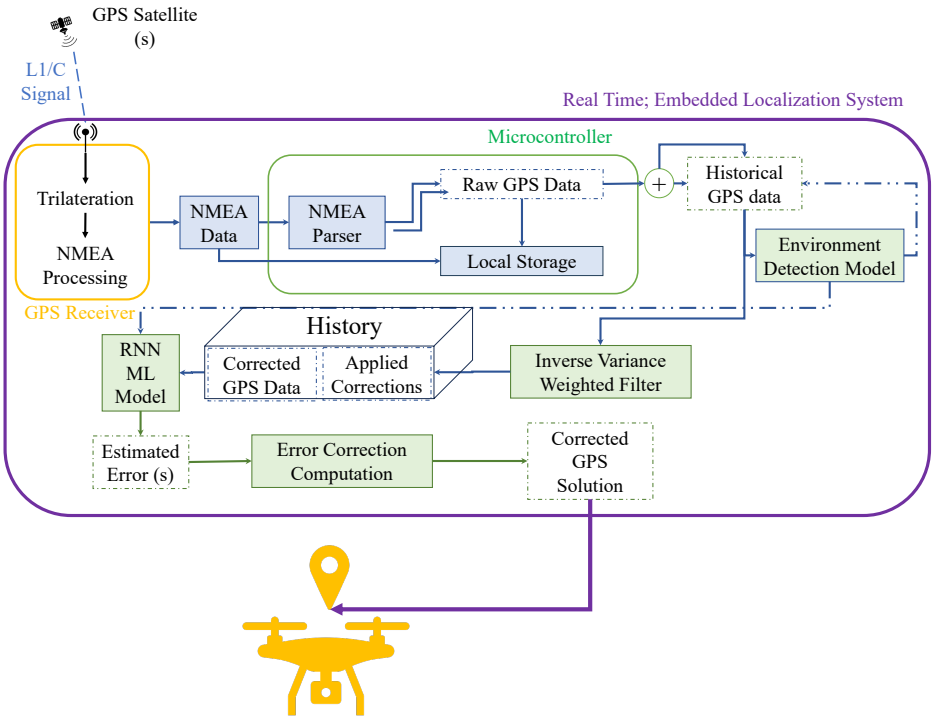

Figure 3-3. Real-Time Embedded GPS DAQ and Correction System for UAVs. These schematic details the flow from GPS data acquisition to error correction within a UAV-specific embedded system. It starts with a microcontroller receiving NMEA data at 10 Hz, parsing it for subsequent processing. The system's co-processor executes trilateration as per Section 2.1.4, while parsed data is stored locally. The microcontroller buffers data for error correction computation using an RNN ML model, with performance details to follow in the next chapter.

The microcontroller then forwards the curated data to an embedded flight computer, which serves as the primary processing unit. Here, the IRNN-DNN Machine Learning (ML) Model is deployed, delving into the GPS data's temporal patterns to identify and correct errors. Operating under the constraints of onboard computing resources, the model dissects the intricacies of GPS signal fluctuations to establish a more accurate positional fix. In tandem with the IRNN-DNN ML Model, the Environment Detection Model runs classification algorithms to discern the operational environment. It intelligently tailors the algorithmic parameters to enhance GPS performance, accounting for extrinsic factors that could affect signal integrity, such as urban landscapes or atmospheric anomalies. The process culminates in the Error Correction Computation phase. Here, the model consolidates inputs from both the IRNN-DNN ML Model and the Environment Detection Model to adjust the GPS data. The refined output, representing the corrected GPS location, is then provisioned for real-time navigation and UAV positional tasks, showcasing the system's readiness for operational deployment.

The GPS Data Acquisition (DAQ) system is designed with a rigorous commitment to adhere to stringent weight and power specifications. This dedication is crucial for maintaining the UAV's optimal flight dynamics, thus ensuring that its operational capabilities are amplified without impairing its performance. The algorithm's architecture, which integrates lightweight yet potent components, is adept at running on low-power microcontrollers and microprocessors. This facilitates an efficient localization process that conserves resources without compromising the system’s efficacy. The GPS DAQ system's algorithmic design, as conceived and developed within the MATLAB environment, reflects a sophisticated blend of computational efficiency and algorithmic portability. MATLAB's intrinsic versatility allows for the design, modeling, training, simulation, and validation of complex machine learning models, such as the IRNN-DNN utilized in this GPS correction system. This model's portability is a central feature of its utility, designed from the ground up to be transferrable across a spectrum of computing platforms, each with their unique constraints and capabilities. The portability of the MATLAB-generated algorithm is a considerable advantage, primarily due to MATLAB’s ability to compile models into a range of formats compatible with different target environments. For instance, MATLAB's automatic code generation can translate the high-level IRNN-DNN model into C code, which can then be refined and optimized to run efficiently on microcontrollers and embedded processors. This code, when deployed, retains the mathematical precision and logic of the MATLAB environment while being

tailored for the specific computational architecture of the target device. Optimizing software components to operate across diverse compute devices involves an intricate understanding of each device's capabilities. Microcontrollers, typically constrained by power and processing capacity, require a lean version of the algorithm that focuses on critical computational tasks to minimize latency and power draw. Meanwhile, more robust embedded flight computers, with greater processing resources, can handle more complex versions of the algorithm, including sophisticated error correction computation and the integration of real-time environmental data. MATLAB aids in this optimization process through specialized toolboxes and compilers designed to fine-tune the performance of algorithms on specific hardware. Furthermore, MATLAB's profiler tools can identify bottlenecks in the algorithm, allowing us to restructure the code to avoid performance lags, ensuring that each software component operates at peak efficiency.

3.5 CHAPTER SUMMARY

This chapter elaborates on the theoretical design and practical implementation of a ML algorithm aimed at enhancing GPS localization accuracy. The subsequent chapter will delve into the functional design of the GPS Data Acquisition system hardware. It will elaborate on the system's hardware and software architecture, detailing the incorporation of embedded controllers and the practical deployment of the algorithm across UAV platforms.

CHAPTER 4. FUNCTIONAL DESIGN OF GPS DAQ SYSTEM AND DRONE PLATFORM

4.1 DRONE PLATFORM

Table 4-1. Drone component specification by frame used

Specification	X500 V2	S500
Motors	2216 KV920 Motor	2216 KV920 (V2) Motor
ESC	BLHeli S ESC 20A	BLHeli S ESC 20A
Battery	4S Lipo Battery 5200mAh 50C	4S Lipo Battery 5200mAh 50C
Receiver	RadioMaster R88 V2 Frsky D8	RadioMaster R81 Frsky D8
Onboard GPS	M8N	-
Flight Computer	Pixhawk 6C	Pixhawk 6C
Mission Payload computer	Teensy 4.1 + Raspberry Pi 4	Teensy 4.1 + Raspberry Pi 4
Flight Time (mins)	18	12

Based on well-established performance characteristics, documented stability, precision, and repeatability across various studies [195]–[197], two drones, the X500 V2 and S500 V2, from Holybro running PX4 autopilot [198], [199]q, were chosen for comprehensive testing in this study. These drones were assembled from pre-designed kits, featuring a carbon fiber frame, 2216 KV920 brushless motors, and AV2-BLHeli S 20A ESCs (Electronic Speed Controllers). The Pixhawk 6C served as the designated flight controller, operating with the PX4 open-source firmware. Communication between the ground station and the drone was facilitated through a 915MHz SiK telemetry radio. X500V2 was selected as the platform of choice for gathering data and testing due to its longer flight time and higher payload capacity when compared to the S500.

4.1.1 *Establishing baseline performance of the drone platform*

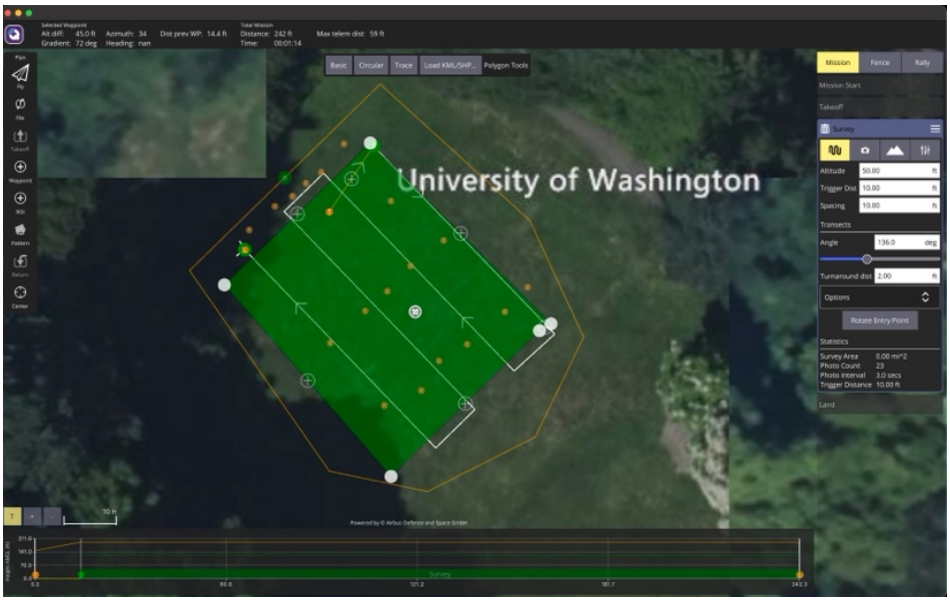

Figure 4-1. Programmed Linear Survey on QGroundControl. This screenshot captures a planned flight mission for the X500V2 drone within QGroundControl, highlighting the corridor scan strategy for assessing flight characteristics.

In this section, we evaluate the drone's GPS accuracy by analyzing its adherence to a pre-defined linear path set through the QGroundControl application. This test is crucial for assessing the reliability of the GPS system under controlled conditions. Figure 4-2 presents a three-dimensional analysis of the drone's flight path, comparing GPS-recorded positions (red dots), the path as fused from onboard sensors, and the intended trajectory as programmed via QGroundControl (Figure 4-1). The graphs are plotted with 'North' and 'East' on the horizontal plane and 'Altitude AGL (Above Ground Level)' on the vertical axis. The accuracy of the drone's flight path was verified against fused flight estimate as reported by the PX4 system, and altitude discrepancies were measured using image data. To ensure the reliability of our findings, each axis—x, y, and z in the NEU frame—was tested individually in separate flights

An examination of the drone's flight path reveals significant insights into the GPS sensor performance and navigational control. The plotted trajectory in Figure 4-2 demonstrates a clear deviation from the intended target flight path, signifying a discrepancy that could be attributed to a multitude of factors including GPS signal inaccuracies, potential errors in the drone's flight control system, or even environmental influences that could affect the drone's adherence to its

programmed route. Notably, the GPS fixes, indicated by red dots, are distributed erratically around the measured fused path, hinting at a degree of imprecision within the GPS data itself. This scatter, particularly evident in the vertical dimension, raises concerns about the drone's ability to maintain a steady altitude, potentially due to common issues like barometric pressure fluctuations. Figure 4-3 shows how drone's actual altitude is around 5 feet AGL, when the flight plan called for a of 10 feet AGL. Furthermore, the actual path taken by the drone, as synthesized from various sensor data inputs from the drone using its own flight controller software, appears to diverge from the designated route. Another area of concern is the evident altitude variability throughout the drone's flight, suggesting difficulties in maintaining a consistent flight level—a challenge that may originate from less reliable vertical positioning data from the GPS or a control system that is not adequately responding to vertical disturbances.

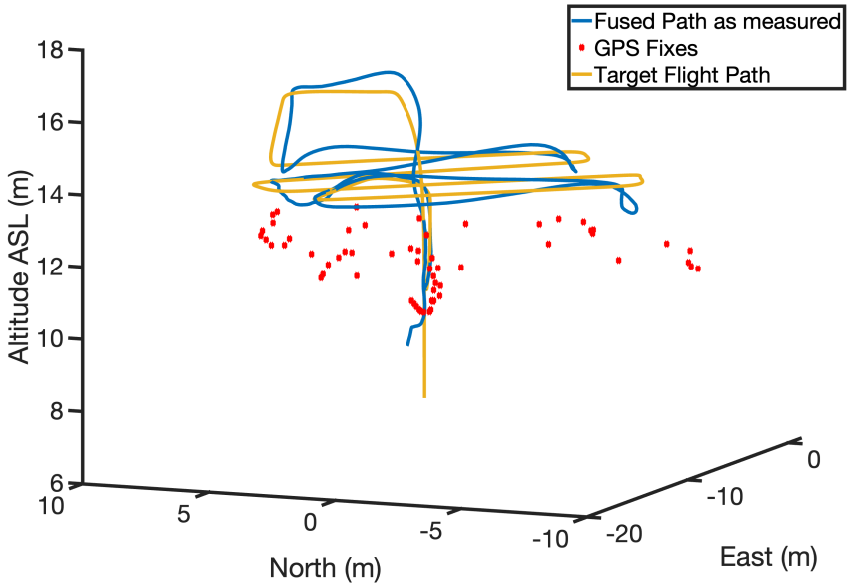

Figure 4-2. 3D reconstruction plot of a drone's flight path during the corridor scan test flight. The 'Target Flight Path' represents the pre-planned trajectory that the drone aims to follow. 'GPS Fixes' are plotted as discrete points, indicating the actual positions recorded by the GPS system during the flight. 'Fused Path as measured' shows the path derived from the onboard sensor fusion algorithm, which integrates data from multiple sensors to provide a more accurate estimate of the drone's trajectory. The discrepancies between these paths highlight the challenges in navigation accuracy and the effectiveness of sensor fusion in correcting for GPS signal errors.

Compared to fully manual rate control, PX4 autopilot-driven flights exhibit significant offset errors, with absolute values of flight parameters notably differing from ground truth values. However, the variation between sequentially collected data points was lower in the

automatic flight mode compared to manual rate control. Further investigation is imperative to analyze the impact of flight mode on residual errors. For the remainder of the tests, we used the drone in manual control mode. The drone was connected to a PC via a 2.4 Ghz datalink, and specific flight commands were transmitted from the PC to the drone. A remote control with a human pilot was on standby to intervene when issues arose during testing. There were multiple incidents that necessitated human intervention in these tests. Given the observed discrepancies and variability in the drone's positional estimates during flight, it becomes imperative to narrow down the focus to a specific phase of flight to gain a more controlled understanding of the system's behavior. Consequently, the next segment of the flight analysis will concentrate on the hover phase. This phase is critical, particularly in addressing the "last ten feet problem" [35]. By isolating and examining the hover phase, we aim to examine GPS performance when the drone is required to maintain a fixed position.

Figure 4-3. Altitude Discrepancy During Corridor Scan Test. Captured at the University of Washington, this still shows the drone's actual flight altitude at 5.6 feet AGL, contrasting with the targeted 10 feet AGL. Such deviation may stem from localization errors, suboptimal GPS signal quality, or barometric pressure variations affecting sensor accuracy.

In wind-affected hover tests, the drone displayed considerable positional instability, as demonstrated in Figure 4-4. Although the drone aimed to maintain a steady hover, GPS

measurements showed an erratic altitude range of 0 to 15 meters AGL and substantial lateral drift, up to 7 meters north and a span of 14 meters eastward (Figure 4-4(a)). These variations far exceeded the drone's observed physical drift, which was approximately ±1 meter in all directions, suggesting a discrepancy between actual drone stability and GPS-reported positions. The divergence of GPS data from the drone's true position indicates a challenge for GPS modules in accurately tracking a UAV during wind-induced movement, underscoring the need for more precise localization techniques. The second plot, Figure 4-4 (b), depicting the fused flight path estimate, is more indicative of the drone's response to wind interference. The trajectory shows significant oscillation around the intended hover point. This oscillation is the drone's attempt to stabilize itself and remain at the hover position, countering the wind's force. However, the spread of the flight path illustrates the limitations of the control system under challenging environmental conditions. The first graph shows a significant spread in the altitude data, indicating that the drone was not only moving laterally but also vertically, struggling to maintain a constant height above ground level. The performance as shown by these graphs highlights the challenges in maintaining a stable hover in adverse weather conditions. Given these challenges, especially prevalent in urban settings with complex wind dynamics, this thesis will mount the drone on a tripod to isolate GPS performance from UAV stabilization issues. This approach will allow for a focused study of GPS errors during hovering, with the aim of enhancing GPS accuracy through algorithmic corrections, irrespective of external environmental influences and ensures compliance with mid-study regulatory changes [200] that restricted drone operations.

Drone performance tests reveals the need for further refinement in both the GPS positional accuracy and the sensor fusion algorithms used for flight control. An examination of Figure 4-4's data shows that the frequency of GPS fixes is considerably lower than the rate at which IMU-derived fused data is gathered. Specifically, the analysis of flight data reveals a GPS fix rate of less than 1 Hz. The most significant delay recorded was during another test involving a circular flight pattern, where only four GPS fixes were obtained over a span of 2 minutes and 42 seconds, highlighting a substantial lag in the GPS data update rate compared to the more consistently streamed IMU data. To address these deficiencies and to expedite the collection of more comprehensive data sets compatible with various UAV systems, a specialized GPS Data Acquisition Unit (DAQ) was developed for this research. The next subsection will present the

DAQ framework created for this thesis, a scalable system capable of rapid GPS data acquisition and processing.

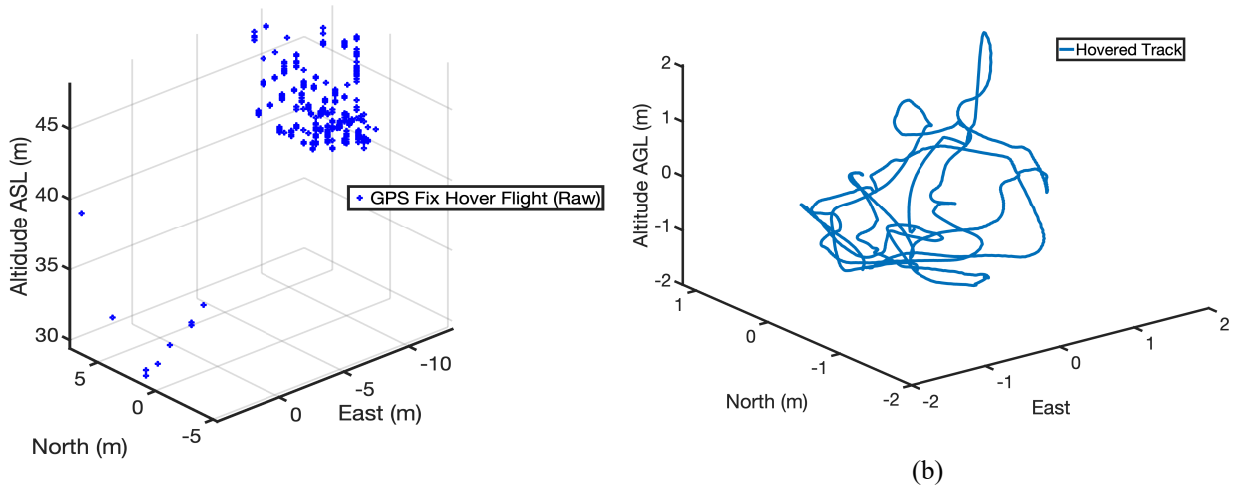

(a) (b)

Figure 4-4. Hover test. Raw data from fused estimate as reported by Drone, and GPS data collected from GPS sensors during the hover portion of the test. a) 3D Scatter of Drone Hover Test. The 3D scatter plot presents GPS data from a hovering drone test. Notably, the GPS data inaccurately positions the drone at various altitudes between 0 to 15 meters AGL (ground height is at 38 m ASL), with a widespread in the North (0-7 meters) and East (4 to -10 meters) directions, revealing significant offset from the true position. B) IMU trajectory plot. In contrast to the GPS data, the IMU data shows a much tighter cluster of the drone's position, with East-West and North-South movements contained within approximately 1.7 meters and 1 meter respectively from the origin, closely matching visual observations and confirming the GPS ineffectiveness in capturing the performance of a hovering drone

4.2 EXPANSIVE FLIGHT FRAMEWORK

The insights gained from studying the current implementation of the Pixhawk controllers on X500V2 are instrumental in evolving the system to accommodate forthcoming sensor technologies. This endeavor establishes the criterion to satisfy for the conceptualization and construction of next-generation flight controllers under the banner of the Expansive Flight Framework (XFF).

- XFF must offer real-time monitoring capabilities to track the status and performance of UAVs during flight. This includes monitoring the UAV's position, altitude, speed, battery level, and other critical parameters.

- XFF must facilitate data acquisition from onboard sensors and payloads mounted on UAVs. It should support various types of sensors, including cameras, LiDAR, thermal imaging, multispectral sensors, and environmental sensors.

- XFF must enable synchronized data collection, timestamping, and geotagging, ensuring the accuracy and integrity of acquired data for subsequent analysis.

- XFF must be designed to be modular and extensible, allowing for seamless integration with third-party software and hardware components. It supports interoperability with existing UAV platforms, ground control stations, simulation environments, and data management systems. Additionally, XFF offers customization options to tailor the framework to specific user requirements and operational workflows.

- XFF must also provide tools for documentation, reporting, and audit trails to support regulatory compliance and certification processes.

The tested hardware configuration of XFF is the Embedded Expansive Flight Framework (EXFF) adopts a mothership design. A microprocessor capable of real-time operations acts as the nexus for all sensory information collection. Each sensor unit is anchored by its own microcontroller, which undertakes the tasks of sensor communication, data capture and storage, as well as the application of filters, data processing, and algorithmic transformations. Post-processing, the refined data is dispatched to the central microprocessor to inform flight controller decisions. The focal point of this thesis revolves around crafting this framework and actualizing a GPS carrier module that seamlessly integrates within the XFF infrastructure. Figure 4-5 depicts the hardware architecture of the EXFF.

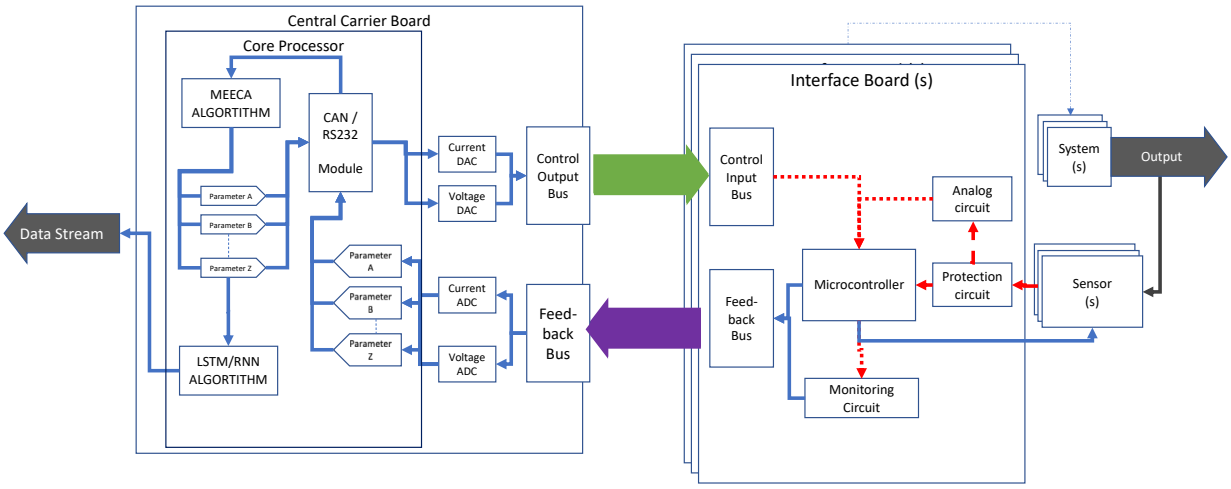

Figure 4-5. embedded Expansible Flight Framework. Architecture of the Embedded Expansive Flight Framework (EXFF). Central to EXFF is the Central Carrier Board with a Core Processor executing ML algorithms, such as LSTM and RNN, for enhanced sensor data analysis. It's supported by Interface Boards managed by dedicated microcontrollers for initial data processing, equipped with protection circuits to maintain system integrity and a monitoring circuit for system health. This configuration underpins the GPS carrier module's integration, crucial to the thesis's aim of refining UAV flight control through advanced data processing.

The **Central Carrier Board (CCB)** constitutes the foundational element of the EXFF, encompassing the Core Processor which is tasked with the execution of intricate Machine Learning algorithms, notably Long Short-Term Memory networks and Recurrent Neural Networks. Furthermore, the board is outfitted with a comprehensive communication suite comprising CAN, UART, and Ethernet modules to establish and maintain robust communicative links for the transmission of essential flight data. A paramount feature of the system is the Feedback Loop mechanism, which underpins the UAV's real-time operational efficacy by enabling dynamic response to sensor inputs, thereby ensuring the stability and adaptability of the UAV under diverse operational conditions. The purpose of the CCB is to act like a RDC to collect and transmit the data to a flight computer.

The **Interface Boards**, which plug into the Central Carrier Board, are each governed by a dedicated microcontroller tasked with the direct acquisition and preliminary processing of data from associated sensors. These microcontrollers facilitate an initial layer of data management, subsequently relaying the processed information to CCB for more complex analyses. A protection circuit, protects against electrical anomalies, preserving the UAV's electronic system integrity and providing necessary electrical isolation for both power and signal conduits. This design ensures

adaptability with UAVs operating across a spectrum of power architectures. Furthermore, the monitoring circuit embedded within enables continuous internal diagnostics, a feature instrumental in conducting predictive maintenance and ensuring the continuous operational health of the system.

The Control Bus and Feedback Bus serve as the interconnect between the CCB and the interface board. The Control Bus is dedicated to command signals for the sensor operations and system, whereas the Feedback Bus carries sensor data along with relevant metadata. The modularity of the interface allows for each sensor's data to be managed individually, ensuring not only scalability but also the isolation of sensor-specific issues, thus enhancing overall system reliability. The following section discusses how a GPS interface board was designed and built to satisfy the EXFF requirements.

4.3 GPS INTERFACE BOARD

A composite system with a daughter GPS interface cards and the central carrier board form the architectural underpinnings of the Position Acquisition Toolkit for High-Frequency Inertial and Navigation Data for Evaluation and Research (PATHFINDER).

4.3.1 *Design requirements of GPS DAQ*

This section details the design requirements of the GPS DAQ system.

4.3.1.1 Microcontroller and GPS sensor choice

The initial experimental phase utilized the Arduino Mega for the GPS data acquisition unit (DAQ) due to its comprehensive C++ library support and ease of interfacing, vital for preliminary tests on GPS receiver performance under varied conditions. The Adafruit Ultimate GPS V3 module, with its MediaTek MTK3339 chipset, was chosen based on its ubiquity in consumer-grade UAV GPS sensors, existing driver support, and prior evaluations in positioning systems [149], [201], [202]. The module's ARM7 co-processor enables onboard trilateration, freeing up the microcontroller for additional tasks—a crucial feature for resource-constrained UAV environments. Additionally, the chipset's capability for up to 10 Hz updates aligns well with the dynamic nature of UAVs, facilitating real-time navigational adjustments Moreover, the module's onboard clock provides a

pulse per second (PPS), a reliable time base that is crucial for coordinating data logging. PPS is essential for aligning the data temporally across multiple sensors and creating a coherent data set for analysis.

(a)

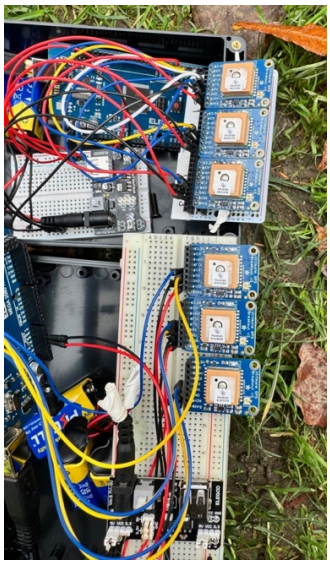

(b)

Figure 4-6. Prototype GPS DAQ System Setup on the Arduino MEGA platform. The compact layout neatly houses the GPS modules and central processing unit, with wiring organized for optimal connectivity and function. (a) showcases the Arduino MEGA platform with three GPS sensors, a real-time clock, and an SD card breakout board for synchronized data logging, all encased for protection. and (b) deployed during a field test.. It reveals an expanded setup with six GPS sensors connected to two Arduino MEGAs, powered by a 9V battery for remote operations, capturing extensive GPS data in a field environment."

However, challenges arose with the serial interface of GPS receivers, particularly the limited UART lanes, three, on the mega. To address this, two Mega units were used with their clocks synchronized with the power-on timing approach, although start-up discrepancies due to power-on timing variances and USB hub-induced delays were encountered. Subsequent investigation revealed that the peak startup power exceeded the USB 2.0 limit of 2.5 W, further complicated by the 500-mA current limiting fuse onboard the Mega Overcoming the power constraints required integrating Adafruit Power Boost 1000C boards [203], each supported by a 2500 mAh battery, were integrated to provide sufficient power for reliable startup and operation.

Data alignment using the Arduino's clock time initially seemed effective but proved problematic above 1 Hz, leading to sensor data misalignment of up to 500 ms. Despite this,

prototype testing yielded insights, notably the inferior performance of internal ceramic antennas compared to external ones, which demonstrated more stability and quicker signal acquisition times. The internal antennas took over 20 minutes to acquire signals, with accuracy varying widely between 10 to 100 meters, heavily influenced by nearby human activity. This inconsistency prompted a shift to an external ceramic patch antenna, which, although improving stability with precision values at approximately 50 to 100 meters, still required a long time for signal acquisition. Ultimately, the adoption of an external antenna [204] with a 28dB gain, featuring an onboard bias-tee supplying 5V, significantly enhanced performance. This antenna reduced signal acquisition time to under two minutes and showed robust resistance to transient noises such as pedestrian traffic.

Additionally, the initial software architecture revealed inadequacies. The SD card experienced multiple failures, and the SPI bus on the Arduino Mega quickly became overloaded, underscoring the limitations of the Mega as a data concentrator. Communication challenges emerged when interfacing with more than seven sensors simultaneously, leading to buffer overflows in the SPI and I2C interfaces due to the influx of sensor messages. Despite extensive efforts to optimize code and implement a FreeRTOS on the platform, these strategies achieved limited success. While the Arduino Mega offered a suitable starting point for the DAQ system, its limitations necessitated a more robust platform for the DAQ.

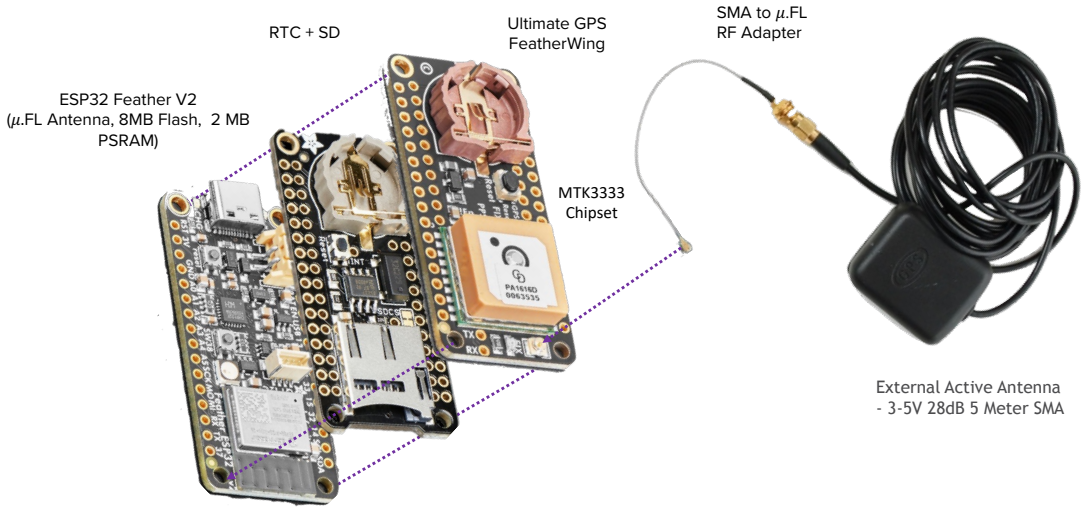

Figure 4-7. Exploded view of GPS DAQ Pod. A built around the MTK3333 chipset, high-quality GPS module that can track up to 33 satellites on 99 channels, has an excellent high-sensitivity receiver (-165 dB tracking), and a built-in antenna. It can do up to 10 location updates a second for high speed, high sensitivity logging, or tracking. Power usage is low at only 40 mA during navigation

The next major hardware iteration leveraged Adafruit Feather and Wings as a test platform. The GPS DAQ Pod, as depicted in Figure 4-7, is engineered around the MTK3333 chipset [205], offering performance and reliability at an economical price point of $30. The module tracks up to 33 satellites across 99 channels. With a receiver sensitivity of up to -165 dB tracking, the GPS DAQ Pod meets the GPS L1 CA signal requirement of -160 dBW at ground level. Despite its functionality, the GPS DAQ Pod maintains minimal power consumption, drawing only 30 mA during tracking, ensuring prolonged operation without high power consumption. An RTC clock was integrated into the embedded hardware stack using the SD card wing, calibrated with the computer time upon software flashing. The RTC chipset (PCF8523) features a precision 1 Hz timer utilized to control GPS localization, temporally aligning the start time and the 1 Hz timer to regulate the sample rate. Data capture was initiated simultaneously using an external interrupt signal.

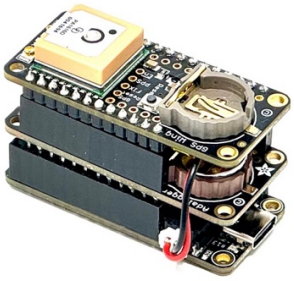

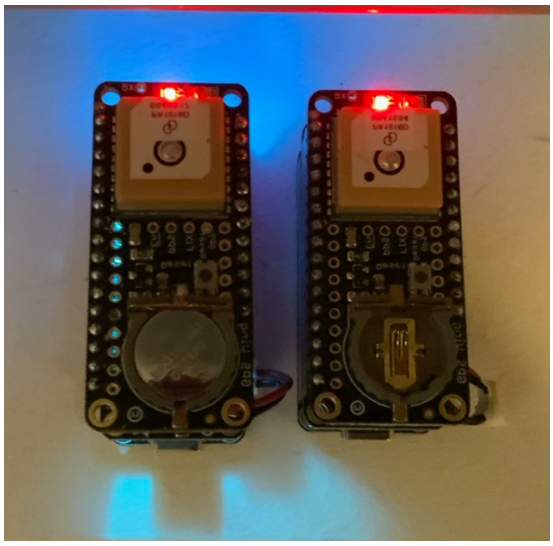

(a) (b)

Figure 4-8. Adafruit GPS sensor POD. (a) A single GPS data logger module equipped with a high-precision GPS receiver, stacked atop a microcontroller and a data storage shield with SD card and RTC. (b). twin GPS modules activated and undergoing testing, with their red status LEDs illuminated, indicating active positioning lock, and the blue led (hidden) indicating storage of data to SD card.

Adafruit ESP32 provided wireless communications via its integrated Wi-Fi transceiver, essential for space-constrained applications like drones. The ESP32's dual-core processor successfully addressed the previous data loss issues encountered with the Mega, efficiently managing data acquisition and real-time processing. Testing revealed interesting insights into the performance of the GPS receivers. The results of the test are discussed in detail in 6.1.

However, challenges arose when integrating more than one GPS sensor due to limited UART lanes. Only 2 lanes of the three available are made available, with one of the two available reserved for USB debugging. Consequently, we constructed multiple test units with Adafruit ESP32 feathers equipped with ADALogger and GPS wings, allowing each GPS sensor to be connected to a single microcontroller, storing both raw NMEA and parsed data. In total, five pods were assembled to facilitate the experimentation. A lipo battery was employed to power each of the pods; given the constraint of each pod being able to collect information from only one GPS receiver, an alternative system design is necessitated for final deployment on drones.

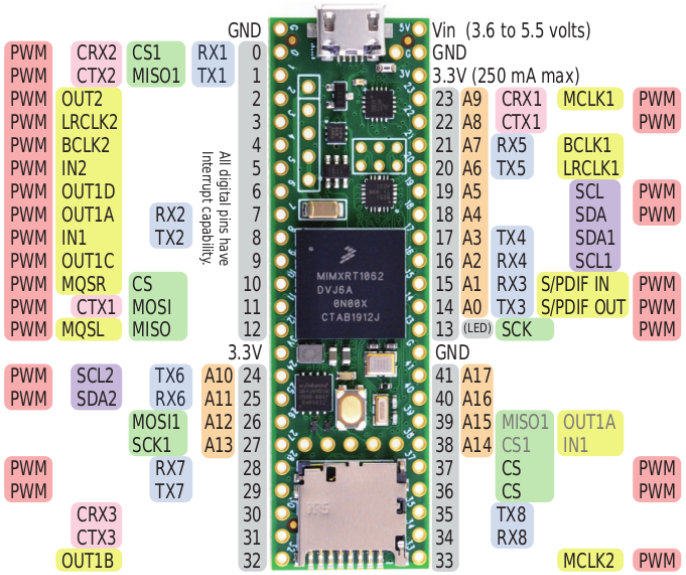

Figure 4-9. pinout diagram of Teensy 4.1, with an ARM Cortex-M7 running at 600 MHz, exposing 8 UART, 3 SPI, 3 I2C ports. [206]

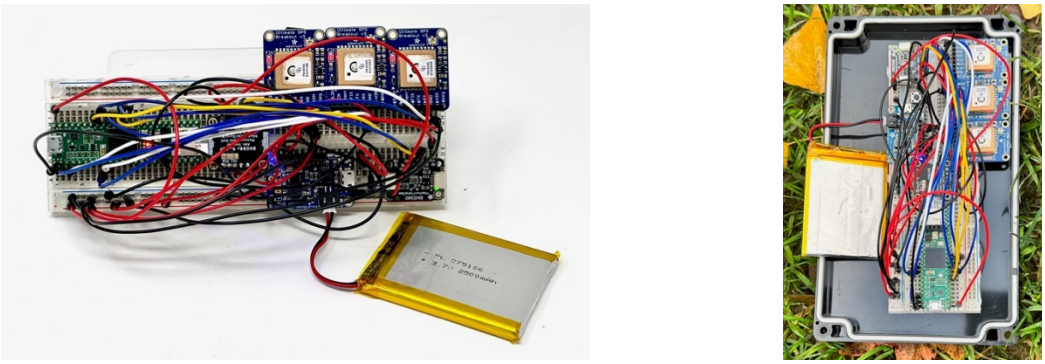

(a) (b)

Figure 4-10. Prototype Teensy 4.1 GPS DAQ System, configured with five synchronized GPS sensors, captures data at 10 Hz for robust operational testing. (a) Arranged on a breadboard with an onboard SD card reader powered by a 2500mAh Li-Po battery. (b) Transferred to a waterproof platform for outdoor field testing. The DAQ performed within spec when tested outdoors in damp conditions as well.

We subsequently adopted the Teensy 4.1 microcontroller [207] due to its superior I/O capabilities, which were essential for our DAQ's extensive communication requirements. The Teensy 4.1, equipped with eight UARTs, two I2C buses, multiple SPI lines, and accurate on-board clock met our high-frequency and data throughput specifications, enabling the progression to the prototype development phase. Figure 4-10 depicts the prototype used in evaluations, which was confirmed to effectively interface with GPS receivers to collect and store NMEA data correctly.

The software initially developed for the GPS POD was revised for compatibility with the Teensy platform and subjected to rigorous testing, the results of which are detailed in Chapter 6. This Teensy-based DAQ system satisfied all requirements of the XFF framework, offering ample serial ports and sufficient computational capacity to manage multiple GPS sensors concurrently. shows the prototype built and used in evaluations. Moving forward, the Teensy-based system was utilized in all machine learning data acquisition, training, and evaluation for this thesis.

4.3.1.2 Hardware and mounting specifications

This section specifies the physical housing requirements for the GPS Data Acquisition (DAQ) system, detailing the enclosure's dimensions, materials, mounting options, ingress protection rating, and environmental suitability. The selected black weatherproof box protects internal electronics from dust, moisture, shock, and vibration. It features dimensions of 7.87 x 4.72 x 2.95 inches (200 x 120 x 75 mm) and includes thermal and cable management solutions, as well as accessible ports for maintenance. The enclosure is equipped with five moisture-protected pass-through ports for radio antennas, using dielectric grease and rubber washers to ensure watertight seal. Inside, the Teensy 4.1 microcontroller interfaces with the 5 Adafruit GPS breakout board. This prototype offers numerous options for mounting of the DAQ. It can be mounted right to the drone or kept separate from the drone, with only the antennas attached to the drone.

Mounting of the GPS antenna and their placement of the drone is critical for performance analysis. The antennas have magnetic back, and the top build plate on the drone has multiple magnetic mount points. VHB is used to bind the sensors firmly onto the top plate. This is done to facilitate rapid changing of the antenna as needed for investigation. This setup maintains the antennas in a fixed position across all tests to prevent variability in data due to hardware changes. Strategic placement of the GPS antennas circumvents potential signal blockages, with the receivers positioned at the extremities of the build plate, in alignment with the four motor arms. An additional receiver is placed forward, orienting towards the drone’s trajectory to ensure optimal directional acquisition. The precise configuration of the sensors relative to each other and to the origin in the drone's body frame is consistently maintained, utilizing the same microcontroller, GPS sensors, antennas, adapters, and cables for all tests to ensure uniformity and comparability of the data collected. This standardized setup underpins the reliability and repeatability of the

experiments, ensuring that any observed variations in performance are attributable to environmental factors and not to changes in equipment configuration.

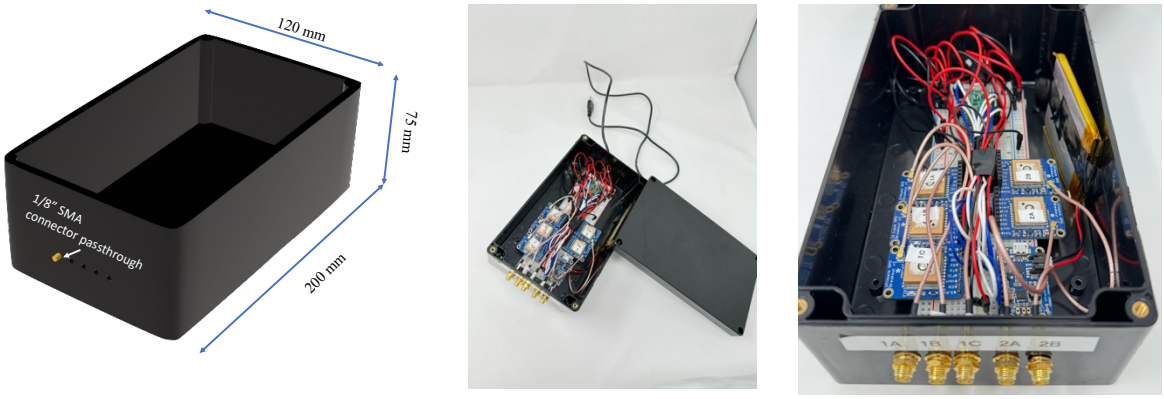

(a) (b) (c)

Figure 4-11. Deployment design for selected GPS sensor with teensy 4.1 for on-drone flight tests. (a) External view of the weatherproof GPS DAQ system enclosure, highlighting the five sealed antenna ports. (b) Open view of the enclosure, displaying the wiring and organization of internal components. (c) Detailed interior view showcasing the GPS modules connected to the Teensy 4.1 microcontroller, with emphasis on the modular design and accessible arrangement for maintenance and adjustments.

4.3.2 *Electronic design of GPS DAQ PCB*

Communication between the MTK3339 based GPS sensors and teensy 4.1 microcontroller is established via UART protocol, with each GPS sensor employing one of Teensy 4.1's available UART ports for data transmission, for a total of 5 ports. Figure 4-12 presents the electronic schematic of the connections. Each GPS antenna is connected to the Adafruit sensor breakout board using SMA to uFL adapters. The operational voltage for the entire circuit is 5 volts, sourced from the power boost 1000C board that supplies additional power for the sensors to operate. A SPI communication lines from the Teensy 4.1 is routed to an edge connector, making it the control and feedback port that can integrate with a flight management controller (FMC).

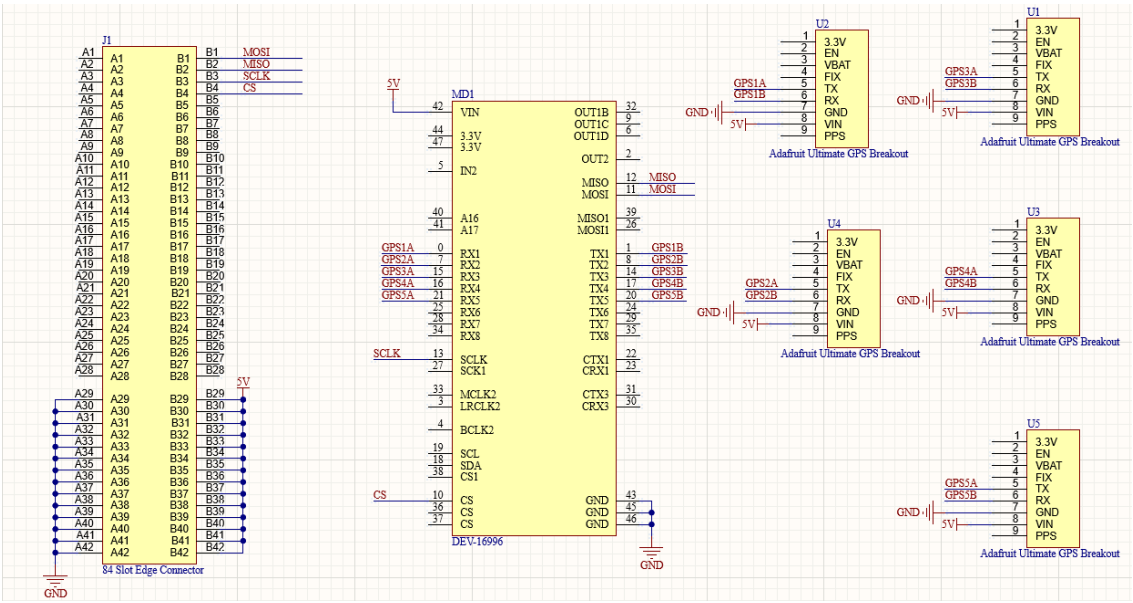

Figure 4-12. Schematic of Teensy 4.1 GPS DAQ System Design. The schematic details the integration of a Teensy 4.1 microcontroller with five Adafruit Ultimate GPS sensors, outlining their connections. UART communication lines link each GPS module to the microcontroller, ensuring continuous data transmission. The SPI communication line to the edge connector is used for interfacing with the flight computer.

Following the electronic design of the GPS DAQ system, the PCB (Printed Circuit Board) layout has been developed. The shared V_{IN} and GND lines deliver a uniform 5-volt power supply across the entire assembly. The PCB, as depicted in Figure 4-13(a), measures approximately 82.68 mm by 85.76 mm in height. The Teensy 4.1 is placed centrally and is flanked by the GPS sensors. The length of the antenna cable and adapter is also specifically matched to ensure that each analog signal has the same distance to travel before reaching the sensors. The PCB design utilizes a 4-layer design. The top layer features a power plane to distribute the 5-volt. The two inner layers function as ground planes. The bottom layer is not used. An M.2 standard interface is implemented for physical connection between the flight computer and the DAQ. The ground planes also serve a thermal management function, helping to dissipate heat generated by the microcontroller and GPS modules.

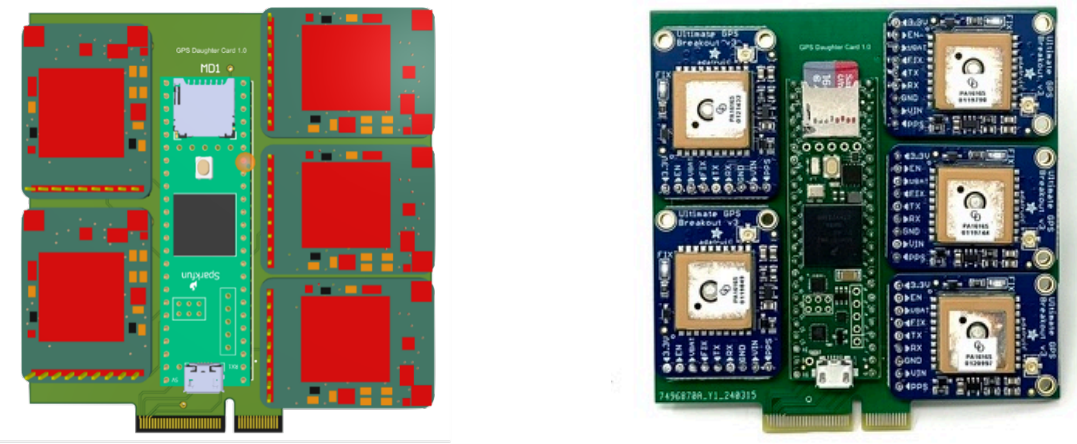

(a) (b)

Figure 4-13. (a) PCB layout for the GPS DAQ system, illustrating the placement of the Teensy 4.1 Microcontroller and GPS sensors, and (b) Final GPS DAQ system as assembled for testing.

4.3.3 *Software architecture of GPS DAQ*

The firmware running on the Teensy 4.1 microcontroller, developed within the Arduino environment, initiates with a setup and calibration phase during boot-up. This initialization process establishes a connection with the flight computer, then initializes a serial connection to each GPS sensor, resets historical data from the GPS sensors to ensure clean session starts, and configuring these sensors to exclusively utilize GPS satellite data. This step disables the onboard logging feature on the GPS sensors to ensure that only live GPS fix data is communicated. The data logging protocols for the microcontroller and flight computer are instead initialized. A unique identifier for each testing session is generated to differentiate between experiment datasets.

Post-initialization, the system transitions to an operational phase governed by a round-robin scheduler. Operating at a 10 Hz frequency, the Teensy 4.1 microcontroller polls each GPS sensor for NMEA data. The retrieved NMEA strings from each sensor are temporarily stored in separate buffers and processed as system resources permit. While high polling rates occasionally result in data loss—further examined in section 6.1.2—the system effectively processes and transmits signals from the GPS sensors to the flight computer. The GPS co-processor's internal clock enables precise timing for the 10 Hz fix rate of the GPS sensor, and this timer is distinct from the Teensy's timer. The sensors transmit the latest fix to the Teensy upon receipt of a localization command, with the corresponding NMEA string relayed.

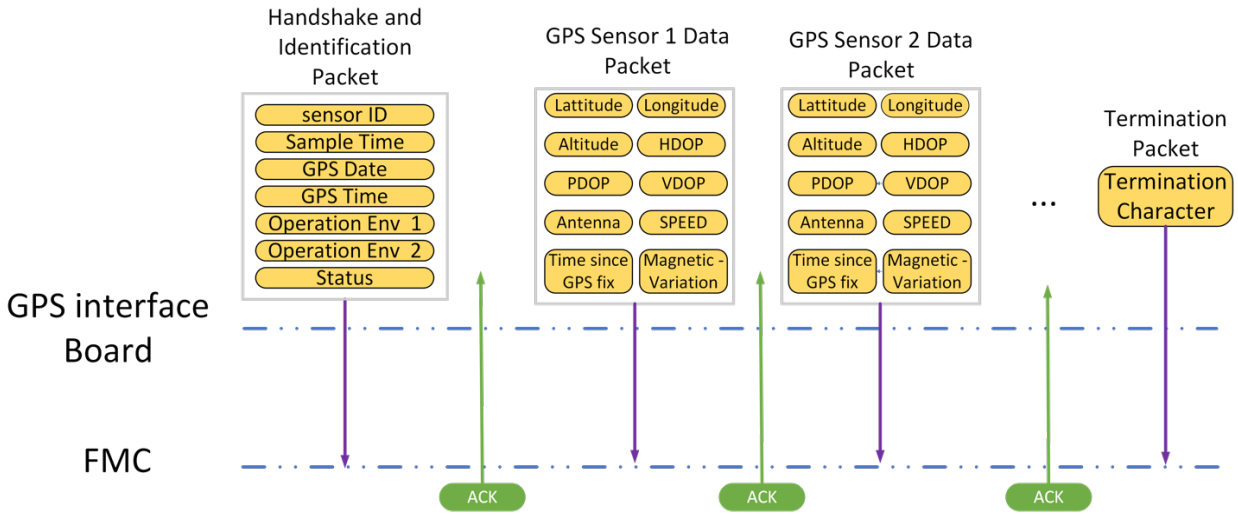

Figure 4-14. GPS Data Acquisition System Communication Sequence. This sequence outlines the structured exchange between GPS sensors and the Flight Management Computer (FMC), starting with an initial handshake that includes sensor identification and environmental data. Following this, GPS data packets are sent, each punctuated by an acknowledgment signal to ensure integrity before the next packet is transmitted.

Data transmission to the flight computer adheres to the EXFF communication protocol. The protocol initiates with a handshake message containing sensor IDs, timestamps, and environmental conditions, followed by the encapsulation of parsed GPS data into scalable data packets. This approach facilitates the potential integration of additional sensors. To ensure data integrity, each packet is acknowledged before the next is dispatched, thus maintaining a reliable and orderly data flow. GPS data is stored in designated NMEA files on the Teensy for each sensor, and a comprehensive data string is compiled and updated with current date, time, location coordinates, satellite positions, and other relevant metrics whenever the sensors achieve a position fix. This data string is subsequently logged onto the micro-SD card for enhanced data security. Figure 4-14 illustrates this communication sequence graphically. For the purposes of this thesis, the integration and testing of the GPS DAQ system are facilitated through a PC setup that includes MATLAB, Arduino IDE, and a serial monitor program. This PC is connected to the Teensy 4.1 microcontroller via a serial interface. This arrangement is compliant with the EXFF framework, which permits the independent replacement and maintenance of the flight computer and sensors. Adopting this approach allows for effective testing and validation, ensuring that all components function correctly together. It also supports comprehensive phases of data collection, machine learning algorithm training, and deployment.

4.3.3.1 Validation of existing libraries

The firmware development for the GPS Data Acquisition (DAQ) system involved extensive validation and modification of existing libraries to ensure compatibility across various microcontroller platforms. Central to this effort was the adaptation of the *Adafruit_GPS* library [208], which was originally tailored for the Arduino Uno platform and equipped with an ATmega328P chip. To accommodate the cross-platform development efforts, the provided APIs and code were re-written and tested for the DAQ .The *Adafruit* and *Paul Stroffregen's SD* libraries [209], [210], required thorough testing and modifications to function effectively on the Teensy 4.1 microcontroller, particularly to ensure accurate serial communication and data parsing.

Adapting the Adafruit_GPS library for deployment on the DAQ required significant modifications to cater to the capabilities of the Teensy 4.1. The robust original library in Python, had a comparatively basic C++ version for Arduino environments. The python library was too slow for the purpose of the DAQ experiments. A comprehensive translation of the GPS library functions to C++ was required. Throughout this translation, numerous errors were encountered with the Arduino's SD library, necessitating the removal of superfluous code to streamline its functionality. The system required a mechanism allowing continuous GPS data polling without delay, even while data processing and logging operations were ongoing. So essential features like non-blocking write operations were carefully re-incorporated to SD library. Originally, the Adafruit_GPS library was configured to process only the RMC and GGA NMEA sentences. Additional parsing functionality was introduced for the GST, GSA, GRS, and GSV sentences. Although ZDA parsing was available from Adafruit, it was not enabled in the default settings. This enhanced library was crucial for experimentation using the Teensy 4.1 DAQ.

4.4 CHAPTER SUMMARY

This chapter established the foundational design elements of the GPS Data Acquisition system and its incorporation into a select range of UAVs, prioritizing those categorized from micro to small sizes. This selection aligns with the operational paradigms of UAM, particularly in the context of package delivery and last-mile logistics. The chapter presented the criteria for drone selection and culminated in the choice of the Holybro X500 V2 drone based on its documented performance.

Additionally, the hover test results underscored the critical need for enhanced GPS precision and informed the test setup.

The capabilities of the PATHFINDER GPS DAQ system were elaborated upon, highlighting the integration of the Teensy 4.1 microcontroller with an extensive array of I/O capabilities crucial for capturing high-speed data from multiple GPS sensors. This integration forms the bedrock of the XFF, ensuring that the PATHFINDER is well-supported by a scalable and robust hardware platform. As the discussion transitions to Chapter 5, the focus shifts to the experimental design that will test the GPS DAQ system under real-world operational conditions.

CHAPTER 5. EXPERIMENTAL DESIGN

The experimental design encapsulated in this chapter is not only geared toward answering the primary motivation of the thesis but also aims to pave the way for future research and development in UAV systems and urban aerospace navigation. This chapter will discuss how the experiments were designed and conducted. This chapter will lay out the methodologies for location selection and classification, detailing the drone hardware setup to mitigate previously identified biases, the software processing implementation, and the exact data metrics collected towards answering the research questions.

5.1 DESIGN OF EXPERIMENTS CONDUCTED TO STUDY GPS CAPABILITIES

This section delineates the experimental designs undertaken to probe the capabilities and performance nuances of embedded GPS technology using the DAQ for use in aerospace industry.

5.1.1 *Experiment to study the impact of microcontroller architectures and capabilities*

This experiment focuses on the performance implications of consolidating multiple GPS sensors onto a single microcontroller. A controlled setup was designed to first connect each sensor to the microcontroller. Then 5 microcontrollers are connected to the microcontroller. All antenna configurations and power distribution schemes were standardized. The sensors were connected to a Teensy 4.1 microcontroller. Studies were run at different frequencies for 30 minutes, twice over. A total of 3000 minutes of GPS data was analyzed. The tested was conducted in semi-urban location 2.

To test the impact of the microcontroller on the GPS error, we ran the test for a continuous 24 hours in the same urban location 4 across each sensor. We tested the GPS sensors in the same configurations with different microcontrollers through two runs in the same location at similar times across days to reduce the effects of satellite and signal-induced error Through these experiments, the consistency of GPS performance was scrutinized across different microcontroller architectures—ATmega (Mega), and ARM (Teensy)—under identical operational conditions.

The dual hypothesis being tested in this experiment are:

- Integrating multiple GPS sensors into a single microcontroller does not significantly affect performance compared to individual microcontrollers for each sensor.
- Changing microcontrollers does not negatively affect the performance of each sensor.

5.1.2 *Experiment to study the impact of update frequency on GPS sensors*

The second experimental design targeted the GPS sensors' update frequency; we systematically varied the update frequency and documented any shifts in positional accuracy and precision. To ensure the validity of the experiment, all other variables, such as sensor placement and environmental conditions, were kept constant. GPS units 1A, 1B, 1C, 2A, and 2B, were used with 100,000 entries aggregated at 0.1 Hz, 1 Hz, 5 Hz, and 10 Hz from the semi-urban location 2 over 4 different days to collect the data. Only the update frequency was altered, which allowed us to attribute changes in performance directly to this parameter. The hypothesis being tested in this experiment is:

- Higher GPS sensor update frequencies result in improved accuracy and precision of positional data

5.1.3 *Experiment to study impact of receiver variation and sensor tolerance*

In this experiment, we investigate the performance consistency of multiple identical GPS receivers operating simultaneously. We aim to assess whether multiple GPS receivers of the same make and model exhibit consistent behavior and provide synchronized position fixes. We performed impedance matching on the external active antennas. They were with 10% of each other. So, the impact of the antenna is minimal. The data was collected at least 3 times in the test location at periods of 15-30 mins each on each sensor. Each location had all 5 sensors running simultaneously on a teensy DAQ. This data was also used for the ML training. Additionally, some of the data collected for previous experiments was also used for this study, as long as the data met the criterion of the data collected as described in the last few lines. This study seeks to identify if any of the small manufacturing, processing, and clock errors within the receivers affect position accuracy and precision. The hypothesis being tested in this experiment is:

- Variations in manufacturing, processing, and clock differences among identical GPS receivers have similar and measurable disparities in positional accuracy and precision.

5.1.4 *Experiment to study impact of operational environment on GPS receivers*

This experiment explores the influence of different operating environments on the performance of GPS receivers. We aim to assess how factors such as urban versus rural settings and open sky versus obstructed environments impact the accuracy and reliability of GPS readings. By conducting experiments in diverse environmental conditions and analyzing the corresponding GPS data, we aim to identify environmental factors that may affect GPS performance and develop strategies to mitigate their effect. No new data was collected for this experiment specifically. The data collected over the previous experiments were used in the study. However, only data collected at 10 Hz is studied to remove the effects of the update frequency on the data. The hypothesis being tested in this experiment is:

- GPS receiver accuracy and reliability are significantly influenced by the operational environment, including urban density and electromagnetic interference

5.2 LOCATION SELECTION

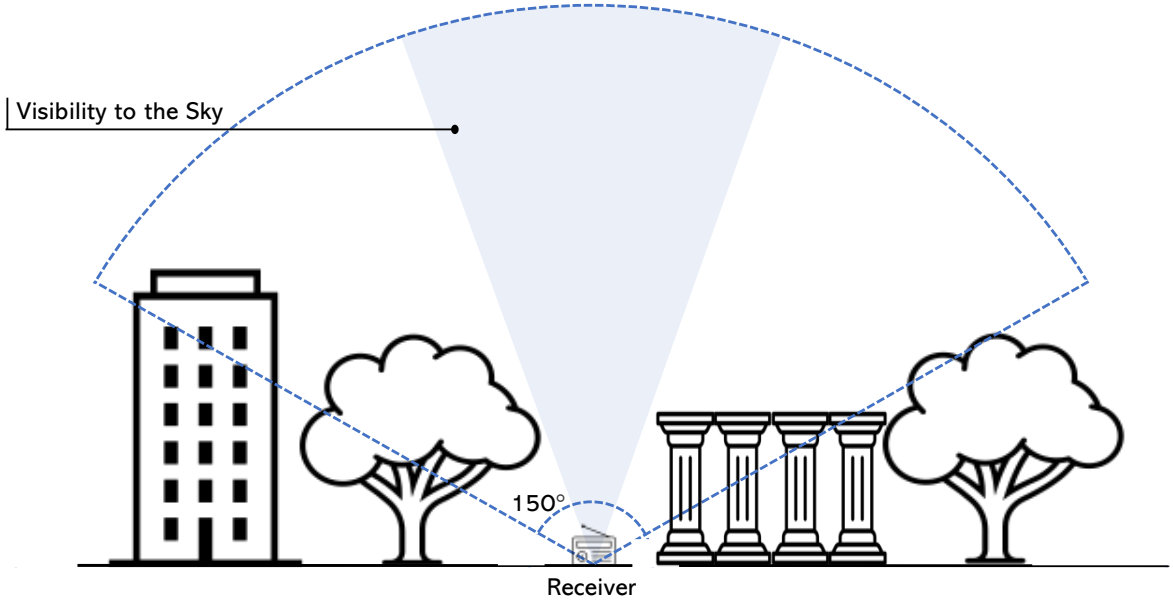

Figure 5-1. Investigation for the presence of high vegetation and buildings in a 250m radius of a GPS receiver. Obstacles of interest include building, dense vegetation and canopy cover, and other static obstacles like monuments that effectively block radio waves. Impact of dynamic obstacles like people moving around the receiver are ignored in this study as they are momentary, and their impact of on GPPS signal availability is minimal

The selection of locations for evaluating the GPS Data Acquisition system is a critical component of the experimental design. The method for classifying locations as urban, semi-urban, or open field is based on a direct visual assessment of the sky from the GPS receiver's perspective. This method of classifying and predicting GPS performance is based on calculating the sky openness ratio is adopted from methodology in [28]. To calculate the sky openness ratio, we employ an antenna 150-degree conical field of view from the receiver's location to determine the extent of sky visibility, as this correlates with the reception field of the GPS antenna employed for testing. Figure 5-1 illustrates the methodology. A 360-degree sky map is created using a camera outfitted with a special 150-degree lens. This image is flattened and is manually inspected to identify percentage of sky visible in the picture. The 250-meter radius was chosen as it comfortably guarantees that far-off obstructions are not included, as any reflected GPS signal of that obstruction will be too weak for the antenna to pick up.

Urban areas are typified by structures that obstruct the GPS line-of-sight and can cause signal attenuation and multipath errors due to narrow streets and reflective surfaces. Such environments, also fraught with high levels of radio frequency (RF) noise, have been underrepresented in GPS performance studies, especially those that contextualize the data with respect to drone operations. Hence, their inclusion is vital. For a location to be classified as urban, the environment must exhibit a high density of tall buildings and/or trees that cover over 50% of the area within a 250m hemisphere radius centered on the GPS sensor. The urban classification is indicative of a setting with numerous potential obstructions to the line of sight between the GPS receiver and the satellites, such as skyscrapers, dense foliage, or other significant structures. This dense arrangement often results in reduced sky visibility and can lead to GPS signal attenuation, multipath errors from signal reflection, and overall decreased accuracy in GPS data due to the 'urban canyon' effect. Urban location 1 was specifically selected to model this urban canyon effect.

Semi-urban areas offer a mix of open spaces and partial obstructions, such as buildings and vegetation, leading to moderate levels of signal blockages and multipath errors. Moderate RF noise in these areas can also impact the GPS signal integrity. These locations represent areas where small pilot drone delivery systems are currently in use, making them relevant to the study. A semi-urban environment is characterized by a moderate presence of tall buildings and trees, accounting for 10% to 50% of the area within the same 250m radius. Such environments present a mixture of open spaces and potential obstructions. This category is a median between urban and open-field classifications, offering a diversified GPS signal reception profile due to the semi-regular interruptions in satellite visibility.

Open-field locations, devoid of tall structures and dense infrastructures, provide the optimal conditions for GPS signal reception due to clear and unobstructed views of the sky. The low RF noise environment of these areas serves to enhance the quality of the GPS signals, making these locations ideal as drone launch points. An open-field environment is defined by very few or no tall buildings and trees, with less than 10% of the area presenting such features.

In an urban setting, despite the prevalence of high-rise buildings, a location such as a rooftop with an unobstructed view of the sky is classified as an open field for this study. This approach is justified by the operational flight patterns of drones, which, as discussed in Chapter 1, navigate

above, between, and sometimes near buildings. The classification is based on the actual flight conditions in urban areas, rather than standard census classifications. This innovative approach allows for a more nuanced classification based on actual conditions affecting GPS signal reception rather than relying solely on conventional land-use designations. It is particularly beneficial for UAV operations, where the navigational context and the immediate surroundings' impact on GPS performance are paramount. This nuanced categorization is particularly relevant for the tests conducted within the city of Seattle, given that drones typically operate within a limited range and do not venture extensive distances for takeoff and landing, and we extend the findings from the research to other locations with significant multi-path reflection and obstructions.

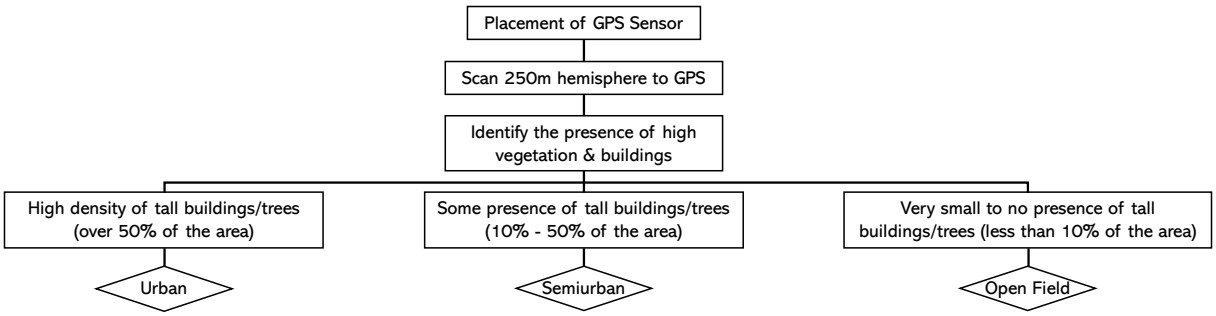

Figure 5-2. Flow chart outlining the method for classifying the operational environment of a GPS sensor. It delineates three distinct categories—urban, semi-urban, and open field—based on the proportion of high vegetation and buildings within a 250m hemisphere surrounding the GPS receiver. The access to open sky determines the type of test environment.

Near the University of Washington, we strategically selected eight distinct locations to collect GPS data to evaluate GPS performance in varying urban landscapes rigorously. This selection included four urban locations, two open-field locations, and two semi-urban locations, all geographically concentrated around the university. Figure 5-3 plots these figures on a map to show the contextual environment surrounding the locations, and Figure 5-4 labels each of these points based on the sky-openness ratio as described in Figure 5-2. The proximity of these locations to the University of Washington is intentional, leveraging the controlled urban environment to simulate typical operational contexts for UAVs. The selection process, guided by the visual assessment method described in the figures, ensures a consistent approach to classification based on direct sky visibility. This methodology offers a practical framework to classify and select operational environments, ensuring the validity and repeatability of the tests conducted in the thesis.

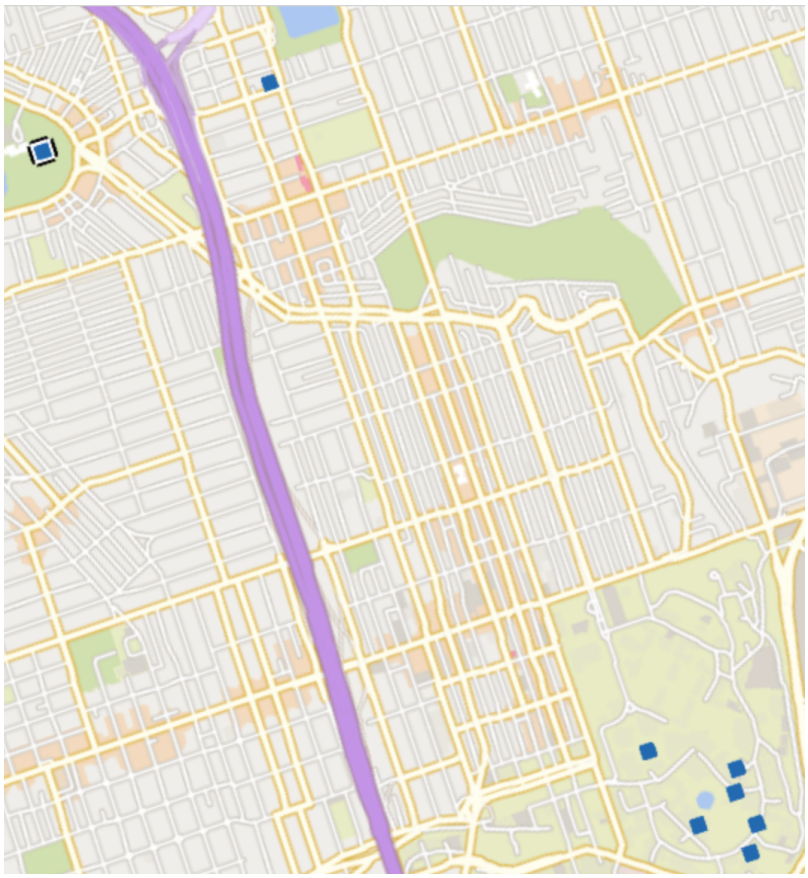

Figure 5-3. GPS Data Collection Sites Near the University of Washington. The red squares indicate the test points. Two test points were located farther way from the core UW campus. The locations were selected as they offered viable mix urban, semi-urban and open-field environment for testing with easy access

Four urban locations were chosen to assess the GPS system's robustness in areas with high-rise buildings and dense infrastructural development. The number of urban locations was higher to ensure a comprehensive analysis of the most challenging environments where drones find it challenging to operate. Two semi-urban locations were identified to represent transitional areas that contain a mix of open spaces, lower buildings, and vegetation. These environments are particularly relevant for understanding GPS performance in suburban settings or on the outskirts of densely populated areas where small-scale drone operations like pilot delivery systems are becoming increasingly prevalent. Two open-field locations were included to serve as a control for optimal GPS signal conditions. These areas, devoid of significant obstructions, offer the clearest line of sight to GPS satellites and are presumed to provide the highest GPS signal quality and

accuracy. Such locations provide the baseline data against which the performance in more complex environments can be measured.

Table 5-1. List of evaluation sites.

Location	Ground truth coordinates	Location Classification	Experiments Targeted
Red Square	47.65587, -122.30964	Semi-urban 1	ML Training, 6.1.4, 8.2
Chem E building	47.65322, -122.30858	Urban 1	ML Training, 6.1.4, 8.2, 8.3
Kirsten Tunnel	47.65447, -122.30605	Urban 3	ML Training, 6.1.4, 8.2, 8.3
Green Lake	47.67982, -122.32730	Open-Field 2	ML Training, 6.1.4
Roosevelt	47.67960, -122.31618	Semi-Urban 2	ML Training, 6.1.1, 6.1.2, 6.1.3, 6.1.4
Rainier Vista	47.65190, -122.30673	Open-Field 1	ML Training,6.1., 6.1.4
ECE	47.65380, -122.30648	Urban 4	6.1.1, 8.1
Sylvan Grove	47.65267, -122.30602	Urban 2	ML Training, 6.1.4, 8.2, 8.3

(a)

(b)

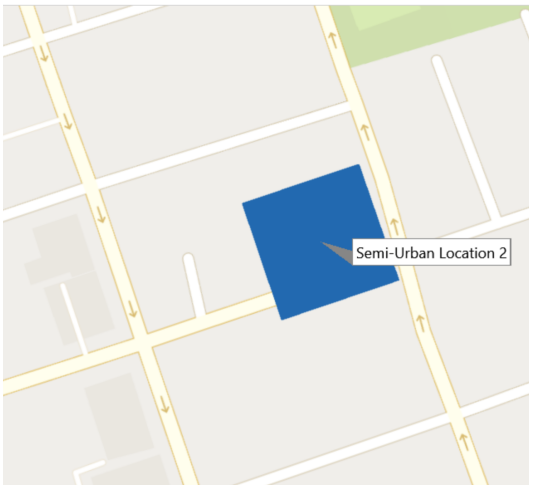

(c)

Figure 5-4. Eight GPS data collection sites, marked with red squares, are categorized into four urban, two semi-urban, and two open-field environments. (a) location clustered around the primary test environment; (b) location selected to geographically distance the test for open-field conditions and (c) semi-urban location 2. The red squares in figures represent the approximate uncertainty in the GPS coordinates positions. Figures (b) and (c) are at a relative zoom level of ~20x, and figure (a) is at relative zoom level of 1x. Semi-urban location 2's uncertainty in location is higher at 0.5 m as it far from any static NOAA markers or other known locations.

5.2.1 *Ground truth generation*

The process of ground truth generation is paramount in the study to ensure the highest level of accuracy in GPS data collection. Ground truth refers to the baseline coordinates obtained through highly reliable and precise means, against which the performance of the GPS system under study can be compared.

The primary source of ground truth for our experiments is derived from NOAA NGS (National Geodetic Survey) markers, which serve as calibration points for GPS systems[211]. These markers' positions are confirmed on survey maps [212], allowing us to calculate the ground truth coordinates accurately using these locations as references. By measuring physical distances from these known landmarks, we ascertain coordinates with a consistent error margin of approximately 5 centimeters. This method, as seen in Figure 5-5, offers a reliable reference for GPS accuracy assessment, leveraging the fixed locations of NGS markers which are also utilized by the GPS ground segment for error correction. Our first source of in situ ground truth is from a commercially available GARMIN GPS device [213], typically delivering an accuracy within a 3-meter radius in most conditions. To supplement this, an iPhone is utilized to provide a fused location estimate. An iPhone shows variable accuracy, in dense urban environments, the precision fluctuates between 15 to 45 centimeters.

In situ testing involved a structured setup, as depicted in Figure 5-6, where a drone was mounted on a tripod at a predefined height. The drone's propellers were activated at full power to simulate operational conditions, while a data tether ensured the direct and reliable transmission of information to a laptop equipped with data capture software. This setup minimized the likelihood of data loss, ensuring a continuous and complete dataset for analysis. The precision of this setup, combined with the ground truth data, forms a robust framework for evaluating GPS performance across various urban terrains.

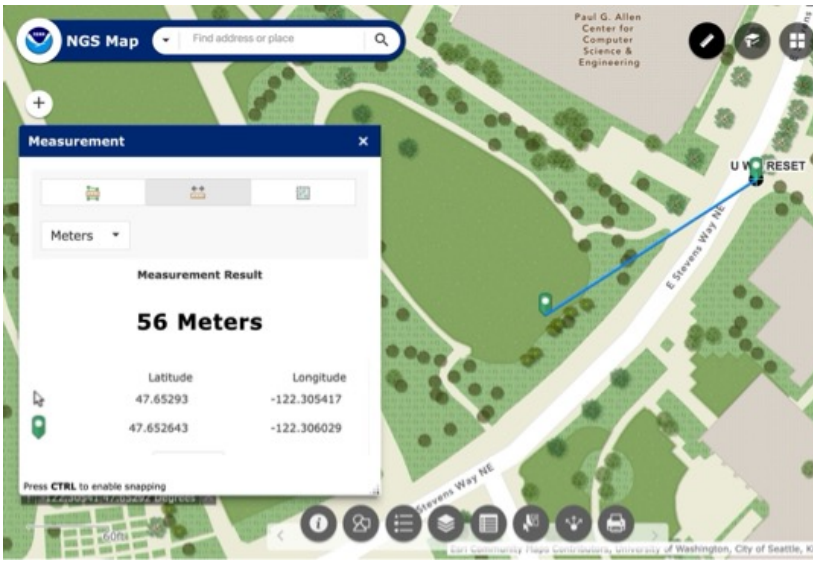

(a)

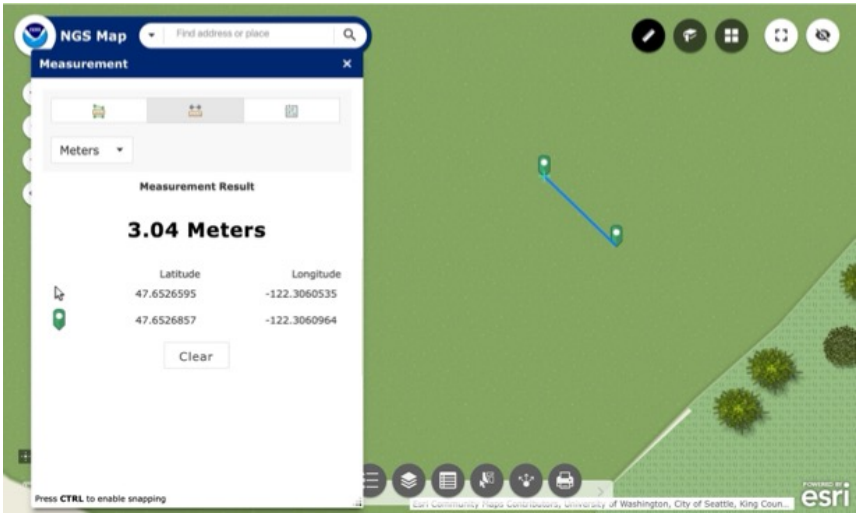

(b)

Figure 5-5. Getting NOAA ground coordinates from known standard markers. One marker is shown for illustration, but multiple markers were used in the. Field, including markers located at known monuments, and other reference structures such as flag poles and statues whose coordinates are known to high degree of precision. The derived coordinate is accurate to 5 cm.

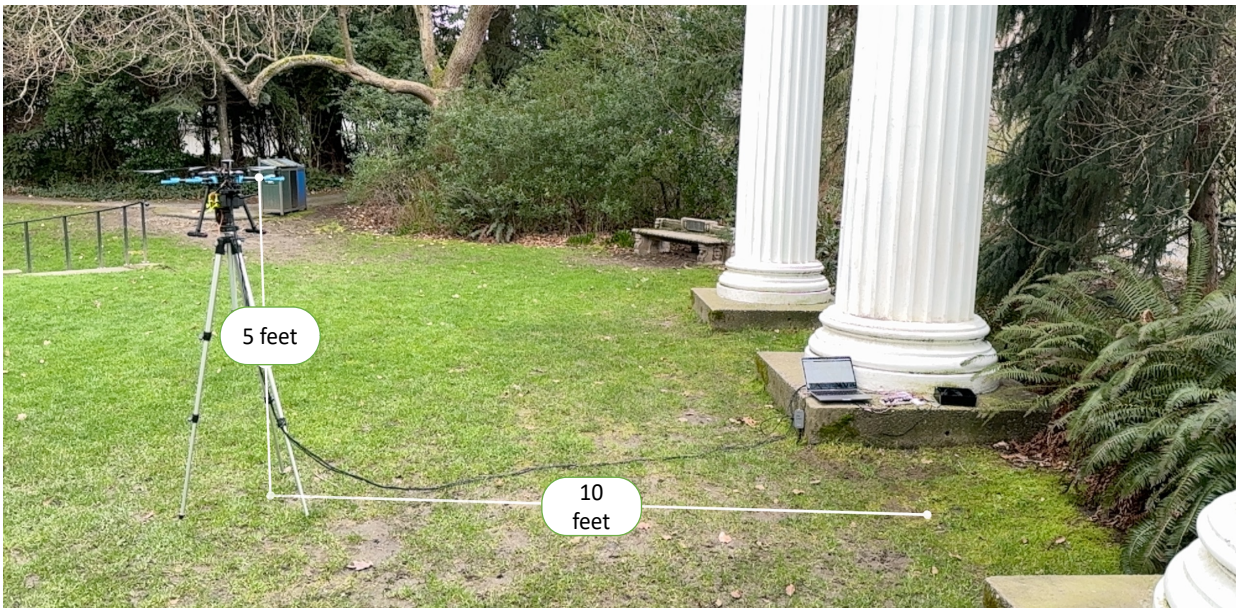

Figure 5-6. Picture of test setup in situ. The drone is mounted on a tripod at a set height and is switched on and propellers are spinning at full power. A data tether is used to transmit the data reliably without dropouts out to a laptop computer running a data capture program. The laptop serves as the central processing unit for the experiment, collating and recording the drone's GPS data. The setup is strategically placed 10 feet from the central column, whose coordinates are exactly known, providing a measure of ground truth against which the GPS data can be compared.

5.3 SETTING UP OF MOUNTED GPS ON DRONE

To establish our experimental GPS system on the drone, strategic placement of GPS receiver antennas was crucial. We positioned one antenna at the front to guide the drone's directional path and placed others at each of the four corners, aligned with the propellers to maximize sky visibility and signal reception. To simulate the impact of RF noise and interference commonly encountered during flight, a remote control (RC) transmitter was actively used near the drone throughout the setup. This preparation aimed to incorporate potential signal degradation into our data collection.

An M8N GPS unit, a recommended model for this drone, was mounted at the rear above the propellers to log GPS signal conditions within the operating environment. While the data from this unit was not analyzed, it provided a reference for the signal quality and integrity necessary for the study. The drone system was linked to a ground-based computer via a telemetry radio, facilitating wireless command transmissions and mirroring the electronic environment typical of drone operations. This setup ensured no positional drift from the drone's inertial sensors, offering

a controlled environment for accurate GPS data acquisition. This meticulous emulation of operational conditions was vital to ensure the collected data authentically reflected the complexities of drone navigation, encompassing all forms of signal interference encountered in actual flight scenarios. The drone's onboard controller, equipped with multiple IMUs and a barometer, is used exclusively for drone control; none of its data was utilized in this study, which focused solely on evaluating the performance of selected GPS receivers.

Figure 5-7. UAV Ground Station Integration Test with experimental GPS DAQ Setup on UAV. This image captures a UAV secured to a tripod, with propellers engaged to emulate in-flight dynamics. A wireless transmitter-receiver, visible next to the computer, relays telemetry data in real time, facilitating direct command transmission and live data monitoring to replicate true flight conditions for rigorous system validation. The antennas of the test system, marked with white labels, are positioned on the drone's extremities to ensure wide sky visibility and accurate signal reception. At the rear, above the propellers for a M8N GPS antenna compatible with the drone's flight controller is mounted.

5.4 PARAMETERS OF INTEREST

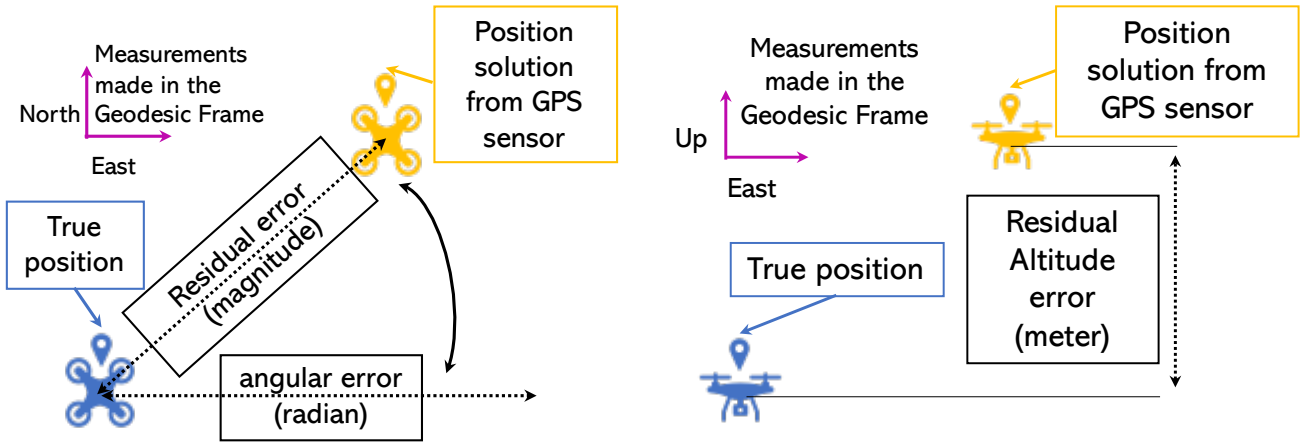

(a) (b)

Figure 5-8. GPS Error Metrics Defined. (a) Residual error, presented as non-negative, pairs with angular error in radians east to define the error vector direction. (b) Altitude error, in meters, with positive values indicating a reported position above the true ground level.

In the exploration of GPS accuracy, we direct the focus to the evaluation of residual errors, which are the variations between the GPS-derived position and the ground truth coordinates. These errors are instrumental in determining the precision of GPS data.

The Residual Magnitude Error is a measure of the distance between the position reported by the GPS and the actual, verifiable location known as the ground truth. Mathematically, this distance is calculated using the haversine formula:

$$d = 2r \arcsin\left(\sqrt{\sin^2\left(\frac{\text{lat}_{\text{gps}} - \text{lat}_{\text{gt}}}{2}\right) + \cos(\text{lat}_{\text{gt}}) \cdot \cos(\text{lat}_{\text{gps}}) \cdot \sin^2\left(\frac{\text{lon}_{\text{gps}} - \text{lon}_{\text{gt}}}{2}\right)}\right) \quad (27)$$

where d represents the distance error, r is the Earth's radius, lat_{gps} and lon_{gps} are the latitude and longitude of the GPS-reported position, and lat_{gt} *and* lon_{gt} and are the latitude and longitude of the ground truth, respectively.

The Angular Error, θ, defines the direction of the Residual Magnitude Error from the ground truth to the GPS-reported position. It provides the angle in radians eastward from true north to the direction of the error and is calculated using the following formula:

$$\theta = \tan^{-1}\left(\frac{\sin(lon_{gps} - lon_{gt})\cos(lat_{gps})\cos(lat_{gt})}{\cos(lat_{gt})\sin(lat_{gps}) - \sin(lat_{gt})\cos(lat_{gps})\cos(lon_{gps} - lon_{gt})}\right) \quad (28)$$

The Residual Altitude Error,e_{alt} , quantifies the difference in altitude between the GPS reading and the ground truth. This error is the vertical component of the residual error and is given by:

$$e_{alt} = alt_{gps} - alt_{gt} \quad (29)$$

where $\mathrm{alt}_{\mathrm{gps}}$ is the altitude reported by the GPS, and $\mathrm{alt}_{\mathrm{gt}}$ is the known altitude of the ground truth location. Figure 5-8 offers a visual representation of these errors in the NEU frame.

The NMEA parameters selected for this study—PDOP, VDOP, HDOP, the number of satellites, antenna status, time since last fix, receiver speed, and magnetic variation—are strategically chosen to align with the precision and reliability requisites for UAV operations. PDOP, VDOP, and HDOP are included due to their indication of the geometric strength of the satellite configuration, which impacts the positional accuracy. These metrics are crucial in assessing the real-time integrity of the GPS signal, an integral aspect for the flight control systems of UAVs that necessitate high-precision navigation. The number of satellites in connection with the GPS receiver is included as it is fundamentally indicative of navigational accuracy. In urban settings, a discrepancy between the expected and actual number of connected satellites can inform environmental classification and enable corrections based on historical signal data.

Antenna status is continuously monitored, serving as a direct reflection of the GPS system's health and functionality. A constant antenna status is expected throughout the experimental trials; any deviations suggest a potential fault, rendering the GPS data unreliable post-issue. Notably, the sensors employed have a fallback ceramic patch antenna which, while not active like the primary

antenna with a 5V bias tee voltage, possesses distinctly different performance characteristics. Time since the last fix is a determinant of dynamic positioning accuracy. Within drone technology, where real-time locational updates are critical, this parameter's freshness is key to making informed operational decisions. Long time between fixes is indicative poor signal conditions.

Receiver speed is measured not for its direct impact on positional accuracy but for its implications on the drone's performance and the GPS's ability to maintain precision at variable velocities—a consideration crucial for UAVs that might require sudden changes in speed. In static experiments conducted in this thesis, this value is expected to be zero; any reported movement may indicate errors, which could be used algorithmically for error correction. Magnetic variation is monitored because it assists in aligning the drone with the NEU (North, East, Up) frame, ensuring accurate heading information for path planning, particularly important in challenging navigation environments.

This study excludes other NMEA parameters that either do not significantly influence the critical navigational operations of UAVs or do not provide insights beyond the selected metrics. One key omission is PSR. This is done as many commercial GPS receivers do not support GRS sentences, and previous works have shown success in using HDOP and VDOP as stand-ins for raw pseudorange measurements [141], [214]. This targeted approach not only enables detailed exploration of the GPS performance factors most pertinent to UAV operations but also ensures efficiency in communication by limiting the data to what is necessary. The goal is to avoid data overload while not omitting valuable information that could enhance GPS data integrity and utility.

5.5 SOFTWARE DESIGN

The software underpinning the experiments detailed in this thesis was developed in MATLAB, version 2023B, with the platform’s extensive aerospace toolbox leveraged for its comprehensive array of functions relevant to GPS and navigation systems. This section outlines the rationale for the software choices and the structured approach to the design and implementation of the software used throughout the experiments. For the analysis of drone flight data, using the Drone Toolbox in MATLAB was crucial. It provided the necessary tools to interpret and analyze data logged in ULog format, typically used for logging data in drones. This specialized toolbox streamlined the process of converting raw flight data into actionable insights. In the process of analyzing GPS data

for UAV navigation, NMEA coordinates are provided in the Degrees, Minutes, and Seconds (DMS) format. To facilitate computation and enhance compatibility with various geospatial analysis tools that require coordinates in a decimal format, a Python parser was utilized within the software framework. The parser's function was to convert the DMS coordinates into the decimal coordinate system. This conversion is essential for accurate location plotting, distance calculations, and integration with machine learning models requiring numerical input for pattern recognition and predictive analytics.

The Python parser operates by extracting the DMS values from the NMEA sentences and then applying the formula:

$$Decimal\ Degrees\ =\ Degrees\ +\frac{\text{Minutes}}{60}\ +\frac{\text{Seconds}}{3600} \tag{30}$$

to each coordinate. This script ensures that all GPS data used in the model is in a consistent format, thus streamlining the subsequent data analysis stages. The transformed decimal data is then used for all ML applications. The Neural Network Toolbox, with its suite of algorithms, functions, and apps, allowed for the design and implementation of neural networks used in the machine learning components of the research. The toolbox's capacity for designing, training, and validating neural networks ensured that the models created were robust and effective for predictive analysis. Incorporating the LSTM RNN, illustrated in Figure 5-9, the software captures not just immediate data but also analyzes historical trends within and across data windows. This analysis is crucial for the LSTM's learning process, enabling it to refine its predictions and adjustments continually. The input to the LSTM is structured as a tensor with dimensions reflecting the number of samples, features, and time steps. In this case, the size of the input tensor is 5x10x25, considering that the GPS date column has been omitted from the feature set. The exclusion of the GPS date is a deliberate choice to prevent model redundancy due to the ever-increasing nature of time values, which could potentially hinder the model's ability to generalize and make accurate predictions. By monitoring the sequence and effectiveness of corrections made by the LSTM, we can assess the overall performance of the system. This continuous evaluation is key to understanding whether the LSTM adjusts appropriately to the complex patterns within the GPS data, which is crucial for optimizing GPS localization technologies in UAV systems. Beyond LSTM, MATLAB's

Regression Learner and Classification Learner apps were employed for developing predictive models with the GPS data. These apps provide an intuitive interface for selecting features, choosing models, and assessing model performance, thereby simplifying the process of machine learning model development. The underlying code, developed in MATLAB, is structured to support various machine learning paradigms, including supervised and unsupervised learning, ensuring a robust and flexible approach to data analysis. Custom scripts supplement the software suite, facilitating data preprocessing, feature selection, real-time error analysis, and plotting of data. This granular approach to the system's architecture allows for the detailed tracking of data through each algorithm step, revealing how input variables are transformed into actionable corrections. This modular design is crucial not only for debugging and optimizing the system but also for understanding the underpinnings of machine learning applications in aerospace GPS technology. The architecture of the experimental software for this thesis is intentionally modular, eschewing a monolithic design in favor of a series of interlinked segments. This facilitates transparency and traceability within each step of the data processing and algorithmic refinement, crucial for the iterative enhancement of GPS localization in UAVs navigating complex urban airspace. Such a design is not merely a preference but a requisite in aerospace software development, aligning with standards and recommendations from authorities like NASA [215]. This approach aligns with the principles of white box software development, where the inner workings of the application are fully exposed for examination and validation, ensuring each component’s function and interaction within the system is clear, understandable, and compliant with stringent aerospace software standards [216], [217]. This chapter seeks to satisfy the white box software development requirements.

The combination of these advanced capabilities and requirements facilitated a comprehensive and detailed analysis of the GPS performance in UAVs in the MATLAB suite. Additionally, MATLAB's development environment is accredited for compliance with aerospace industry standards, meeting stringent validation and certification requirements [112]. MATLAB ensures stability across different platforms and offers comprehensive technical support. Its robustness is vital when the software must be tested on various computers, as is common in aerospace applications where flight computers may operate on diverse operating systems, including proprietary ones [116].

Throughout the experimentation and analysis phases, CoolTerm was used in the experiment to intercept and monitor the serial data stream. This ensured that the inputs fed into MATLAB were correct and reliable, providing a trustworthy foundation for subsequent analysis. The software design articulated in this section underpins the experiments carried out to scrutinize GPS performance. By leveraging MATLAB's advanced toolboxes and applications, we have established a methodological framework that is both robust and adherent to industry benchmarks.

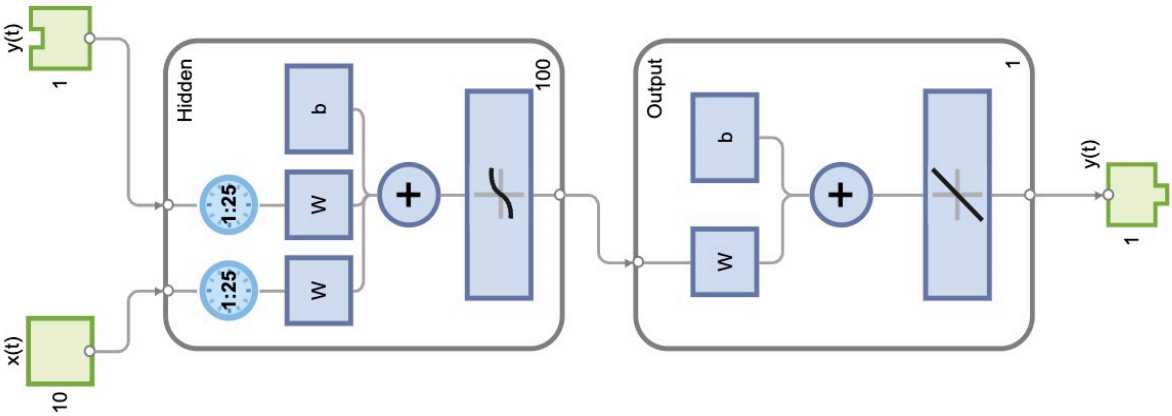

Figure 5-9. LSTM Neural Network Architecture in MATLAB. This schematic illustrates the LSTM recurrent neural network used for time-series prediction. The network intakes a 5x10x25 dimensional tensor 'X' at each timestep, encapsulating the last 25 samples of data. The 'Hidden' block represents the LSTM layers, each taking the input and the previous time step's hidden state to compute the current output. The 'Output' block then transforms the LSTM outputs to the desired target prediction size, outputting a one-dimensional 'y(t)' at every time step, signifying the network's prediction.

5.6 CHAPTER SUMMARY

This chapter details the methodology and structure of experiments conducted to assess the capabilities of embedded GPS technology and its application within the aerospace industry. Key experiments were designed to examine the effects of various microcontroller architectures, update frequencies on GPS sensors, receiver variation, and sensor tolerance, and the influence of different operating environments on GPS receiver performance. These controlled experiments aimed to isolate and identify the impact of each variable on the precision and reliability of GPS technology in urban settings.

The chapter discusses the selection and categorizing of locations, for evaluating the PATHFINDER GPS, based on the extent of sky visibility in urban, semi-urban, and open fields. Furthermore, the chapter elaborates on the mounted GPS setup on drones, which is crucial for the collection of experimental data. Parameters of interest for the study include residual errors and their evaluation. The chapter explains the importance of understanding these errors for the refinement of GPS data. To achieve empirical rigor in the experiments, the chapter outlines the use of the NMEA parameters selected for the study, considering the precision and reliability requirements for UAV operations. The software underpinning the experiments is meticulously designed within MATLAB, using the platform's comprehensive aerospace toolbox. This software design is critical for the real-time analysis and interpretation of drone flight data, showcasing the advanced capabilities of MATLAB for machine learning and GPS performance analysis in UAVs.

While Chapter 5 discusses experimental design and procedures employed to test and validate the capabilities of GPS technology for urban aerospace navigation, 6.1’s focus shifts to the detailed analysis and interpretation of the experimental data. 6.2 will delve into the learnings of the various tests conducted, examining the correlations and insights drawn from the intricate dataset. This upcoming chapter aims to synthesize the findings into actionable knowledge geared towards the evaluation and testing of the proposed ML algorithms.

CHAPTER 6. DISCUSSION OF RESULTS

In this chapter, the results obtained from the experiments structured in Chapter 5 are analyzed. The goal of this chapter is to establish baseline performance of the PATHFINDER hardware, elucidating the insights gleaned from sensor behavior that predict the effectiveness of the proposed ML strategy. Over 350 hours of GPS data were amassed specifically for validating PATHFINDER hardware. For conciseness, comprehensive data sets have been condensed, and selected sensor data is visualized in plots.

Chapter 6 is organized to directly align the presentation of experimental data and the implications of these findings on the EXFF, PATHFINDER, and IRNN-DN based on the experiments designed in Chapter 5. Each subsection from 6.1.1 to 6.1.4 corresponds to the respective experiments from 5.1.1 to 5.1.4. Section 6.2 discusses the impact of data gathered with PATHFINDER hardware on the overall IRNN-DNN algorithm.

6.1 ANALYZING THE PERFORMANCE OF GPS SENSORS IN THE EMBEDDED SYSTEM

This section evaluates the core performance metrics of GPS sensors within embedded systems. By examining sensor data under a variety of testing conditions, we aim to derive meaningful insights into their operational effectiveness. The findings are crucial for evaluating the reliability and accuracy of the machine learning algorithms, which will be explored in Chapter 7.

6.1.1 *Impact of microcontroller architectures and capabilities*

Our investigation extends to multiple GPS sensors interfacing with a single microcontroller versus each sensor being allocated to its microcontroller. The pivotal question was whether consolidating sensors onto a single microcontroller would affect the system's precision and accuracy. A granular analysis was conducted on sensors 1A, 2A, 1B, and 2B, examining their longitude, latitude, and altitude data for consistency and spread, and consequently, their combined residual error. This experiment was conducted semi-urban location 2.

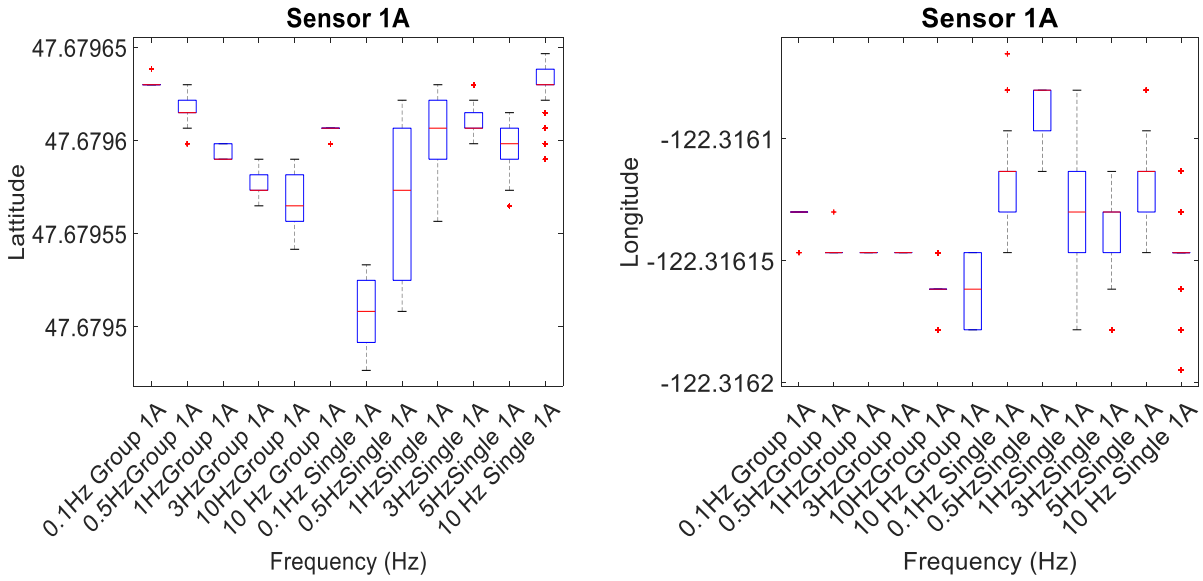

(a) (b)

Figure 6-1. Variability Analysis of GPS Sensor Performance at Different Frequencies. The latitude and longitude box plots represent the data recorded by GPS sensor 1A at varied update frequencies, comparing individual sensor performance (labeled 'Single') against performance when grouped with multiple sensors on one microcontroller (labeled 'Group'). (a) Latitude data points exhibit increased spread at lower frequencies, with a pronounced interquartile range and noticeable outliers. (b) Longitude values also show a wider distribution at lower frequencies,. The median lines across all frequencies suggest a stable central tendency despite outliers.

In the analysis of Sensor 1A's performance through the boxplot depicted in Figure 6-1 (a) we assess latitude and longitude variations at different frequencies. At lower frequencies, such as 0.5 and 1 Hz, the data shows a notable spread, characterized by a wider interquartile range (IQR) and outliers. This suggests variable sensor performance potentially due to a lower sampling rate's inability to capture dynamic changes, or increased susceptibility to environmental noise and signal multipath effects common in semi-urban settings. Despite these outliers, the median, indicating the central tendency, remains relatively consistent whether the sensor operates alone or in conjunction with others, suggesting stable average performance despite occasional signal loss or drift at lower frequencies.

Figure 6-1 (b) corroborates that Sensor 1A performs better in a group configuration than when operating solo, with fewer outliers and a more compact spread of values. The IQR is largest at 1 Hz, the operational frequency recommended by the board integrator for this sensor. The enhanced variability in GPS performance observed when fewer systems are active may be linked

to the electrical characteristics of the embedded system. Specifically, the integration of multiple sensors increases the total capacitance on the power supply line, which can act as a buffer or filter. This smoothing effect from the capacitors helps stabilize voltage spikes and dips, providing a reservoir of energy that maintains consistent voltage levels essential for the high-frequency crystal oscillators in GPS modules. These oscillators are crucial for maintaining timing accuracy, which underpins precise positioning. When operating with fewer sensors, the diminished collective capacitive effect results in less effective voltage stabilization, thereby increasing the likelihood of power supply fluctuations that can adversely affect GPS accuracy. This dynamic underscore the importance of power supply quality in maintaining the integrity of GPS data, particularly in configurations where the load variability significantly influences power characteristics, such as in battery-powered drone systems. The magnitude of the latitude and longitude spread is about the same (~17x12 m). Suggesting no one error axis is preferred.

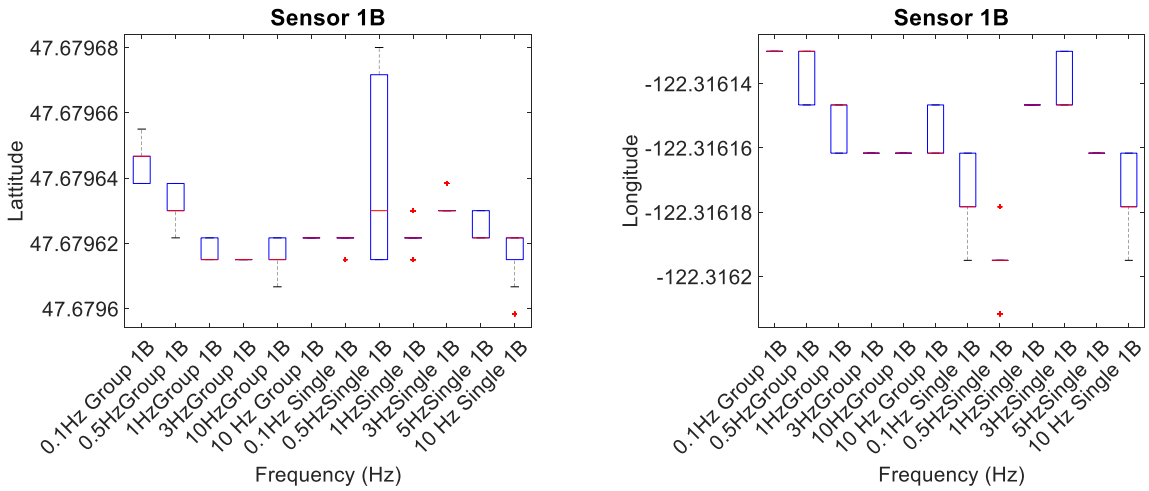

(a) (b)

Figure 6-2. Box plot(s) showing the GPS sensor 1B performance connected to single dedicated microcontroller (Single) and sharing one microcontroller across a group of multiple sensors (Group) at multiple operating frequencies. At higher frequencies such as 5 Hz, the sensor displays reduced spread in data. The relatively smaller spread in the group configuration across both latitude and longitude values suggests that the sensor's performance is not compromised when sharing a microcontroller with other sensors. (a) Variation reported in latitude vales; (b) variation reported in longitude values

Sensor 1B, Figure 6-2, demonstrates a tighter spread of latitude and longitude data at higher frequencies, particularly at 5 Hz. This suggests that Sensor 1B benefits from increased sampling rates, which may provide a more consistent and continuous stream of data, allowing for better signal processing and reduced influence from transient noise. The consistency of Sensor 1B's performance when running alone compared to in a group can be inferred by comparing the spread and outliers in its respective boxplots. The magnitude of the latitude and longitude spread is about the same (9 x 6 m). Suggesting no one error axis is preferred. The magnitude of the error is approximately half that of sensor 1A. The spread is significantly smaller in the group configuration, indicating no performance degradation due to crosstalk or computational limitations of the microcontroller handling multiple sensors. For the longitude readings of Sensor 1B, we observe a consistent pattern with the 0.1 Hz frequency exhibiting more variability, like the latitude readings. However, at 5 Hz, the spread is narrower, suggesting better performance and perhaps more accurate readings due to a higher sampling rate capturing more data points.

From the analysis of both sensors mounted in the front of the drone, 1A and 1B, it seems that lower GPS fix frequencies, such as 0.1 Hz, result in a broader spread of readings, potentially affecting the precision of the GPS data. Conversely, higher frequencies allow for more consistent and possibly more precise readings, albeit with the caveat that they may also capture more noise. The comparison between the two sensors suggests that while both exhibit variability at lower update frequencies, their performance may differ at higher frequencies, with Sensor 1B showing a narrower spread in longitude data at 5 Hz compared to Sensor 1A. This could imply that Sensor 1B is more adept at handling higher update rates without sacrificing accuracy.

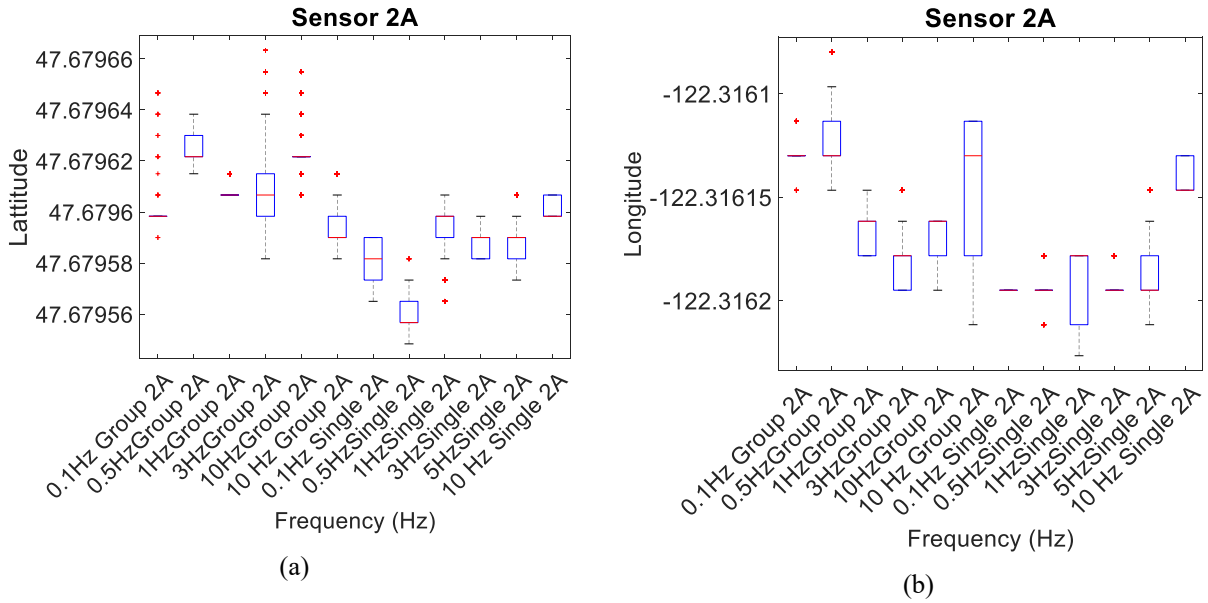

Figure 6-3. Variability in GPS Sensor 2A at Different Frequencies: Latitude and longitude box plots showing variations under different frequencies, comparing single sensor (Single) versus multi-sensor (Group) microcontroller configurations. (a) Latitude readings display a relatively stable median value with compact interquartile ranges, although some outliers are evident at the lowest (0.1 Hz) and highest (5 Hz) frequency settings, suggesting occasional signal instability or environmental noise influence. (b) Longitude data reveals a substantial spread, particularly at the 1 Hz frequency, indicative of a higher degree of variability which appears to be lessened at the highest tested frequency of 10 Hz, pointing towards improved consistency with increased data sampling.

Sensor 2A, positioned at the rear of the drone and depicted in Figure 6-3, demonstrates a stable performance in latitude, with an ~11m spread and a consistent median value across different frequencies. The interquartile range (IQR) is compact, although outliers are present at both the lower (0.1 Hz) and higher (5 Hz) frequency extremes. In contrast, longitude readings display considerable variability, especially at the intermediate frequency of 1 Hz, which diminishes at the higher frequency of 10 Hz, with a spread of ~10.49 m. Altitude measurements show variability at both 1 Hz and 10 Hz frequencies, suggesting these frequencies may yield less reliable altitude data due to potential signal fluctuations, with an overall range of about 10m. When comparing solo versus group configurations, Sensor 2A exhibits a smaller IQR when operating independently. However, the distribution of longitude errors is widest when the sensor is part of a group operating at 10 Hz, indicating possible interactions or interference from other system components. Despite this, the magnitude of errors remains consistent across different frequencies and configurations, suggesting that the microcontroller's handling capacity and the inherent electrical characteristics of the sensor setup do not adversely affect the absolute accuracy of the measurements. This insight

underscores the importance of considering sensor placement and configuration to optimize performance and reliability in UAV applications.

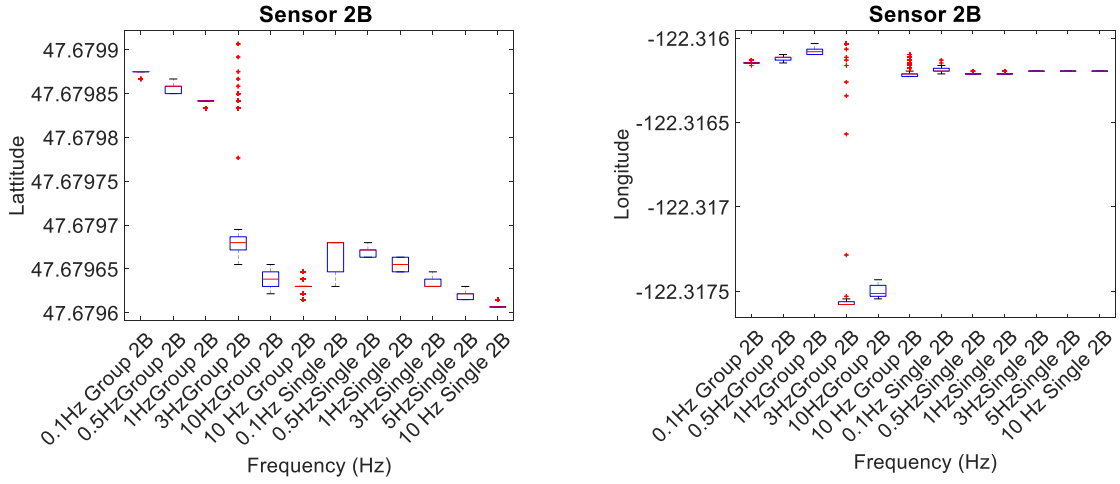

(a) (b)

Figure 6-4. Variability in GPS Sensor 2B data across frequencies: comparison between individual and shared microcontroller setups. (a) latitude readings reveal a broader variance at the lower frequency of 0.1 Hz yet display a trend toward stabilization as the frequency increases, with 10 Hz frequency exhibiting a notably tighter spread, which may indicate enhanced signal tracking capabilities at this sampling rate. (b) The longitude measurements depict a more consistent and condensed distribution, indicating reliable sensor performance. The data shows minimal outliers, particularly at higher frequencies, suggesting stability in capturing GPS signals

Sensor 2B demonstrates high consistency and reliability in latitude measurements with minimal outliers, as shown in Figure 6-4 (b). The longitude measurements exhibit a broader spread at the lowest frequency of 0.1 Hz but become more stable at 10 Hz. Similarly, altitude readings (Figure 6-5(d)) show decreased variability at higher frequencies, particularly at 5 Hz and 10 Hz, suggesting better performance with increased data sampling rates.

Comparative analysis of Sensors 2A and 2B reveals that both sensors achieve more consistent performance at higher update frequencies, attributed to a denser data collection that likely enhances GPS positional accuracy. Sensor 2A, however, exhibits greater longitude variability at lower and intermediate frequencies than Sensor 2B, potentially indicating higher sensitivity to environmental factors or inherent variations in sensor manufacturing and performance.

Overall, the performance of Sensors 2A and 2B underscores the importance of selecting appropriate update frequencies to optimize GPS accuracy. The observed consistency at higher frequencies suggests that increasing the update rate may mitigate the impact of errors and environmental interference, enhancing the reliability of GPS data in UAV applications.

Figure 6-5 illustrates the performance of embedded GPS sensors at a constant altitude, revealing varied sensor characteristics across different frequencies. Sensor 1A shows considerable variability in altitude readings at lower frequencies (0.1 Hz), with a broad interquartile range (IQR) that tightens significantly at higher frequencies (5 Hz and 10 Hz), indicating more stable measurements. In contrast, Sensor 1B demonstrates a consistently narrower IQR across the frequency spectrum, suggesting a more stable performance, particularly at higher frequencies where it maintains a compact spread, indicative of its superior capability to deliver consistent altitude measurements under dynamic UAV operational conditions. For Sensors 2A and 2B, Sensor 2A displays a relatively uniform spread of altitude readings, indicating stable performance across various frequencies. Sensor 2B, however, exhibits increased variability and outliers at lower frequencies, suggesting heightened sensitivity to lower update rates which may affect the reliability of altitude measurements.

The analysis underscores that Sensors 1A and 1B perform optimally at higher frequencies, with Sensor 1B showing slightly superior stability. Sensors 2A and 2B present distinct performance profiles, emphasizing the need to tailor the update frequency to each sensor's characteristics and the specific requirements of the application. These findings provide critical insights for the design and optimization of embedded GPS systems in UAVs, guiding the selection of sensors and configuration settings to enhance operational performance and reliability.

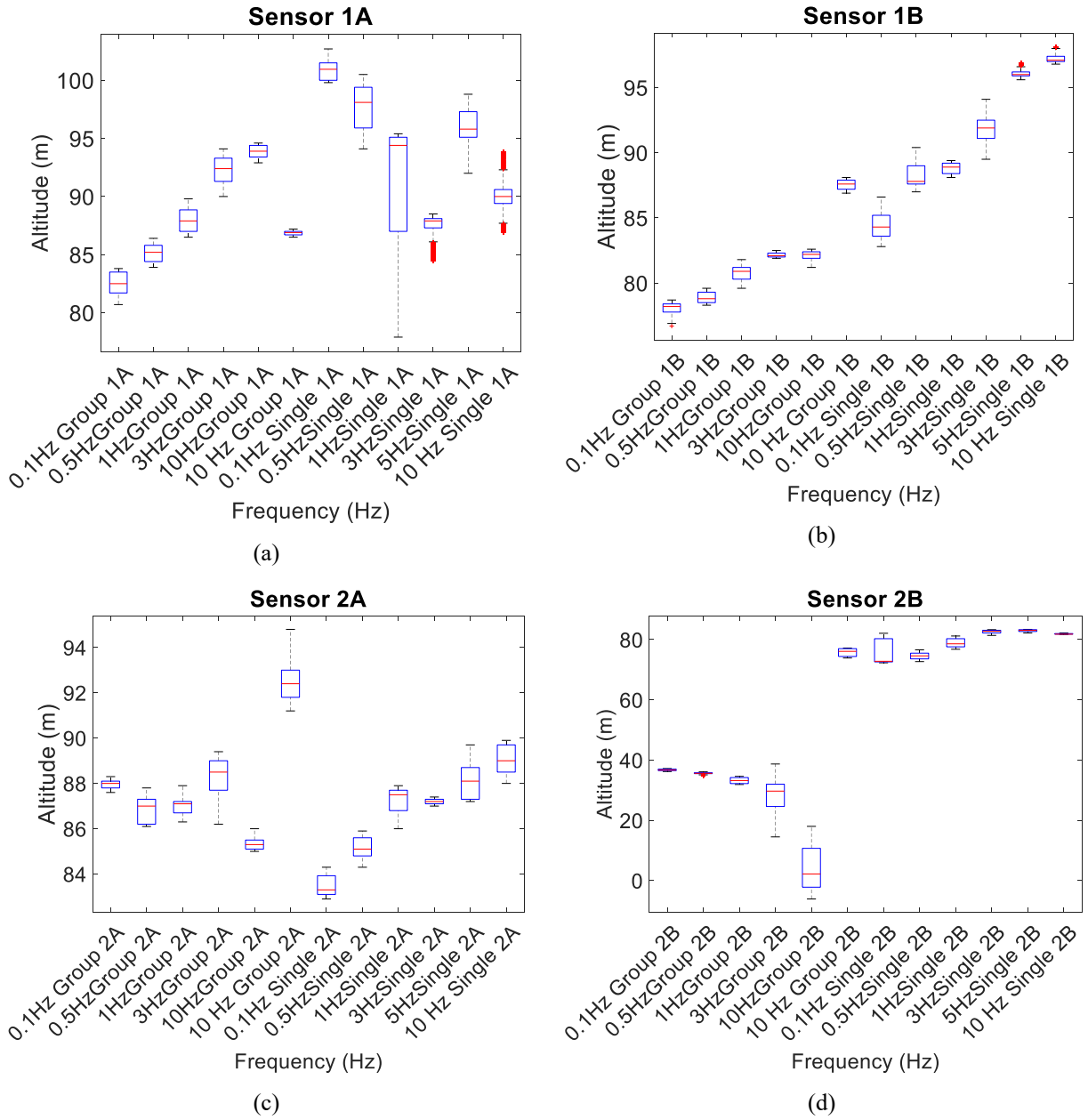

Figure 6-5. Altitudinal Performance Variance of GPS Sensors Across Different Update Frequencies. These box plots delineate altitude readings captured by four distinct GPS sensors, designated as 1A, 1B, 2A, and 2B. Each sensor's performance is assessed individually (labeled 'Single') and as part of a collective group managed by a single microcontroller (labeled 'Group'). (a) Sensor 1A displays notable variation in altitude at lower frequencies, with outliers indicative of sporadic deviations from expected values. (b) Sensor 1B reveals tighter consistency, especially at higher frequencies, signifying dependable altitude tracking. (c) Sensor 2A's altitude data exhibits moderate spread across frequencies with occasional anomalies, potentially reflecting environmental influences or sensor idiosyncrasies. (d) Sensor 2B shows distinct reliability, with reduced variability at increased frequencies, suggesting robust altitude determination capabilities in varied operational settings.

Running the sensors individually versus in a group does not show a consistent pattern of interference or performance degradation, suggesting that the microcontroller system can effectively handle multiple sensors without introducing additional noise or errors. This finding has important implications for system design and optimization, as it suggests that the use of a single microcontroller can streamline hardware integration without sacrificing accuracy or reliability. Moving forward, further research may explore additional factors influencing sensor performance and scalability considerations for large-scale deployment scenarios. The experimental data suggests valuable insights regarding the first hypothesis in question. Integrating multiple GPS sensors into a single microcontroller does not significantly affect performance compared to individual microcontrollers for each sensor

To investigate the second hypothesis concerning the influence of microcontroller type on GPS sensor performance, we compared the operation of sensors 1A, 1B, and 1C when interfaced with an Arduino Mega and a Teensy 4.1 microcontroller. The analysis, excluding data from different sensor setups and focusing on urban location 4, is Figure 6-14, Figure 6-15, and Figure 7-1 ((a),(c),(e)) and the statistics are summarized in Table 6-1. The data for test was collected in urban location 4. The statistical evaluation highlighted discernible disparities in sensor outputs when transitioning between microcontrollers.

The analysis revealed that switching from Arduino to Teensy 4.1 microcontrollers resulted in varied sensor performance as evidenced by shifts in mean, standard deviation (SD), and root mean square (RMS) values of altitude, residual magnitude, and angular errors. For example, Sensor 1A exhibited a mean altitude error reduction of 2.6 m on the Teensy (~Δ2.6/11 m $\approx$ 24% improvement), suggesting an improvement in accuracy. However, this was accompanied by a slight increase in residual magnitude error (~5%) and a substantial rise in angular error (~84%), indicating potential data capture issues with the Arduino.Similarly, Sensors 1B and 1C improved altitude error mean with the Teensy. Nevertheless, both sensors showed increases in residual magnitude and angular errors, with Sensor 1C recording the most pronounced improvement in altitude error mean alongside increases in error variability.

For Sensor 1A, the standard deviation (SD) for altitude error marginally decreased from 18.2654 to 17.9635, suggesting a slight improvement in measurement consistency with Teensy

4.1. However, the residual magnitude error's mean slightly increased from 27.1901 to 28.8255, and its SD increased from 18.0468 to 20.5957, pointing to more variability with Teensy 4.1.

Sensor 1B showed a small improvement in altitude error mean, decreasing from -18.7950 to -17.9807. Nevertheless, the SD for altitude error showed negligible change, moving from 21.4509 to 21.1937. The residual magnitude error mean increased from 31.5387 to 33.0507, and the angular error mean also rose from 0.7556 to 1.5858, both indicative of worsened performance in these metrics with Teensy 4.1. Sensor 1C exhibited the most substantial mean altitude error improvement, dropping significantly from -16.9624 to -9.3860, alongside an SD increase from 17.7701 to 22.0468, which implies greater dispersion of measurements with Teensy 4.1. The residual magnitude error's mean showed an increase from 23.3855 to 27.6662, and the SD decreased from 21.6481 to 18.2269, suggesting less variability but higher errors on average.

RMS values for altitude error decreased for Sensors 1A and 1C, corroborating improvements in altitude measurement with the Teensy. However, increased angular RMS across all sensors indicated a change in angular measurement precision. ANOVA tests underscored these observations, revealing statistically significant differences in error means between the two microcontroller types, as evidenced by extremely low p-values and high F-statistics in Table 6-2. The extremely low p-values, all effectively zero, strongly indicate that there are statistically significant differences in the means of the errors between the two microcontrollers for each sensor. This signifies that changing microcontrollers does have a statistically significant impact on the performance of the sensors across all measured error types. The F-statistics are quite high in all cases, reinforcing the conclusion that the performance differences are significant and systematic rather than random variations. Given these results, we must reject the null hypothesis that swapping microcontrollers does not affect sensor performance. Instead, we conclude that the type of microcontroller significantly impacts sensor readings. Consequently, the choice of microcontroller for PATHFINDER needs to be validated.

Table 6-1. Signal statistics reported by sensors 1A,1B, and 1C when connected to Arduino mega and a Teensy 4.1 microcontroller at Urban Location 4.

Sensor	Microcontroller	Error	Mean	Median	SD	RMS
1A	Arduino	Altitude	-21.4723	-23.0700	18.2654	28.1901
		Residual Magnitude	27.1901	22.0245	18.0468	32.6341
		Angular	0.6520	1.9263	2.0826	2.1823
	Teensy 4.1	Altitude	-18.8130	-21.4700	17.9635	26.0118
		Residual Magnitude	28.8255	23.3829	20.5957	35.4272
		Angular	1.1997	1.9632	1.7562	2.1268
1B	Arduino	Altitude	-18.7950	-16.4700	21.4509	28.5201
		Residual Magnitude	31.5387	23.3058	23.7673	39.4915
		Angular	0.7556	1.8200	1.9302	2.0729
	Teensy 4.1	Altitude	-17.9807	-18.5700	21.1937	27.7935
		Residual Magnitude	33.0507	30.0544	19.5299	38.3896
		Angular	1.5858	2.1381	1.5513	2.2185
1C	Arduino	Altitude	-16.9624	-19.6700	17.7701	24.5662
		Residual Magnitude	23.3855	14.1612	21.6481	31.8673
		Angular	0.3969	1.7016	2.2066	2.2420
	Teensy 4.1	Altitude	-9.3860	-13.3700	22.0468	23.9616
		Residual Magnitude	27.6662	25.6796	18.2269	33.1306
		Angular	1.6718	1.9440	1.2885	2.1107

Very small Values and very large values are rounded to 0 and inf respectively

Table 6-2. ANOVA Testing statistics of signals from Arduino mega and Teensy 4.1 microcontrollers.

Sensor	Error Type	F-Statistic	T-Statistic	P-Value
1A	altitude	4198.959	-64.800	0
	magnitude	1389.869	-37.281	0
	angular	15750.496	-125.501	0
1B	altitude	284.162	-16.858	0
	magnitude	941.393	-30.682	0
	angular	43794.850	-209.272	0
1C	altitude	27896.403	-167.022	0
	magnitude	8916.171	-94.425	0
	angular	97004.172	-311.455	0
Very small Values and very large values are rounded to 0 and inf respectively				

For accurate 3D localization using latitude, longitude, and altitude data, the sensor's ability to provide precise and consistent readings is paramount. Given that residual and angular errors are derived from latitude and longitude—which relate to the horizontal positioning—and altitude provides the vertical component, the microcontroller that consistently yields lower errors in these metrics would be preferable. Teensy 4.1 appears to reduce mean altitude errors for sensors 1A to 1C, which is beneficial for vertical localization accuracy.

The Residual Magnitude Error impacts the overall 2D position estimation as it is derived from latitude and longitude. A lower residual error is indicative of more accurate 2D positioning. The Teensy 4.1 demonstrates a slight increase in mean residual errors for sensors 1A and 1B, but a decrease in standard deviation for sensor 1C, suggesting a trade-off between increased average error magnitude and consistency of measurements. Angular accuracy is crucial for orientation. The Teensy 4.1 shows an increase in mean angular errors across all sensors. However, there is a decrease in standard deviation for sensors 1A and 1B, suggesting that while the average error is higher, the variability of those errors is less. This could be advantageous for ML applications where consistent error patterns are more predictable and can be corrected algorithmically.

Considering these aspects, and the significantly higher speed, multiple IO, Teensy 4.1 could be the preferred choice for PATHFINDER. For machine learning purposes, consistent error

patterns, even if the errors are somewhat larger, can be more beneficial because the algorithms can easily learn to correct consistent errors. Given that the Teensy 4.1 shows more consistent (less variable) errors, it might still be the better option for feeding data into an ML model aimed at enhancing 3D localization accuracy. The machine learning model can be trained to identify and correct for the systematic errors that are introduced by the Teensy microcontroller, leading to a robust 3D localization system.

6.1.2 *Impact of update frequency on GPS sensors*

This section evaluates the impact of polling frequency on the data parsing integrity of GPS sensors using Teensy 4.1. The integrity assessment involved comparing the GPS coordinates parsed on nmeaParser in MATLAB [218], with those parsed directly on the microcontroller, transmitted to the host PC. The study was conducted using sensors 1A, 1B, 1C, 2A, and 2B, collecting 100,000 entries at 1 Hz, 5 Hz, and 0.1 Hz from two different open-field locations across four days to reduce potential GPS signal distortion effects. The different errors we are testing for in this experiment are

- Parsing Accuracy Evaluation: Accuracy was assessed by verifying the congruence between the count of NMEA sentence lines and the number of GPS fixes. The microcontroller, for each GPS sensor, appends two newline characters post-fix, allowing a Python script to equate the count of new line characters to GPS fixes, thus confirming no data loss occurred between fixes.

- String Length Verification: The consistency of data string lengths was ensured, with any strings deviating from the expected length either omitted or flagged for further analysis.

- Range Validation: The dataset underwent a validation check on a PC using Python to confirm that all values fell within their expected ranges and that no corrupted characters were present.

- NMEA String Sample Assessment: A sample of NMEA strings was evaluated for parsing accuracy by comparing reported and parsed locations within a ±1 second window from the reported time, ensuring consistency across frequencies

- Uncategorized errors: Some errors led to data being dropped or ignored, possibly due to anomalies in the serial monitor capture program or the Python environment rather than the NMEA processor itself.

Table 6-3. NMEA Adafruit Parsing Library error rate and contributing factors.

Frequency	Error Count	Data points collected (cumulative)	Error Rate	Length Error	Value Validation	NMEA Parsing Issues	Uncategorized error
0.1	800	100000	0.8	749	21	30	0
1	1044	100000	1.044	873	45	126	0
5	2302	100000	2.302	991	1153	158	0
10	3909	50000	7.818	2179	1352	366	12

Accepted strings are strings that have been written to the SD card and passed validation tests. We observe in Table 6-3 that at a frequency of 5 Hz, the likelihood of data corruption is higher than at 1 Hz and 0.1 Hz. However, no significant difference was detected between the corruption rates at 0.1 Hz and 1 Hz. At 1 Hz, 1,044 lines out of 100,000 collected were corrupted. When two consecutive lines were corrupted, At 10 Hz sampling rate, we noted an increase in the corruption rate compared to both 1 Hz and 5 Hz. Particularly, the "Value Validation" error escalates significantly at 5 Hz and 10 Hz, highlighting the decreased reliability of the system at these frequencies.

Despite the increase in error rates, a 10 Hz frequency allows for the accumulation of a larger volume of valid data; out of 50,000 data points, 3,909 were identified as corrupted, translating to an error for approximately every 13 correct readings. The errors do not exhibit a systematic pattern, with the most extended sequence of consecutive errors being three, a rare occurrence within the dataset. The most common error configuration we recorded was a pattern of three valid readings followed by two errors, occurring 579 times in the test. No additional predominant error patterns were detected. This highlights that the errors are random and not due to communication issues like buffer overflow, which would indicate themselves in a clear pattern. All frequencies tested revealed no parsing discrepancies between accepted strings and their corresponding NMEA strings. However, an analysis of erroneous strings rejected during the process uncovered multiple instances of data mismatch, the introduction of extraneous characters, and missing characters within numerical values, e.g., a reported NMEA HDOP value of 0.763 being printed as 0.73 but reported in the API as 0.763. These errors hint that some of the

opportunistic processing of data is interrupted by the arrival of new information within the the transmission buffer. Consequently, around 10 Hz is an upper bound on the transmission rate of the GPS data for 5 GPS sensors, all sending approximately 5 NMEA sentences every fix. To increase the rate of transmission means reducing the number of NMEA parameters being transmitted or increasing the UART baud rate.

Figure 6-6 shows a timing diagram that effectively illustrates the effective impact of the most common error modes on GPS and predictor extraction for the IRNN-DNN algorithm. At 1 HZ, the most common error pattern was one invalid fixed data line for every three valid lines of lines. This reduction in the effective data rate is significant because when GPS signal corruption occurs, the slower fix rate combined with data corruption elongates the interval between accurate GPS localizations. However, at 10 Hz, even with 3 lines of consecutive corruption, the signal loss was only 0.3 secs. 0.3 seconds translates to 3.3 HZ. This sufficiently short interval has major implications IRNN-DNN algorithm. The IRNN-DNN should be able to robust against bad or corrupted missing data that can appear as many as three consecutive values. The analysis also reveals that the corruption rate per sensor remains consistent, with an average of 80,000 errors each, across five sensors managed by a single Teensy controller result in 398,157 corrupted lines out of 6,000,000 readings. This finding suggests that error distribution is evenly spread across the sensors, without any single sensor displaying a disproportionate error rate. While polling at higher frequencies, the average error rate increases by at least a factor of 3; the effective localization rate, as provided by the GPS, is significantly higher. Despite a higher absolute number of errors at increased frequencies, the ratio of valid data to corrupted data suggests that the impact on the effective localization rate is less severe than might be expected based solely on the error rate. This suggests that higher frequency polling can still yield a net gain in usable localization data for applications where more frequent updates are critical. Consequently, the pathfinder system can parse the data at 10 Hz.

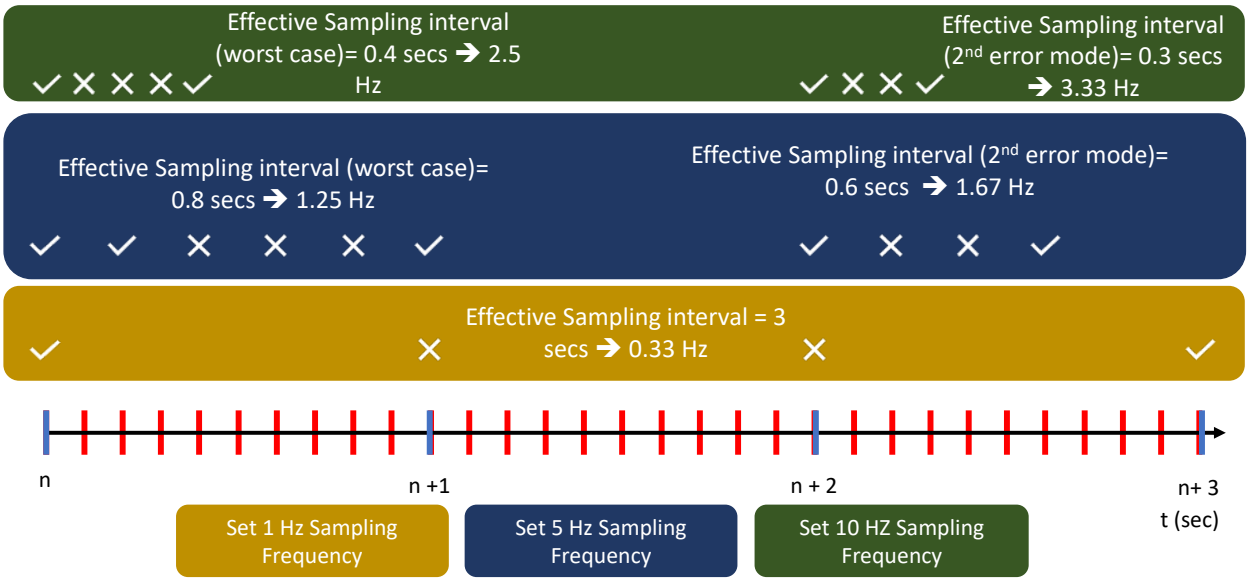

Figure 6-6. Evaluation of Optimal Operational Frequency Despite Error Occurrences. The diagram contrasts effective sampling intervals across different operational scenarios. Despite a set 1 Hz sampling frequency, error instances (depicted as crosses) can significantly lower the effective sampling frequency, but at the optimal frequency (green), the system maintains an effective 2.5 Hz despite higher number of errors. Higher set frequencies, like 10 Hz, endure errors without a substantial drop in effective frequency, indicating a benefit in data collection. Checkmarks show successful data captures. The 2nd error mode only increases the effective frequency

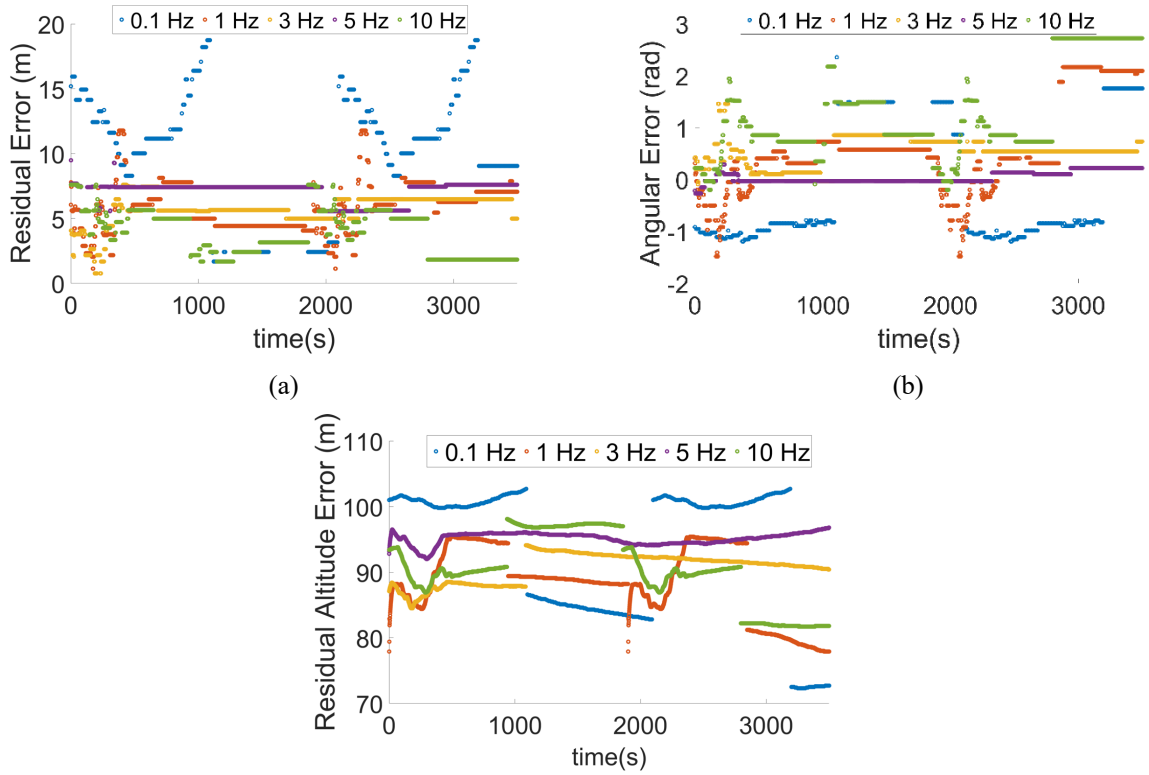

Figure 6-7. Time Scatter Plot Analysis of GPS Sensor Performance at different update frequencies over time in semi-urban location 2. (a) The residual error scatter plot showcases the stability of GPS signal accuracy across different update frequencies. Occasional sharp declines in error suggest improvements in accuracy, likely due to additional satellites coming into the sensor's field of view, reducing signal masking. (b) The angular error plot indicates sudden shifts in error direction, hinting at changes in satellite positioning relative to the sensor. Notably, a change to positive 2π radians suggests the new satellite signal is from a westerly direction, aligning with typical GPS satellite movement from west to east. (c) The altitude error plot correlates with the other two, where a decrease in error magnitude coincides with the satellite visibility, supporting the hypothesis that new satellite data can significantly impact sensor accuracy.

Transmission and polling rate is one half of the coin. The other is if GPS fix rate. Fix rate is number of times the GPS sensors and their co-processor process the signals revived from the satellite and perform trilateration calculations. Having a higher effective fix rate means that the effects of the environment on satellite signals can be more easily distinguished. However, very high frequency rates may also mean that signal artifacts and other noises are more prevalent in the signal.

In the context of stationary GPS sensors capturing data for analysis, periodicity within the error measurements is a significant factor that can be exploited for error correction. A distinct alignment of error periodicity is visually observed at a 1, 3 and 10 Hz update frequency, seen in Figure 6-7. This suggests that at these frequencies, the sensor is neither too slow to miss the periodic event nor too fast to introduce excessive noise. Figure 6-7 (b) highlights the presence of noise amidst the oscillation in altitude errors. While the noise complicates the direct use of these oscillations for error correction, the underlying periodicity is still a valuable characteristic. however, by corelating the periodicity of the altitude height, it is possible to identify a periodic nature of the angular error. This means that we can predict an inverse corrector for the GPS error in the future to account for offset angle based on past performance. The identification of periodic nature in angular errors, correlated with altitude height, provides an opportunity to design predictive models that can counteract GPS errors. If the periodic errors are consistent and predictable, a model could be trained to apply an inverse correction factor to the GPS data, effectively compensating for the anticipated error at any given time. An RNN could learn the temporal patterns of these errors, using historical data to predict the phase and magnitude of the error and apply a real-time corrective offset. RNNs are well-suited to this task due to their inherent design, which allows them to recognize and predict sequences in time-series data. By training an RNN on the historical GPS data, including the identified periodic errors, the network could learn to predict future errors. This predictive capability could then be used to apply an inverse corrector to the incoming GPS data, potentially improving accuracy by compensating for the periodic error component.

The time scatter plots, Figure 6-7, illustrate marked fluctuations in GPS signal accuracy, delineated by breaks in the data corresponding to sudden jumps in error, likely caused by changes in satellite visibility. Specifically, in Figure 6-7 (c), we observe that the radial altitude error decreases markedly at certain frequencies, indicating the potential acquisition of a signal from a new GPS satellite coming into view. In the second plot, Figure 6-7 (b), there is an immediate reversal in the direction of the error following the decrease, which supports the hypothesis of altered satellite visibility. This sudden directional change in error, accompanied by a substantial reduction in the magnitude of the residual error, Figure 6-7 (a), points to a significant latitude error component, as suggested by the orientation of the sensors in the North-East-Up (NEU) coordinate frame during the experiment. The positive angular shift of approximately $+2\pi$ radians implies an

error predominantly in the westerly direction, consistent with the expected movement of GPS satellites from west to east. The concurrent drop in altitude error further bolsters the argument that a newly visible satellite contributed positively to signal accuracy. Finally, the plot captures a pronounced increase in error magnitude roughly 1000 seconds later, which could be attributed to a GPS satellite moving out of visibility, instantaneously exacerbating the error. These observations, captured through the scatter plots, offer substantive evidence of how GPS signal quality is dynamically modulated by the shifting coverage of the satellite constellation. The in-depth analysis of stationary GPS sensor data reveals that periodicity in altitude and latitude errors, particularly evident at specific update frequencies, can be harnessed for predictive error correction. We can look at Table 6-5 and Table 6-6 to see if it is possible to identify other secondary relationships through a co-factor analysis. This is done in section 6.2.

Across all sensors, there is a discernible effect of sampling frequency on data variability. Sensors tend to perform differently at specific frequencies, which should be considered when setting up the data collection protocol or training ML models. The performance of each sensor appears to be individualistic, with some showing better precision at higher frequencies and others at lower frequencies. This individual performance characteristic should be factored into an ML model as it can affect the prediction depending on which sensor's data it is processing. The provided information in Figure 6-7 indicates that there are observable periodic trends in the altitude and latitude errors, particularly at certain update frequencies. When examining the altitude error across various frequencies, any periodic behavior suggests an underlying systematic influence on the GPS sensor's readings. For example, if the altitude error displays regular oscillations, it could be indicative of atmospheric conditions, satellite geometry, or multi-path effects that have a cyclical nature. This periodicity could be influenced by factors like satellite positions changing in a predictable pattern. Urban locations with strong reflectors can change this periodicity, by blocking the signal, or having signal propagate for a longer distance through multi-path reflections. IRNN-DNN can exploit this periodicity for error correction. Consequently, a high fix rate is needed for the algorithm to function more effectively.

Our study demonstrates that consolidating sensor connections onto a single microcontroller does not compromise system performance or introduce significant errors. This finding has important implications for system design and optimization, as it suggests that using a single

microcontroller can streamline hardware integration without sacrificing accuracy or reliability. Moving forward, further research may explore additional factors influencing sensor performance and scalability considerations for large-scale deployment scenarios. Additionally, given that each sensor functions better at a different frequency, we could use corrective and inverse variance weighting methods to account for the GPS sensor-specific and operating frequency-specific methods. This evidence validates the application of the inverse variance-based weighted filter discussed in section 3.2. While no evidence supported the hypothesis that faster GPS fixes will result in more accurate localization fixes, potential trends were found in the GPS error signals that may be utilized for error correction. Running the entire embedded stack at these higher speeds of 10 Hz allows for a significantly greater volume of data points that can be analyzed for pattern-based collection.

6.1.3 *Impact of receiver variation and sensor tolerance*

In examining the impact of receiver variation and sensor tolerance on GPS data accuracy and precision, our study targeted hypothesis that disparities in manufacturing, processing, and internal clock timing among identical GPS receivers result in measurable differences in positional data quality. To address this, we conducted a detailed comparative analysis of multiple GPS receivers of the same make and model. Each receiver was equipped with external active antennas that had undergone impedance matching within a 10% tolerance range, reducing potential discrepancies due to antenna variations. This setup allowed us to focus on intrinsic differences between the receivers themselves.

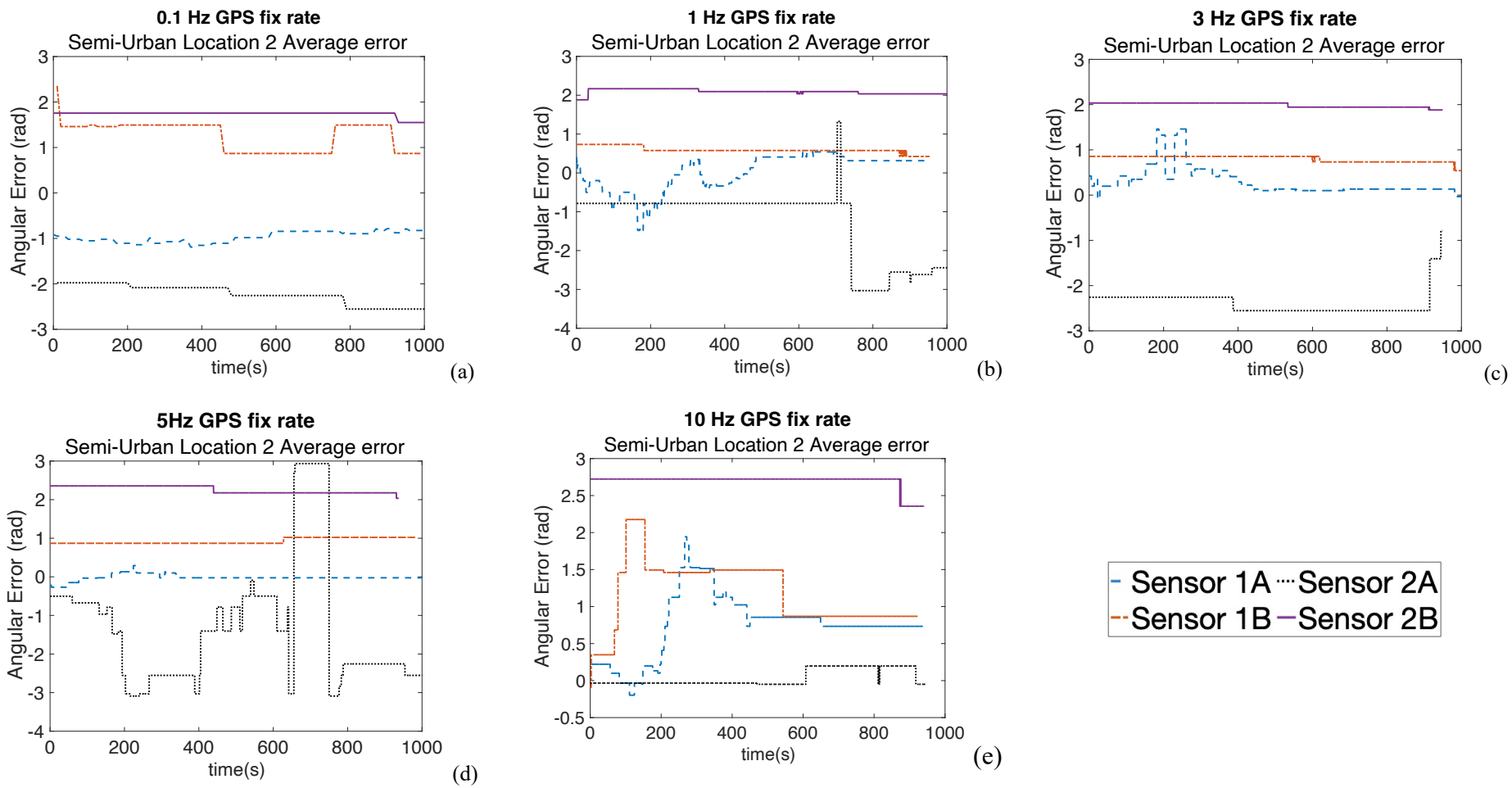

Figure 6-8. Temporal Angular Error Analysis for GPS Sensors at Varied Frequencies. These plot trace angular error over time for GPS sensors 1A, 1B, 2A, and 2B at different frequencies. (a) At 0.1 Hz, errors are stable with occasional spikes. (b) Increasing the frequency to 1 Hz, more frequent deviations in error occur, which may correspond to more dynamic environmental factors or sensor sensitivity to signal changes. (c) At 3 Hz, the errors are more pronounced and erratic, possibly reflecting the compounded effect of increased data capture rate and environmental noise. (d) The 5 Hz frequency plot reveals a pattern of sharp peaks, indicating significant, abrupt changes in the error magnitude, possibly due to sudden shifts in GPS satellite visibility or signal multipathing effects. (e) At the highest frequency of 10 Hz, the angular error demonstrates high variability, with rapid oscillations that suggest the sensor's heightened reactivity to satellite dynamics or immediate environmental disruptions.

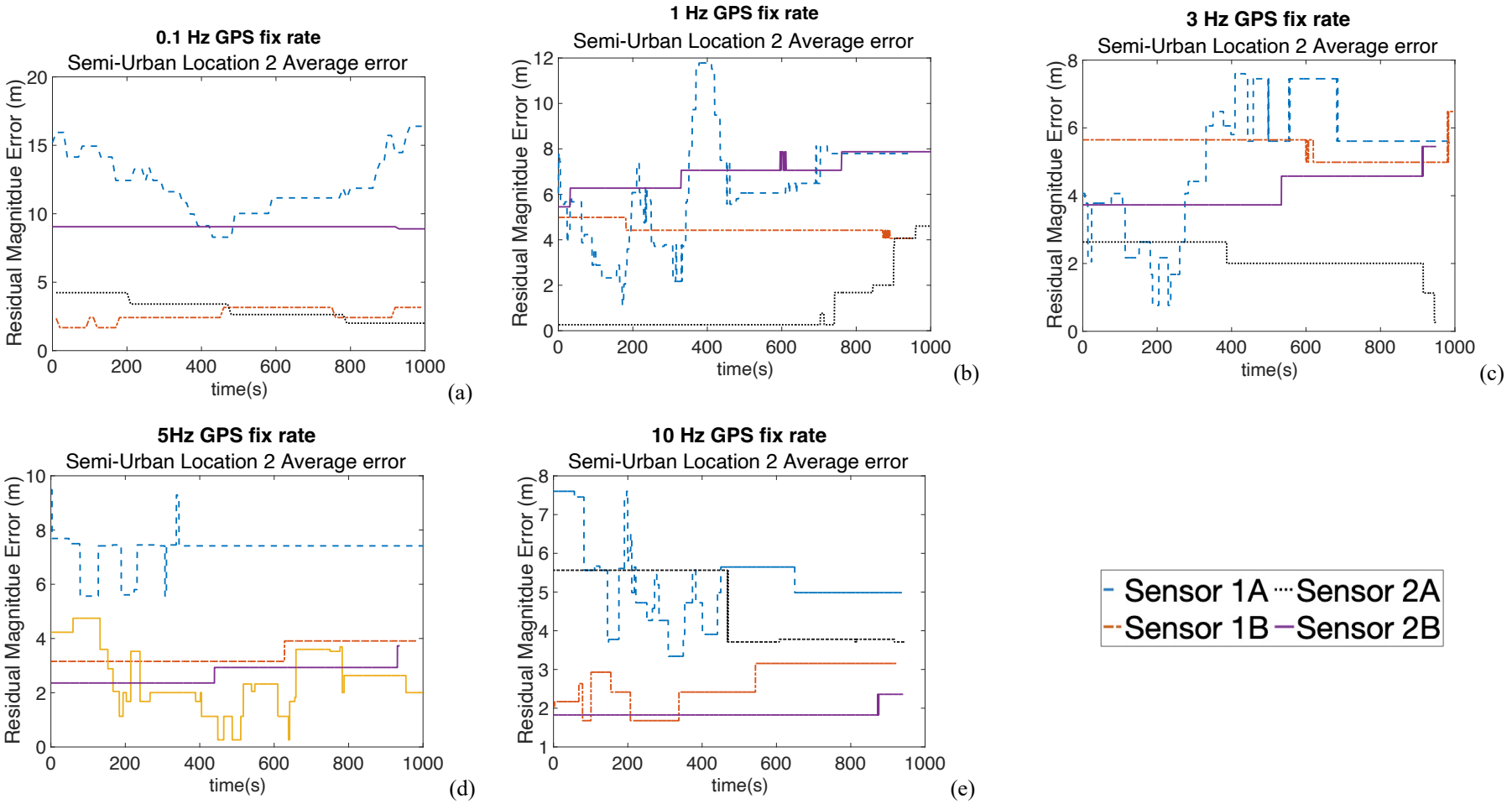

Figure 6-9. Overview of GPS Sensor Residual Magnitude Errors Across Frequencies. These graphs depict the deviation from true position by various sensors over time, showing their performance at different update rates. (a) Sensor 1A is highly variable at 0.1 Hz. (b) At 1 Hz, volatility arises in all sensors except 1B. (c) Sensor 1A displays erratic behavior at 3 Hz. (d) At 5 Hz, Sensors 1A and 2A's errors surge, indicating high-frequency sensitivity. (e) At 10 Hz, Sensor 1A's errors escalate, 1B lacks stability, 2A's performance improves, while 2B consistently maintains accuracy. This contrast underscores the necessity for selective frequency application to match sensor capabilities with operational demands.

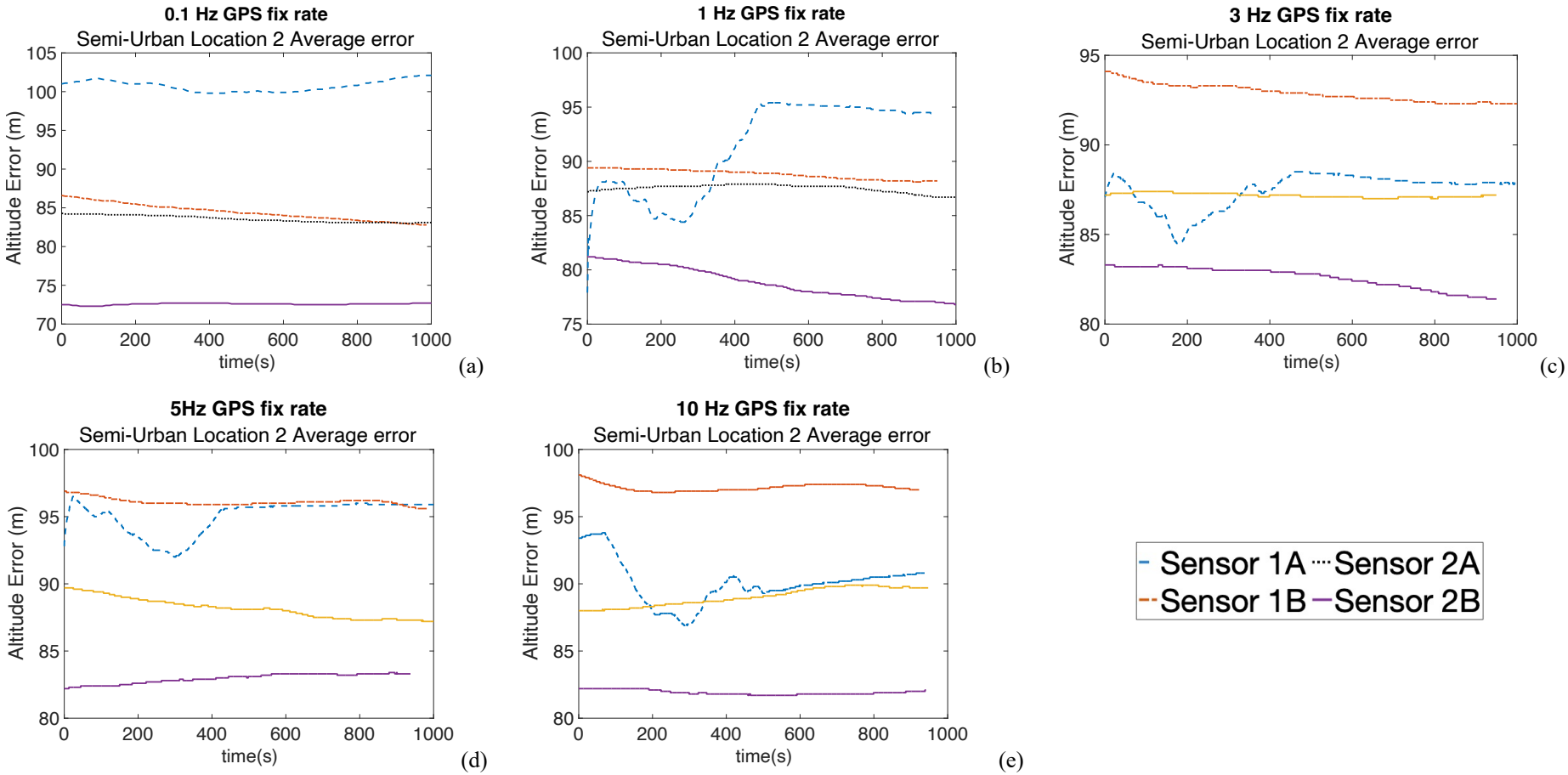

Figure 6-10. Altitude Error Fluctuations at Varied Sampling Frequencies. Displays altitude error trends for the same GPS sensors at different GPS 'fix' frequencies. (a) At 0.1 Hz, stable altitude with minimal error suggests consistent signals. (b) At 1 Hz, altitude errors are constant, with a decreasing trend for sensors located on the right-hand side of the drone, indicating possibly improved data due to frequent updates. (c) At 3 Hz, errors show peaks and troughs, hinting at signal or atmospheric disturbances. (d) At 5 Hz, notable error deviations emerge, indicating increased environmental sensitivity. (e) At 10 Hz, altitude error variability peaks, suggesting noise influence or rapid satellite changes. This suggests higher frequencies may increase data volume and noise-related errors.

The analysis of the data collected in identical test conditions is presented in Figure 6-8, Figure 6-9, and Figure 6-10 which presents evidence of distinct performance characteristics among the receivers, which exhibited variances in signal processing capabilities and precision.

At higher frequencies, sensor 1A showed signal integrity, suggesting robust internal processing that could counteract the expected increase in error rates typically associated with rapid data capture. Sensor 1A demonstrated this resilience, particularly at 10 Hz, where it managed to keep the residual error below the anticipated threshold, as shown in the residual error plot, where its curve remains lower compared to its counterparts. Conversely, Receiver 1B achieved optimal performance at a lower frequency of 1 Hz. Its data output revealed a significant reduction in angular and residual altitude errors when compared to its performance at 10 Hz, which was evident from the angular error graph where its error rate notably decreased. Receiver 2A, displayed a high level of precision in angular error at 3 Hz amidst urban multipath propagation, whereas Receiver 2B showed substantial signal degradation under similar conditions. A statistical analysis elucidated that the performance between different receivers was not correlated, signifying manufacturing variations did not translate to a uniform impact on performance. The temporal synchronization of the receivers also allows us to discern collective error trends. Altitude error trends are discernible at 3 Hz, manifesting across several units simultaneously. This commonality in error occurrence points to the potential for system-wide correction strategies.

The overall consistency of each sensor's performance was similar when repeated runs were conducted at high frequencies (Table B-1 and Table B-2). This repeatability is pivotal as it implies that the inherent errors within a receiver remain stable over time at higher frequencies, which is beneficial for developing correction algorithms. Significant is the consistency at higher operating frequencies. This is a secondary validation of the finding that the GPS sensors need to operate at high frequency for repeatable performance. Consequently, 5+Hz is a good target frequency for the operation frequency for PATHFIINDER.

Examining the information presented in Table B-1 and Table B-2 and comparing it with the temporal plots in Figure 6-8, Figure 6-9, and Figure 6-10 at a significance level of 0.05, we observed consistent performance in the following sensor-frequency-error type combinations during two separate testing instances. This consistency is evidenced by P-Values exceeding 0.05

and F-Statistics approximating 1 for the following senor, parameter, and operating speed parameters:

- Sensor 1A at 10Hz for all distance, altitude, and angular errors
- Sensor 1B at 3+ Hz for angular and distance error
- Sensor 1B at 10 Hz for altitude error
- Sensor 2A at 10 HZ for all distance, altitude, and angular errors
- Sensor 2B at 10 HZ for all distance, altitude, and angular errors

At various other points and during other testing iterations, the results also indicate marked discrepancies in the variability and average values across the lower frequencies. With P-values registering well below the threshold of 0.05, the statistical significance of these discrepancies is affirmed, endorsing the hypothesis that sensor data exhibit variability. Furthermore, the F-Statistics generally deviate from unity, pointing to unequal variances and suggesting that the data display heteroscedasticity, which is the presence of non-constant variability within the dataset. Thus the sensor noise is unpredictable at lower frequencies. At higher frequencies (above 5 Hz), we see indications of significantly lower heteroscedasticity and minor indications of homoscedasticity within the dataset(s).

This leads to following conclusions: Our study refutes the hypothesis that identical GPS receivers inherently experience measurable performance disparities due to manufacturing, processing, and clock differences. The performance profile of each receiver is unique and more stable at higher frequencies. These individualistic performance characteristics emphasize the necessity of accounting for each receiver's unique behavior in data collection and processing. It also highlights the potential for using machine learning models, like RNNs, to correct for errors, especially given the periodic nature of certain discrepancies.

6.1.4 *Impact of location on residual error*

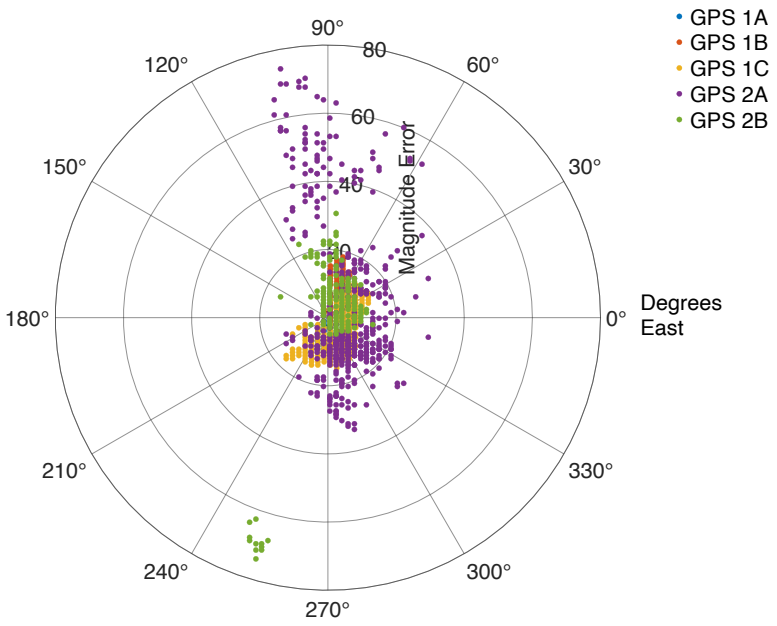

Figure 6-11. GPS Error Distribution in Semi-Urban Environment. This polar scatter plot illustrates the magnitude and direction of GPS errors for four sensors (1A, 1B, 1C, 2A) in a semi-urban setting. Data points represent the angular deviation and distance from true position; closer clusters suggest higher accuracy. Distinct colors for each sensor reveal their error profiles, with denser clusters indicating more consistent readings. The plot indicates moderate GPS performance, with errors less scattered than in dense urban areas but less concentrated than in open fields, supporting the theory of environmental complexity affecting GPS accuracy.

The hypothesis being tested posits that the operational environment significantly influences GPS receiver accuracy and reliability. The visual data presented in Figure 6-11, Figure 6-12, and Figure 6-13 supports this hypothesis. Given the large volume of data collected, the figures are plotting the data collected by the sensors at one example test site for semi-urban, urban, and open field locations respectively. Table B-3 to Table B-8 present the key statistical parameters about the data captured at the locations studied in this section and used to train the IRNN-DNN model. Previous sections have established that the sensors are all unique and individually contribute negligibly to the overall error characteristics at any one location. Any trends observed in all sensors performance across the different locations are most strongly influenced by the location rather than other characteristics. All the data compared was collected at frequency of 10Hz. The spatial distribution of GPS data across different environments reveals telling insights into the impact of operational

settings on GPS receiver accuracy and reliability. Examining the figures corresponding to each environment, we observe distinct patterns that further support the hypothesis of environmental influence.

In an open-field environment, as shown in Figure 6-13, the scatter plot from this environment demonstrates relatively lower residual errors, indicating a higher level of precision in the GPS data. The magnitude of the spread is with 5 to 8 m radius. Sensors 1B and 2B exhibit a ~30 (0.52 rad) and ~330 (~5.76 rad) east angular error. 1A and 2A do not present any significant preference in the axis of spread. The error distribution for open-field locations shows a more circular spread, which conveys a relatively uniform dispersion of GPS errors in all directions. This pattern is expected in open-field scenarios where the absence of significant obstacles allows for a clear line of sight to GPS satellites, resulting in more consistent signal reception and fewer directional errors.

In urban settings (Figure 6-12), the same GPS sensor's performance displays noticeable degradation. In urban areas, the spatial error distribution of GPS readings exhibits elongated ellipses, indicative of a directional bias in the GPS errors. Sensor 1B is particularly affected with error magnitudes of 146 meters. The other sensors have errors concentrated in the 50-75 m range. The angular error is well constrained between the 30° to 60° arc and the 210° to 240° east arc. This shape suggests a prevalent influence of signal reflection and multipath interference caused by tall buildings and dense infrastructure. The presence of a well-defined primary and secondary axis within these ellipses implies that certain directions within the urban landscape are more susceptible to GPS inaccuracies due to consistent, directional sources of interference when operating in a stationary location.

In semi-urban environments, the results (Figure 6-11) present an intermediate state between open fields and dense urban landscapes. The error spread in these conditions, while more pronounced than in open fields, is less severe than in urban settings at 20-35 meters. This outcome is aligned with the hypothesis, revealing a direct correlation between environmental complexity and GPS performance. Sensor 2B and 2A have a North-South spread. 2B has initial cluster of values far from the definite cluster. This is possibly an artifact from the trilateration process taking too long to solve for a position upon cold start. This is statistically significant and can be ignored in the

study. The semi-urban environment, lying between the complexity of urban settings and the openness of fields, presents a hybrid pattern. The spread of GPS data is larger than in open fields, suggesting increased signal disruption compared to open environments. However, the definition of the primary and secondary axes is less distinct than in urban environments. This less defined axis suggests that while there are obstructions causing GPS signal errors, they do not produce as consistent directional bias as seen in densely built urban areas. The error distribution is somewhat elongated, yet lacks the pronounced directional bias of urban readings, indicating a more randomized array of obstructions affecting the signal.

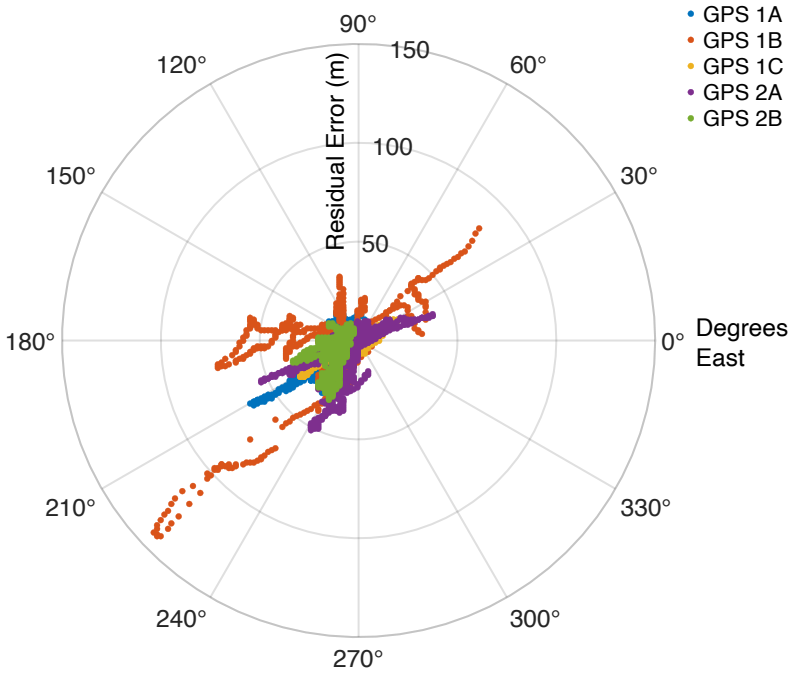

Figure 6-12. GPS Error Distribution in an Urban Setting. The graph illustrates spatial error patterns of GPS sensors in an urban area, with the elongated ellipses representing directional biases in GPS errors. These biases highlight the impact of signal reflection and multipath interference, causing consistent inaccuracies in specific directions. The pronounced axes of the ellipses signify predictable error vectors, pointing to the directional nature of urban GPS interference.

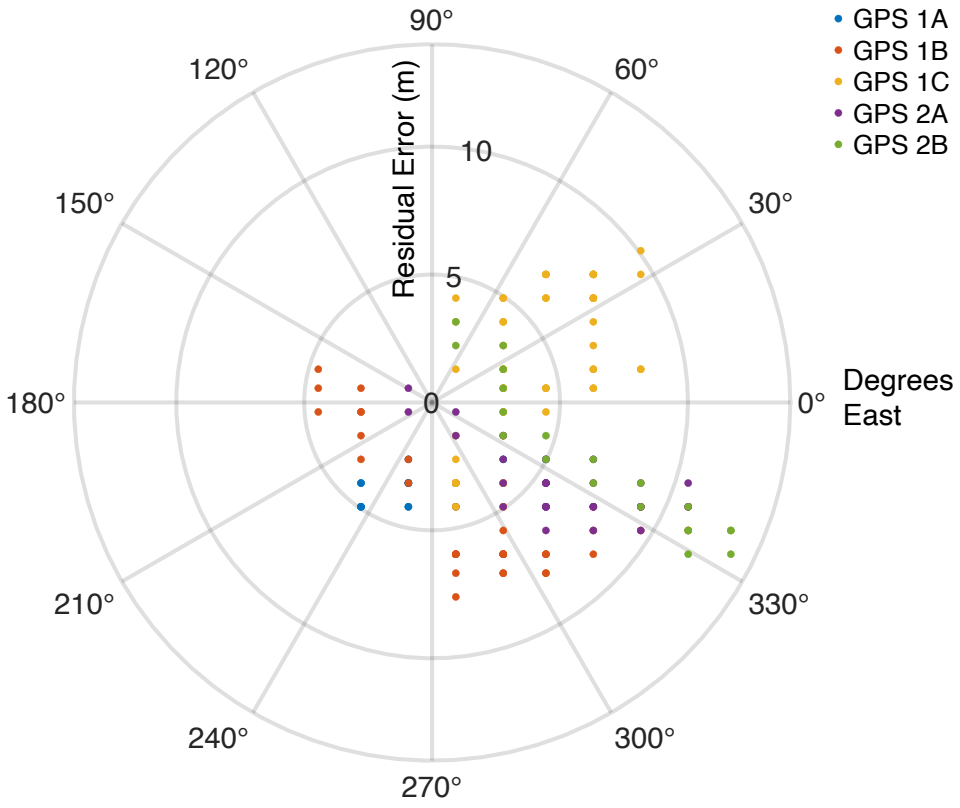

Figure 6-13. GPS Error Characterization in Open Field Conditions. The polar plot displays the distribution of GPS errors for multiple sensors in an open field, a setting with minimal signal obstructions. The radial spread indicates the magnitude of error from the true position, with a tighter cluster suggesting higher accuracy. The plot reflects lower error values and less directional bias, confirming the expected superior performance of GPS in open-field environments.

The operational environment's influence on GPS reliability and accuracy is corroborated by these findings. Urban environments, with their inherent challenges, significantly impact the quality of GPS data. In contrast, open fields, with clear lines of sight to satellites and minimal electromagnetic interference, yield the most reliable GPS signals.

6.2 A DISCUSSION ON THE IMPLICATION FOR GPS MACHINE LEARNING

The spatial characteristics reflect the varying degrees of GPS signal interference present in each environmental context. In designing and optimizing GPS-dependent applications for different operational environments, these insights are critical. They emphasize the need for adaptive systems capable of accounting for environmental-specific error patterns to maintain GPS accuracy and reliability. For instance, UAV navigation systems could be equipped with environmental-aware

algorithms that adjust for the observed spatial error tendencies, ensuring better localization accuracy regardless of the operational setting. These systems can also monitor and assign confidence to each of error prediction, discarding low confidence predictions. This potentially adds to the overall stability and accuracy of the localization system.

In urban settings, GPS sensors 1A, 1B, and 1C's time series performance, as depicted in Figure 6-14, Figure 6-15, and Figure 6-16, reveals various signal characteristics crucial for machine learning model training.

For Sensor 1A, the original signal is characterized by high volatility with pronounced spikes, suggesting possible large instantaneous errors in position estimation. After applying an inverse variance weighting filter, the filtered signal demonstrates a reduction in noise, offering a clearer view of underlying trends. This indicates that preprocessing steps like filtering benefit machine learning models by allowing them to concentrate on significant trends over noise.

Sensor 1B exhibits a similar original signal to Sensor 1A, albeit with diminished volatility. Given its distinct behavior, the ML model may require different parameters or thresholds for training on data from this sensor. The filtered signal for Sensor 1B also demonstrates substantial fluctuations, hinting at periodic patterns in the filtered signal, which could be a valuable feature for time-based learning in the ML model.

The time series for Sensor 1C shows the least volatility in its original signal, indicating more stability or fewer abrupt errors. It's important for the ML model to be trained to handle this stability without overfitting, as it may encounter different scenarios in practice. The lower variability in the filtered signal for Sensor 1C suggests that the inverse variance weighting filter is effective, and the ML model should incorporate this stability into its error estimation.

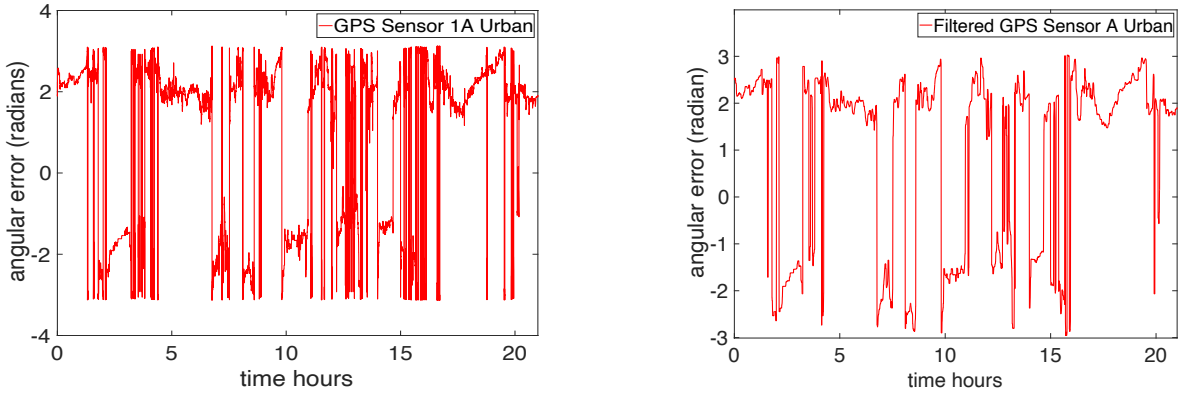

(a)

(b)

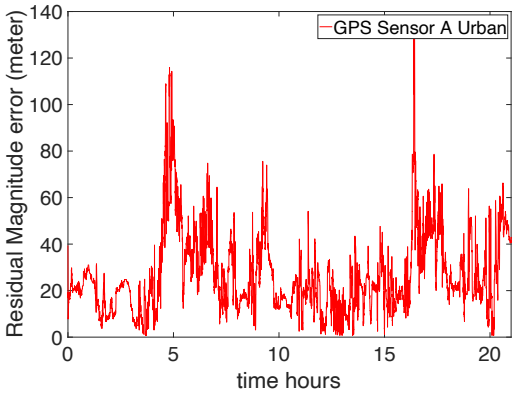

(c)

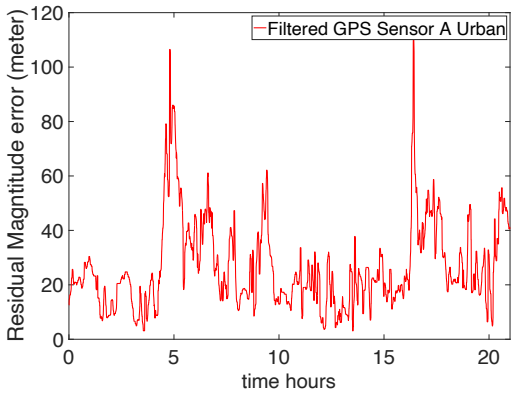

(d)

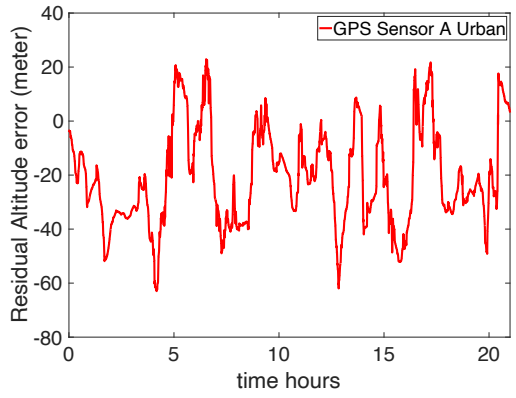

(e)

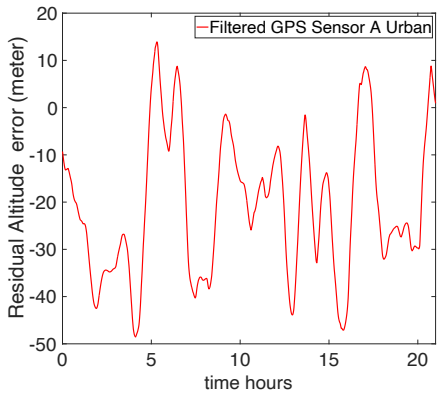

(f)

Figure 6-14. Time series plot of error signals from GPS sensor 1A operating in urban location 4, (a) raw angular error signals as reported by GPS DAQ system; (b) angular error signals after the application of Windowed inverse variance weighted correction filter; (c) raw magnitude error signals as reported by GPS DAQ system; (d) magnitude error signals after the application of Windowed inverse variance weighted correction filter; (e) raw altitude error signals as reported by GPS DAQ system; (f) altitude error signals after the application of Windowed inverse variance weighted correction filter.

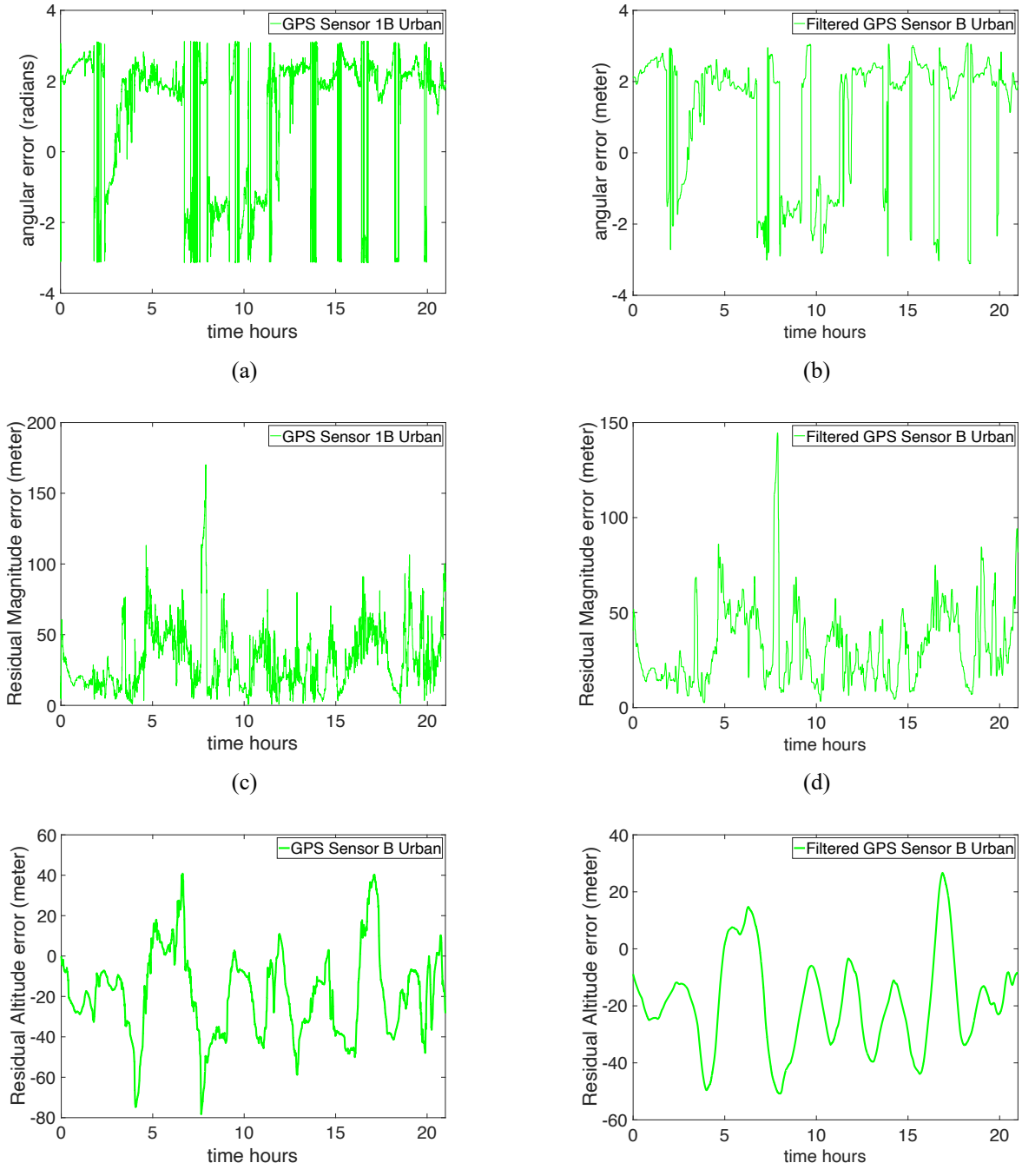

Figure 6-15. Time series plot of error signals from GPS sensor 1B operating in urban location 4, (a) raw angular error signals as reported by GPS DAQ system; (b) angular error signals after the application of Windowed inverse variance weighted correction filter; (c) raw magnitude error signals as reported by GPS DAQ system; (d) magnitude error signals after the application of Windowed inverse variance weighted correction filter; (e) raw altitude error signals as reported by GPS DAQ system; (f) altitude error signals after the application of Windowed inverse variance weighted correction filter.

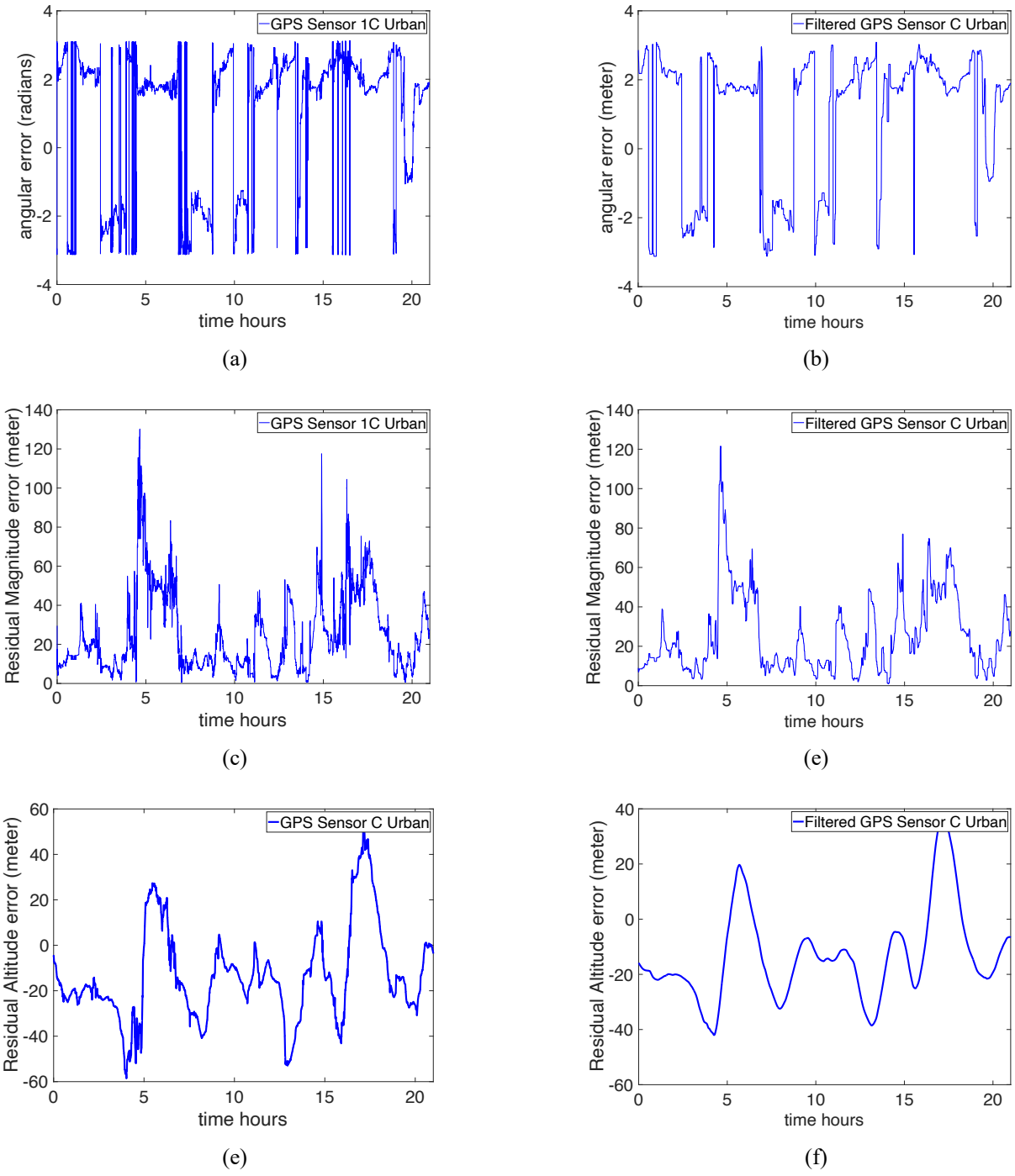

Figure 6-16. Time series plot of error signals from GPS sensor 1C operating in urban location 4, (a) raw angular error signals as reported by GPS DAQ system; (b) angular error signals after the application of Windowed inverse variance weighted correction filter; (c) raw magnitude error signals as reported by GPS DAQ system; (d) magnitude error signals after the application of Windowed inverse variance weighted correction filter; (e) raw altitude error signals as reported by GPS DAQ system; (f) altitude error signals after the application of Windowed inverse variance weighted correction filter.

Table 6-4. Statistical properties of error signal before and after applying the waited inverse variance filter.

Sensor	Error Type	RMSE pre-filtering	RMSE post-filtering	ΔRMSE	Variance pre-filtering	Variance post-filtering	ΔVariance	ΔdB
1A	Altitude	27.123	25.186	1.936	329.924	228.505	101.418	1.595
	Angular	2.155	2.108	0.047	3.786	3.474	0.312	0.373
	Magnitude	34.059	33.356	0.703	375.604	343.522	32.082	0.388
1B	Altitude	28.159	24.784	3.376	454.823	273.515	181.308	2.209
	Angular	2.147	2.115	0.032	3.239	3.064	0.174	0.240
	Magnitude	38.944	38.316	0.628	473.723	435.217	38.507	0.368
1C	Altitude	24.266	21.055	3.211	415.270	269.796	145.474	1.873
	Angular	2.177	2.151	0.026	3.671	3.574	0.097	0.116
	Magnitude	32.505	32.210	0.295	405.012	391.659	13.353	0.146

The inverse variance weighted filter, applied over a window size of $\boldsymbol{W} = 1500$ data points, corresponding to approximately 150 seconds or 2.5 minutes of data, carries significant implications for the preprocessing of GPS sensor errors in machine learning applications. This window size, precisely a multiple of 25, was deliberately selected by the author for testing purposes, based on observational insights, as a suggested parameter for filtering the data prior to input into MATLAB for signal processing. Further investigation is warranted to comprehensively elucidate its effects. Section 7.1disscusses this further.

The analysis of the GPS sensor errors before and after the application of the inverse variance weighting filter is summarized in Table 6-4, showing the RMSE values and the corresponding improvement. The 'Improvement (Δ)' column indicates how much the error has been reduced by the filter. A positive value indicated that the filtered signal is cleaner than the unprocessed signal. To understand the impact of the filter, we look at the data with a short window of 2.5 minutes. For all sensors and error types, the application of the inverse variance weighting filter has led to an improvement in signal quality, as evidenced by a decrease in RMSE and variance values.

Sensor 1C showed the greatest improvement with a reduction of 3.2110 in RMSE, followed by sensor 1B (3.3755) and sensor 1A (1.9364). This suggests that the filter is particularly effective in environments with altitude-related GPS signal interference. The improvement is less pronounced across all sensors for angular error, with the greatest improvement being 0.0470 for sensor 1A. This could indicate that angular errors are less susceptible to the noise that the inverse variance weighting filter is targeting. There is a moderate improvement in magnitude error for all sensors, with sensor 1A seeing the largest reduction in RMSE by 0.7032.

The 'Variance Reduction' column quantifies the decrease in the power of the noise or unwanted variations in the signal. Sensor 1B shows the most significant reduction in variance for altitude error (181.3083), which is congruent with the greatest improvement in RMSE. The altitude error has generally seen a substantial variance reduction across all sensors, suggesting that the filter is particularly effective at enhancing the altitude signal's characteristics for the algorithm.

For angular and magnitude errors, while the improvement in RMSE is less than for altitude error, there is still a notable reduction in variance, indicating a purer signal for these error types as well. The improvement in RMSE and variance reduction across different error types and sensors confirm the filter's effectiveness and its positive impact on the machine learning algorithm's potential performance, with a consistent enhancement across different error types and sensors.

By examining the correlation coefficients from Table 6-5 and Table 6-6 and integrating insights from the signal-to-noise ratio analyses performed earlier, we can construct a narrative on optimizing and explaining IRNN-DNN model performance for GPS error correction application.

Table 6-5. Co-relation coefficient table of offset error by GPS at different open field locations and signal characteristics.

Height Above Ground (m)	GPS ID	Number of satellites in view	GPS reported HDOP	GPS reported VDOP	GPS Reported Altitude	Time since last GPS fix	Average Error (m @°N)	Average Altitude Reported above sea-level (m)
0	1A	0.2969	-0.2330	0.1988	0.6556	0.0246	3.1505@300.87°	27.988633
0.75		-0.2879	0.2767	-	0.6705	0.0497	3.1505@285.06°	28.315909
1.041		-0.1369	0.1190	0.0938	0.2407	0.0006	3.1505@228.58°	28.907131
1.45		0.6426	-0.5492	-0.7073	-0.2484	-0.0822	70.8763@44.41°	28.039234
0	1B	-0.1094	0.1458		-0.8888	0.1048	1.8949@249094°	30.480926
0.75		-0.0726	0.1708	-	0.8387	-0.1009	4.9819@337.83°	34.225513
1.041		0.2458	-0.3473	-	0.4127	0.0152	4.9818@321.79°	36.597355
1.45		0.0041	-0.0187	-	-0.2568	-0.0202	79.4214@50.042°	34.362493
0	1C	-0.1527	-0.0402		-0.5478	0.0048	0.5560@7.125°	38.522933
0.75		-0.8824	0.8479	-	0.8623	0.0028	5.0038@340.794°	33.506901
1.041		-0.0419	-0.0755	-0.1937	0.3799	0.0052	5.0038@36.77°	32.886812
1.45		0.0109	0.1476	-	0.1857	0.0060	89.4273@48.40°	34.108926
0	2A	0.3608	-0.3643		-0.9716	0.0284	2.6375@325.890°	34.468170
0.75		-0.0924	0.0542	-	0.2489	0.1000	3.1505@311.64°	39.985089
1.041		-0.0926	0.3465	-	-0.2516	0.0080	3.1505@327.62°	39.108253
1.45		0.7132	-0.7661	-	-0.7661	0.0321	79.9270@46.22°	37.396417
0	2B	-0.0048	0.0400		0.9231	0.0299	0.3967@13.12°	38.535369
0.75		-0.5516	0.5439	-0.1871	0.4799	-0.0451	5.9304@329.35°	37.586280
1.041		-0.1569	0.2968	-	-0.3985	0.0364	4.0771@337.83°	38.130874
1.45		0.5626	-0.5581	-	-0.6976	-0.0275	92.0965@48.61°	37.569811

Locations tested had an average height of 32.95 meters above sea level. Heights were measured against the NOAA height marker with designation - U OF W MON 15. Data composite from open field locations 1 and 2. At 1.45 m above the ground, all 5 GPS sensors reported dramatic increase in the average error. This is most like caused either by reflections of GPS signals from ground, or some other unforeseen interference. The 1.45 m data will be, however, used in the training of the model, as the ML test system is also placed at the height of approximately 1.45 m AGL.

Table 6-6. Co-relation coefficient table of offset error by GPS at different urban locations and signal characteristics.

Height Above Ground (m)	GPS ID	Number of satellites in view	GPS reported HDOP	GPS Reported Altitude	Time since last GPS fix	Average Error (m @ °N)	Average Altitude Reported above sea-level (m)
0	1A	-	0.5607	0.2993	-0.0266	9.6332@218.12	51.304
0.75		-0.6187	0.6075	-0.6381	0.0548	16.8514@282.22	81.814
1.041		-0.4703	0.4807	0.8794	0.0104	17.3939@277.86	82.877
1.45		-0.6992	0.6034	0.3372	0.0790	16.4668@259.38	70.084
0	1B	-0.6900	0.6497	0.9386	-0.0260	16.7152@251.67	63.622
0.75		-0.4123	0.2477	-0.5854	0.0267	20.075@330.24	37.851
1.041		-0.5265	0.5807	0.2643	0.1082	38.2415@274.64	61.351
1.45		0.0041	-0.0187	-0.2568	-0.0125	38.2415@274.64	87.386
0	1C	-0.8610	0.4287	0.9059	0.0037	11.8277@255.63	45.932
0.75		0.2969	-0.0855	-0.8540	-0.0914	17.1251@254.14	85.472
1.041		0.5923	-0.5739	-0.2005	-0.0089	38.2415@274.64	82.513
1.45		0.0109	0.1476	0.1857	0.0225	14.3849@248.59	86.982
0	2A	0.0177	0.1048	0.5123	-0.0242	15.9227@294.83	38.115
0.75		0.1734	-0.3432	-0.8176	0.0020	18.6703@274.12	85.041
1.041		-0.0849	-0.0167	0.2181	0.0359	10.6437@371.40	99.103
1.45		0.7132	-0.7661	-0.8534	0.0332	21.1100@262.73	91.647
0	2B	-0.5460	0.5237	0.3156	-0.0688	16.3922@200.28	40.432
0.75		0.6830	-0.6816	-0.5210	0.1460	14.8708@298.92	81.269
1.041		0.2027	-0.2153	-0.4190	-0.0644	7.8350@284.93	87.308
1.45		0.5626	-0.5581	-0.6976	-0.0601	20.4525@266.56	81.908

Locations tested had an average height of 59.890 meters. Heights were measured against the NOAA height marker with designation - U W 4 RESET. Data composite from urban location1, urban location 2 and urban location 3. Urban location 1 was not included in the analysis for sensors 2A, 2B

In open fields, the absence of significant obstructions leads to straightforward signal acquisition, characterized by lower HDOP and VDOP values. The correlation coefficients are generally in line with expectations. For instance, GPS ID 1A and 2A in open fields exhibit weaker correlation coefficients than their urban counterparts, suggesting a less challenging environment for signal processing. Specifically, GPS 1A at the height of 1.45 meters shows a strong positive correlation with the number of satellites in view (0.6426), but a strong negative correlation with GPS-reported VDOP (-0.7073). This indicates that while satellite visibility is good, the vertical precision is compromised, likely due to the positioning of the satellites. This simplicity, while facilitating clear signal reception, provides less "raw material" for machine learning algorithms that thrive on complex patterns (Table 6-5). Thus, the impact of the IRNN-DNN in relatively good signal conditions is limited. However, in urban conditions, with complex multi-path effects, the correlation values are not straight-forward.

In Table 6-6, error magnitude shows complex correlation relationships with signal quality predictors. Typically, one expects a positive correlation between HDOP and errors: as HDOP improves (i.e., decreases), the accuracy and precision of the GPS readings should improve (i.e., errors decrease). however, GPS 1A at 0.75 m instead presents a high negative correlation with HDOP (-0.6187). Altitude variances further indicate the differential effects of urban structures on GPS accuracy when placed at different heights from the ground. For example, GPS 1A reports an altitude of 81.814 meters ASL when placed at 0.75 AGL and 70.084 meters ASL at 1.45 meters AGL; receivers report an 11.73 m change in height when the actual height has changed by 0.7 meters. Similarly, other GPS sensors also misrepresent the altitudinal change by significant margins. The presence of strong correlations, even when they are counterintuitive, serves as potent learning indicators for ML models. An example is the strong negative correlation between the number of satellites and accuracy observed in GPS 1C at ground level (-0.8610). Contrary to expectations, an increased number of satellites in dense urban areas does not necessarily improve accuracy due to the increased likelihood of signal reflection and refraction from surrounding buildings. GPS 1A shows a correlation coefficient of -0.6187 at 0.75 meters for HDOP, indicating a strong negative relationship, whereas at 1.45 meters, the coefficient is -0.6992, suggesting an even stronger influence of HDOP on accuracy as altitude increases. This trend is consistent across other sensors, such as GPS 1B and GPS 1C, indicating that higher altitudes may exacerbate the negative impact of HDOP on GPS accuracy. This could be due to the increased exposure to satellite

signals at higher altitudes, which might introduce more multipath and signal masking noise through additional signal paths that are less obstructed, leading poorer trilateration solutions. Training machine learning models to account for these variances can significantly improve their ability to predict GPS errors by incorporating how altitude differences, relative to sensor height, influence positional accuracy.

The varying correlation coefficients among different predictors across GPS sensors underscore the complex and heterogeneous nature of environmental influences on GPS accuracy. Sensor 2B shows moderate negative co-relation with number of available satellites, when at 0m AGL and becomes moderately positively corelated at 1.45 m AGL, with the correlation magnitude being approximately the same. The diversity in predictor impact in Table 6-5 reveals that GPS error characteristics are not universally consistent but rather depend on specific conditions and sensor configurations. This highlights how environmental and sensor-specific factors can alter the traditional expectations of HDOP's impact on positional accuracy. These differences suggest that models need to be context-aware, adapting to the specific characteristics of each sensor's data and its interaction with the environment. Thus IRNN-DNN needs to have individualized models for different errors at different locations.

Building upon the detailed insights derived from the analysis of urban and open field environments, the proposed IRNN-DNN model performance in urban areas can be explained by its ability to integrate and leverage complex relationships and correlations identified in the GPS data. Additionally, the model benefits from incorporating temporal data and subtle patterns, such as the changes in error magnitude with altitude and the variance in error correlations with signal predictors.

The RNN component of the model is adept at capturing the dynamics within time series data. An examination of the spectrograms (Figure 6-17(a) and Figure 6-17 (b)), reveals distinct characteristics of the GPS error signals. The spectrogram analyses, essentially short-time Fourier transforms across a small temporal window, displayed in Figure 6-17 (a) and Figure 6-17 (b) characterize the GPS error signals across open-field and urban environments. Figure 6-17 (a), illustrating an open field scenario, shows a consistent spectral power distribution concentrated primarily in the lower frequencies with minimal activity above 0.1 Hz throughout the 10-minute

recording. This uniformity suggests stable GPS signal conditions typical in open fields, where interference is minimal. Conversely, Figure 6-17 (b), depicting an urban setting, presents a more complex spectral profile characterized by intermittent spikes of spectral power at higher frequencies, notably around the 0.5-,2-, 6.5-, and 9-minute marks. These peaks indicate disruptions likely caused by urban structures affecting signal path and integrity. The time series data in Figure 6-17 (c) provides further clarity on these observations. The green line, representing the open field, maintains a low and stable error margin close to the baseline, confirming the minimal signal disturbance. In contrast, the urban setting (red line) exhibits notable volatility with sharp error peaks, particularly aligning with the spectral bursts observed at 0.5, 2, 6.5, and 9 minutes in Figure 6-17 (b), underscoring the significance of the temporal study of GPS disruptions.

These insights drawn from the spectrograms and time series plots underscore the complex nature of GPS errors in urban landscapes, suggesting that transient and high-frequency errors dominate in such settings. This temporal complexity is critical for selecting appropriate modeling techniques like Long Short-Term Memory (LSTM) networks over simpler Deep Neural Networks (DNNs). Unlike DNNs, LSTMs are equipped to leverage their memory capabilities to predict future values based on learned data dependencies over time, which is ideal for the error characteristics observed. LSTM preferred over other types o

The choice of LSTM parameters is directly informed by these spectral and temporal analyses. Given the data's sampling rate of 10 Hz over an 11-minute duration, the selected spectrogram resolution of 50 seconds with a 50% window overlap provides a comprehensive view of the significant low-frequency content and its variations over time. To align with these insights, the LSTM's input sequence length is set at 25 samples, corresponding to a 2.5-second window. This setup allows the LSTM to detect and respond to rapid changes within the overarching patterns identified in the spectrogram, offering a finer temporal resolution that is crucial for effective navigation and error correction in dynamic urban environments.

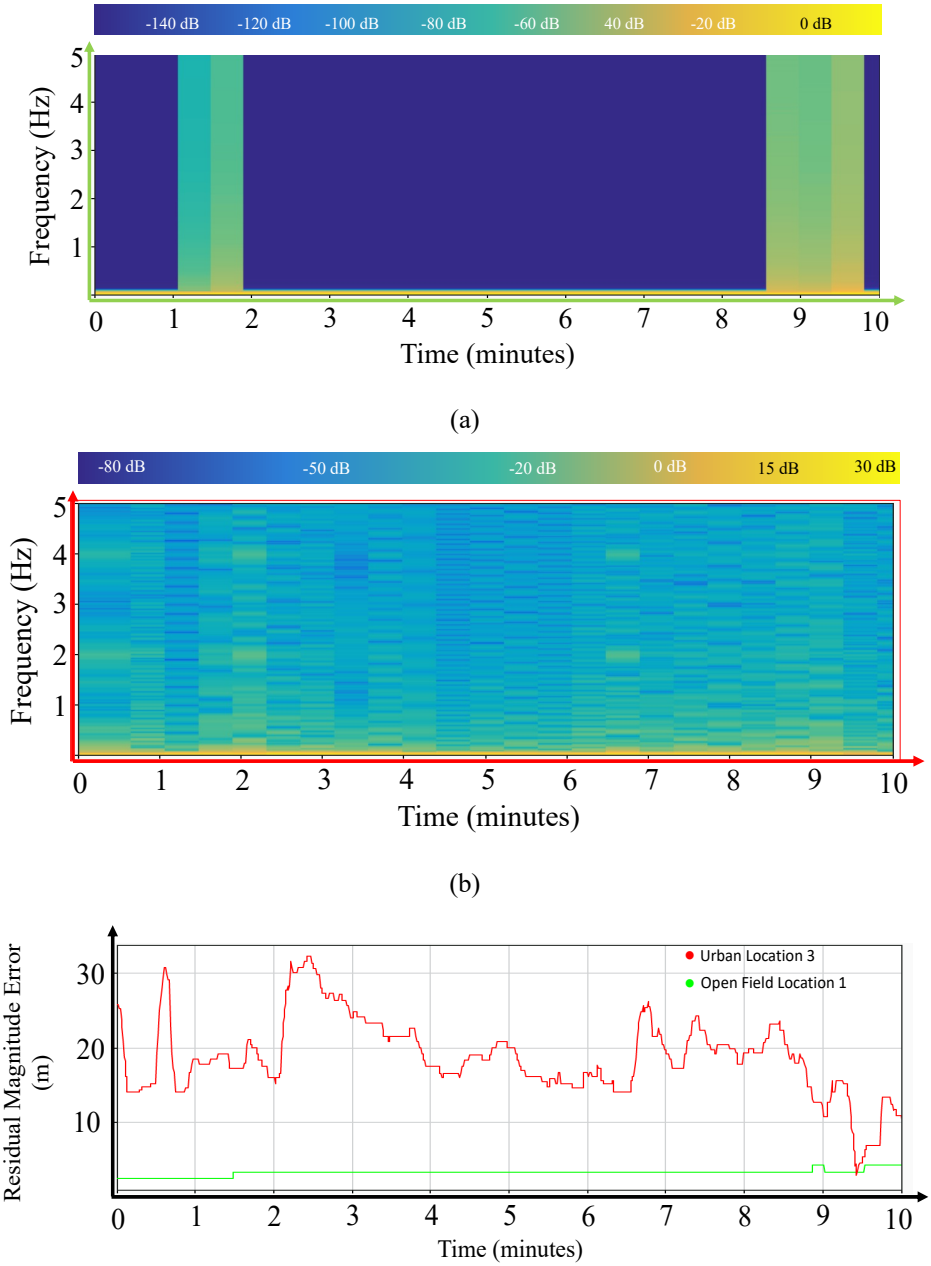

Figure 6-17. Comparative analysis of GPS error signals from sensor 1A in Open Field location 2 and Urban Location 3. (a) Spectrogram for open field shows stable, low-frequency signal distribution, indicating minimal interference. (b) Urban environment spectrogram exhibits intermittent high-activity bursts at specific intervals (2, 5, and 9 minutes), reflecting signal disruptions by urban structures. (c) Time series plot correlates with spectrogram data, showing stable error margins in open field 2 (green) and fluctuating errors in urban location 3(red), supporting the use of LSTM for dynamic error correction.

Additionally, the LSTM model's ability to maintain 10 historical hidden states over 25-second windows (totaling 250 seconds) allows it to encompass longer temporal patterns that match the error peaks observed in the urban GPS data. This capability is essential for understanding and predicting the error dynamics over intervals highlighted in the spectrograms, such as the recurring disturbances at specific minutes marked by increased spectral power.

Ultimately, the detailed examination of the spectrogram's temporal and frequency data not only justifies the use of LSTM for modeling GPS errors in urban settings but also guides the specific starting configuration of the model to optimize performance, with the subsequent DNN layers effectively generalize these features to make accurate predictions. This two-tiered approach ensures that both temporal patterns and deep-seated correlations are utilized, making the model robust against the diverse conditions encountered in different environments.

The rationale for employing an environmental classifier in conjunction with an RNN+DNN model also stems from the distinct variations in GPS signal behavior observed across different settings, as detailed in Table 6-5 and Table 6-6. The different co-relation(s) discussed previously also show that each location is unique and having IRNN-DNN model individually trained to perform in each of these locations has the potential to be inherently superior and more explainable than a single composite model. An environmental classifier would thus be instrumental in discerning the type of environment based on identifiable GPS signal characteristics and selecting the most appropriate RNN+DNN model tailored to that environment's specific challenges. This approach allows for the dynamic optimization of model performance by leveraging environment-specific features and correlations highlighted in the tables. As this model is interested in relationships between data rather than temporal characteristics, a conventional neural network or K-nearest neighbors or decision tree would ideal. In this thesis a neural network classifier model is studied in the following chapter.

6.3 CHAPTER SUMMARY

In summary, Chapter 6 presents a comprehensive analysis of the impact of various factors on GPS sensor performance, reinforcing key hypotheses and providing new insights into the design and optimization of PATHFINDER systems. The findings underscore that while the type of microcontroller significantly affects sensor readings, integrating sensor connections into a single

microcontroller does not degrade system performance or introduce substantial errors. The chapter also illustrates how each sensor functions optimally at distinct frequencies, pointing to the utility of corrective and inverse variance weighting methods to account for sensor-specific and frequency-specific variations, as explored in section 6.1.2. Running the entire embedded stack at increased speeds, such as 10 Hz, facilitates the collection of a larger volume of data points, enhancing the system's capability for pattern-based data analysis and collection. Furthermore, variations in manufacturing, processing, and clock differences among identical GPS receivers result in notable disparities in positional accuracy and precision. This variability highlights the need for calibration and filtering.

Overall, 6.2 supports the study's core hypotheses and lays a solid foundation for the design and optimization of a GPS-only localization system incorporating a single microcontroller. The insights derived from this thorough analysis are vital for advancing GPS system integration and enhancing the explainability and navigational accuracy of the IRNN-DNN model in various operational contexts. While the chapter primarily focuses on technical performance, precision, and accuracy measures, we can also make specific statements about the power consumption of the GPS localization system. Operating efficiently at 5V with a total peak current draw of 265 mA, the system includes a Teensy 4.1 microcontroller drawing 100 mA, along with five GPS antennas and five GPS sensors consuming 15 mA and 30 mA each, respectively. Converting this setup to watts, based on the set requirement in watts, reveals a theoretical max power consumption of 1.625 Watts. During physical testing in an urban environment with significant processing demands, the GPS localization system sustained operations for over 8 hours on a 2500 mAh battery rated at 3.7V. From this, we calculated the actual power consumption to be approximately 1.16 Watts. This real-world testing confirms that under demanding conditions, the system efficiently processes and gathers GPS data while consuming significantly less power than the 15-Watt limit set for operations in Table 1-2. This performance not only demonstrates the system's energy efficiency but also ensures its practical applicability in extended operational scenarios, comfortably adhering to stringent power consumption constraints.

CHAPTER 7. TESTING ALGORITHM PERFORMANCE

This chapter evaluates the performance of the IRNN-DNN algorithm developed in this study. The IRNN-DNN model was trained using data from sensor sets 1A to 2B, across multiple locations described in 5.2. The model was tested on data from geographically similar locations, and on unseen data from the original training sites to assess generalization capabilities. Evaluation data was captured in a separate test than that of the training dataset.

The first section of this chapter focuses on validating the inverse variance weighted filter. This involves a statistical analysis to compare the error signals before and after the application of the filter. Subsequently, the chapter evaluates the machine learning classifier algorithm, developed in MATLAB. This algorithm's performance was tested using data from previously unseen data collected from the same sensor sets but at slightly different time. Finally, the accuracy of the IRNN-DNN model is investigated in terms of capability and explainability.

7.1 TESTING THE INVERSE VARIANCE WEIGHTED FILTER

Table 7-1. ANOVA Results for Filtered vs. Unfiltered Data in urban location.

Sensor	Error Type	F-Statistic	P-Value (0.05 threshold)
1A	Altitude	0.0138	0.9065
	Angular	363.548	<0.0001
	Magnitude	81.904	<0.0001
1B	Altitude	5.3187	0.0211
	Angular	33.547	<0.0001
	Magnitude	20.733	<0.0001
1C	Altitude	0.004	0.9497
	Angular	7.334	0.0068
	Magnitude	12.516	0.0004

The application of a moving inverse variance weighted filter to the dataset significantly enhances the Angular and Magnitude error signals across the sensors, as evidenced by the Analysis of Variance (ANOVA) results (see Table 7-1). This filtering method has proven effective in

stabilizing these error signals, leading to significant improvements in data quality. For instance, the Angular error in Sensor 1A demonstrated a remarkable reduction in variance (F-Statistic: 363.548, P-Value: <0.0001), confirming the filter's efficacy in environments where precision is paramount. Similarly, the Magnitude error signal showed a notable enhancement (F-Statistic: 81.904, P-Value: <0.0001). However, the Altitude error signals across Sensors 1A and 1C exhibited negligible changes post-filtering (F-Statistics: 0.0138 and 0.004 respectively), suggesting that either the altitude data inherently displays low variance or that it is less amenable to this filtering approach. Conversely, Sensor 1B's Altitude data indicated a moderate improvement (F-Statistic: 5.3187, P-Value: 0.0211), which highlights some sensor-specific variability in filter performance. Collectively, these results validate the moving inverse variance weighted filter as a robust method for improving Angular and Magnitude signals in urban localization tasks, underscoring its relevance and utility in enhancing the precision and reliability of sensor data in variable urban environments.

The inverse variance weighted filter, applied over a window size of 1500 data points, corresponding to approximately 150 seconds or 2.5 minutes of data, has implications on the preprocessing of GPS errors predictors used in IRNN-DNN. A visual examination of filtered data in Figure 6-14-Figure 6-16 suggest that the window size used in the moving inverse variance weighted filter is chosen to balance noise reduction with responsiveness to changes in the signal. The filtered data demonstrates a significant decrease in the frequency and amplitude of noise spikes, suggesting that the window size is large enough to effectively smooth high-frequency disturbances. Simultaneously, the retention of essential signal dynamics and a lack of phase shift or lag in response to changes in the unfiltered signal indicate that the window size is not excessively large, thereby preserving the responsiveness and integrity of the GPS error signals. This careful balance is critical in urban environments, where maintaining the precision and reliability of GPS data amidst frequent disruptions is paramount. The chosen window size ensures that important navigational details are clearly maintained while minimizing disruptive noise, facilitating accurate and dependable GPS-based applications.

This window size likely facilitated the extraction of longer-term patterns within the GPS signal. This enhancement in performance can be directly correlated with the altitude error plots from sensors shown in Figure 6-14(c), Figure 6-15(c), and Figure 6-16(c). These plots reveal near-

periodic differences in altitude errors, which align with the approximately 6.6-minute period it takes for a GPS satellite to appear and disappear from the horizon—indicative of the VDOP showing a periodic frequency signal.

The computed metrics (Table 6-4) for the signal-to-noise ratio (SNR) and mean squared error (MSE) provide compelling evidence of the effectiveness of the filtering process applied to the GPS data. The ΔSNR_{avg} measured at 17.271 dB, indicates a strong enhancement in the relative strength of the signal compared to the background noise, which is critical for high-quality data inputs. A higher SNR typically signifies a cleaner and more discernible signal, which is beneficial for any applications that require precision and reliability. Meanwhile, the MSE of 20.858 quantifies the average power of the noise reduction achieved by the filter, measuring the square of the error between the unfiltered and filtered signals. This metric helps understand the extent to which noise has been minimized, aiding in better data interpretation and utilization.

These improvements make the GPS data more stable and consistent, which is crucial for training IRNN-DNN. With more reliable data, the noise artifact variance within the training set is reduced, allowing the RNN to effectively learn the true underlying patterns rather than noise, thus optimizing the learning process. Additionally, the enhanced SNR ensures that the RNN can operate more efficiently. With a clearer signal that is less obscured by noise, the RNN is better positioned to focus on modeling the true signal dynamics. Inverse variance filter plays a key role in explaining the performance the IRNN-DNN model.

In conclusion, this analysis underscores the substantial benefits of inverse variance-weighted filtering in preparing data for complex machine-learning applications. As we transition to Section 8.2, which discusses deploying a machine learning-based location classifier algorithm, the foundation set by the enhanced data quality and improved learning conditions is invaluable.

7.2 ENVIRONMENT CLASSIFICATION USING MACHINE LEARNING.

This section explores the advancements achieved in environment classification through the application of a Deep Neural Network (DNN), developed to interpret and categorize GPS data across different urban environments. Leveraging the preprocessed data enhanced by the inverse

variance weighted filter, the DNN showcases a notable proficiency in distinguishing between urban, semi-urban, and open field environments based on GPS signal characteristics.

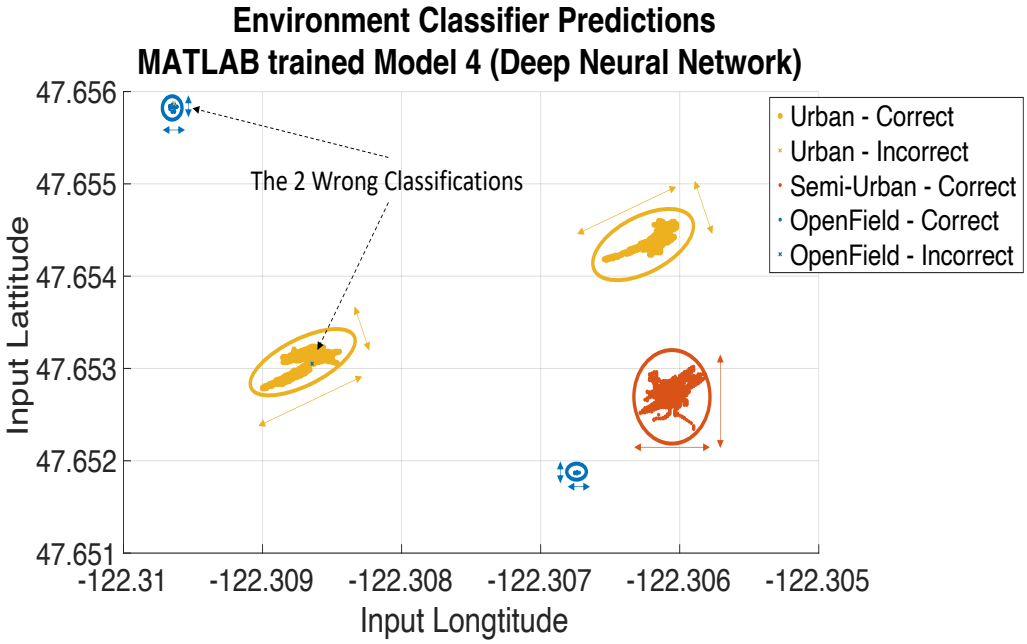

Figure 7-1. Classifier Performance in GPS Data Categorization. This scatter plot represents the classification of various GPS data points. Correctly identified data are shown in solid dots, while misclassified points are in cross marks. The accuracy in identifying urban, semi-urban, and open-field environments is evident, with most data points correctly classified. The two misclassified instances of interest are marked separately. The elliptical spread of correctly urban areas suggests directional GPS errors, the larger circular spread in semi-urban areas and the compact distribution in open fields potentially indicate how the model interprets and labels points.

Figure 7-1 displays a scatter plot of GPS data points as interpreted by the classifier. The plot predominantly demonstrates accurate classifications, yet two outliers' merit particular attention. They indicate that while the DNN excels in densely populated data clusters, it struggles with spatial outliers or edge cases. Though three errors are noted, one misclassification—labeling open field data as urban—is deemed insignificant for this analysis, which focuses on the model's performance in urban navigation enhancement.

7.2.1 *Explanation of results spatial spread of coordinates*

The classifier's ability to distinguish between various environments based on the spatial distribution of GPS coordinates is evident in Figure 7-1. Urban areas reveal a distinct longitude spread in GPS data, with an approximate range of 0.00094 degrees, corresponding to 52 meters.

Despite the presence of three buildings surrounding one urban sensor in the test are, causing a non-circular pattern in reflections, the longitude and latitude spreads are relatively similar, each spanning about 12.02 meters. This similarity across diverse urban locations, even with varying building obstructions, suggests a degree of consistency in GPS signal distortion.

In semi-urban areas, the spatial pattern differs with a smaller longitude spread of 0.00068 degrees (37.75 meters) and a latitude spread of 0.0007 degrees (28.05 meters). The GPS points form a more circular pattern due to fewer and less dense obstructions, leading to moderate multipath effects and a more dispersed signal due to line of sight and signal masking errors.

These distribution patterns, when correlated with standard NMEA data that provides a baseline for GPS signal quality and positional accuracy, enable the classifier to infer the environment type. A broader longitudinal spread indicates an urban setting, while narrower spreads point to open fields. In the model, the spread in GPS coordinates observed in various environments is internally represented through NMEA data, specifically using the HDOP parameter rather than actual latitude and longitude values. This representation allows the model to interpret broader longitudinal spreads typically seen in urban settings and narrower one's indicative of open fields. The HDOP value serves as a proxy, where the model interprets a decrease in HDOP as an indication of an open-field environment rather than an urban one. Thus, when HDOP values drop, the model may inaccurately classify urban locations as open-field due to the perceived improvement in signal quality, which the model equates with fewer obstructions and clearer signal paths. The incorrectly classified points point to this being the case.

In studying the erroneously classified within the vicinity of the urban cluster, tagged as 'OpenField – Incorrect', an examination of the raw predictor data for the incorrect prediction shows rapid reduction in HDOP, VDOP and speed values. This may be due to processing, artifact, and or minor improvements in GPS conditions at that instant. Such reductions typically signal better signal clarity, which the model might incorrectly associate with open-field conditions. This issue exposes the classifier's limitations in handling rapidly changing or unusual signal patterns. The narrow or stringent decision parameters of the model could be failing to adequately account for these outliers, potentially leading to overfitting on densely populated data regions. This overfitting could diminish the model's effectiveness in accurately identifying less frequent or more complex

patterns, suggesting a need for broader parameter tuning or a more adaptive learning approach to improve its generalization across varying environmental conditions. To understand the effects of the different predictors on the response, we need to study correlations between the predictors and labels,

7.2.2 *Explanation of results using co-relation factor*

Figure 7-2 and Figure 7-3 showcase the hyperparameter tuning and classification performance of a Deep Neural Network (DNN) across various environments. The hyperparameter tuning curve in Figure 7-2 exhibits a sharp decline in classification error up to the 6th iteration, indicating that the DNN quickly capitalizes on distinct, well-separated features for efficient classification, achieving an optimal fit early in the tuning process. This rapid enhancement in performance stabilizes thereafter, suggesting diminishing returns from further adjustments and a potential performance plateau, highlighting the DNN's efficient exploitation of data features early in the model training.

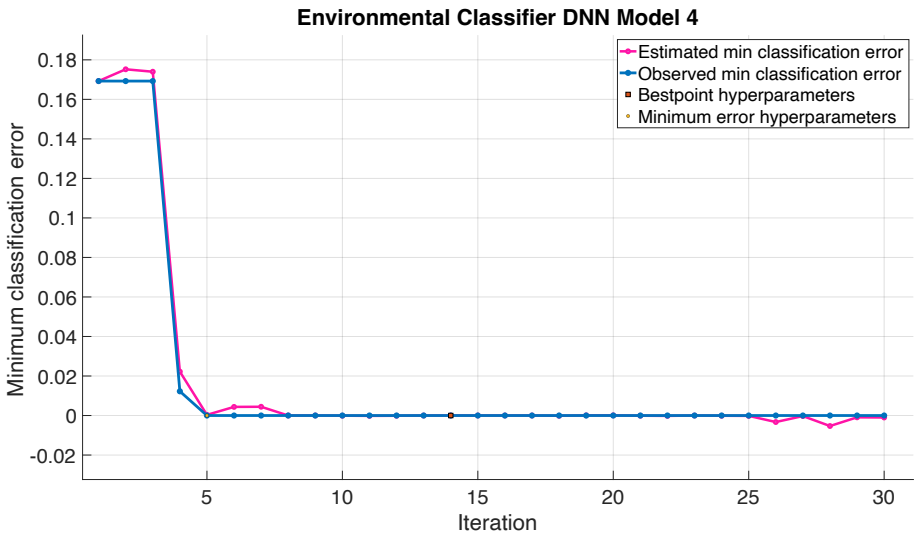

Figure 7-2. Hyperparameter Optimization Results. The plot shows the convergence of estimated and observed classification errors through iterations, indicating effective parameter tuning. The marked 'Bestpoint' signifies the optimal hyperparameters with the lowest error, demonstrating the model's improved accuracy during the optimization process.

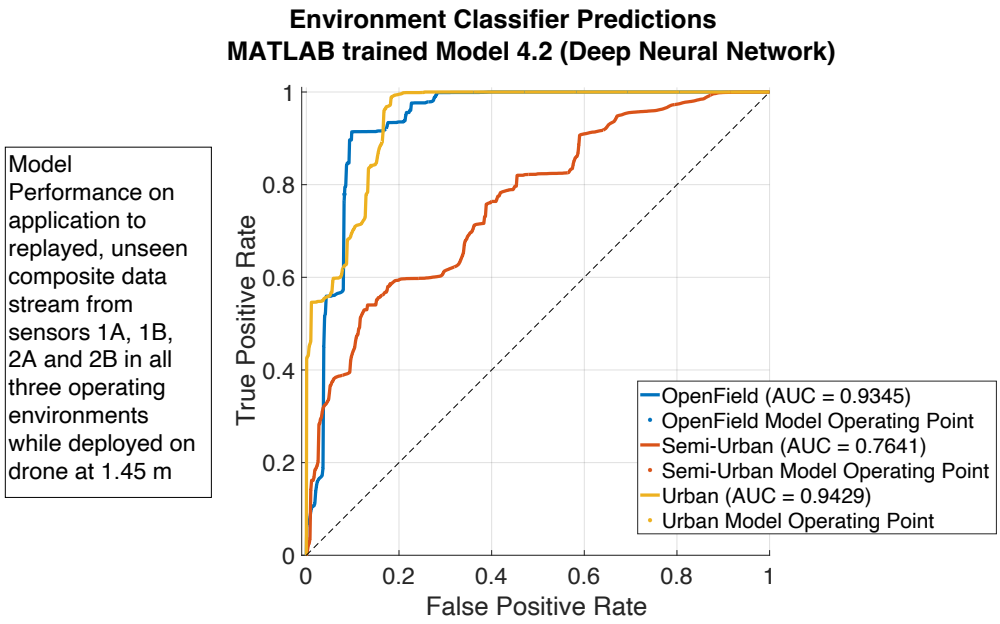

Figure 7-3. Model Performance on application to replayed, unseen composite data stream from sensors 1A, 1B, 2A, and 2B in all three operating environments while deployed on the drone at 1.45 m. It highlights the model's adaptability to different sensors and proficiency in handling unseen datasets. The Urban classification's high precision is a testament to the model's capability in utilizing urban-specific GPS signal distortions, while the Semi-Urban classification's lower precision signals a need for model enhancement or redefinition of environmental features

Figure 7-3 further elaborates on the classifier's effectiveness through ROC curves and AUC scores across three distinct environments: OpenField, Semi-Urban, and Urban. The AUC scores for OpenField (0.9345) and Urban (0.9429) indicate high accuracy, affirming the model's capability to reliably identify these environments. Conversely, the Semi-Urban environment, with a lower AUC of 0.7641, reveals challenges in model performance, suggesting ambiguities due to overlapping environmental characteristics that require further model refinement, possibly through the inclusion of more distinctive features or an expanded data set. The detailed analysis of standard deviations in classification features as depicted in Figure 7-5 corroborates these findings. Correct classifications generally show lower standard deviations, indicating confident and consistent model predictions. Particularly, stable predictors like Satellite Count exhibit low variability across all environments, underlining their robust predictive power. However, higher variability in HDOP and VDOP during incorrect classifications suggests confusion in environmental differentiation, likely due to similar dilution of precision values across different settings. This variability is particularly notable in urban settings, where HDOP values fluctuate due to obstructions like

buildings, which the model uses to distinguish urban environments effectively. Furthermore, the transitional nature of semi-urban areas, which blend characteristics of both urban and open fields, poses classification challenges as indicated by the 'Semi-Urban - Incorrect' segment in Figure 7-5. This overlap leads to higher standard deviations and misclassifications, as observed in Figure 7-6 where urban environments are occasionally misclassified as open fields due to shared signal characteristics under certain conditions.

The classifier has demonstrated robust accuracy in classifying urban and open-field scenarios, not limited to specific sensor data, as it successfully generalizes across data from multiple sensors (1A, 1B, 2A, and 2B). This broad applicability confirms the model's capability to handle diverse GPS data effectively, including scenarios with missing data. The Urban Model Operating Point shows a high True Positive Rate (TPR) and a low False Positive Rate (FPR), corroborating the model’s precision in identifying urban environments. This accuracy likely exploits the unique and complex GPS signal attributes caused by urban structures and multipath effects.

Figure 7-4 demonstrates that for certain features such as Sensor 1A's HDOP and VDOP, high standard deviations are associated with incorrect classifications. This variability suggests inconsistency in the model's predictions when misclassifying environments, potentially due to overlapping feature characteristics between the environments. In contrast, correct classifications exhibit lower standard deviations, indicating a higher confidence and consistency in predictions. A detailed examination of the features reveals differential impacts on classification confidence. For instance, the Satellite Count of Sensor 1A maintains a narrow standard deviation across all environments, suggesting it is a robust predictor across various settings. However, features like HDOP exhibit greater variance, particularly in incorrect predictions, hinting at potential confusion between environmental types due to similar HDOP readings across different settings. This evidence supports the explanation proposed in section 7.2.1. While Figure 7-4 only analyzes the parameters of sensor 1A, the analysis is consistent for other sensors as well. However, the magnitude of the correlation varies as seen in Figure 7-5.

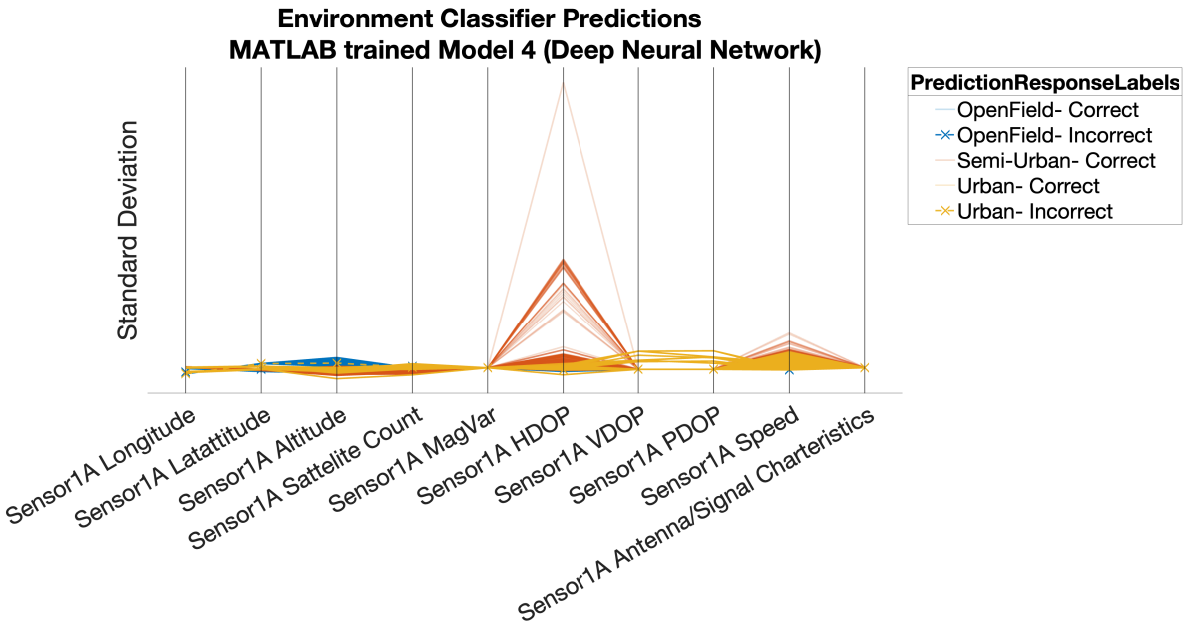

Figure 7-4. Feature Importance in Environmental Classification. This graph depicts the standard deviation of features used by a MATLAB-trained DNN for classifying environments. High deviation in HDOP and Speed during misclassifications indicates potential feature overlap between environments. Lower deviation across correct predictions, especially in satellite count, suggests reliable feature use for accurate classifications.

As seen in the Figure 7-5, the correct classifications for all environment types generally maintain lower standard deviations, indicative of consistent and confident predictions by the model. Specifically, features such as Satellite Count and Signal-to-Noise Ratio (SNR) demonstrate tight clusters with low variability, suggesting their strong predictive power and the model's reliance on them for accurate environmental classification. Conversely, features such as HDOP and VDOP show wider spreads in standard deviation for incorrect predictions, revealing the challenges the model faces when environmental features overlap, leading to misclassification. The analysis of DOP values across all sensors and their impact on the classification model's accuracy is a significant observation. HDOP and VDOP values are crucial as they represent the geometric strength of satellite configurations for horizontal and vertical position information, respectively. In urban environments, GPS signals can be obstructed or reflected by buildings, which would lead to a greater fluctuation in HDOP values as satellites come into or go out of line-of-sight. This fluctuation is a distinct characteristic that the model seems to utilize effectively to differentiate between urban and less obstructed environments like semi-urban or open fields. The observation that HDOP, VDOP, and PDOP values significantly vary suggests that the model leverages these variables as key indicators of environmental context. A higher HDOP value could indicate

potential signal degradation or obstruction, which is common in urban settings. Therefore, by recognizing the patterns in these values, the model can discern the likelihood of a location being urban based on the expected GPS signal quality and integrity. This reliance on DOP values for classification aligns with the understanding that GPS accuracy and reliability are compromised in areas with limited sky views. The precision of GPS data, including the DOP metrics, becomes a valuable feature for the deep learning model to make distinctions between different environments. Consequently, a model that can accurately interpret these variations is more capable of classifying the geographical context, aiding in applications like localization correction, where understanding the environment is essential for decision-making. It's notable that the model shows a consistent pattern across which parameters the model relies on across all the sensors when predicting 'Urban -Correct' classifications, indicated by the narrow spread in standard deviation. This pattern further suggests that urban environments have distinct GPS signal characteristics that the model can reliably identify.

The classification model, therefore, plays a crucial role in the IRNN-DNN framework by determining the most suitable RNN model for handling specific error dynamics of each classified environment. This capability is essential for enhancing the overall effectiveness of the GPS localization system, ensuring that environmental contexts are analyzed with the most appropriate computational strategies. Despite the high accuracy in classifying urban and open-field scenarios, the model faces challenges with semi-urban environments and specific outlier conditions, which could be addressed through additional training data and refined NMEA predictors, marking potential areas for future research.

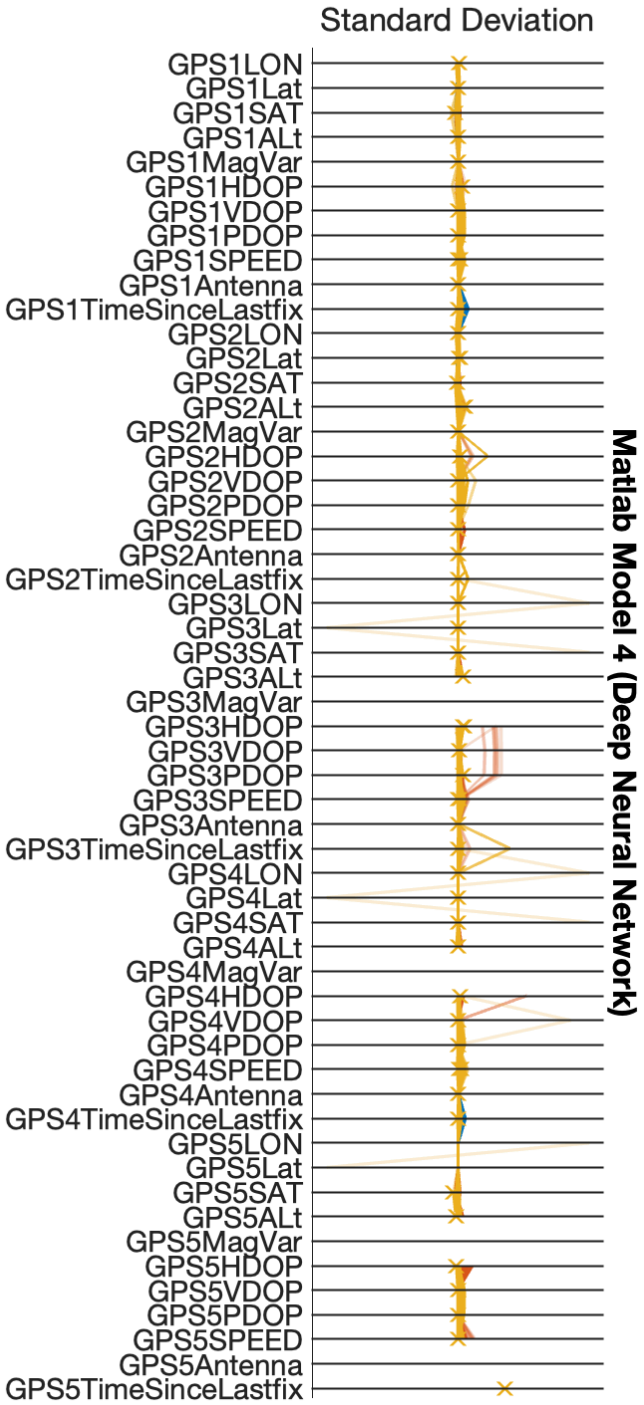

Figure 7-5. Consistency of DNN Environmental Classifications by Feature Variability. The chart displays the standard deviation for each feature used by a deep neural network (DNN) in environmental classification. Lower deviations for Satellite Count on correct predictions underscore its stable predictive power. In contrast, higher deviations for HDOP and VDOP during misclassifications indicate environmental feature overlap.

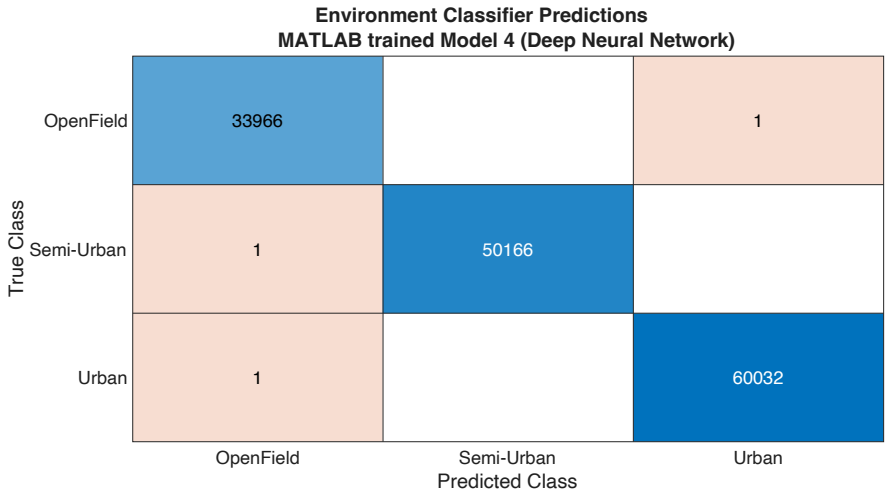

Figure 7-6. Classifier model confusion matrix. The classifier model shows high predictive accuracy in classifying OpenField (33,966 cases), Semi-Urban (50,166 cases), and Urban (60,032 cases) environments. Misclassifications are minimal, indicating the model's effectiveness. The rare errors suggest slight feature overlap between categories.

In summary, the robustness of the DNN classifier in navigating complex GPS environments and its strategic role in selecting the optimal RNN model based on the environment validate its utility in improving GPS accuracy and reliability, especially in urban and open-field contexts. This evidence-based validation supports the continued development and refinement of the classifier to better accommodate the nuances of semi-urban environments and enhance its overall predictive accuracy.

7.3 USE OF LSTM RNN NEURAL NETWORKS ON STATIC GPS DATA

Given the generally compact and circular distribution of coordinates in an open field scenario and considering the relative efficacy of the inverse variance filter, this thesis will not dwell on the algorithm's performance in such environments. Instead, the following sections will characterize, evaluate, and elucidate the performance of the LSTM and the composite IRNN-DNN model in semi-urban and urban areas. To support this analysis, GPS data were gathered using five sensors connected to a Teensy 4.1 data acquisition system. At each test location, data were recorded in 15-minute intervals, with a GPS fix and polling rate of 10 Hz, while the DAQ system was mounted on a powered and active drone. The drone was affixed to a tripod and weighted for stability at a constant height of 1.45 m AGL. LSTM was trained on MATLAB and the predicted error for each sensor was exported from the figures to the MATLAB workspace. In the following section, the results of LSTM network in predicting in urban location 1, 2, 3 and semi-urban location 1 is

investigated. Other locations were not tested due to lack of sufficient data and the complexity in manually managing such a large dataset. The data from these locations were also not used for training the LSTM. Additional work needs to be done to generalize these findings and deploy them in situ on drones. This will comprise the future work undertaken by the author.

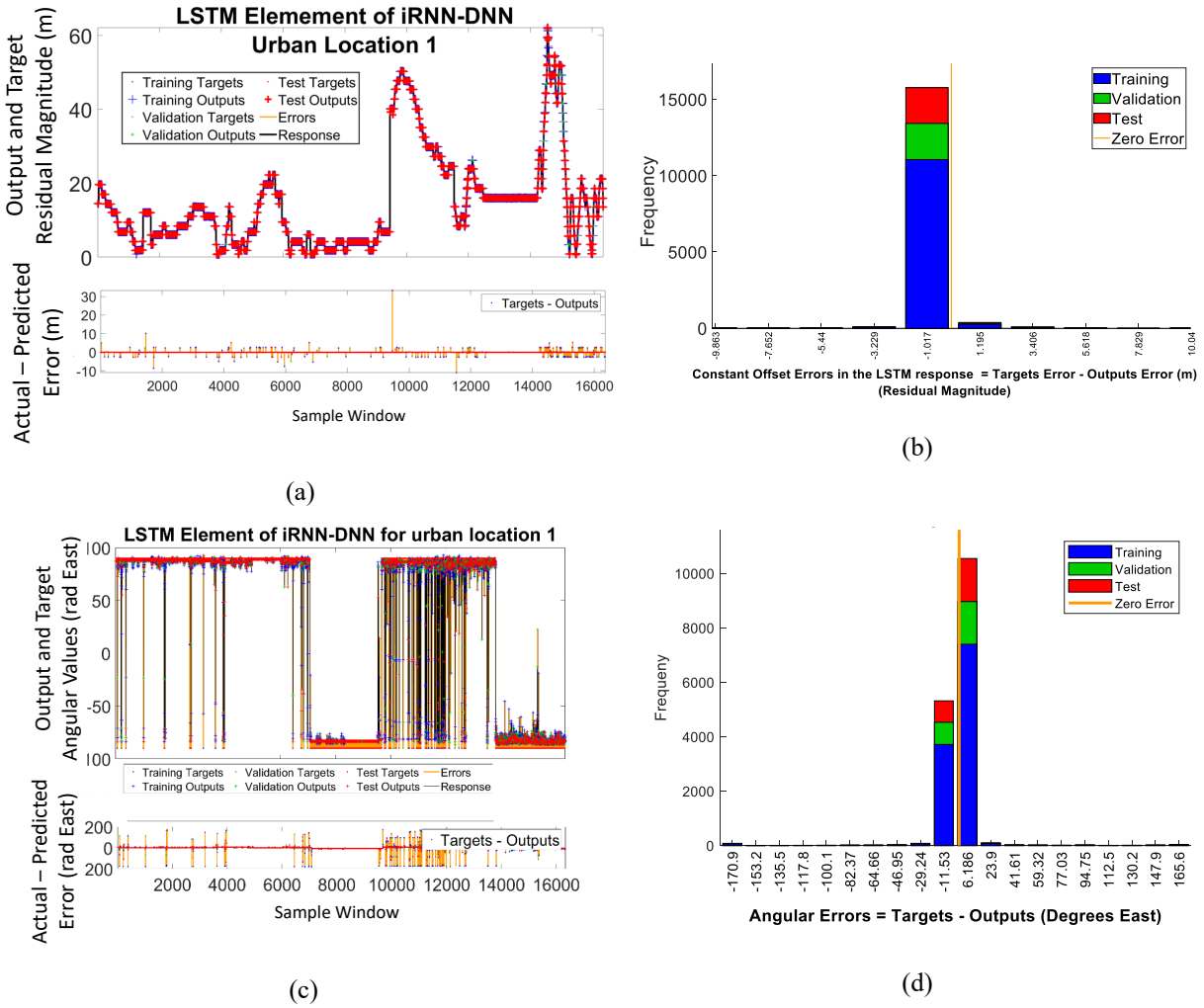

Figure 7-7. LSTM IRNN-DNN Model's Urban Performance in Urban Location 1. (a) Exhibits fidelity in error magnitude prediction with minor deviations; notably, a significant offset occurs at ~920 seconds. (b) The residual error shows a minor consistent bias. (c) Uncovers angular error inconsistencies, deviating by ±90 degrees, indicating directional prediction issues. (d) Error distribution is skewed, indicating room for model improvement, especially in angular error refinement.

Urban Location 1, surrounded by reflectors on three sides (see Figure 7-16(a)), poses a significant challenge for the LSTM models of angular error prediction. Figure 7-7 (a) shows the model's predicted error magnitude closely tracking the actual error, with the most notable deviation

occurring at approximately 920 seconds into the experiment. The residual error distribution, depicted in Figure 7-7 (b), indicates a consistent offset bias in the model, quantified at -1.017 meters. This implies that the model is over predicting the magnitude errors. This is indicative of overfitting of the model. However, considering the average raw error magnitude in urban conditions is 19.057 m (Table), this 1-meter deviation corresponds to approximately a 5% offset error. This is positive indication that the model is able accurately account for complex multi-path signals and predict the magnitude of the predicted error accurately.

While the model effectively handles magnitude errors, it struggles with angular errors, as shown in Figure 7-7 (c). where errors vary by ±90 degrees East. This variance indicates a significant misalignment in angular tracking, suggesting that the model, when facing north, erroneously predicts south. This lack of precision in angular error tracking underscores a critical area for improvement in the model's temporal accuracy. Tracking, is defined as the congruence between the model's predictions and the actual error values. Examining Figure 7-7 (c) closely, it is visible that errors are alternating between over prediction and underprediction, signified by the alternating magnitude of the “actual -predicted Error (rad East)” graph. This could be indicative of the fact that the LSTM model maybe lagging in its prediction. The training process has inadvertently introduced a phase shift in error signal. Alternatively, the GPS receiver is attempting to use phase difference to mitigate multi-path errors in this location before trilateration, and the LSTM has essentially undone this filtering step done by the receiver. As the processing performed in the sensor is a black-vox operation, examination of the performance of the LSTM component in other locations may reveal which hypothesis is more accurate.

The histogram in Figure 7-7 (d) indicates an imbalanced prediction distribution, with one-third of predictions overcompensating and two-thirds undercompensating. This skew suggests that the LSTM may not be fully capturing certain error influences, possibly related to latitude. Despite capturing the general trend of errors well, the model's persistent offset highlights the need for integrating a DNN component to correct this bias and improve overall model accuracy. Further correlation analysis could help identify the primary factors influencing the observed biases, which would inform enhancements to the IRNN-DNN composite model. Addressing these biases is crucial for improving the model's performance in urban environments, where it must manage

complex multipath errors. Overall, while the model shows strong potential, its efficacy in angular error prediction and bias correction needs refinement.

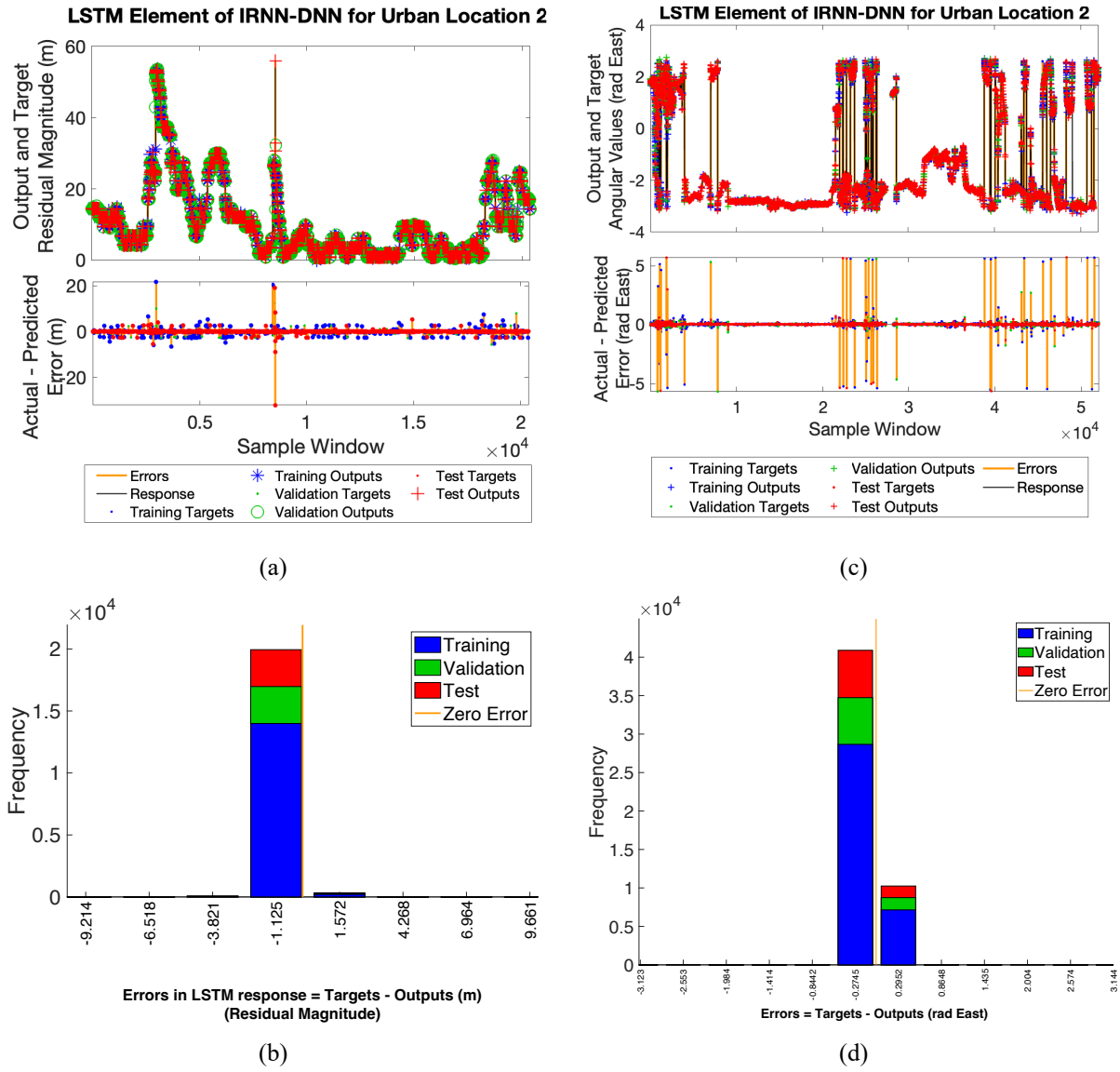

Figure 7-8. LSTM IRNN-DNN Model's Urban Performance in Urban Location 2. (a) Residual error magnitude closely aligning with targets, barring a few significant outliers. (b) The residual error shows a minor consistent bias. (c) Uncovers fewer angular error inconsistencies, indicating directional prediction issues. (d) Error distribution is skewed towards over-correction, indicating room for model improvement.

Urban Location 2, characterized by a simpler setup with a southeast-oriented reflector, the LSTM model shows notable accuracy in tracking error magnitude, as illustrated in Figure 7-8 (a). The data exhibits minimal deviations except for a significant outlier around 800 seconds. Despite

this, Figure 7-8 (b) exposes an offset bias in the model's predictions, measured at -1.125 meters. This bias, albeit slight, indicates an overcorrection trend in the error magnitude. While the model demonstrates improvement in angular error tracking compared to Urban Location 1, with fewer and less severe spikes, it still displays spikes up to 5 radians (230 degrees) East, indicating potential latency in response. The periodicity in the “actual -predicted Error (rad East)” graph continues to lead credence to both theories about LSTM’s lag behavior. The location with significantly less complex multi-path environment, presents less opportunity for the receiver to perform phase based multi-path rejection. Directly supporting the hypothesis fewer spikes are observed in the angular error tracking graph. Alternatively, the soft reflections, and periodic signal masking may also contribute to the reduced lag of the model.

The histogram in Figure 7-8 (d) analyzes the congruence between the model's predictions and actual error values, revealing that one-third of the predictions underestimate by 0.3 radians (17.2 degrees) and two-thirds overestimate by 0.275 radians (15.7 degrees) East. This skewed distribution from zero implies that the model may not fully account for certain factors, likely related to the latitude component, leading to systematic errors in the predictions. This would mean that over time a distinctively arching pattern can be seen. This is in direct agreement with the behavior seen in Figure 7-12.

Although the LSTM model significantly improves tracking, the persistent bias in latitude adjustments underscores the need for further refinement. Incorporating a Deep Neural Network (DNN) post-LSTM could help rectify these biases by providing additional error correction capabilities. Future research should focus on identifying the specific factors contributing to this bias.

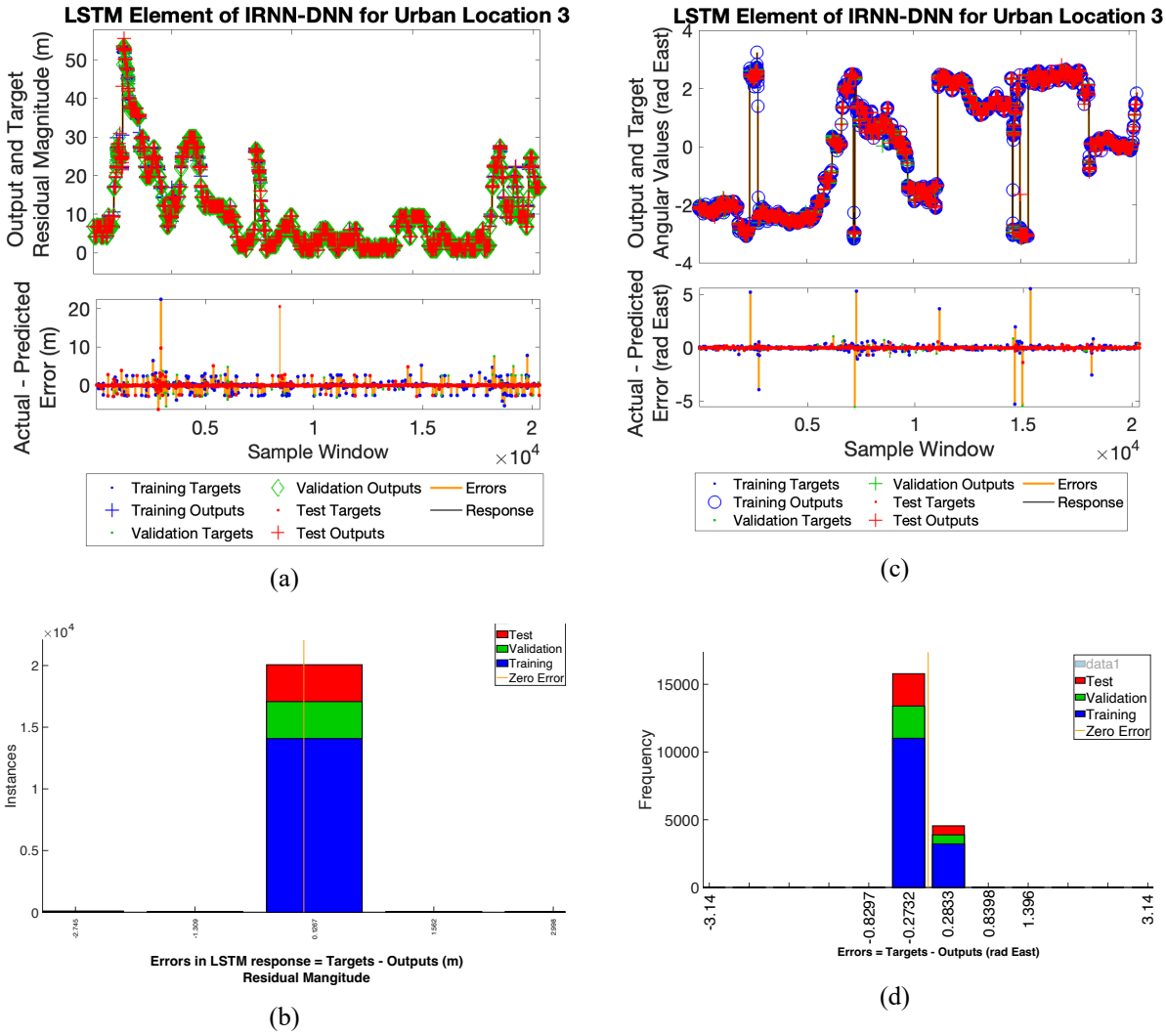

Figure 7-9. LSTM's performance in Urban Location 3. Plot (a) tracks error magnitude closely with notable outliers. Plot (b) indicates a slight offset in magnitude error correction. In (c), angular error deviations suggest the need for model refinement. Plot (d) reveals a slight bias in error predictions, underscoring the potential for improved model accuracy.

Urban Location 3, framed by two perpendicular reflectors perfectly aligned along the north-south axes and equidistant to both the east and west, presents a moderately challenging, and significant scenario for the LSTM model.

As illustrated in Figure 7-9 (a) the LSTM model effectively tracks magnitude errors with notable precision, except for sporadic spikes at around 300 and 800 seconds, peaking at 20 meters. The residual magnitude error distribution, depicted in Figure 7-9 (b), reveals a minimal offset bias

of 0.1267 meters, suggesting the LSTM model's effectiveness in determining the magnitude of errors.

The angular error tracking, visualized in Figure 7-9 (c), reveals less fluctuation and smoother transitions than in other locations, but still includes significant spikes, with the largest deviations reaching up to 5 radians (230 degrees) East. Because the reflectors are aligned to the east and west, the signals will have similar phase shifts. The lack of any significant phase delay in the angular error tracking in this example clearly shows that the LSTM is actually not introducing any significant phase delay into the error stream itself. The phase delay seen in the other urban locations is due to an artifact of the interactions between the signal processing done by the GPS receiver and the LSTM. This is a simpler problem to overcome by adding more varied datasets, getting more data points, and adding an additional filter. If the pattern continues to hold in the semi-urban location, this will be strong indication that model is very suitable for complex multi-path error resolution.

The error distribution histogram in Figure 7-9 (d) portrays an error distribution histogram with the majority of predictions understating the error by 0.2732 radians (15.65 degrees) East. Despite the proximity of this predictions to accurate tracking, the distribution's lack of centralization around zero confirms an underrepresentation of certain error components, possibly latitude-related, which introduces a systematic directional error.

In conclusion, while the LSTM model demonstrates proficiency in estimating error magnitude within Urban Location 3, its performance in angular error tracking has critical implications.

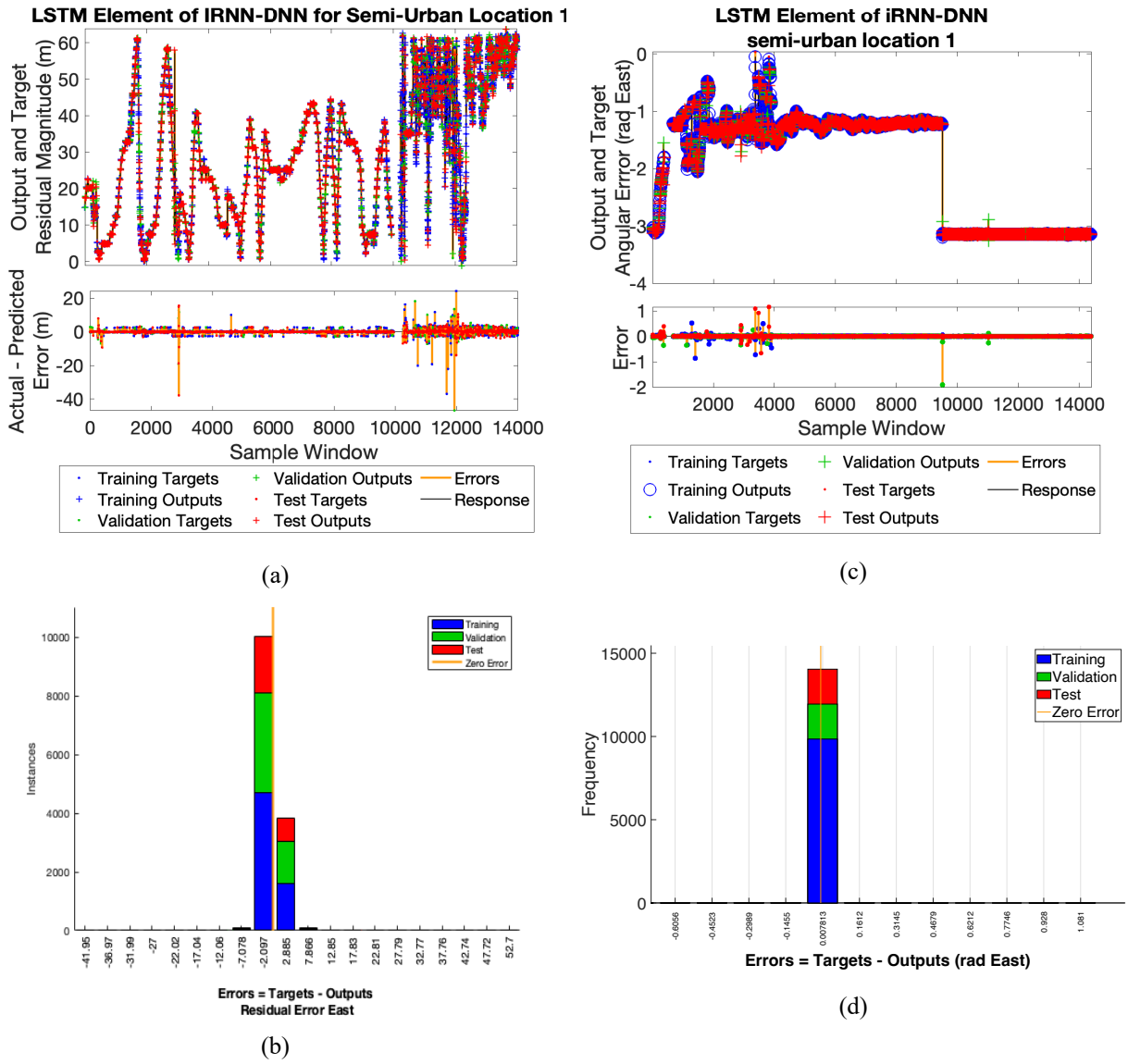

Figure 7-10. LSTM's performance in Semi-Urban Location 1. Plot (a) tracks error magnitude closely with notable outliers at 300 secs. Plot (b) indicates an overcorrection tendency in magnitude error correction. In (c), angular error tracking is accurate, with a large offset observed at 950 seconds. Plot (d) reveals that the model is very effective tracking angular errors with very little over/under-correction tendencies.

Semi-Urban Location 1 is characterized by reflectors situated at distances of 50-100 meters from the receiver in all directions. This setting provides a point of comparison with the LSTM model's urban performance. In Figure 7-10 (a), the LSTM exhibits moderately good error magnitude tracking. There are a few significant spikes present, the most notable being around 50 meters at 300 seconds into the experiment. The occurrence of a rapid oscillation tracking errors suggest that the lack of noise and multi-path actually hurts the LSTM as it does not have enough

historical information to learn the behavior of the error signal. This tracks with was expected based on the error signals studied in section 6.1.4. Interesting behavior is noted after 9500 samples. The error direction rapidly changes, and the system can effectively track the change. However, the magnitude error tracking becomes significantly noisier. It can be hypothesized that, because the direction of the error changed significantly, a new satellite came into or left the view of the receiver. Given that the NMEA shows no change in the number of satellites in the entire window of time captured expect for one at around the 250 second mark, with the satellite count dropping by one, it means that there was some alignment between when a new satellite came into view and a old satellite left. This potentially caused the direction of the error to change. However, since the other predictors were similar, including DOP values, the LSTM may have struggled with predictions of the error.

Continuing the examination of Figure 7-10 (c), the no significant lag is observed. The angular error spread, presented in Figure 69 (d), centers around 0.007 radians East. Given that few, if any multi-path is expected in the semi-urban location tested, there should limited phase difference in the received signals. Since the angular error tracking, does not show any lag, it provides another validation evidence to the hypothesis that the LSTM can track angular errors effectively, and the phase shift seen in urban locations 1 and 3, are due to processing artifacts.

Overall, the LSTM model, while showing promise in magnitude error tracking, clearly requires further optimization for angular error predictions. Incorporating a DNN post-LSTM could potentially address these discrepancies, enhancing the model's overall accuracy and making it more adept at navigating the complexities of urban GPS signal environments. Further research should focus on refining the model's capacity to handle angular discrepancies and integrating advanced filtering techniques to improve both magnitude and angular error predictions.

7.4 A DISCUSSION ON THE IRNN-DNN MODEL

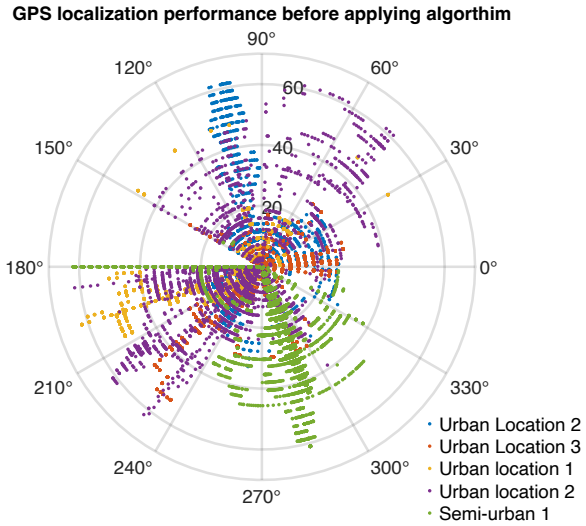

Figure 7-11. Error in GPS localization signal in urban and semi-urban environments. This polar scatter plot visualizes the raw GPS data collected from four distinct locations for algorithmic testing. Each color corresponds to a different environment, demonstrating the variance in signal reception. Semi-urban location has a constant DC offset error, 275° East, with dynamic frequency component. In contrast urban locations, have relatively little observable DC error signals. 0,0 signifies relative ground truth position for each location.

The IRNN-DNN model, takes the predicted error from the LSTM model and combines with the raw data to create composite data feed into a regression function that can correct for GPS localization errors. The task of the regression layer is to remove and DC bias present in the error signal. This section examines the overall performance of the model in terms of horizontal position accuracy, examines the contributing factors and finally examines the residual altitude error. IRNN-DNN is also referred to as the composite model in this document. The terms are used interchangeably. The same data used to evaluate the LSTM model is used in the IRNN-DNN evaluation. The data sets were manually appended together and run through the MATLAB regression learning app to train and test the final regression model. 65% of the available data was used for training, 15% of the data for validation and the remaining 20% set aside for testing. The final plots as seen in the section are for the entirety of the dataset. Urban location 2 data was collected twice, as the DAQ ran out of battery in the first test after data capture was started. A second session was started. The data from both data capture sessions are used to understand the performance of the model as the locations were the same.

Figure 7-11 presents the raw unprocessed residual magnitude and angular error from the ground truth location in radial plot. Only one sensor value (sensor 1A) is plotted to improve the clarity of the figure. All sensors showed similar characteristics as described. Notably, there is a distinct directionality to the spread in each location, with error magnitudes spanning from 0 to 60 meters. Urban location 2 initially shows a preference to spread along the North-South axis in the first trial and 45°-215° East in trial 2. Semi-urban location has a constant DC offset error, 180°-275° East, with the dynamic frequency component. In contrast urban locations, have relatively little observable DC error signals. 0,0 signifies relative ground truth position for each location. The offset values demonstrate a broad distribution without a singular discernible pattern. Interestingly, there is an error component that is consistently 180° east. This would signify that the latitude errors are higher, with longitude errors close to zero.

Figure 7-12 plots residual data and angular error after application of the iRNN-DNN algorithm in a radial plot. Post-correction, the predicted error magnitude and bearing are superimposed onto the initial GPS coordinates to get new coordinates using the inverse haversine formula, followed by recalculating the residual magnitude and angular error from the original ground truth. The algorithm precipitates a significant contraction in error magnitude, congregating the majority of data points across all locations within an error magnitude bracket of 1-2 meters. The lowest magnitude of residual error magnitude is at 1.81(5) m (2σ) in urban location 1 (see Table B-8). The highest magnitude of error is at semi-urban location 1 at 2.87 (5) m (2σ) (see Table). Examining the distribution patterns of the error, we see the residuals of semi-urban location 1 are distributed along 188° and 241° east. Urban location 3, and Urban location 1 both near similar patterns. Urban location 2 is the most interesting. There are clear deviations from the distribution lines. There are both arcs and line error patterns. This indicates that the ML prefers one direction over the other.

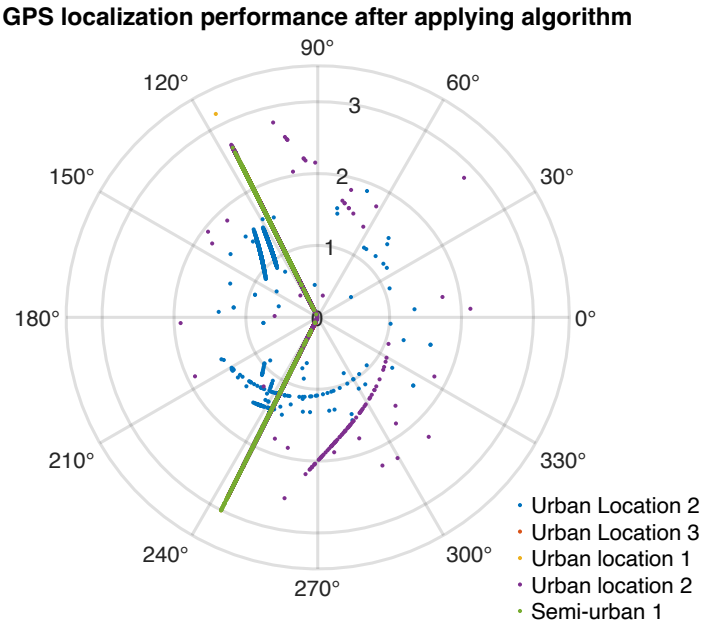

Figure 7-12. Errors in GPS system, after the application of the IRNN-DNN algorithm. The radar plot showcases the dispersion of GPS data points (2σ with outliers rejected). 0,0 signifies relative ground truth position. A marked reduction in error magnitude is observed after application of the composite IRNN-DNN model.

To study the machine learning model's preferential accuracy in correcting errors along one axis over another, an in-depth examination is required. This investigation will be conducted within the NEU reference frame. Adopting the NEU frame facilitates the alignment of satellite orbital dynamics with the drone's operational environment in a coherent reference system. It is important to note that satellites used for GPS, typically have an orbital path that moves from west to east. From the vantage point of a ground receiver, this equatorial orbit means satellites traverse latitudinal lines while maintaining a relatively fixed position along the longitudinal axis. This inherent movement pattern may impact the GPS signal characteristics and, consequently, the errors associated with latitude and longitude differently. By examining these dynamics within the NEU frame, we can better understand the directional sensitivities of the model and refine its predictive capabilities accordingly. Given the relative constancy of North error (Figure 7-13), it infers that the machine learning model might be less equipped to tackle the angular component of the multipath error. Based on work presented in [141] and [219] to develop hypotheses that can account for these observations, one might consider environmental variables such as structural interference that contribute to GPS signal multipath errors. The data presented in Figure 7-12

shows that all predictions from the composite model, except one outlier, is within the three-meter horizontal error requirement specifications in Table 1-2.

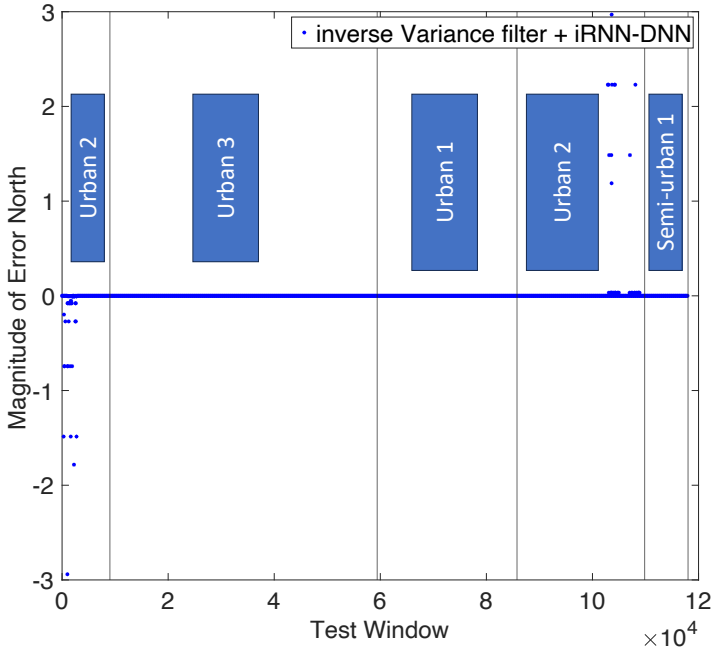

Figure 7-13. Error Correction Efficacy in North Direction. This graph illustrates the model's capacity to mitigate northward positioning errors in urban and semi-urban environments, with test windows showing significant error reduction after applying the inverse variance filter and IRNN-DNN model. Each test window represents a 25-sample size at 10 Hz frequency, emphasizing the algorithm's ability to reduce errors significantly, especially in challenging urban settings.

The NEU errors are presented in Figure 7-13, Figure 7-14, and Figure 7-15 respectively. For isolating the north component of the error, we will consider the latitude difference as negligible, in line with equation (27) to zero. The experimental setup aligns the drone to face north, thus any longitudinal error directly translates to an error in the north component. Similarly, the east error is derived from the latitude error, and this method of error computation is valid specifically due to the drone's northward alignment during the experimental phase.

Figure 7-13 reveals that the north error remains close to zero across all environments for most of the dataset. However, urban location 2 is noted to have a few outliers. The mean error in the north direction is reported as -0.04 m with a standard deviation (SD) of 0.005 m. This suggests a remarkably consistent and excellent model performance in correcting longitude-derived north directional errors. A closer look at the east error component is necessary to understand the

performance of the composite model. Given the position of the test site(s), away from the equator, a larger latitude error is expected [220].

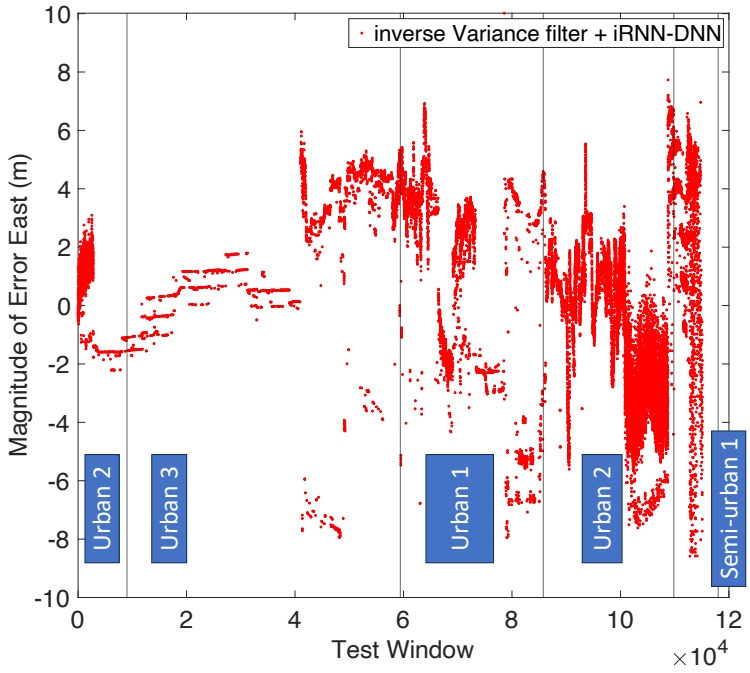

Figure 7-14. Eastward Error Correction Analysis. IRNN-DNN algorithm displays a variability in the reduction of errors in urban and semi-urban locations.

For the east error component, we observe a distinct spread of around ±2m during the initial trial at Urban location 2, whereas in the subsequent trial, the error narrows to a range between -6 to 0m. This variance indicates potential issues with the latitude error model's robustness and its ability to handle noise, as evidenced by the output's high noise levels. Investigating the errors at Urban location 1, we notice an approximate sinusoidal oscillation pattern in the error magnitude, recurring approximately every 16.67 minutes—derived from a 10,000-window period correlating to 1,000 seconds of sampled data. This periodicity mirrors the intervals during which breaks in satellite visibility were recorded in early calibration experiments. This suggests a correlation with satellite visibility; as satellites come into and leave the line of sight, the error performance is affected. Given that 16.67 minutes is approximately the duration a GPS satellite is visible to a stationary ground receiver, this pattern could indicate errors caused by satellite visibility cycles. East errors have consistently had higher magnitude errors compared to North errors in literature [220]. Specific experiments are warranted to explore further and confirm the impact of satellite

visibility on model accuracy. Preliminary observations suggest that the model can rapidly adjust for this cyclical error, as the sinusoidal error pattern is identifiable across other locations, albeit with less clarity. Further investigation is needed to understand the broader implications of these findings, including the presence of potentially longer-term error patterns that could be influencing model output. To address these cyclical and longer-term error patterns, a cascaded LSTM model may be beneficial, possibly requiring a lengthier data window to encapsulate and learn from these periodicities. Such an adaptation could help the model capture and correct for temporal dependencies that extend beyond the immediate window of data points. Other proposed neural network-based GPS error correction methods [12], [111], [162], [220] have seen similar relationships in terms of north and east accuracy. Models can reliably account for one error axis better than the other axis. This finding can explain the specific error plot patterns seen in Figure 7-12. Let's examine equation 63 and take its derivative, as shown in the equation below:

$$\frac{\partial \theta}{\partial lat_{gt}} \approx \frac{\left(lon_{gps} - lon_{gt}\right)\cos^2\left(lat_{gps}\right)}{\left(lon_{gps} - lon_{gt}\right)^2 \cos^2\left(lat_{gps}\right)\cos^2\left(lat_{gt}\right) + \sin^2\left(lat_{gps} - lat_{gt}\right)} \tag{31}$$

If $lon_{gps}\ and\ lon_{gt}$ are very similar, we can use small angle approximations. The numerator of the function inside the arctangent simplifies to a small value, and the primary influence on the term is through the $\sin(lat_{gps})$ term. The behavior of equation (31), is then large dependent on the $\sin^2\left(lat_{gps} - lat_{gt}\right)$ term, where lat_{gt} is a constant. Thus, the periodicity of the angular errors post processing through the composite model can be explained by the individual LSTM performance.

In urban locations, the patterns of latitude values increasing and decreasing explain the observed spiral and circular patterns in the data. For semi-urban environments, the almost straight-line spread of errors can be attributed to the high frequency of data point movements. This observation aligns with the large magnitude of east error movements seen in the east error time plot and Figure 7-10 (c). Such behaviors may result from the constantly changing errors in the test location, as highlighted by the error plot in Figure 7-10 (a), where errors cluster closer to the beginning and end points, suggesting instability or high variability in the model performance.

Adapting measurements to degrees rather than radians or adding additional random multiples of 2π to the longitude values could potentially help in scaling the values appropriately, allowing the algorithm to converge on longitude errors with greater precision. This approach is informed by similar issues encountered in the classifier, as indicated by the HDOP spike seen in Figure 7-4 for both correct and incorrect urban classifications.

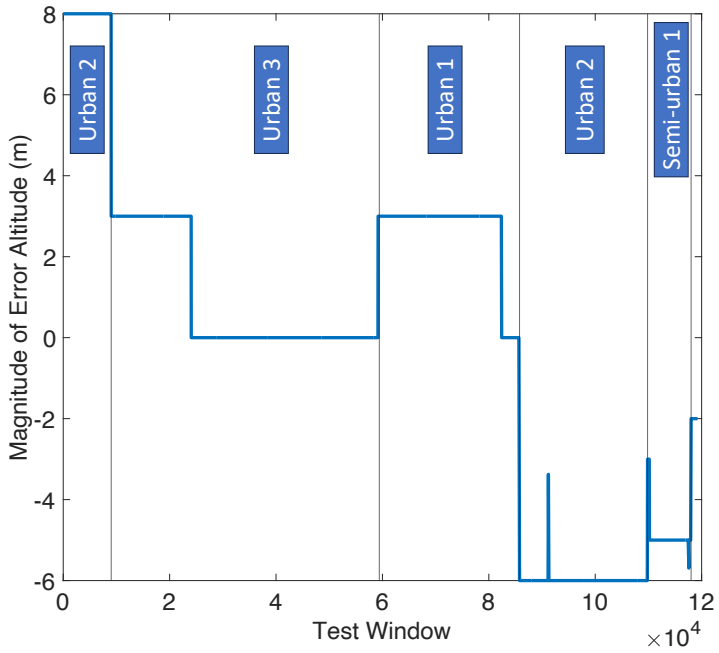

Figure 7-15. Altitude Error Correction in Diverse Environments. The plot illustrates altitude error magnitude across urban and semi-urban test locations, showcasing the model's ability to mitigate altitude errors to be relatively constant. Changes to the satellite availability influence the magnitude of the altitude error.

Figure 7-15 indicates that the composite model does not consistently achieve sub 12.5 ft (3.81 m) accuracy under all conditions. However, the presence of near-constant offsets, rather than variable altitude readings, suggests that the model is successfully capturing some complex interactions. Urban Areas 1 and 3 consistently show accuracy within 3.81 meters, but this level of precision is not replicated in the semi-urban environment or Urban Location 2. Notably, Semi-Urban Location 1 features distant obstacles, and Urban Location 2 has obstacles only in one direction, which may affect model performance. Figure 7-16 captures the 3D isometric views of the test location. It is plausible that the LSTM model utilizes phase errors from multiple reflected paths to compensate for inaccuracies in more complex environments, as evidenced by the periodic

nature of altitude errors observed in urban settings. However, the presence of a DC offset in the altitude error signal, suggests the DNN component, has not significantly addressed the data variations. The near constant outputs indicate systemic bias in the output. Further research is required to determine if alternative structures could enhance the model's accuracy post-LSTM correction, or if such adjustments are even necessary.

Backing up the mathematical explanation of the results, a physical system can be realized by studying how GPS signal from a satellite propagates to the receiver from first acquisition to last acquisition. In Urban 1 and Urban 3 (Figure 7-16 (a) and (b)) scenarios, the signal from a GPS satellite exhibits significant multipath errors as it first becomes visible to the receiver, originating from the west and moving east. Multipath errors tend to decrease when the satellite is at its zenith, directly overhead, where the signal path is least obstructed. As the satellite moves away, multipath interference increases again. The signal-to-noise ratio for each satellite varies throughout its passage across the sky. This variation introduces a periodicity in the PSR measurements' reliability, with the GPS solution quality being initially poor due to multipath effects, improving as the satellite approaches optimal azimuth and elevation, and then deteriorating again as it departs is reflected in the HDOP values. The LSTM component of the proposed RNN-DNN model is designed to exploit this periodicity. It can learn from the time series of HDOP measurements, recognizing patterns where the signal quality oscillates due to the changing satellite positions relative to urban reflectors. By doing so, the model effectively anticipates and compensates for the systematic errors associated with multipath, refining the GPS localization. In contrast, in environments like Urban 2 (Figure 7-16 (c)) and Semi-Urban 1 (Figure 7-16(d)), where reflective surfaces are sparse, the periodicity in the PSR error is less pronounced. The LSTM's effectiveness is thus diminished due to the lack of consistent temporal patterns to learn from. Urban 2, although categorized as an urban environment, might present a heterogeneous mix of signal masking and multipath reflections, making the PSR errors more erratic and less predictable. Semi-Urban 1 lacks substantial structures to cause predictable multipath errors, resulting in a less cyclic error pattern for the LSTM to identify and correct.

Figure 7-16. Isometric 3D view of GPS test locations illustrating signal reflection challenges. The green arrow represents the signal from a satellite at first acquisition, and purple the last signal received from the satellite before line sight is lost. (a) Urban location 1 with a narrow alley enclosed by high walls, illustrating substantial GPS signal reflection and multipath effects due to the urban canyon environment. (b) Urban location 3 is bordered by tall buildings on two sides, with a third reflector in the southerly direction a distance away. It depicts a lower level of GPS signal interference with more open sky visibility compared to urban location 1. (c) Urban location 2 with 'soft' obstacles (vegetation with varying density) and marble columns to the north, showing mixed GPS signal reception conditions due to partial blockage on one side. (d) Semi-urban, a relatively more open area with obstructions for GPS signals located near the test field's edge with clear line-of-sight access to the sky in the center of the reception field, indicative of more favorable conditions for GPS reception.

The comparison of performance across Urban Location 3 with Urban Location 1 and Semi-Urban 1 highlights the model's dependency on environmental consistency to form predictive temporal models. The LSTM's strength lies in its ability to model errors with periodicity, such as those observed in Urban 1 and 3, where satellite signals undergo predictable quality changes due to the urban landscape. In less structured environments like Semi-Urban 1 or areas with mixed reflective profiles like Urban 2, the LSTM may not perform as effectively because the error patterns do not present the same level of periodicity for the LSTM to utilize.

Table 7-2. Co-relation factors between average GPS performance and GPS error metrics in semi urban location 1.

	Unprocessed Magnitude Error	Unprocessed Angular Error	Processed Altitude Error	Processed Magnitude Error	Processed Angular Error
Average GPS Longitude	0.6098	-0.7381	-0.0098	0.2815	0.161
Average GPS Latitude	-0.5118	0.6414	0.0062	0.25	-0.1978
Average GPS count	-0.484	0.483	-0.0056	0.284	-0.0911
Average GP S altitude	-0.5734	0.7625	0.009	0.0615	-0.2564
Average GPS magnetic Variation	NaN	NaN	NaN	NaN	NaN
Average GPS HDOP	0.2296	-0.2389	-0.0025	-0.2062	0.0265
Average GPS VDOP	-0.067	-0.019	-0.0015	0.1228	0.0635
Average GPS PDOP	-0.0692	-0.0191	-0.0015	0.1265	0.065
Average GPS Speed	0.0983	-0.0864	-0.0122	-0.2664	-0.1534
Antenna Status	NaN	NaN	NaN	NaN	NaN
Average time since Last fix	0.0406	-0.0198	-0.0033	-0.096	0.0346

Table 7-2 presents the correlation factors between various average GPS performance metrics and the associated GPS error metrics in semi urban location 1. The first column reflects the average values aggregated from all five GPS sensors utilized during the experiment, with each sensor's data summed and then divided by the number of devices active at that time. The presence of NaaN values is expected as these parameter**s** are not expected to change. Changes would signify a change in the environmental and experimental setup.

The analysis of the IRNN-DNN model's performance, as delineated in Table 7-2, Table 7-3, and Table 7-4, illustrates its intricacies in correlation to the data it has been trained on. Statistically re-explaining the same composite model's performance, High negative correlations between 'Average GPS longitude' and 'Unprocessed Angular Error' (-0.7381), suggesting that angular deviations errors increase with longitude. Proof of the mathematical and physical analysis conducted in the previous section. For an ideal model, the post processing correlation should tend towards zero. Correlation values thar exhibit a transition from negative to positive and vice versa, implies that the model is starting to over fit to th e data with stronger overfitting meaning that the model is fitting to noise in the data rather than generalizing. Generally, however, lower correlations with processed error compared to raw signal, indicating improvements or stabilizations due to processing.

Table 7-3. Co-relation factors between average GPS performance and GPS error metrics in urban location 1.

	Unprocessed Magnitude Error	Unprocessed Angular Error	Processed Magnitude Error	Processed Angular Error
Average GPS Longitude	0.2173	-0.2774	-0.1547	-0.0248
Average GPS Latitude	-0.1749	0.2304	0.0557	-0.1713
Average GPS count	0.0075	0.1733	-0.0367	-0.2128
Average GPS Altitude	-0.2653	0.2956	0.1534	-0.0478
Average GPS magnetic Variation	NaN	NaN	NaN	NaN
Average GPS HDOP	0.0379	-0.0924	-0.0275	0.0703
Average GPS VDOP	0.007	0.164	0.121	0.045
Average GPS PDOP	0.0072	0.1677	0.1251	0.0461
Average GPS Speed	0.0409	-0.0973	0.1668	0.1693
Antenna Status	NaN	NaN	NaN	NaN
Average time since Last fix	0.018	-0.0187	-0.031	-0.049

Table 7-3 presents the correlation factors between various average GPS performance metrics and the associated GPS error metrics in urban location 1. The first column reflects the average values aggregated from all five GPS sensors utilized during the experiment.

Table 7-3 provides the correlation factors between average GPS performance metrics and GPS error measurements, both processed and unprocessed, for an urban location 1. The table drops parameters with 'NaN' entries for certain metrics, such as magnetic variation, which indicates no measurable change in these parameters throughout the experiment. Such invariance is anticipated

for certain variables—magnetic variation and Antenna status in particular—since the drone maintained a constant position, and no variation was expected. It should be noted that this might differ when the drone is in motion. A moderate positive correlation of 0.2173 between 'Average GPS longitude' and 'Unprocessed Magnitude Error' suggests a significant relationship wherein increases in longitude readings may be associated with increases in the magnitude of errors. On the other hand, 'Unprocessed Angular Error' has a negative correlation with 'Average GPS longitude' (-0.2774), implying that larger longitude errors could coincide with a reduction in angular errors. This relationship is moderate and does not necessarily imply a strong direct cause-and-effect linkage. On the other hand, when examining processed errors, improvements become apparent. 'Processed Magnitude Error' is negatively correlated with 'Average GPS longitude' (-0.1547), indicating that the magnitude of errors has diminished following processing. Additionally, 'Processed Angular Error' exhibits a slight negative correlation with longitude (-0.0248), denoting a notable improvement from the unprocessed state. This implies that the processing steps within the IRNN-DNN model have successfully reduced the severity of these errors, enhancing the GPS performance in an urban context where complex error patterns are expected.

Table 7-4. Co-relation factors between average GPS performance and GPS error metrics in urban location 2.

	Unprocessed Altitude Error	Unprocessed Magnitude Error	Unprocessed Angular Error	Processed Altitude Error	Processed Magnitude Error	Processed Angular Error
Average GPS Longitude	0.7217	0.3598	-0.4371	-0.2217	-0.3843	0.2908
Average GPS Latitude	-0.6079	-0.2042	0.2451	0.0979	0.3359	-0.4057
Average GPS count	-0.4065	-0.1737	0.1627	0.4064	0.2148	-0.1651
Average GPS Altitude	-0.7569	-0.3311	0.4344	0.0588	0.3653	-0.3464
Average GPS HDOP	0.2241	0.1072	-0.1245	-0.2241	0.0201	0.0125
Average GPS VDOP	-0.0604	0.1292	0.1212	0.0604	-0.0799	0.0793
Average GPS VDOP	-0.0619	0.1287	0.1242	0.0619	-0.0797	0.082
Average GPS Speed	0.116	-0.0441	-0.0076	-0.116	-0.0165	0.032
Average time since Last fix	0.026	0.011	-0.0029	-0.026	-0.029	0.0353

Table 7-4 presents the correlation factors between various average GPS performance metrics and the associated GPS error metrics in urban location 2. The first column reflects the average values aggregated from all five GPS sensors utilized during the experiment.

From Table 7-4, a strong negative correlation is evident between 'Average GPS altitude' and 'Unprocessed Altitude Error' (-0.7569), suggesting that as GPS altitude measurements increase, the unprocessed altitude errors decrease. Additionally, there's a considerable positive correlation with 'Unprocessed Angular Error' (0.4344). These correlations might point to the altitude measurements being inversely impacted by altitude errors in the urban environment. When it comes to processed data, a noteworthy improvement in correlation is observed, which implies effective error mitigation through the IRNN-DNN model's processing steps. For instance, the negative correlation for 'Average GPS longitude' with both 'Processed Magnitude Error' (-0.3843) and 'Processed Altitude Error' (-0.2217) suggests that processing the GPS data reduces both the error magnitude and the altitude error, with longitude demonstrating a significant influence on these error reductions. Further analysis of unprocessed errors reveals that longitude is positively correlated with 'Unprocessed Angular Error' (0.7217), indicating a strong influence of longitudinal errors on the direction of the error vector. Conversely, there is a substantial inverse relationship with altitude errors, as shown by the negative correlation with 'Unprocessed Altitude Error' (-0.7569). This could indicate a complex interaction between the GPS signal's longitudinal

component and the vertical error. In terms of latitude correlations, 'Average GPS Latitude' demonstrates a negative correlation with 'Unprocessed Magnitude Error' (-0.2042), and post-processing, a positive correlation emerges with 'Processed Magnitude Error' (0.3359). This shift suggests that latitude errors significantly affect the magnitude of errors and that they are not as effectively mitigated by the model's processing as longitude errors are. This is a statistical validation of the analysis performed previously in urban location 2.

Table 7-5. Co-relation factors between average GPS performance and GPS error metrics in urban location 3.

	Unprocessed Magnitude Error	Unprocessed Angular Error	Processed Magnitude Error	Processed Angular Error
Average GPS Longitude	-0.458	0.6372	-0.0733	0.5546
Average GPS Latitude	0.4195	-0.5069	-0.0973	-0.4199
Average GPS count	0.3077	-0.4589	-0.031	-0.2508
Average GP S Altitude	0.4655	-0.6293	0.0523	-0.5782
Average GPS HDOP	-0.1464	0.1996	-0.0301	0.163
Average GPS VDOP	0.0218	-0.0735	0.0854	-0.0796
Average GPS VDOP	0.0223	-0.0751	0.0883	-0.0815
Average GPS Speed	0.0611	-0.0463	0.0374	0.0446
Average time since Last fix	-0.0561	0.0203	0.0252	0.0259

Table 7-5 presents the correlation factors between various average GPS performance metrics and the associated GPS error metrics in urban location 3. The first column reflects the average values aggregated from all five GPS sensors utilized during the experiment, with each sensor's data summed and then divided by the number of devices active at that time.

Table 7-5 provides an overview of the correlation factors between average GPS performance metrics and GPS error metrics for urban location 3. A strong positive correlation exists between 'Average GPS longitude' and 'Unprocessed Angular Error' (0.6372), revealing a substantial relationship where errors in longitudinal readings significantly influence the direction of the angular error. This is further exemplified in Figure 7-11, where persistent errors in the second and third quadrants indicate that most of the errors contribute positively to the primary error vector. On the other hand, 'Average GPS longitude' also shows a negative correlation with

'Unprocessed Magnitude Error' (-0.458), suggesting that higher longitudinal errors could correspond to a decrease in the overall error magnitude, perhaps due to compensatory effects in other error components. After processing, this correlation decreases to -0.0733 for 'Processed Magnitude Error', demonstrating an improvement but still indicating the presence of directional errors associated with longitudinal readings. Latitude correlations undergo a noticeable shift from the unprocessed to the processed state, from -0.5069 to -0.0973, indicating a reduction in the effect of latitude on error magnitude after processing. However, 'Processed Angular Error' maintains a relatively high correlation with 'Average GPS longitude' (0.5546), suggesting a persistent directionality in the errors related to longitude, which does not diminish considerably with processing. The processed data for Urban Location 3 shows a reduced correlation in magnitude errors but a remaining high correlation in angular errors with both longitude and latitude. This indicates that the model's processing is more effective in reducing the magnitude of errors rather than the directional component. Furthermore, 'Average GPS Latitude' sees a decrease in correlation from unprocessed to processed states, indicating a lessened impact on the magnitude of errors, although directionality issues continue to persist.

Upon reviewing the performance of the IRNN-DNN model as revealed in the correlation data, it becomes evident that while the model can reduce the magnitude of GPS errors, there is a persistent correlation between errors and predictors, even after processing. This persistence, especially noted in the urban locations, could suggest a tendency towards overfitting, where the model, instead of generalizing from the input data, captures noise or random fluctuations inherent within the GPS signals. Such overfitting is indicated by the fact that despite processing, the output errors remain correlated with the GPS measurements, a trait not observed with the LSTM model. This continued correlation post-processing implies that while the model has learned to reduce the magnitude of errors—perhaps to a level comparable with highly precise mapping-grade receivers—it might still be homing in on some remaining stochastic elements of the dataset. However, the reduction in magnitude errors and the model's performance, possibly rivaling that of precise receivers, underscore the efficacy of the method and the potential of the IRNN-DNN model. It implies that the foundation of the model is sound and with further refinement, particularly in addressing overfitting by distinguishing between noise and actual signal, the model's accuracy and reliability can be significantly enhanced. Future iterations of the model could benefit from integrating strategies to prevent overfitting, such as regularization techniques or the introduction

of noise-reduction algorithms that can discern and minimize the influence of random fluctuations in the training data. More about this is discussed in section 8.3

7.5 CHAPTER SUMMARY

Chapter 7 provides an analysis of the performance of the IRNN-DNN composite algorithm in correcting GPS navigation errors across various environmental settings. The chapter evaluates the inverse variance weighted filter. It then transitions to an examination of the LSTM model's performance on static GPS data, assessing its effectiveness in urban and semi-urban environments characterized by different levels and complexities of multipath in urban environments, then evaluates the data derived from the IRNN-DNN model's application across various urban settings demonstrates a robust capability in addressing and mitigating multipath errors, with an intriguing correlation between environmental complexity and model performance. We find that the error after processing through the IRNN-DNN reduces to under 2 meters horizontal offset errors, more than 95% percent of the time (2-sigma distribution).

Notably, in Urban Location 1, which is characterized by the presence of three reflectors, the model exhibits high precision in capturing and correcting multipath errors. This level of accuracy, nearly paralleling that of Urban Location 3, which has reflectors on two parallel sides, suggests that the model’s error correction mechanisms are adept at navigating complex multipath conditions. In contrast, Urban Location 2, with only one reflector, shows a less optimal performance, underscoring the model's enhanced functionality in more intricate settings.

The comparative analysis indicates that the IRNN-DNN model is particularly effective in environments with multiple reflectors. This finding is counterintuitive, as such settings are typically prone to increased GPS signal distortion. However, the model not only copes with this complexity but also appears to leverage it to improve its error correction capabilities. This is exemplified by the performance in Urban Location 1, where the multipath components are effectively discerned and mitigated, resulting in a level of GPS accuracy that is compelling when considering the challenges posed by such environments.

The metrics support the conclusion that the IRNN-DNN model excels in urban conditions with more complex reflector configurations, potentially surpassing traditional expectations for

GPS accuracy in such contexts. This outcome implies that the model is capturing essential characteristics of the multipath interference, which are then being used to fine-tune the algorithm's correction parameters.

In summary, the findings from Urban Locations 1, 2, and 3 contribute to a key thesis conclusion: the IRNN-DNN algorithm demonstrates a remarkable capacity for understanding and mitigating multipath errors, especially in urban environments of increased complexity. The evidence suggests that the model's effectiveness is not diminished but rather enhanced by such conditions, offering a promising direction for further research and development towards the development of GPS based drone localization system.

CHAPTER 8. LIMITATIONS, CONCLUSION AND FUTURE WORKS

8.1 A SUMMARY ON THE KEY FINDINGS

This thesis embarked on an exploration of how recent advancements in signal processing, machine learning, and embedded systems contribute to the enhancement of GPS localization technology in drone and aerospace systems operating in urban environments. It began by questioning the performance capabilities of embedded GPS receivers compared to traditional survey-grade receivers, specifically within the context of urban air mobility applications. The investigation revealed that while embedded GPS receivers offer a cost-effective alternative, they face challenges such as increased susceptibility to signal reflection, obstruction, and multipath interference in dense urban settings. Secondly, the thesis examined the trade-offs between single and multi-GPS receiver systems, uncovering that multiple receivers, despite their higher energy consumption and cost, provide improved accuracy and reliability crucial for critical aerospace applications. Lastly, our exploration into machine learning applications demonstrated significant potential for enhancing GPS sensor performance through predictive modeling and error correction, improving the accuracy and reliability of GPS data in real-time. Through these inquiries, this thesis contributes to the field of electrical engineering by showcasing the integration, efficiency, and reliability of GPS technology, especially within the demanding environments of urban navigation.

Table 8-1. Evaluation of proposed GPS localization system with IRNN-DNN against technical requirements

Technical Requirement	Condition Met (Yes/Partially/No)	Explanation
Update rate of at least 10 Hz; latency under 50 ms	Yes	GPS sensor can operate at 10 Hz Algorithm corrects the outputs in under 50ms
Accuracy condition met 95.5% of time	Partially	Horizontal accuracy met in all urban, semi-urban, and open-field environments tested. Vertical measurements were met in Urban Locations 1 and 3, but not in Urban Location 2 and semi-urban location. However, the values are highly repeatable. Meeting the 95.5% threshold
Error under 3 m horizontally	Yes	Horizontal accuracy met in all urban, semi-urban, and open-field environments tested.
Error under 12.5 ft vertically	Partially	Vertical measurements were met in Urban Locations 1 and 3, but not in Urban Location 2 and semi-urban location.
Onboard processing of GPS	Yes	All algorithms can be run on lower power hardware typical of the flight computers used
Antenna placement to enhance signal and reduce noise	Yes	The antennas were located around the drone. The algorithm can effectively enhance the accuracy of the sensors
Firm-real time operation	Yes	The system is real-time capable from both the hardware, and software perspective and architecture and implementation perspective.
Power consumption under 15 Watts	Yes	Actual power consumption is significantly below the limit, at approximately 1.625 Watts during peak operations,
Scalability to adapt to different UAV configurations and operational demands	Partially	The algorithm is scalable in design and implementation. Additional testing needs to be done on new platform to verify compatability

Table 8-1 evaluates the GPS DAQ hardware enhanced by the IRNN-DNN model against precise technical requirements informed by proposed UAM operations. The composite model consistently achieves horizontal accuracy under 3 meters across varied environments—urban,

semi-urban, and open fields—demonstrating its robustness and adaptability in complex navigational contexts. IRNN-DNN model achieves at a rate of 10Hz, significantly higher than system with comparable levels of accuracy. This thesis now introduces the Dynamic Accuracy Index (DAI), a metric that quantifies the balance between positional accuracy and data processing speed. Lower the DAI values the better.

$$\text{Dynamic Accuracy Index} = \frac{Mean\ Accuracy\ (2\sigma)}{Frequncy\ of\ Position\ Reports} \tag{32}$$

The proposed IRNN-DNN method has a mean error of 1.8 m in a static position test operating at 10 Hz in urban environments. This represents a 47% improvement over other proposed alternative neural network models [111]. The experimental results reveal our system's proficiency, particularly evident in its Dynamic Accuracy Index (DAI) of 0.18 meter/Hz, surpassing other filter methods operating at ~1 Hz with a DAI of 5.11 meter/Hz [111]. It also exceeds the proposed filter + neural network methods presented in the literature with DAIs of 3.41[111] and 2.17 [220]. It compares effectively with vision-based system with DAI of 0.15m/Hz (4.50 meters in horizontal accuracy at 30 fps) [221] It excels in real-time processing, maintaining firm real-time operations with minimal latency, crucial for UAV operations requiring immediate data processing and response. The system's architecture, featuring non-blocking polling operations and a Last In, First Out (LIFO) data window approach, plays a critical role in enhancing the overall efficiency and real-time performance of the GPS localization system. Non-blocking operations ensure that data processing does not wait for other operations to complete, eliminating queues or halts that could introduce delays. The system in experimental testing showed a maximum delay of 10 ms between data capture and final localization estimate. Additionally, the LIFO data window approach prioritizes the processing of the most recently received data first. This method is particularly beneficial in navigation systems where the latest data is often the most relevant. By prioritizing newer data, the system can more rapidly adjust to new information, such as sudden changes in the drone's position due to external factors like wind or obstacles. This approach minimizes the influence of outdated data, which might no longer accurately represent the current situation, thereby enhancing the accuracy and reliability of the system's outputs. Furthermore, the system showcases exceptional energy efficiency, consuming well below the 15-watt limit during peak

operations, which affirms its suitability for field use. The model also shows promise for cross-compatibility with other inertial navigation sensors, though full integration remains a goal for future development. Despite these strengths, the system struggles with vertical accuracy in specific settings like Urban Location 2 and semi-urban areas, failing to consistently meet the 12.5 feet standard and suggesting a targeted area for technological enhancement. Additionally, while maintaining a minimum distance of 10 meters from sensitive areas, this aspect was not empirically tested, relying instead on the theoretical accuracy capabilities of the system. Moving forward, the subsequent section will address the limitations of this study, which is vital for framing the encountered challenges and outlining potential avenues for the author's future research to refine the localization system's effectiveness in urban aerospace applications.

8.2 LIMITATIONS IN STUDY

This section identifies the study's limitations and proposes strategies to address these issues in future research. By resolving these constraints, future studies can improve robustness and applicability.

8.2.1 *Geographical diversity and multipath complexity*

Our research highlighted the critical influence of the operational environment on GPS signal accuracy. The study's scope was limited by the number of locations tested and time available for data collection. We observed that the complexity of the environment, particularly regarding multipath effects, is a determining factor in the performance of our algorithms. In more intricate settings, the increased error and positional variance offer rich data for algorithm optimization. Expanding the geographical diversity of test locations is a crucial next step to ensure our findings and GPS error correction methods are robust and generalizable across varied urban landscapes.

8.2.2 *Data and training complexity*

Given the short time available for effective data collection using the validated PATHFINDER system, data available from experiments for training, validating, and deploying the ML model was limited. A significant portion of the study's future work is to gather more data. The models trained in MATLAB are also not suitable for direct deployment on drone platform due to significant

limitations. While the MATLAB model was chosen for a good reason in this thesis, testing with highly validated and tested model from literature, it is considered not ready to deploy. A significant limitation was the manual moving and processing of data from one step of the composite model to the next. Large datasets will only amplify this problem. Alternative techniques need to be investigated. The study's attempts in training the similar model in Azure cloud platform and Python varied in effectiveness. A large caveat to the work presented is that while the model shows repeatable results for the given test dataset, it was not tested with wild data from a drone in full hover in a random location.

8.2.3 *Hardware and firmware compatibility*

Initial investigations suggest that hardware versatility and cross-compatibility of algorithms may allow for the use of diverse GPS sensors and manufacturers' firmware. Despite a lack of correlation in performance among identical GPS sensors, preliminary evidence supports a hardware-agnostic approach for our system. Future testing will explore the extent to which different GPS sensors and firmware can maintain system performance, contributing to the flexibility and scalability of the solution.

8.2.4 *Comprehensive flight phase testing*

The thesis study was constrained to the hover phase of drone operations due to regulatory changes during the research period. The investigative efforts were particularly impacted by recent amendments to the FAA\regulations, specifically the Remote Identification (Remote ID) rule for drones, which came into effect during our study period. Remote ID requires that drones operating in the national airspace system broadcast identification, location, and performance information. These rules necessitate that drones are equipped with Remote ID transmitters, which were not readily available at the onset of their enforcement. Consequently, our field operations were restricted This limited our data collection to indoor environments, which are not representative of the data required for robust model training and validation. With the recent acquisition of compliant ID beacons, we are now positioned to initiate controlled hover flight tests, which will serve as a baseline for comparison with our previous stationary GPS tests.

8.2.5 *Propeller interference phenomenon*

A significant and unforeseen observation was recorded during the static testing phase: propellers fabricated from non-metallic materials, such as nylon and ABS, substantially interfered with the signal reception of GPS receivers. This disturbance, although mitigated during our study by operating the propellers, unveils a critical avenue for further exploration. A comprehensive understanding of the interference caused by propeller materials could lead to enhanced drone design parameters and optimal placement of GPS receivers to minimize such disruptions.

8.2.6 *Equivalence of data sets and experiments*

In the context of our study's constraints, establishing a methodological equivalence between the static test conditions—wherein drones were immobilized—and the dynamic flight scenarios, which involve close-to-the-ground maneuvers, emerges as a critical undertaking. This is particularly salient given that the static tests, while controlled, do not encapsulate the full spectrum of variables that drones encounter in active flight. Confirming this equivalence would substantiate the hypothesis that extensive datasets derived from alternative yet analogous mobility patterns, such as those of vehicular traffic, could significantly augment the scope and depth of our data. Such augmentation is imperative for a rigorous and comprehensive training regime of our machine learning models, which underpins the robustness and validity of the GPS error correction techniques we have developed.

The incorporation of this diversified and enriched data pool has the potential to refine the precision of the algorithms that form the backbone of our GPS error correction methodologies. By simulating a more varied range of operational dynamics within our data-driven frameworks, we can enhance the models' ability to generalize across different flight conditions. This advancement is of paramount importance for the evolution of UAV navigation systems, ensuring that they operate with heightened accuracy and reliability, even within the multifaceted and often unpredictable urban airspaces.

Therefore, the subsequent phase of our research will involve a concerted effort to methodically correlate the data obtained from stationary testing platforms with that derived from drones in active flight. By bridging this gap, we aim to bolster the robustness of our error correction

mechanisms, thereby contributing to the overarching goal of achieving a higher standard of navigational integrity for UAV systems in diverse operational contexts.

8.2.7 *Extension of data collection duration*

Extending the data collection duration is a foundational component of this research, imperative for capturing comprehensive GPS performance metrics over time. During the initial phases of the study, data capture was conducted in relatively short increments due to the limitations imposed by both drone battery life and operational constraints. Although over 550 hours of usable test data were amassed, the temporal granularity of these datasets was often constrained, with most data samples reflecting brief snapshots of GPS performance. This limitation is particularly impactful because longer-duration datasets enable the observation of nuanced patterns in GPS signal behavior that may manifest only over extended periods or under varying environmental conditions. Therefore, the need for continuous, long-term data collection is evident to enhance the depth and fidelity of our analysis. To address this, we are initiating the development of R-sensors based on Van Hunter Adams's pioneering work at Cornell[222]. These low-power, distributed DAQ systems will facilitate extended remote measurement and data streaming, bolstering our dataset's comprehensiveness. This development has broad applications, including micro-satellites, environmental modeling, state-space monitoring, and precision agriculture, and will be a focal point of my continued research efforts. These low-power, distributed data acquisition systems are engineered to facilitate prolonged and autonomous data collection, wirelessly transmitting pertinent parameters of interest to a centralized server. This technology will allow for an uninterrupted and comprehensive capture of GPS data, overcoming the challenges of limited battery life and manual data retrieval.

8.3 FUTURE RESEARCH CONTRIBUTIONS

This section outlines the future work to be undertaken by the author and potentially others in the field based on the findings of this study. It emphasizes potential advancements and research directions informed by the current results.

8.3.1 *Multi-gated recurrent neural networks*

Currently, the neural networks employed in our studies are adaptations of established architectures readily available in the market. These pre-existing models have been repurposed to facilitate our training requirements. However, we have not ventured into the design of novel machine learning structures specifically tailored for our unique application needs. Based on the insights gleaned from the thesis, there are specific elements within neural network architecture that warrant further exploration to fully exploit their potential in our domain. These elements include the architecture's capability to perform both short-term and long-term error correction. Such a dual approach is essential for addressing a spectrum of errors, from high-frequency noise typically associated with short-term fluctuations to low-frequency, periodic errors that manifest over longer time frames.

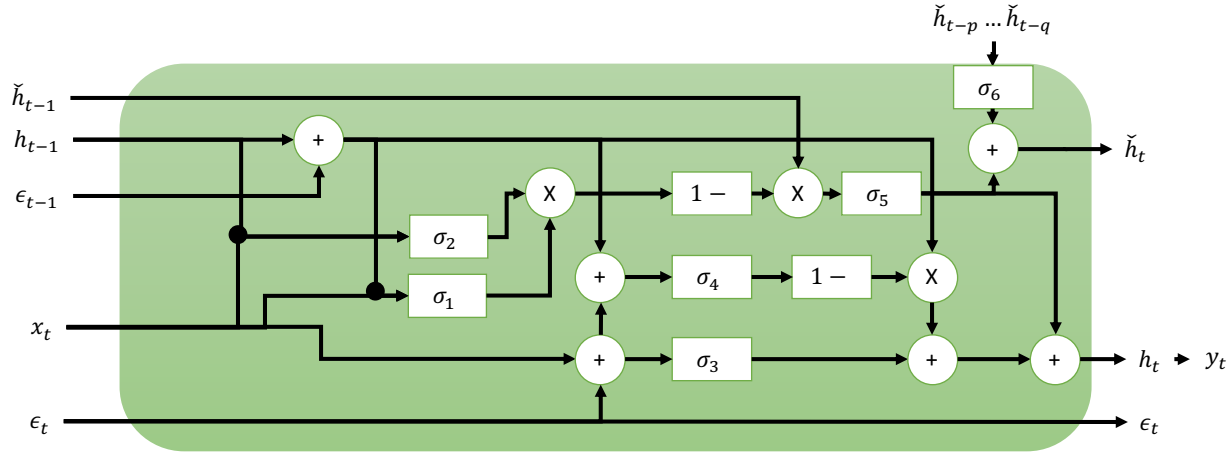

Figure 8-1. A RNN cell designed for signal processing, featuring two distinct pathways for error correction. The cell inputs a signal $\mathbf{x_t}$ and outputs a corrected signal $\mathbf{y_t}$. Internally, it manages two hidden states, $\mathbf{h_t}$ and $\check{\boldsymbol{h}}_{\boldsymbol{t}}$, which are responsible for short-term high-frequency and long-term periodic error correction, respectively. The system utilizes a novel error function, COBECA, aimed at outperforming traditional metrics like RMSE and MAE by generating a trace error that captures both high-frequency and periodic signal error.

The next step in the research will involve an in-depth exploration of an RNN cell specifically designed for signal processing. This cell will be characterized by dual pathways for error correction, aligning with findings related to the optimal window size for the algorithm. The cell will process input signals xt and produce corrected outputs yt, managing two hidden states ht and $\check{h}_t$. ht will address short-term, high-frequency noise, while the latter $\check{h}_t$will correct long-term, periodic errors. This design is informed by our previous work, which indicated that varying the

window size can significantly impact the performance of the algorithm, particularly in isolating and correcting different error frequencies.

The system's efficiency will hinge on the COBECA error function, developed to enhance accuracy beyond what RMSE and MAE offer. By capturing both high-frequency and periodic signal errors, COBECA aims to provide a comprehensive trace error metric that is sensitive to the diverse error dynamics encountered in UAV signal processing. The validation of this RNN cell and the COBECA function will necessitate empirical testing across various datasets to ensure robust performance and the adaptability of the cell to different error characteristics.

8.3.2 *COBECA*

The Convex Optimization-Based Error Correcting Algorithm (COBECA) represents a advancement in the field of autonomy, specifically tailored for the task of trace comparison. COBECA leverages spatial digital signal processing to transform temporal data into a spatial series, enabling the sophisticated application of convex optimization techniques. This process facilitates the precise fitting of ellipsoids to trajectory data within configuration spaces, thus allowing for detailed comparisons of paths. By quantifying deviations in terms of translation, rotation, noise, and scaling, COBECA offers a robust and dynamic tool for analyzing the intricate behaviors of autonomous systems based on their movement patterns. This makes COBECA an indispensable algorithm for ensuring the accuracy and reliability of trajectory data in real-time applications, spanning from autonomous navigation to health device tracking.

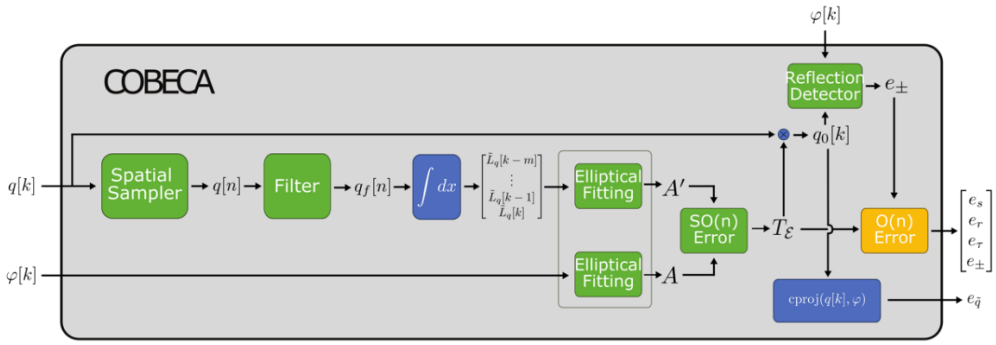

Figure 8-2. A block diagram overview of COBECA highlight four key components. Spatial sampler converts a time series is converted to a "spatial series" with samples evenly spaced in distance. The spatial samples are fed into a spatial filter which spatial noise. These filtered samples are integrated to generate estimates of the distance traveled (a metric of the progress through a path). SO(n) Error block takes these estimates to match the current path to the expected path to estimate the mean rotation and scaling. Reflection detector detects whether reflection is present in the path. Eproj block estimates the perturbation in the path.

Further work is currently underway to validate and enhance the Convex Optimization-Based Error Correcting Algorithm (COBECA). This effort focuses on rigorously testing the algorithm's performance, elucidating its underlying mathematical properties, and demonstrating its broad application spectrum. Specifically, COBECA's ability to accurately derive complex, path-specific GPS errors is being explored to ensure its effectiveness in dynamic environments. Additionally, by encoding the dynamics of motion within the error components, COBECA can be integrated into a Recurrent Neural Network (RNN). This integration allows for the correction of motion-derived inaccuracies, such as changes in the angle of a GPS antenna during maneuvers like turns or alterations in a drone's flight path. This advanced capability enhances the precision of trajectory tracking and navigation systems, making COBECA a crucial tool for improving the reliability and functionality of autonomous technologies.

8.3.3 *Frame-embedded sensors and long-term integration with PATHFINDER*

A subsequent research phase aims to integrate Fiber Bragg Grating (FBG) sensors into the sensor fusion matrix of UAV navigation systems, capitalizing on the precision strain and stress data to refine localization techniques. By correlating the physical deformations captured by FBGs with the aircraft's spatial orientation and movement, we envision a novel approach to enhance both outdoor and indoor localization. The integration of this data with existing GPS and IMU sensors could lead to significant improvements in localization accuracy, potentially unlocking new

applications for UAVs in environments where traditional navigation systems are less effective. While work was done developing the EXFF framework in this thesis, additional work must be done to integrate different sensor-hardware systems. Work has been done to build and assemble IMU daughter cards and an integrated central carrier board. Future work would include a hardware study, and integration with the algorithms developed based on the work discussed in this thesis.

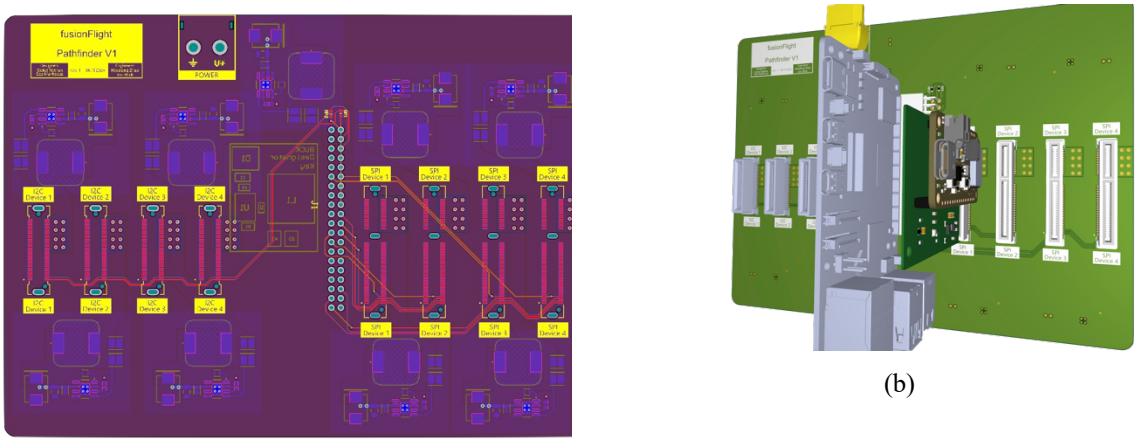

(a) (b)

Figure 8-3. Integrated central carrier board designed during research study. (a) X-ray view of the carrier board PCB layout, with top layer connections in red. The Ports are based on the PCIe express m.2 connector standard, with the traces connecting to different SPI and I2C ports on a raspberry Pi computer. (b) A 3D model of the assembled central carrier board with the IMU daughter card attached.

8.3.4 *Inertial navigation sensors and PATHFINDER*

While the current model relies solely on GPS data, a more robust model may be developed integrating IMU data. The scalable architecture of our model facilitates the inclusion of additional parameters such as accelerometer, gyroscope, barometer, and magnetometer data. This potential improvement represents a significant avenue for future research, which I plan to pursue immediately at the onset of my PhD studies. The incorporation of these diverse sensor inputs is expected to mitigate the limitations of relying exclusively on GPS data by providing a more comprehensive dataset for modeling drone behavior, especially in complex environmental conditions. This approach will aim to improve the accuracy and reliability of localization algorithms, aligning with the broader goals of advancing drone navigation technologies.

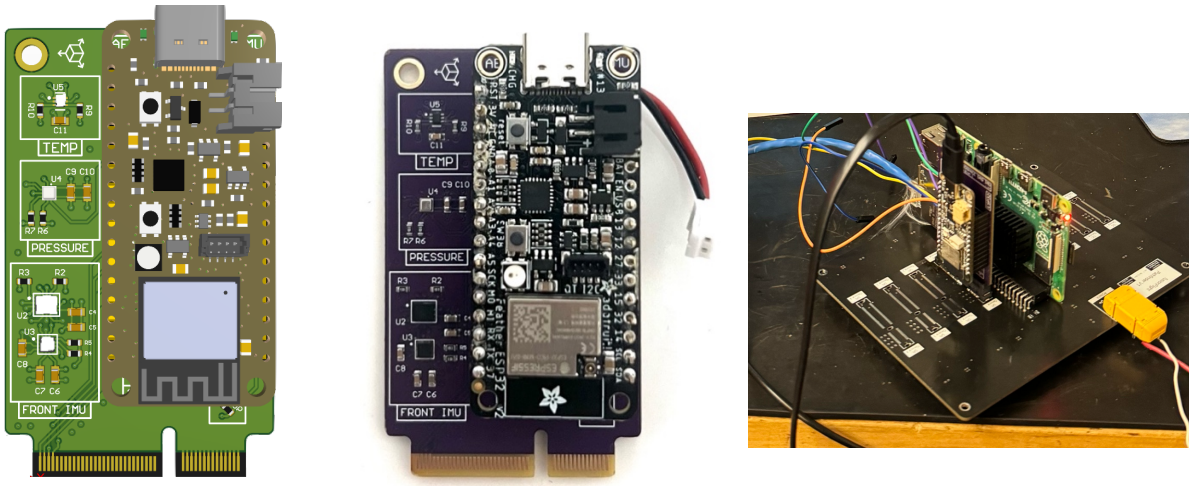

(a) (b) (c)

Figure 8-4.(a) IMU PCB model; (b) assembled IMU board. Additional testing is to be carried out to investigate the inclusion of IMU data to augment GPS positioning accuracy. (c) IMU board attached to a partially assembled CCB for testing.

8.3.5 *R-sensors*

R-sensors build upon the foundational work accomplished in the GPS POD, utilizing insights from the r-selection ecological strategy to optimize the deployment across distributed sensor networks [223].This approach involves integrating a wide array of sensors, both on and off the vehicle, to form a composite network that delivers high-resolution insights into system states under varying conditions, significantly enhancing sensing techniques for Urban Air Mobility (UAM). In my ongoing research, I aim to leverage this methodology in conjunction with embedded Fiber Bragg Grating (FBG) sensors for stress and strain monitoring, creating a distributed system that not only tracks drone activities but also the specific actions of each drone component. This comprehensive data collection facilitates the development of composite models that are not only accurate and swift but also grounded in explainable physical and statistical phenomena, thereby advancing our understanding and control of UAV systems in complex operational environments.

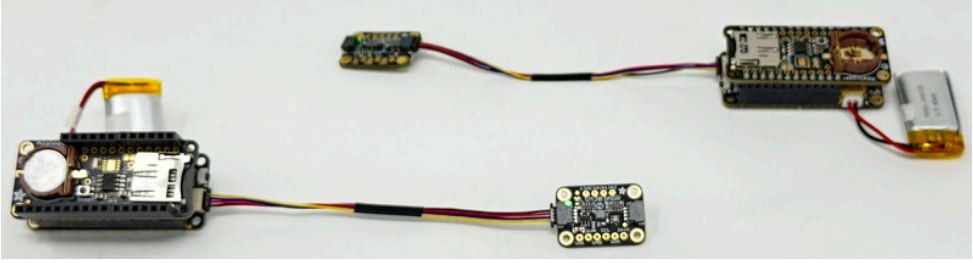

Figure 8-5. A pair of basic test R-sensor module with IMU and magnetometer attached.

8.4 FUTURE COMMERCIALIZATION WORK

As we advance from theoretical exploration to commercial application, our engagement with the National Science Foundation's Innovation Corps (I-Corps) program marks a crucial transition. Our participation will focus on the GPS Data Acquisition (DAQ) system, which has demonstrated significant promise in enhancing the accuracy and reliability of UAV localization in urban settings. Through I-Corps, we aim to validate the market viability of the GPS DAQ system, identify potential customer segments, refine the value proposition based on stakeholder feedback, and develop a sustainable business model that addresses all aspects of production, distribution, and support. This process will expand our industry network, enhance our team's entrepreneurial skills, and ultimately contribute to the growth of the urban air mobility ecosystem. The PATHFINDER project, which integrates a GPS carrier card with a backplane flight computer, is another focus area. Here, more experimentation, design, and analysis are needed to optimize performance and ensure system reliability under diverse operational conditions. These initiatives are expected to propel our technology from lab to market, ensuring that our research has a tangible impact on the field and remains aligned with industry needs and challenges.

BIBLIOGRAPHY

[1] Federal Aviation Administration, 'Advanced Air Mobility Implementation Plan', Washington D.C., AAM-I28, Jul. 2023.

[2] United States Congress, *National Drone and Advanced Air Mobility Initiative Act*. 2022[Online]. Availablehttps://www.congress.gov/bill/117th-congress/house-bill/9376/text?s=1&r=65.

[3] M. Wiedemann et al., 'Advanced Air Mobility: A comparative review of policies from around the world—lessons for Australia', *Transportation Research Interdisciplinary Perspectives*, vol. 24, p. 100988, Mar. 2024 [Online]. Available: 10.1016/j.trip.2023.100988.

[4] S. Mishra and P. Palanisamy, 'Autonomous Advanced Aerial Mobility—An End-to-End Autonomy Framework for UAVs and Beyond', *IEEE Access*, vol. 11, pp. 136318–136349, 2023 [Online]. Available: 10.1109/ACCESS.2023.3339631.

[5] T. G. Reid and A. Neish, 'Localization & mapping requirements for level 2+ autonomous vehicles', presented at the Proceedings of the 2023 International Technical Meeting of The Institute of Navigation, 2023, pp. 107–123.

[6] S. Bijjahalli et al., 'GNSS Performance Modelling and Augmentation for Urban Air Mobility', *Sensors*, vol. 19, no. 19, p. 4209, Sep. 2019 [Online]. Available: 10.3390/s19194209.

[7] M. Hussein et al., 'Key technologies for safe and autonomous drones', *Microprocessors and Microsystems*, vol. 87, p. 104348, Nov. 2021 [Online]. Available: 10.1016/j.micpro.2021.104348.

[8] F. Jametoni and D. E. Saputra, 'A Study on Autonomous Drone Positioning Method', in *2021 Sixth International Conference on Informatics and Computing (ICIC)*, 2021, pp. 1–5 [Online]. Available: 10.1109/ICIC54025.2021.9632926.

[9] F. Al-Turjman, 'A novel approach for drones positioning in mission critical applications', *Transactions on Emerging Telecommunications Technologies*, vol. 33, no. 3, p. e3603, 2022.

[10] E. Anyaegbu and P. Hansen, 'GNSS Performance Evaluation for Deep Urban Environments using GNSS Foresight', in *Proceedings of the 35th International Technical Meeting of the Satellite Division of The Institute of Navigation (ION GNSS+ 2022)*, 2022, pp. 1127–1136.

[11] A. Elmezayen et al., 'Examining the Capabilities of Smartphone-Based High Precision Positioning in Challenging Suburban Environments', in *Proceedings of the 35th International Technical Meeting of the Satellite Division of The Institute of Navigation (ION GNSS+ 2022)*, 2022, pp. 2329–2338.

[12] S. Gupta et al., 'Designing Deep Neural Networks for Sequential GNSS Positioning', in *Proceedings of the 35th International Technical Meeting of the Satellite Division of The Institute of Navigation (ION GNSS+ 2022)*, 2022, pp. 1209–1219.

[13] Z. Kassas et al., '2022 ION GNSS+ Paper: Protecting the Skies: GNSS-less Aircraft Navigation with Terrestrial Cellular Signals of Opportunity.', in *Proceedings of the 35th International Technical Meeting of the Satellite Division of The Institute of Navigation (ION GNSS+ 2022)*, 2022.

[14] X. Bai et al., ‘Time-Correlated Window-Carrier-Phase-Aided GNSS Positioning Using Factor Graph Optimization for Urban Positioning’, *IEEE Trans. Aerosp. Electron. Syst.*, vol. 58, no. 4, pp. 3370–3384, Aug. 2022 [Online]. Available: 10.1109/TAES.2022.3149730.
[15] K. Gamagedara et al., ‘Quadrotor State Estimation With IMU and Delayed Real-Time Kinematic GPS’, *IEEE Transactions on Aerospace and Electronic Systems*, vol. 57, no. 5, pp. 2661–2673, Oct. 2021 [Online]. Available: 10.1109/TAES.2021.3061795.
[16] X. Liu et al., ‘Instantaneous GNSS Ambiguity Resolution and Attitude Determination via Riemannian Manifold Optimization’, *IEEE Trans. Aerosp. Electron. Syst.*, vol. 59, no. 3, pp. 3296–3312, Jun. 2023 [Online]. Available: 10.1109/TAES.2022.3223330.
[17] A. H. -P. Chu et al., ‘GPS Multireceiver Direct Position Estimation for Aerial Applications’, *IEEE Transactions on Aerospace and Electronic Systems*, vol. 56, no. 1, pp. 249–262, Feb. 2020 [Online]. Available: 10.1109/TAES.2019.2915393.
[18] N. Sokhandan et al., ‘High resolution GNSS delay estimation for vehicular navigation utilizing a doppler combining technique’, *The Journal of Navigation*, vol. 67, no. 4, pp. 579–602, 2014.
[19] Y. Gao et al., ‘Analysis of multipath parameter estimation accuracy in MEDLL algorithm’, presented at the China Satellite Navigation Conference (CSNC) 2013 Proceedings: BeiDou/GNSS Navigation Applications• Test & Assessment Technology• User Terminal Technology, 2013, pp. 597–606.
[20] S. Rougerie et al., ‘A New Multipath Mitigation Method for GNSS Receivers Based on an Antenna Array.’, *International Journal of Navigation & Observation*, 2012.
[21] R. L. Fante and J. J. Vaccaro, ‘Evaluation and reduction of multipath-induced bias on GPS time-of-arrival’, *IEEE Transactions on Aerospace and Electronic Systems*, vol. 39, no. 3, pp. 911–920, 2003.
[22] A. Van Dierendonck and M. S. Braasch, ‘Evaluation of GNSS receiver correlation processing techniques for multipath and noise mitigation’, presented at the Proceedings of the 1997 National Technical Meeting of The Institute of Navigation, 1997, pp. 207–215.
[23] R. D. Van Nee, ‘Multipath effects on GPS code phase measurements’, *Navigation*, vol. 39, no. 2, pp. 177–190, 1992.
[24] F. Zangenehnejad and Y. Gao, ‘GNSS smartphones positioning: Advances, challenges, opportunities, and future perspectives’, *Satellite navigation*, vol. 2, pp. 1–23, 2021.
[25] C. H. J. Wang et al., ‘Investigation and Modeling of Flight Technical Error (FTE) Associated With UAS Operating With and Without Pilot Guidance’, *IEEE Transactions on Vehicular Technology*, vol. 70, no. 12, pp. 12389–12401, 2021 [Online]. Available: 10.1109/TVT.2021.3117081.
[26] J. Georgy et al., ‘Low-Cost Three-Dimensional Navigation Solution for RISS/GPS Integration Using Mixture Particle Filter’, *IEEE Transactions on Vehicular Technology*, vol. 59, no. 2, pp. 599–615, Feb. 2010 [Online]. Available: 10.1109/TVT.2009.2034267.
[27] M. A. Quddus et al., ‘Current map-matching algorithms for transport applications: State-of-the art and future research directions’, *Transportation Research Part C: Emerging Technologies*, vol. 15, no. 5, pp. 312–328, Oct. 2007 [Online]. Available: 10.1016/j.trc.2007.05.002.
[28] C. Deng et al., ‘Investigation of using Sky openness ratio as predictor for navigation performance in urban-like environment to support PBN in UTM’, *Sensors*, vol. 22, no. 3, p. 840, 2022.

[29] D. Grejner-Brzezinska et al., ‘On improving navigation accuracy of GPS/INS systems’, *Photogrammetric engineering & remote sensing*, vol. 71, no. 4, pp. 377–389, 2005.
[30] D. Sathyamorthy et al., ‘EVALUATION OF THE ACCURACY OF GLOBAL POSITIONING SYSTEM (GPS) SPEED MEASUREMENT VIA GPS SIMULATION.’, *Defence S&T Technical Bulletin*, vol. 8, no. 2, 2015.
[31] O. G. Crespillo et al., ‘Tightly coupled GNSS/INS integration based on robust M-estimators’, in *2018 IEEE/ION Position, Location and Navigation Symposium (PLANS)*, 2018, pp. 1554–1561.
[32] P. Cao et al., ‘Mission-Oriented Trajectory Optimization for Search-and-Rescue Multirotor UAVs in Cluttered and GPS-Denied Environments’, in *AIAA AVIATION 2022 Forum*, 2022, p. 3999.
[33] M. R. Fernandes et al., ‘GNSS/MEMS-INS Integration for Drone Navigation Using EKF on Lie Groups’, *IEEE Trans. Aerosp. Electron. Syst.*, vol. 59, no. 6, pp. 7395–7408, Dec. 2023 [Online]. Available: 10.1109/TAES.2023.3290575.
[34] McKinsey & Company, ‘Drones take to the sky, potentially disrupting last-mile delivery’. [Online]. Availablehttps://www.mckinsey.com/industries/aerospace-and-defense/our-insights/future-air-mobility-blog/drones-take-to-the-sky-potentially-disrupting-last-mile-delivery[Accessed: 19November2023].
[35] McKinsey & Company, (May. 05, 2023), ‘Solving the “last-meter” challenge in drone delivery’. [Online]. Availablehttps://www.mckinsey.com/industries/aerospace-and-defense/our-insights/future-air-mobility-blog/solving-the-last-meter-challenge-in-drone-delivery#.
[36] Markets and Markets, ‘Drone Sensor Market by Sensor Type, platform type, application (navigation, collision, detection and avoidance, data acquisition, motion detection, air pressure measurement), and user industry and geography – global forecast 2023’, Jan. 2018[Online]. Availablehttps://www.marketsandmarkets.com/Market-Reports/drone-sensor-market-241127051.html.
[37] Precedence Research, ‘Sensor Fusion Market (By Technology: Mems, Non – Mems; By Product Type: Radar Sensors, Image Sensors, IMU, Temp Sensors; By End User: Consumers Electronics, Automotive, Home Automation, Medical, Military, Industrial) - Global Industry Analysis, Size, Share, Growth, Trends, Regional Outlook, and Forecast 2023-2032’, Jan. 2023[Online]. Availablehttps://www.precedenceresearch.com/sensor-fusion-market#:~:text=The%20global%20sensor%20fusion%20market,forecast%20period%202023%20to%202032.
[38] A. W. Sudbury and E. B. Hutchinson, ‘A COST ANALYSIS OF AMAZON PRIME AIR (DRONE DELIVERY)’.
[39] Levitate Capital, ‘The Future of the Drone Economy’, White Paper[Online]. Availablehttps://levitatecap.com/levitate/wp-content/uploads/2020/12/White-Paper-v4.pdf.
[40] L. A. Haidari et al., ‘The economic and operational value of using drones to transport vaccines’, *Vaccine*, vol. 34, no. 34, pp. 4062–4067, 2016 [Online]. Available: https://doi.org/10.1016/j.vaccine.2016.06.022.
[41] S. A. H. Mohsan et al., ‘Unmanned aerial vehicles (UAVs): practical aspects, applications, open challenges, security issues, and future trends’, *Intel Serv Robotics*, Jan.

2023[Online]. Availablehttps://link.springer.com/10.1007/s11370-022-00452-4[Accessed: 19November2023].
[42] R. Depaola et al., 'Uav navigation with computer vision–flight testing a novel visual odometry technique', presented at the 2018 AIAA Guidance, Navigation, and Control Conference, 2018, p. 2102.
[43] Y. Alkendi et al., 'State of the Art in Vision-Based Localization Techniques for Autonomous Navigation Systems', *IEEE Access*, vol. 9, pp. 76847–76874, 2021 [Online]. Available: 10.1109/ACCESS.2021.3082778.
[44] A. Couturier and M. A. Akhloufi, 'A review on absolute visual localization for UAV', *Robotics and Autonomous Systems*, vol. 135, p. 103666, 2021.
[45] B. Li et al., 'Analysis of automotive camera sensor noise factors and impact on object detection', *IEEE Sensors Journal*, vol. 22, no. 22, pp. 22210–22219, 2022.
[46] L. Chen et al., 'Robustness, security and privacy in location-based services for future IoT: A survey', *Ieee Access*, vol. 5, pp. 8956–8977, 2017.
[47] Y. Pan et al., 'An unmanned aerial vehicle navigation mechanism with preserving privacy', presented at the ICC 2019-2019 IEEE International Conference on Communications (ICC), 2019, pp. 1–6.
[48] D. Caveney, 'Cooperative vehicular safety applications', *IEEE Control Systems Magazine*, vol. 30, no. 4, pp. 38–53, 2010.
[49] M. Elsheikh et al., 'Integration of GNSS precise point positioning and reduced inertial sensor system for lane-level car navigation', *IEEE Transactions on Intelligent Transportation Systems*, vol. 23, no. 3, pp. 2246–2261, 2020.
[50] R. Reynaud and G. S. Seetharaman, 'Embedded Systems for Intelligent Vehicles'.
[51] J.-S. Um and J.-S. Um, 'Location sensors', *Drones as Cyber-Physical Systems: Concepts and Applications for the Fourth Industrial Revolution*, pp. 143–176, 2019.
[52] D. B. Barber et al., 'Autonomous landing of miniature aerial vehicles', *Journal of Aerospace Computing, Information, and Communication*, vol. 4, no. 5, pp. 770–784, 2007.
[53] R. Abeyratne, 'Convention on international civil aviation', *A Commentary, Switzerland*, 2014.
[54] P. Fontaine, 'Urban Air Mobility (UAM) Concept of Operations 2.0', Federal Aviation Administration, Apr. 2023[Online]. Availablehttps://www.faa.gov/sites/faa.gov/files/Urban%20Air%20Mobility%20%28UAM%29%20Concept%20of%20Operations%202.0_0.pdf[Accessed: 11March2024].
[55] K. H. Low, 'Framework for Urban Traffic Management of Unmanned Aircraft System (UTM-UAS)', presented at the Singapore: ICAO. Available online: https://www. icao. int/Meetings/UAS2017/Documents/KimHuatLo_Singapore_UTM_Day1. pdf (accessed on 5 May 2022), 2017.
[56] J. Cho and Y. Yoon, 'How to assess the capacity of urban airspace: A topological approach using keep-in and keep-out geofence', *Transportation Research Part C: Emerging Technologies*, vol. 92, pp. 137–149, 2018.
[57] S. Watkins et al., 'Ten questions concerning the use of drones in urban environments', *Building and Environment*, vol. 167, p. 106458, 2020.
[58] A. Mohamed et al., 'Gusts encountered by flying vehicles in proximity to buildings', *Drones*, vol. 7, no. 1, p. 22, 2023.

[59] S. Giersch et al., ‘Atmospheric flow simulation strategies to assess turbulent wind conditions for safe drone operations in urban environments’, *Journal of Wind Engineering and Industrial Aerodynamics*, vol. 229, p. 105136, 2022.
[60] A. Bauranov and J. Rakas, ‘Urban air mobility and manned eVTOLs: safety implications’, in *2019 IEEE/AIAA 38th Digital Avionics Systems Conference (DASC)*, 2019, pp. 1–8 [Online]. Available: 10.1109/DASC43569.2019.9081685.
[61] Federal Aviation Administration, *Consolidated Wake Turbulence (CWT)*. 2021[Online]. Availablehttps://www.faa.gov/documentLibrary/media/Order/2021-11-08_JO_7110.126B_Consolidated_Wake_Turbulence__FINAL.pdf.
[62] Y. Lin and S. Saripalli, ‘Sampling-Based Path Planning for UAV Collision Avoidance’, *IEEE Transactions on Intelligent Transportation Systems*, vol. 18, no. 11, pp. 3179–3192, Nov. 2017 [Online]. Available: 10.1109/TITS.2017.2673778.
[63] D. Geister and B. Korn, ‘Density based Management Concept for Urban Air Traffic’, in *2018 IEEE/AIAA 37th Digital Avionics Systems Conference (DASC)*, 2018, pp. 1–9 [Online]. Available: 10.1109/DASC.2018.8569491.
[64] M. G. Wu et al., ‘Well clear trade study for unmanned aircraft system detect and avoid with non-cooperative aircraft’, presented at the 2018 Aviation Technology, Integration, and Operations Conference, 2018, p. 2876.
[65] A. Famili et al., ‘PILOT: High-Precision Indoor Localization for Autonomous Drones’, *IEEE Transactions on Vehicular Technology*, vol. 72, no. 5, pp. 6445–6459, May 2023 [Online]. Available: 10.1109/TVT.2022.3229628.
[66] J. Yousaf et al., ‘Drone and Controller Detection and Localization: Trends and Challenges’, *Applied Sciences*, vol. 12, no. 24, p. 12612, Dec. 2022 [Online]. Available: 10.3390/app122412612.
[67] A. Bauranov and J. Rakas, ‘Designing airspace for urban air mobility: A review of concepts and approaches’, *Progress in Aerospace Sciences*, vol. 125, p. 100726, Aug. 2021 [Online]. Available: 10.1016/j.paerosci.2021.100726.
[68] M. Doole et al., ‘Constrained Urban Airspace Design for Large-Scale Drone-Based Delivery Traffic’, *Aerospace*, vol. 8, no. 2, p. 38, Feb. 2021 [Online]. Available: 10.3390/aerospace8020038.
[69] D. Geister and B. Korn, ‘Concept for urban airspace integration DLR U-Space blueprint’, *German Aerospace Center-Institut of Flight Guidance*, 2017.
[70] P. D. Vascik and R. J. Hansman, ‘Scaling constraints for urban air mobility operations: Air traffic control, ground infrastructure, and noise’, presented at the 2018 aviation technology, integration, and operations conference, 2018, p. 3849.
[71] B. Rao et al., ‘The societal impact of commercial drones’, *Technology in society*, vol. 45, pp. 83–90, 2016.
[72] C. Al Haddad et al., ‘Factors affecting the adoption and use of urban air mobility’, *Transportation research part A: policy and practice*, vol. 132, pp. 696–712, 2020.
[73] Y. Wang et al., ‘Flying eyes and hidden controllers: A qualitative study of people’s privacy perceptions of civilian drones in the US’, *Proceedings on Privacy Enhancing Technologies*, 2016.
[74] S. Park and K. Lee, ‘Developing criteria for invasion of privacy by personal drone’, presented at the 2017 International Conference on Platform Technology and Service (PlatCon), 2017, pp. 1–7.

[75] P. Nysten, ‘Radio Wave Propagation from LOS to Street-Level in an Urban Area’, Royal Institute of Technology, Stockholm, Sweden, 2015.
[76] G. Zhang and L. Hsu, ‘Performance assessment of GNSS diffraction models in urban areas’, *Navigation*, vol. 68, no. 2, pp. 369–389, 2021.
[77] J. Meguro et al., ‘GPS multipath mitigation for urban area using omnidirectional infrared camera’, *IEEE Transactions on Intelligent Transportation Systems*, vol. 10, no. 1, pp. 22–30, 2009.
[78] D. Weng et al., ‘Characterization and mitigation of urban GNSS multipath effects on smartphones’, *Measurement*, vol. 223, p. 113766, 2023.
[79] M. Wildemeersch et al., ‘Acquisition of GNSS signals in urban interference environment’, *IEEE Transactions on Aerospace and Electronic Systems*, vol. 50, no. 2, pp. 1078–1091, 2014.
[80] A. Siemuri et al., ‘A Systematic Review of Machine Learning Techniques for GNSS Use Cases’, *IEEE Trans. Aerosp. Electron. Syst.*, vol. 58, no. 6, pp. 5043–5077, Dec. 2022 [Online]. Available: 10.1109/TAES.2022.3219366.
[81] A. Soloviev and D. Venable, ‘Integration of GPS and vision measurements for navigation in GPS challenged environments’, presented at the IEEE/ION Position, Location and Navigation Symposium, 2010, pp. 826–833.
[82] M. Majoral et al., ‘Implementation of GNSS Receiver Hardware Accelerators in All-programmable System-On-Chip Platforms’, presented at the Proceedings of the 31st International Technical Meeting of the Satellite Division of The Institute of Navigation (ION GNSS+ 2018), 2018, pp. 4215–4230.
[83] T. Tsujii et al., ‘GNSS Array Antenna for Mitigating Multipath Errors in Urban Environment’, presented at the E3S Web of Conferences, 2019, vol. 94, p. 03009.
[84] S. Gupta, ‘HIGH-INTEGRITY URBAN LOCALIZATION: BRINGING SAFETY IN AVIATION TO AUTONOMOUS DRIVING’, STANFORD UNIVERSITY.
[85] N. Sünderhauf and P. Protzel, ‘Towards robust graphical models for GNSS-based localization in urban environments’, presented at the International Multi-Conference on Systems, Signals & Devices, 2012, pp. 1–6.
[86] H. Pesonen, ‘Robust estimation techniques for GNSS positioning’, presented at the Proceedings of NAV07-The Navigation Conference and Exhibition, 2007, vol. 31, no. 1.11, p. 2007.
[87] K. Amer et al., ‘Convolutional neural network-based deep urban signatures with application to drone localization’, presented at the Proceedings of the IEEE International Conference on Computer Vision Workshops, 2017, pp. 2138–2145.
[88] J. Wang and J. Luo, ‘No Perfect Outdoors: Towards a Deep Profiling of GNSS-Based Location Contexts’, *Future Internet*, vol. 14, no. 1, 2022[Online]. Availablehttps://www.mdpi.com/1999-5903/14/1/7.
[89] C. H. Chen and R. S. Cheng, ‘Improving Indoor Localization Based on Artificial Neural Network Technology’, *EAI Endorsed Transactions on Internet of Things*, vol. 4, no. 16, pp. e5–e5, 2018.
[90] L. K. L. Tan et al., ‘Public acceptance of drone applications in a highly urbanized environment’, *Technology in Society*, vol. 64, p. 101462, 2021.
[91] R. Jain et al., ‘Towards a smarter surveillance solution: The convergence of smart city and energy efficient unmanned aerial vehicle technologies’, *Development and Future of Internet of Drones (IoD): Insights, Trends and Road Ahead*, pp. 109–140, 2021.

[92] ICAO, ‘Global Navigation Satellite Sysem (GNSS) Manual’. International Civil Aviation Organization, 2005[Online]. Availablehttps://www.icao.int/Meetings/PBN-Symposium/Documents/9849_cons_en%5B1%5D.pdf.
[93] Federal Aviation Administration, ‘Policy Statement for the Reported Geometric Altitude of the Control Station of a Standard Remote Identification Unmanned Aircraft’, Federal Aviation Administration, FAA-2019-1100-53294, Nov. 2021[Online]. Availablehttps://www.regulations.gov/document/FAA-2019-1100-53294.
[94] International Civil Aviation Organization, Ed., *Performance-based navigation (PBN) manual*, 3rd. ed. Montreal: ICAO, 2008.
[95] Y. Xu and W. Chen, ‘Performance Analysis of GPS/BDS Dual/Triple-Frequency Network RTK in Urban Areas: A Case Study in Hong Kong’, *Sensors*, vol. 18, no. 8, 2018 [Online]. Available: 10.3390/s18082437.
[96] C. Savas et al., ‘A comparative performance analysis of GPS L1 C/A, L5 acquisition and tracking stages under polar and equatorial scintillations’, *IEEE Transactions on Aerospace and Electronic Systems*, vol. 57, no. 1, pp. 227–244, 2020.
[97] R. Odolinski and P. J. G. Teunissen, ‘Best integer equivariant estimation: performance analysis using real data collected by low-cost, single- and dual-frequency, multi-GNSS receivers for short- to long-baseline RTK positioning’, *J Geod*, vol. 94, no. 9, p. 91, Sep. 2020 [Online]. Available: 10.1007/s00190-020-01423-2.
[98] Z. Nie et al., ‘Real-time precise point positioning with a low-cost dual-frequency GNSS device’, *GPS Solut*, vol. 24, no. 1, p. 9, Jan. 2020 [Online]. Available: 10.1007/s10291-019-0922-3.
[99] B. Karki and M. Won, ‘Characterizing Power Consumption of Dual-Frequency GNSS of a Smartphone’, in *GLOBECOM 2020 - 2020 IEEE Global Communications Conference*, 2020, pp. 1–6[Online]. Availablehttp://arxiv.org/abs/1910.13041[Accessed: 27January2024].
[100] Shinn Yan Lin and Z. Jiang, ‘GPS all in view time comparison using multi-receiver ensemble’, in *2017 Joint Conference of the European Frequency and Time Forum and IEEE International Frequency Control Symposium (EFTF/IFCS)*, Besancon, 2017, pp. 362–365[Online]. Availablehttps://ieeexplore.ieee.org/document/8088892/[Accessed: 27January2024].
[101] L. Heng et al., ‘Reliable GPS-based timing for power systems: A multi-layered multi-receiver architecture’, in *2014 Power and Energy Conference at Illinois (PECI)*, Champaign, IL, USA, 2014, pp. 1–7[Online]. Availablehttp://ieeexplore.ieee.org/document/6804565/[Accessed: 27January2024].
[102] N. Stenberg et al., ‘Results on GNSS Spoofing Mitigation Using Multiple Receivers’, *navi*, vol. 69, no. 1, p. navi.510, 2022 [Online]. Available: 10.33012/navi.510.
[103] D. Dhahbane et al., ‘Robust attitude estimation for an unmanned aerial vehicle using multiple GPS receivers’, *Proceedings of the Institution of Mechanical Engineers, Part G: Journal of Aerospace Engineering*, vol. 236, no. 16, pp. 3540–3553, Dec. 2022 [Online]. Available: 10.1177/09544100221089220.
[104] S. K. Pagoti and S. I. D. Vemuri, ‘Development and performance evaluation of Correntropy Kalman Filter for improved accuracy of GPS position estimation’, *International Journal of Intelligent Networks*, vol. 3, pp. 1–8, 2022 [Online]. Available: 10.1016/j.ijin.2022.01.002.

[105] ArduPilot Dev Team, 'GPS Blending (aka Dual GPS)', Manual ROVER 4,4.0, Jan. 2024[Online]. Availablehttps://ardupilot.org/copter/docs/common-gps-blending.html.
[106] S. Gopinath, 'GPS power savings using low power sensors', Dec. 2011.
[107] P. d'Harcourt et al., 'Improving Accuracy and Algorithm Integrity for Train Localization in Harsh Urban Environments Using GNSS Time-Difference Carrier-Phase Displacement and GNSS Map-Modulation with Inertial Navigation Over Hundreds of Hours of Real-Life Data', in *Proceedings of the 36th International Technical Meeting of the Satellite Division of The Institute of Navigation (ION GNSS+ 2023)*, 2023, pp. 2270–2281.
[108] O. K. Isik et al., 'Integrity Analysis for GPS-Based Navigation of UAVs in Urban Environment', *Robotics*, vol. 9, no. 3, 2020 [Online]. Available: 10.3390/robotics9030066.
[109] D.-K. Lee et al., 'Android GNSS/INS Using Complementary Filter', in *Proceedings of the 36th International Technical Meeting of the Satellite Division of The Institute of Navigation (ION GNSS+ 2023)*, 2023, pp. 2644–2652.
[110] A. V. Kanhere et al., 'Improving GNSS Positioning using Neural Network-based Corrections'. arXiv, Jun. 21, 2022[Online]. Availablehttp://arxiv.org/abs/2110.09581[Accessed: 20November2023].
[111] A. Mohanty and G. Gao, 'Learning GNSS positioning corrections for smartphones using graph convolution neural networks', *NAVIGATION: Journal of the Institute of Navigation*, vol. 70, no. 4, 2023.
[112] C. Bell, 'FusionFLight UW - iCorp Interview 11', Jan. 30, 2024.
[113] M. Alkeryd, 'Evaluation of position sensing techniques for an unmanned aerial vehicle', Linköpings universitet, Linköping, Sweden, 2006[Online]. Availablehttps://www.diva-portal.org/smash/get/diva2:21740/FULLTEXT01.pdf.
[114] C. Eling et al., 'Real-Time Single-Frequency GPS/MEMS-IMU Attitude Determination of Lightweight UAVs', *Sensors*, vol. 15, no. 10, pp. 26212–26235, 2015 [Online]. Available: 10.3390/s151026212.
[115] S. J. Comstock, 'Development of a low-latency, high data rate, differential gps relative positioning system for uav formation flight control', 2006.
[116] F. M. Lambert, Apr. 05, 2024.
[117] US Space Force, (2022, June.28), *Space Segment*. [Online]. Available: https://www.gps.gov/systems/gps/space/. [Accessed: 22 Jan. 2024].
[118] V. K. Abdrakhmanov et al., 'Research of the Implementation Possibility of the Precise GPS Positioning Technology', presented at the 2021 International Ural Conference on Electrical Power Engineering (UralCon), 2021, pp. 234–238.
[119] P. Das et al., 'Performance limits of GNSS code-based precise positioning: GPS, galileo & meta-signals', *Sensors*, vol. 20, no. 8, p. 2196, 2020.
[120] P. de T. S. Júnior et al., 'Multi-GNSS positioning', *Rev. Bras. Cartogr*, vol. 72, no. 50th, 2020.
[121] R. T. Anthony and R. M. Kerns, 'IS-GPS-200N'.
[122] US Space Force, 'L1 C/A PRN CODE ASSIGNMENTS', US SPACE FORCE, PRN CODE IS-GPS-200, Apr. 2023[Online]. Availablehttps://www.gps.gov/technical/prn-codes/L1-CA-PRN-code-assignments-2023-Apr.pdf.
[123] G. Blewitt, 'Basics of the GPS technique: observation equations', *Geodetic applications of GPS*, vol. 1, p. 46, 1997.

[124] P. A. Zandbergen and S. J. Barbeau, ‘Positional Accuracy of Assisted GPS Data from High-Sensitivity GPS-enabled Mobile Phones’, *J. Navigation*, vol. 64, no. 3, pp. 381–399, Jul. 2011 [Online]. Available: 10.1017/S0373463311000051.
[125] Christopher Hegarty and Elliott Kaplan, *Understanding GPS Principles and Applications, Second Edition*. Artech, 2005[Online]. Availablehttp://ieeexplore.ieee.org/document/9106073.
[126] H. Arneja et al., ‘Solving the GPS Equations’. George Mason University[Online]. Availablehttps://mason.gmu.edu/ treid5/Math447/GPSEquations/.
[127] J.-M. Zogg, ‘GPS basics’, *Switzerland: u-blox*, 2002.
[128] K. Madhu et al., ‘New Multi-Step Iterative Methods for Solving Systems of Nonlinear Equations and Their Application on GNSS Pseudorange Equations’, *Sensors*, vol. 20, no. 21, 2020 [Online]. Available: 10.3390/s20215976.
[129] N. Sirola, *Mathematical methods for personal positioning and navigation*. Tampere University of Technology, 2007.
[130] K. W. Alter, ‘USING WIDE AREA DIFFERENTIAL GPS TO IMPROVE TOTAL SYSTEM ERROR FOR PRECISION FLIGHT OPERATIONS’, STANFORD UNIVERSITY, Palo Alto, CA, 2000[Online]. Availablehttps://web.stanford.edu/group/scpnt/gpslab/pubs/theses/KeithAlterThesis00.pdf.
[131] A. Michalski and J. Czajewski, ‘The accuracy of the global positioning systems’, *IEEE Instrumentation & Measurement Magazine*, vol. 7, no. 1, pp. 56–60, 2004.
[132] M. G. Wing and J. Frank, ‘Vertical measurement accuracy and reliability of mapping-grade GPS receivers’, *Computers and electronics in agriculture*, vol. 78, no. 2, pp. 188–194, 2011.
[133] W.-S. Chan et al., ‘Assessment of dynamic measurement accuracy of GPS in three directions’, *Journal of surveying engineering*, vol. 132, no. 3, pp. 108–117, 2006.
[134] National Marine Electronics Association (U.S.), ‘NMEA 0183--Standard for interfacing marine electronic devices’. NMEA, [New Bern, North Carolina], 2002.
[135] F. Andert et al., ‘A flight state estimator that combines stereo-vision, INS, and satellite pseudo-ranges’, presented at the Advances in Aerospace Guidance, Navigation and Control: Selected Papers of the Second CEAS Specialist Conference on Guidance, Navigation and Control, 2013, pp. 277–296.
[136] A. Grenier et al., ‘Towards Smarter Positioning through Analyzing Raw GNSS and Multi-Sensor Data from Android Devices: A Dataset and an Open-Source Application’, *Electronics*, vol. 12, no. 23, p. 4781, 2023.
[137] L. Bao et al., ‘MT-e&R: NMEA Protocol-Assisted High-Accuracy Navigation Algorithm Based on GNSS Error Estimation Using Multitask Learning’, *IEEE Transactions on Intelligent Transportation Systems*, vol. 23, no. 11, pp. 20464–20475, 2022.
[138] D.-K. Lee et al., ‘Detection of gnss spoofing using nmea messages’, presented at the 2020 European Navigation Conference (ENC), 2020, pp. 1–10.
[139] D. Jagiwala and S. N. Shah, ‘Possibilities of AI Algorithm Execution in GNSS’, presented at the 2022 URSI Regional Conference on Radio Science (USRI-RCRS), 2022, pp. 1–4.
[140] B. Xu et al., ‘Intelligent GPS L1 LOS/Multipath/NLOS Classifiers Based on Correlator-, RINEX- and NMEA-Level Measurements’, *Remote Sensing*, vol. 11, no. 16, 2019[Online]. Availablehttps://www.mdpi.com/2072-4292/11/16/1851.
[141] A. K. Ramavath and N. K. Perumalla, ‘A machine-learning approach to estimate satellite-based position errors’, *Journal of Applied Geodesy*, vol. 18, no. 2, pp. 335–344, 2024.

[142] SiRF Technology, Inc., 'NMEA Reference Manual', San Jose, CA, |1050-0042, Dec. 2007[Online]. Availablehttps://www.sparkfun.com/datasheets/GPS/NMEA%20Reference%20Manual-Rev2.1-Dec07.pdf.
[143] Y. Y. Lin et al., 'Design and implementation of a dual-antenna GPS receiver', *J. Phys.: Conf. Ser.*, vol. 1509, no. 1, p. 012029, Apr. 2020 [Online]. Available: 10.1088/1742-6596/1509/1/012029.
[144] D&D Larix, (Sep. 12, 2018), 'GPS Collection Devices - Resource Analysis'. [Online]. Availablehttp://resource-analysis.com/geospatial/gps-collection-devices/[Accessed: 24April2024].
[145] K. Serr et al., 'Comparing GPS Receivers: A Field Study', vol. 18, no. 2, 2006.
[146] Geomatics Land Surveying and M. Patricia, 'Trimble Geo 7X handheld GNSS system'. 2020[Online]. Availablehttp://www.toserbamarket.com/index.php?route=product%2Fproduct&product_id=271.
[147] T. Center and Electronic Company, 'Trimble GPS GeoExplorer 6000 New'. 2020[Online]. Availablehttp://www.toserbamarket.com/index.php?route=product%2Fproduct&product_id=271.
[148] Missouri Department of Transportation, 'Missouri Department of Natural Resources, Geological Survey and Resource Assessment Division, Land Survey Program'. Feb. 08, 2005[Online]. Availablehttps://oa.mo.gov/sites/default/files/CC-MapGradeGPSARCApp.pdf.
[149] MediaTek, 'MT3339 All-in-One GNSS Datasheet'. MediaTek, 2016[Online]. Availablehttps://cdn.compacttool.ru/downloads/MT3339_Mediatek_Datasheet.pdf.
[150] R. C. W. Jr et al., 'Accuracy Assessment of Recreational and Mapping Grade GPS Receivers', vol. 63, 2009.
[151] G. Lachapelle et al., 'Augmentation of GPS/GLONASS for vehicular navigation under signal masking', presented at the Proceedings of the 10th International Technical Meeting of the Satellite Division of The Institute of Navigation (ION GPS 1997), 1997, pp. 1511–1519.
[152] G. Vyasaraj and S. Vijay, 'An innovative approach to overcome GPS signal masking during maneuvers in aircraft or satellite', presented at the Proceedings of the 20th International Technical Meeting of the Satellite Division of The Institute of Navigation (ION GNSS 2007), 2007, pp. 2999–3007.
[153] G. Novella et al., 'From ICAO GNSS Interference Mask to Jamming Protection Area For Safe Civil Aviation Operation', presented at the 34th International Technical Meeting of the Satellite Division of The Institute of Navigation (ION GNSS+ 2021), St. Louis, Missouri, 2021, pp. 834–854[Online]. Availablehttps://www.ion.org/publications/abstract.cfm?articleID=17936[Accessed: 27January2024].
[154] N. S. Gowdayyanadoddi et al., 'A Ray-Tracing Technique to Characterize GPS Multipath in the Frequency Domain', *International Journal of Navigation and Observation*, vol. 2015, pp. 1–16, Sep. 2015 [Online]. Available: 10.1155/2015/983124.
[155] J.-H. Moon et al., 'Database based Global Positioning System Correction', *The Journal of Korea Robotics Society*, vol. 7, no. 3, pp. 205–215, Aug. 2012 [Online]. Available: 10.7746/jkros.2012.7.3.205.

[156] D. Simon and H. El-Sherief, 'Design of global positioning system receivers for integrated inertial navigation systems', in *Proceedings of 32nd IEEE Conference on Decision and Control*, San Antonio, TX, USA, 1993, pp. 1476–1477[Online]. Availablehttp://ieeexplore.ieee.org/document/325432/[Accessed: 8February2024].
[157] N. Gerrard et al., 'Exploration of Unintentional GNSS RFI Sources: Causes, Occurrence Rates, and Predicted Future Impact', presented at the Proceedings of the 35th International Technical Meeting of the Satellite Division of The Institute of Navigation (ION GNSS+ 2022), 2022, pp. 3925–3934.
[158] M. Scaramuzza et al., 'GNSS RFI detection: Finding the needle in the haystack', presented at the Proceedings of the 28th International Technical Meeting of the Satellite Division of The Institute of Navigation (ION GNSS+ 2015), 2015, pp. 1617–1624.
[159] J. Querol et al., 'Study of RFI signals in protected GNSS bands generated by common electronic devices: Effects on GNSS-R measurements', presented at the 2014 IEEE Geoscience and Remote Sensing Symposium, 2014, pp. 4050–4053.
[160] Y. Quan et al., 'Convolutional neural network based multipath detection method for static and kinematic GPS high precision positioning', *Remote Sensing*, vol. 10, no. 12, p. 2052, 2018.
[161] P. Xu et al., 'PositionNet: CNN-based GNSS positioning in urban areas with residual maps', *Applied Soft Computing*, vol. 148, p. 110882, 2023.
[162] A. V. Kanhere et al., 'Improving gnss positioning using neural-network-based corrections', *NAVIGATION: Journal of the Institute of Navigation*, vol. 69, no. 4, 2022.
[163] S. Gupta and G. X. Gao, 'Reliable GNSS Localization Against Multiple Faults Using a Particle Filter Framework', *arXiv preprint arXiv:2101.06380*, 2021.
[164] S. Gupta and G. X. Gao, 'Reliable urban vehicle localization under faulty satellite navigation signals', *EURASIP Journal on Advances in Signal Processing*, vol. 2024, no. 1, p. 53, Apr. 2024 [Online]. Available: 10.1186/s13634-024-01150-2.
[165] C. Milner and M. Daly, 'CAA PAPER 2007/06 RNAV (GNSS) Non-Precision Approach–Flight Trials Analysis Report'.
[166] United States. Federal Aviation Administration, 'Global Positioning System wide area augmentation system (WAAS) performance standard.', United States. Federal Aviation Administration, USA, Repository & Open Science Access Portal GPS WAAS PS, Oct. 2008[Online]. Availablehttps://rosap.ntl.bts.gov/view/dot/16922[Accessed: 15October2022].
[167] R. Sabatini and G. Palmerini, *Differential global positioning system (DGPS) for flight testing*. The Research and Technology Organisation, 2008.
[168] M. G. Wing and A. Eklund, 'Performance comparison of a low-cost mapping grade global positioning systems (GPS) receiver and consumer grade GPS receiver under dense forest canopy', *Journal of Forestry*, vol. 105, no. 1, pp. 9–14, 2007.
[169] M. Matosevic et al., 'A comparison of accuracy using a GPS and a low-cost DGPS', *IEEE Transactions on Instrumentation and Measurement*, vol. 55, no. 5, pp. 1677–1683, 2006.
[170] Y. Feng and J. Wang, 'GPS RTK performance characteristics and analysis', *Positioning*, vol. 1, no. 13, 2008.
[171] T. Lipecki, 'The modern technologies of DGPS and RTK corrections transfer', *Geomatics and Environmental Engineering*, vol. 1, no. 3, pp. 67–76, 2007.
[172] W. Chen et al., 'Critical issues on GPS RTK operation using Hong Kong GPS active network', *Journal of Geospatial Engineering*, vol. 4, no. 1, pp. 31–40, 2002.

[173] A. Martín et al., ‘PPP technique analysis based on time convergence, repeatability, IGS products, different software processing, and GPS+ GLONASS constellation’, *Journal of Surveying Engineering*, vol. 137, no. 3, pp. 99–108, 2011.
[174] P. Teunissen and A. Khodabandeh, ‘Review and principles of PPP-RTK methods’, *Journal of Geodesy*, vol. 89, no. 3, pp. 217–240, 2015.
[175] R. M. Alkan et al., ‘A comparative study for accuracy assessment of PPP technique using GPS and GLONASS in urban areas’, *Measurement*, vol. 69, pp. 1–8, 2015.
[176] T. Ocalan, ‘Accuracy assessment of GPS precise point positioning (PPP) technique using different web-based online services in a forest environment’, *Šumarski list*, vol. 140, no. 7–8, pp. 357–367, 2016.
[177] M. Kim and J. Kim, ‘GPS-SBAS-Based Orbit Determination for Low Earth Orbiting Satellites’, *International Journal of Aerospace Engineering*, vol. 2023, 2023.
[178] Federal Aviation Association, ‘WIDE AREA AUGMENTATION SYSTEM PERFORMANCE ANALYSIS REPORT’, FAA William J. Hughes Technical Center, Atlantic City International Airport, NJ, 87[Online]. Availablehttps://www.nstb.tc.faa.gov/reports/FAA_WAAS_PAN_Report_87_v1.0.pdf.
[179] G. L. Dillingham, ‘NATIONAL AIRSPACE SYSTEM: Problems Plaguing the Wide Area Augmentation System and FAA’s Actions to Address Them’.
[180] U. N. Patel and I. A. Faruque, ‘Multi-IMU Based Alternate Navigation Frameworks: Performance & Comparison for UAS’, *IEEE Access*, vol. 10, pp. 17565–17577, 2022.
[181] L. A. Fagundes-Junior et al., ‘Machine Learning for Unmanned Aerial Vehicles Navigation: An Overview’, *SN Computer Science*, vol. 5, no. 2, pp. 1–26, 2024.
[182] S. Rezwan and W. Choi, ‘Artificial intelligence approaches for UAV navigation: Recent advances and future challenges’, *IEEE access*, vol. 10, pp. 26320–26339, 2022.
[183] A. Dosovitskiy et al., ‘An image is worth 16x16 words: Transformers for image recognition at scale’, *arXiv preprint arXiv:2010.11929*, 2020.
[184] S. J. Koiloth et al., ‘ML-based LOS/NLOS/multipath signal classifiers for GNSS in simulated multipath environment’, *Aerospace Systems*, pp. 1–14, 2023.
[185] L. Liu et al., ‘Spacecraft anomaly detection with attention temporal convolution networks’, *Neural Computing and Applications*, vol. 35, no. 13, pp. 9753–9761, 2023.
[186] M. N. A. Islam et al., ‘Towards an Annotated All-Weather Dataset of Flight Logs for Small Uncrewed Aerial System’, presented at the AIAA AVIATION 2023 Forum, 2023, p. 3856.
[187] D. E. Rumelhart et al., ‘Learning representations by back-propagating errors’, 1986.
[188] T. Meng et al., ‘A survey on machine learning for data fusion’, *Information Fusion*, vol. 57, pp. 115–129, 2020.
[189] R. F. Brena et al., ‘Choosing the best sensor fusion method: A machine-learning approach’, *Sensors*, vol. 20, no. 8, p. 2350, 2020.
[190] G. R. Arce, ‘A general weighted median filter structure admitting negative weights’, *IEEE Transactions on signal processing*, vol. 46, no. 12, pp. 3195–3205, 1998.
[191] H. Kaur and B. Dhaliwal, ‘Design of Low Pass FIR Filter Using Artificial NeuralNetwork’, *International Journal of Information and Electronics Engineering*, vol. 3, no. 2, p. 204, 2013.
[192] N. Abdelkrim et al., ‘Robust nonlinear filtering for INS/GPS UAV localization’, presented at the 2008 16th Mediterranean Conference on Control and Automation, 2008, pp. 695–702.

[193] B. A. Shenoi, *Introduction to digital signal processing and filter design*, vol. 169. John Wiley & Sons, 2005.
[194] M. Tamazin, 'HIGH RESOLUTION SIGNAL PROCESSING TECHNIQUES FOR ENHANCING GPS RECEIVER PERFORMANCE'.
[195] E. L. De Angelis and F. Giulietti, 'An Improved Method for Swing State Estimation in Multirotor Slung Load Applications', *Drones*, vol. 7, no. 11, p. 654, Oct. 2023 [Online]. Available: 10.3390/drones7110654.
[196] S. Alexovič et al., '3D Mapping with a Drone Equipped with a Depth Camera in Indoor Environment', *Acta Electrotechnica et Informatica*, vol. 23, no. 1, pp. 18–24, Mar. 2023 [Online]. Available: 10.2478/aei-2023-0003.
[197] B. Ford, 'Towards Flight Readiness In Unmanned Aerial Systems', 2023.
[198] *PX4 Development Kit - X500 v2*, Holybro Store. [Online]. Available: https://holybro.com/products/px4-development-kit-x500-v2. [Accessed: 01 Jun. 2024].
[199] *S500 V2 Development Kit*, Holybro Store. [Online]. Available: https://holybro.com/products/s500-v2-development-kit. [Accessed: 01 Jun. 2024].
[200] *PART 89—REMOTE IDENTIFICATION OF UNMANNED AIRCRAFT*. 2023[Online]. Availablehttps://www.ecfr.gov/current/title-14/chapter-I/subchapter-F/part-89.
[201] Y. Su et al., 'Precision Differential Drone Navigation', 2022.
[202] B. Suwandi et al., 'OBD-II Sensor Approaches for The IMU and GPS Based Apron Vehicle Positioning System', presented at the 2019 International Conference on Sustainable Engineering and Creative Computing (ICSECC), 2019, pp. 251–254.
[203] A. Industries, *PowerBoost 1000 Charger - Rechargeable 5V Lipo USB Boost @ 1A*. [Online]. Available: https://www.adafruit.com/product/2465. [Accessed: 22 Apr. 2024].
[204] A. Industries, *GPS Antenna - External Active Antenna - 3-5V 28dB 5 Meter SMA*. [Online]. Available: https://www.adafruit.com/product/960. [Accessed: 01 May 2024].
[205] MediaTek Labs, 'MT3333 All-in-One GNSS Datasheet', 2016[Online]. Availablehttps://d86o2zu8ugzlg.cloudfront.net/mediatek-craft/documents/mt3333/MT3333_Datasheet.pdf.
[206] By, (May. 10, 2020), 'Teensy-4.1-pinout', Hackaday. [Online]. Availablehttps://hackaday.com/2020/05/11/new-teensy-4-1-arrives-with-100-mbps-ethernet-high-speed-usb-8-mb-flash/teensy-4-1-pinout/[Accessed: 7May2024].
[207] *Teensy® 4.1*. [Online]. Available: https://www.pjrc.com/store/teensy41.html. [Accessed: 07 May 2024].
[208] L. Fried, 'Adafruit GPS Library'. Aug. 22, 2023[Online]. Availablehttps://github.com/adafruit/Adafruit_GPS?tab=readme-ov-file.
[209] P. Atoffregen, 'SD'. Jul. 08, 2023[Online]. Availablehttps://github.com/PaulStoffregen/SD.
[210] W. Greiman., 'SD Library for Arduino (SDfatlib)'. Oct. 11, 2019[Online]. Availablehttps://github.com/arduino-libraries/SD/tree/master/docs.
[211] N. US Department of Commerce, *Shoreline Mapping Data and Products*. [Online]. Available: https://geodesy.noaa.gov/datasheets/ngs_map/. [Accessed: 02 May 2024].
[212] *NGS Map*. [Online]. Available: https://noaa.maps.arcgis.com/apps/webappviewer/index.html?id=190385f9aadb4cf1b0dd8759893032db. [Accessed: 02 May 2024].

[213] Garmin and G. L. or its subsidiaries, *Garmin GLO™ 2 | BlueTooth GPS Receiver*, Garmin. [Online]. Available: https://www.garmin.com/en-US/p/645104. [Accessed: 02 May 2024].
[214] M. Fortunato et al., 'The whole works: A GNSS/IMU tight coupled filter for android raw GNSS measurements with local ground augmentation strategies', presented at the Proceedings of the ION GNSS, 2021.
[215] S. Nelson, 'Certification processes for safety-critical and mission-critical aerospace software', 2003.
[216] F. C. Briggs, 'Aerospace Software Testing Techniques', presented at the AIAA Infotech@ Aerospace (I@ A) Conference, 2013, p. 5221.
[217] D. C. Sharp et al., 'Challenges and solutions for embedded and networked aerospace software systems', *Proceedings of the IEEE*, vol. 98, no. 4, pp. 621–634, 2010.
[218] 'nmeaParser - Parse data from standard and manufacturer-specific NMEA sentences sent from marine electronic devices - MATLAB'. MATLAB[Online]. Availablehttps://www.mathworks.com/help/nav/ref/nmeaparser-system-object.html[Accessed: 4May2024].
[219] S. H. Byun et al., 'Development and application of GPS signal multipath simulator', *Radio Science*, vol. 37, no. 6, pp. 10–1, Dec. 2002 [Online]. Available: 10.1029/2001RS002549.
[220] A. Mohanty and G. Gao, 'Tightly coupled graph neural network and kalman filter for smartphone positioning', presented at the Proceedings of the 36th International Technical Meeting of the Satellite Division of The Institute of Navigation (ION GNSS+ 2023), 2023, pp. 175–187.
[221] S. Sohn et al., 'Vision-based real-time target localization for single-antenna GPS-guided UAV', *IEEE Transactions on Aerospace and Electronic Systems*, vol. 44, no. 4, pp. 1391–1401, 2008 [Online]. Available: 10.1109/TAES.2008.4667717.
[222] V. Hunter Adams and M. Peck, 'R-selected spacecraft', *Journal of Spacecraft and Rockets*, vol. 57, no. 1, pp. 90–98, 2020.
[223] V. H. Adams, 'Theory and Applications of Gram-Scale Spacecraft', 2020.
[224] Z. Benic et al., 'Mathematical Modelling of Unmanned Aerial Vehicles with Four Rotors', : *Interdiscip. Descr. Complex Syst.*, vol. 14, no. 1, pp. 88–100, 2016 [Online]. Available: 10.7906/indecs.14.1.9.
[225] V. Artale et al., 'Mathematical modeling of hexacopter', *ams*, vol. 7, pp. 4805–4811, 2013 [Online]. Available: 10.12988/ams.2013.37385.
[226] J. -H. Wang and Y. Gao, 'Land Vehicle Dynamics-Aided Inertial Navigation', *IEEE Transactions on Aerospace and Electronic Systems*, vol. 46, no. 4, pp. 1638–1653, Oct. 2010 [Online]. Available: 10.1109/TAES.2010.5595584.
[227] T. Imbiriba et al., 'Augmented physics-based machine learning for navigation and tracking', *IEEE Trans. Aerosp. Electron. Syst.*, pp. 1–13, 2023 [Online]. Available: 10.1109/TAES.2023.3328853.
[228] K. D. Sebesta and N. Boizot, 'A Real-Time Adaptive High-Gain EKF, Applied to a Quadcopter Inertial Navigation System', *IEEE Trans. Ind. Electron.*, vol. 61, no. 1, pp. 495–503, Jan. 2014 [Online]. Available: 10.1109/TIE.2013.2253063.
[229] T. U. Omali, 'Coordinate Transformation of GPS Measurement Results using the Cartesian-to-Ellipsoidal Transformation System', *Int. J. Sci. Res. in Mathematical and Statistical Sciences Vol*, vol. 10, no. 4, 2023.

[230] A. Sofwan et al., ‘Vehicle distance measurement tuning using Haversine and micro-segmentation’, presented at the 2019 International Seminar on Intelligent Technology and Its Applications (ISITIA), 2019, pp. 239–243.
[231] S. S. Alam et al., ‘A low-cost GPS based application for navigating shallow waters’, presented at the 2018 International Conference on Innovations in Science, Engineering and Technology (ICISET), 2018, pp. 92–97.

APPENDIX A: MATHEMATICAL FOUNDATIONS OF DRONE LOCALIZATION

The precision of GPS is crucial for the localization of UAVs. Achieving this precision requires a deep understanding of the mathematical methodologies that facilitate the conversion of coordinate data across multiple reference frames—geodesic, North-East-Up (NEU), body-centric, and inertial. These transformations are essential for accurate real-time navigation and the execution of complex flight maneuvers. This section amalgamates and summarizes the relevant drone navigation mathematics presented in the literature [49], [180], [224]–[228]. It explores the Newtonian mechanics underpinning these transformations and introduces machine learning techniques as potential enhancements. By drawing parallels between traditional Newtonian formulations and contemporary ML approaches, this discussion aims to identify and address gaps in the application of ML to drone localization. The integration of ML with established mathematical frameworks is proposed to potentially improve localization accuracy in UAV operations.

FRAMES OF REFERENCE

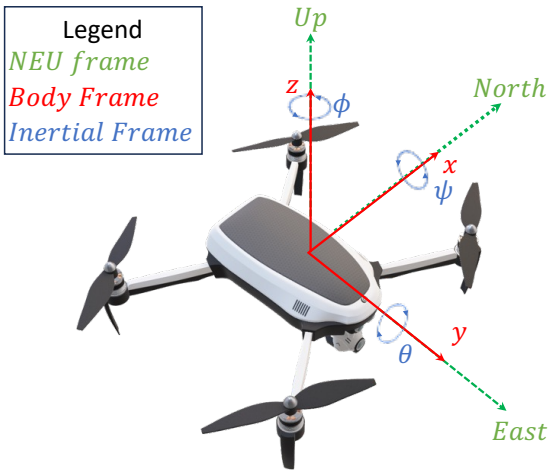

Figure A-1. Frames of reference. The inertial frame is aligned with the body frame. NEU frame is the operational frame in which data from different sensors in different frames are fused together. NEU frame is aligned with the Earth-referenced coordinate system at the launch point.

The NEU frame is an Earth-referenced coordinate system that provides a consistent global context for positioning. Its axes are oriented toward the true north (N), the east (E), and the vertical direction pointing away from the center of the Earth, known as up (U). This frame's immobility relative to the Earth allows for a uniform reference for GPS coordinates globally, ensuring that positional data from GPS satellites are interpreted consistently across different geographic locations.

In contrast to the NEU frame, the body frame is a moving coordinate system that is aligned with the drone's current orientation and position. The body frame's axes are defined with respect to the drone's structure: the forward axis (positive X-axis), the leftward axis (positive Y-axis), and the upward axis (positive Z-axis). This frame is essential for the drone's onboard systems to understand its orientation in space, which directly influences thrust vectoring, stabilization, and flight dynamics.

We define four primary reference frames for the analysis:

- Global Frame (G): A geodesic reference frame where the GPS operates. It is considered an absolute reference frame in space.
- Inertial Frame (I): The inertial frame is a theoretical reference frame in which Newton's laws of motion hold without any corrections for gravitational forces. In practice, this frame is approximated by a frame fixed relative to the center of mass of the drone.
- Navigation Frame (N): A local frame defined with respect to a point on Earth, typically aligned to the North-East-Up (NEU) convention.
- Body Frame (B): This frame is aligned with the center of gravity of the object under study and moves with it. The coordinates in space are denoted as $X^i = (x, y, z)^T$, where i is the index variable and T is the frame of reference.

$$X^i = (x, y, z)^T \tag{33}$$

OPERATIONS IN REFERENCE FRAMES

Geodesic to NEU frame[1]

The conversion from geodesic coordinates to the North-East-Up (NEU) frame is a critical operation. This transformation translates GPS coordinates, provided in terms of latitude, longitude, and altitude, into a local coordinate system aligned with the drone's orientation and motion in reference to a known reference point, most commonly the launch point. This conversion involves a series of transformations that account for the Earth's curvature and the drone's spatial orientation. While the WGS84 ellipsoid model is commonly employed for such calculations due to its compatibility with global navigation systems [229], the haversine formula presents a viable alternative, particularly for applications where simplicity and computational efficiency are paramount [230], [231]. The haversine formula calculates the great-circle distance between two points on a sphere using their latitudinal and longitudinal coordinates. Mathematically, it can be expressed as:

$$\Delta\phi = \phi_2 - \phi_1 \tag{34}$$

$$\Delta\lambda = \lambda_2 - \lambda_1 \tag{35}$$

$$a = \sin^2\left(\frac{\Delta\phi}{2}\right) + \cos(\phi_1) \cdot \cos(\phi_2) \cdot \sin^2\left(\frac{\Delta\lambda}{2}\right) \tag{36}$$

$$c' = 2 \cdot \operatorname{atan2}\left(\sqrt{a}, \sqrt{1-a}\right) \tag{37}$$

$$d = R \cdot c' \tag{38}$$

[1] Thanks to Alperen Cuci for his contributions in writing this section of my Thesis.

where $(\emptyset_1, \lambda_1)$and $(\emptyset_2, \lambda_2)$ are the latitudinal and longitudinal coordinates of two points respectively, the haversine formula computes the distance, d, between them. R is the mean radius of the Earth in meters.

Let (lat_0, lon_0, h_0) represent the initial GPS coordinates (latitude, longitude, altitude) of the starting point, and (lat_k, lon_k, h_k) denote the current GPS fix. Using equation (38), we can get the distance between the launch point and the current position. After obtaining the distance, we proceed to calculate the North-South, ${}^{gps}_{k}\vec{\boldsymbol{x}}$; East-West, ${}^{gps}_{k}\vec{\boldsymbol{y}}$; and vertical, ${}^{gps}_{k}\vec{\boldsymbol{z}}$, components of the displacement vector, ${}^{gps}_{k}\vec{\boldsymbol{d}} = \langle {}^{gps}_{k}\vec{\boldsymbol{x}}, {}^{gps}_{k}\vec{\boldsymbol{y}}, {}^{gps}_{k}\vec{\boldsymbol{z}} \rangle^T$.

$$ {}^{gps}_{k}\vec{\boldsymbol{x}} = d \cdot \cos(lat_k) \cdot \sin(lon_k - lon_0) \tag{39} $$

$$ {}^{gps}_{k}\vec{\boldsymbol{y}} = d \cdot [\sin(lat_k) \cdot \cos(lat_0) \; - \; \cos(lat_k) \cdot \sin(lat_0) \cdot \cos(lon_k - lon_0)] \tag{40} $$

$$ {}^{gps}_{k}\vec{\boldsymbol{z}} = h_k \; - \; h_0 \tag{41} $$

To derive velocity and acceleration from GPS data in the North-East-Up (NEU) frame, we employ a systematic approach that leverages consecutive GPS readings. This process involves calculating the change in position over time to obtain velocity and then determining the change in velocity over time to derive acceleration.

Velocity is a vector quantity that describes both the speed and direction of motion. In the NEU frame, velocity components, $\langle V_N, V_E, V_U \rangle_{GPS}{}^T$, correspond to the North, East, and Up directions, respectively. To calculate these components, we first need a series of position measurements ${}^{gps}_{k}\vec{\boldsymbol{d}}$ at known time intervals, t, from the GPS.

$$ {}^{gps}_{N}\mathbf{V}_k = \begin{bmatrix} {}^{gps}_{k}V_N \\ {}^{gps}_{k}V_E \\ {}^{gps}_{k}V_U \end{bmatrix} = \begin{bmatrix} \frac{\partial\, {}^{gps}_{k}\vec{x}}{\partial t} \\ \frac{\partial\, {}^{gps}_{k}\vec{y}}{\partial t} \\ \frac{\partial\, {}^{gps}_{k}\vec{z}}{\partial t} \end{bmatrix} \approx \begin{bmatrix} \frac{{}^{gps}_{k}\vec{\boldsymbol{x}} - {}^{gps}_{k-1}\vec{\boldsymbol{x}}}{t_k - t_{k-1}} \\ \frac{{}^{gps}_{k}\vec{\boldsymbol{y}} - {}^{gps}_{k-1}\vec{\boldsymbol{y}}}{t_k - t_{k-1}} \\ \frac{{}^{gps}_{k}\vec{\boldsymbol{z}} - {}^{gps}_{k-1}\vec{\boldsymbol{z}}}{t_k - t_{k-1}} \end{bmatrix} \quad (42) $$

These calculations provide the instantaneous velocity, ${}^{gps}_{N}\mathbf{V}_k$, of the drone in the NEU frame, considering the displacement in each direction divided by the time elapsed between two consecutive GPS readings. The acceleration of the drone, ${}^{gps}_{N}\mathrm{a}_k$, is given by:

$$ {}^{gps}_{N}\mathbf{a}_k = \begin{bmatrix} {}^{gps}_{k}a_N \\ {}^{gps}_{k}a_E \\ {}^{gps}_{k}a_U \end{bmatrix} = \begin{bmatrix} \frac{\partial\, {}^{gps}_{k}V_N}{\partial t} \\ \frac{\partial\, {}^{gps}_{k}V_E}{\partial t} \\ \frac{\partial\, {}^{gps}_{k}V_U}{\partial t} \end{bmatrix} \approx \begin{bmatrix} \frac{{}^{gps}_{k}V_N - {}^{gps}_{k-1}V_N}{t_k - t_{k-1}} \\ \frac{{}^{gps}_{k}V_E - {}^{gps}_{k-1}V_E}{t_k - t_{k-1}} \\ \frac{{}^{gps}_{k}V_U - {}^{gps}_{k-1}V_U}{t_k - t_{k-1}} \end{bmatrix} \quad (43) $$

Inertial to NEU frame

The conversion from inertial to North-East-Up (NEU) frame for sensors' data, notably from accelerometers and gyroscopes, plays a crucial role in localization systems of drones. The raw measurements provided by these sensors form the basis for estimating the orientation and position of the vehicle in three-dimensional space, enabling precise navigation and motion control.

The accelerometer measures acceleration in the inertial frame, equation (44), capturing the drone's linear acceleration excluding gravity. Gyroscope data, represented in equation (45), provides angular velocities around the drone's principal axes, corresponding to roll (φ), pitch (θ), and yaw (ψ) rates of change.

$$\vec{a}_i =< a_x, a_y, a_z >_{inertial} \tag{44}$$

$$\vec{g}_i =< \dot{\varphi}, \dot{\theta}, \dot{\psi} >_{gyro} \tag{45}$$

$$X^i = (x, y, z)^T \tag{46}$$

The raw sensor data from accelerometers and gyroscopes is the starting point for state estimation. The accelerometer provides a vector of accelerations in the inertial frame, while the gyroscope yields angular velocities $< \dot{\varphi}, \dot{\theta}, \dot{\psi} >_{gyro}$ associated with the Euler angles. Euler angles $< \varphi, \theta, \psi >_B^T$ offer a compact way to represent the orientation of the body frame B in respect to the inertial frame. They describe the sequence of rotations about the principal axes that align the body frame with the inertial frame. Estimation of this sequence of rotations is a critical step in orientation estimation.

To transition between the rotational frames, we use transformation matrices. The rotation matrix $R_x(\emptyset)$ for a rotation about the x-axis is given by:

$$R_x(\emptyset) = \begin{bmatrix} 1 & 0 & 0 \\ 0 & \cos(\emptyset) & -\sin(\emptyset) \\ 0 & \sin(\emptyset) & \cos(\emptyset) \end{bmatrix} \tag{47}$$

$$R_y(\theta) = \begin{bmatrix} \cos(\theta) & 0 & \sin(\theta) \\ 0 & 1 & 0 \\ -\sin(\theta) & 0 & \cos(\theta) \end{bmatrix} \tag{48}$$

$$R_z(\psi) = \begin{bmatrix} \cos(\psi) & -\sin(\psi) & 0 \\ \sin(\psi) & \cos(\psi) & 0 \\ 0 & 0 & 1 \end{bmatrix} \tag{49}$$

Similarly, rotations about the y and z-axes, denoted as $R_y(\theta)$ and $R_z(\psi)$, respectively, follow the standard formulation for 3D rotations.

To localize effectively, a drone must translate acceleration and rotation data between its local body frame and the global NEU frame. This process utilizes rotation matrices, which mathematically represent the drone's orientation through roll, $R_x(\emptyset_B)$, pitch, $R_y(\theta_B)$, and yaw, $R_z(\psi_B)$, angles. These angles correspond to rotations about the body frame's X, Y, and Z-axes, respectively. The combined rotation matrix, R, is the product of these individual rotation matrices:

$$R_{B_2N} = R_z(\psi_B) * R_y(\theta_B) * R_x(\phi_B) \tag{50}$$

This rotation matrix transforms acceleration vectors from the body frame to the NEU frame, allowing the drone's movements to be interpreted within the global context. The transformed acceleration vector in the NEU frame at a kth time instance is expressed as:

$$^{imu}_{N}\mathrm{a}_k = R_{B_2N} * \mathrm{a}_B \tag{51}$$

where $\mathrm{a_b}$ is the acceleration vector measured in the body frame. The IMU derived acceleration $^{imu}_{N}\mathrm{a}_k$ in the navigational frame can be derived from the body frame acceleration a_{B_k}, at time k as follows:

$$^{imu}_{N}\mathrm{a}_k = \begin{bmatrix} ^{imu}_{k}a_N \\ ^{imu}_{k}a_E \\ ^{imu}_{k}a_U \end{bmatrix} = R_{B_2N} * \mathrm{G}(\mathrm{a}_{B_k}) \tag{52}$$

where $\mathrm{G}(^{imu}_{N}\mathrm{a}_k)$ represents the gyroscopic filter applied to the body frame acceleration. The gyroscopic filter accounts for the non-linear gyroscopic precision effects of rotational acceleration on linear acceleration measurements and vice versa.

The velocity $^{imu}_{N}V_k$ and position $^{imu}_{N}X_k$ in the navigation frame can then be computed by integration over time, with the application of appropriate filtering techniques to reduce noise and bias.

$$
\begin{aligned}
{}^{imu}_{N}V_k = \begin{bmatrix} {}^{imu}_{k}V_N \\ {}^{imu}_{k}V_E \\ {}^{imu}_{k}V_U \end{bmatrix} &= \begin{bmatrix} {}^{imu}_{k-1}V_N + \int_{t_{k-1}}^{t_k} a_n \, dt \\ {}^{imu}_{k-1}V_E + \int_{t_{k-1}}^{t_k} a_E \, dt \\ {}^{imu}_{k-1}V_U + \int_{t_{k-1}}^{t_k} a_U \, dt \end{bmatrix} \\
&= \begin{bmatrix} {}^{imu}_{k-1}V_N + \left({}^{imu}_{k}a_N - {}^{imu}_{k-1}a_N\right) \cdot (t_k - t_{k-1}) \\ {}^{imu}_{k-1}V_E + \left({}^{imu}_{k}a_E - {}^{imu}_{k-1}a_E\right) \cdot (t_k - t_{k-1}) \\ {}^{imu}_{k-1}V_U + \left({}^{imu}_{k}a_U - {}^{imu}_{k-1}a_U\right) \cdot (t_k - t_{k-1}) \end{bmatrix}
\end{aligned} \tag{53}
$$

$$
\begin{aligned}
{}^{imu}_{N}X_k = \begin{bmatrix} {}^{imu}_{k}X_N \\ {}^{imu}_{k}X_E \\ {}^{imu}_{k}X_U \end{bmatrix} &= \begin{bmatrix} {}^{imu}_{k-1}X_N + \int_{t_{k-1}}^{t_k} V_n \, dt \\ {}^{imu}_{k-1}X_E + \int_{t_{k-1}}^{t_k} V_E \, dt \\ {}^{imu}_{k-1}X_U + \int_{t_{k-1}}^{t_k} V_U \, dt \end{bmatrix} \\
&\approx \begin{bmatrix} {}^{imu}_{k-1}V_N \cdot (t_k - t_{k-1}) + \frac{1}{2}\left({}^{imu}_{k}a_N\right) \cdot (t_k - t_{k-1})^2 \\ {}^{imu}_{k-1}V_E \cdot (t_k - t_{k-1}) + \frac{1}{2}\left({}^{imu}_{k}a_E\right) \cdot (t_k - t_{k-1})^2 \\ {}^{imu}_{k-1}V_U \cdot (t_k - t_{k-1}) + \frac{1}{2}\left({}^{imu}_{k}a_U\right) \cdot (t_k - t_{k-1})^2 \end{bmatrix}
\end{aligned} \tag{54}
$$

Operations in NEU frame

In the NEU frame, various operations are conducted to facilitate drone navigation, including position estimation, velocity calculation, and attitude determination. These operations involve a combination of mathematical transformations and sensor data processing to ensure accurate and reliable navigation in three-dimensional space.

Sensor fusion: complementary filter

The Complementary Filter combines data from both GPS and IMU sensors by blending their respective measurements. It is designed to leverage the strengths of each sensor while compensating for their individual weaknesses.

Let θ_{IMU} denote the orientation angle obtained from the IMU, and θ_{GPS} represents the orientation angle derived from GPS measurements. The Complementary Filter can be expressed mathematically as:

$$[\theta_{\text{fused}} = \alpha \cdot \theta_{\text{IMU}} + \beta \cdot \theta_{\text{GPS}} + \cdots \delta\theta_{\delta}\,]\; s.t. |\alpha + \beta + \cdots + \delta| = 1 \tag{55}$$

where $\alpha, \beta, \cdots, \delta$are the blending factors that determine the contribution of each sensor. Typically, $\alpha, \beta, \cdots, \delta$ is chosen to favor one sensor over the other based on their respective accuracies and update rates.

Sensor fusion: madgwick filter

The Madgwick Filter is an advanced algorithm that effectively combines GPS and IMU data by utilizing sensor fusion techniques, such as quaternion-based orientation estimation. It employs a gradient descent approach to optimize the orientation quaternion.

Let $\boldsymbol{q}$ denote the orientation quaternion representing the rotation from the body frame to the Earth frame, and $\boldsymbol{a}$ and $\boldsymbol{\omega}$ represent the specific force and angular rate measurements from the IMU, respectively. The Madgwick Filter updates the orientation quaternion based on the IMU data and corrects it using GPS measurements. The algorithm can be summarized as follows:

$$[\dot{\boldsymbol{q}} = \frac{1}{2}\boldsymbol{q} \otimes \begin{pmatrix} 0 \\ \boldsymbol{\omega} \end{pmatrix} - \beta \cdot \boldsymbol{P} \cdot \boldsymbol{a}] \tag{56}$$

where $\otimes$ denote quaternion multiplication, β is a filter gain parameter, and $\boldsymbol{P}$ is a positive definite symmetric matrix that determines the contribution of accelerometer measurements to the orientation estimation.

Equivalence of state estimation and neural networks

This section bridges the conceptual divide between a traditional vector transformation equation (51) and its ML equivalent, offering a clear comparison and demonstrating equivalence under specific conditions. The first step will be to establish clear analogies of classical vector transformation and their neural network counterparts, then represent the transformation equations into neural network expression using model representation before applying machine learning extension and loss function optimizations to the model.

Staring with the transformation of coordinate data between the Earth-centric NEU frame and the drone-specific body frame, the application of ML in GPS technology for UAVs involves equation (51), where $\vec{a}_N$ and $\vec{a}_B$ represent vectors in possibly different vector spaces or coordinate systems, and R is a transformation matrix. In ML, particularly within neural networks, the operation of applying weights to an input feature vector is given by:

$$\vec{y} = W * \vec{x} + \vec{b} \tag{57}$$

where, $\vec{y}$ is the resulting vector post-transformation, W is the weight matrix, $\vec{x}$ is the input vector, and $\vec{b}$ represents a bias vector. In ML, the weight matrix W is typically derived through a learning process, often using optimization algorithms that minimize a loss function. In contrast, the transformation matrix R in classical vector equations is usually defined by the physical laws governing the system or the required coordinate transformation. W is randomly defined as a large, valued matrix. However, by seeding W to be R (refer to page 204), we establish a connection between the ML weight initialization process and the underlying physics governing the system. Using data-driven insights, models will be specifically selected to take advantage of the signal characteristics and use these insights to improve the performance of GPS localization systems. Moreover, this initialization approach provides a solid foundation for Machine Learning models, potentially leading to faster convergence to optimal solutions. Unlike random initialization, seeding W to mimic R allows the optimization process to focus on refining small discrepancies between the model predictions and the real-world data, rather than recreating the underlying physics from scratch. The concept of seeding W to match R also opens avenues for developing

hybrid models that integrate classical physics principles into Machine Learning algorithms. Such hybrid models not only benefit from the explainability provided by physics-based approaches but also meet the stringent certification requirements in aerospace environments. To explore the implications further, adopting a grid search algorithm can ensure comprehensive coverage of the solution space within the model. Comparing equation (51) and (57) gives an idea for a similar approach:

$R \leftrightarrow W$: Transformation matrix in (51) is analogous to the weight matrix in ML.

$\vec{a}_B \leftrightarrow \vec{x}$: Input vector in (51) is analogous to the input feature vector in ML.

$\vec{a}_N \leftrightarrow \vec{y}$: Resultant vector in (51) is analogous to the output vector in ML before bias adjustment.

Through these established parallels, it becomes evident that the transformation matrix R plays a similar role to the weight matrix W in altering the state of the input vector through a linear operation. This reveals a fundamental unity in the operations conducted in classical vector transformations and neural network computations.

APPENDIX B

Table B-1. Repeatability of sensor performance I.

Sensor	Frequency	Error Type	F-Statistic	T-Statistic	P-Value	Sensor	Error Type	F-Statistic	T-Statistic	P-Value
		altitude	1.000	0.000	0.90		altitude	1.00	0.00	0.96
	0.1	angular	1.000	0.000	1.00		angular	1.00	0.00	0.97
		magnitude	1.000	0.000	1.00		magnitude	1.00	-0.013	0.98
		altitude	0.196	-14.79	0.00		altitude	3.16	-27.71	0.00
	1	angular	2.215	-18.65	0.00		angular	1.00	0.013	1.00
		magnitude	0.250	-10.63	0.00		magnitude	1.00	0.013	1.00
		altitude	0.776	35.71	0.00		altitude	21.59	-25.72	0.00
1A	3	angular	0.714	-16.45	0.00	2A	angular	1.00	0.00	1.00
		magnitude	0.432	10.95	0.00		magnitude	1.00	-0.043	1.00
		altitude	10.663	7.35	0.60		altitude	1.24	40.41	0.00
	5	angular	0.128	-42.61	0.35		angular	0.00	32.79	0.00
		magnitude	0.215	16.88	0.28		magnitude	0.00	-32.79	0.00
		altitude	3.087	-0.327	0.80		altitude	1.00	0.091	1.00
	10	angular	1.000	-0.016	1.00		angular	1.00	-0.026	1.00
		magnitude	1.000	-0.050	1.00		magnitude	1.00	0.00	1.00

Hypothesis: All sensors perform identically across multiple test runs

Large values p-values are approximated to 1 and small p-values are approximated to be 0

Large values f-values are represented as >> and small f-values are represented as <<

Table B-2. Repeatability of sensor performance II.

Sensor	Frequency	Error Type	F-Statistic	T-Statistic	P-Value	Sensor	Error Type	F-Statistic	T-Statistic	P-Value
		altitude	1.00	0.00	0.97		altitude	1.00	0.012	0.99
	0.1	angular	1.00	0.00	0.95		angular	1.00	-0.040	0.98
		magnitude	1.00	-0.017	1.00		magnitude	1.00	-0.029	1.00
		altitude	0.50	38.60	0.00		altitude	0.23	36.06	0.00
	1	angular	>>	25.56	0.00		angular	7.69	2.117	0.03
		magnitude	>>	25.56	0.00		magnitude	0.56	-22.03	0.00
		altitude	3.795	37.49	0.00		altitude	1.94	4.756	0.00
1B	3	angular	1.00	0.00	0.99	2B	angular	1.00	0.00	0.99
		magnitude	1.00	0.012	1.00		magnitude	1.00	0.00	1.00
		altitude	0.61	29.68	0.00		altitude	>>	-30.99	0.00
	5	angular	1.00	0.00	0.980		angular	1.00	0.038	0.99
		magnitude	1.00	0.091	0.90		magnitude	1.00	-0.026	0.99
		altitude	0.76	33.62	1.00		altitude	1.00	-0.026	1.00
	10	angular	>>	-5.72	1.00		angular	1.00	0.000	1.00
		magnitude	>>	-5.72	1.00		magnitude	1.00	0.014	0.97

Hypothesis: All sensors perform identically across multiple test runs

Large values p-values are approximated to 1 and small p-values are approximated to be 0

Large values f-values are represented as >> and small f-values are represented as <<

Table B-3. Key Statistics from the Open-Field 2 Data.

Statistic	GPS1	GPS2	GPS3	GPS4	GPS5
Count	8760.0	8760.0	8760.0	8760.0	8760.0
Mean	3.79 m	5.49 m	3.74 m	10.32 m	9.97 m
Std	0.13 m	0.41 m	0.62 m	0.35 m	0.82 m
Min	3.44 m	5.07 m	2.29 m	9.67 m	8.38 m
25%	3.84 m	5.07 m	3.26 m	10.13 m	9.31 m
50%	3.84 m	5.39 m	3.58 m	10.20 m	10.20 m
75%	3.84 m	5.95 m	4.38 m	10.52 m	10.23 m
Max	3.84 m	5.95 m	4.51 m	10.89 m	11.12 m

Table B-4. Key Statistics from the Urban-3 location Data.

Statistic	GPS1	GPS2	GPS3	GPS4	GPS5	After IRNN-DNN Application
Count	32955.0	32246.0	32955.0	32955.0	32955.0	NA
Mean	72.42 m	79.12 m	78.21 m	76.41 m	75.90 m	2.108 m
Std	8.90 m	8.42 m	8.20 m	11.05 m	5.45 m	0.71 m
Min	47.11 m	18.67 m	62.17 m	37.05 m	53.60 m	0.0
25%	65.60 m	76.29 m	74.68 m	69.95 m	73.79 m	-
50%	69.68 m	78.74 m	78.21 m	77.60 m	76.29 m	-
75%	78.90 m	80.87 m	81.19 m	82.08 m	78.21 m	-
Max	98.10 m	154.01 m	100.18 m	108.41 m	92.57 m	5.7 m

Table B-5. Key Statistics from the Open-Field 1 location Data.

Statistic	GPS1	GPS2	GPS3	GPS4	GPS5
Count	34021.0	34021.0	34021.0	34021.0	34021.0
Mean	210.45 m	211.27 m	204.69 m	210.46 m	209.89 m
Std	0.63 m	1.82 m	2.67 m	1.18 m	2.32 m
Min	209.10 m	206.19 m	200.77 m	206.67 m	203.96 m
25%	210.23 m	210.67 m	201.90 m	209.92 m	209.00 m
50%	210.36 m	211.04 m	204.77 m	210.84 m	210.67 m
75%	211.16 m	212.89 m	206.33 m	210.94 m	211.59 m
Max	211.41 m	214.66 m	211.16 m	211.87 m	212.51 m

Table B-6. Key Statistics from the Semi-Urban 1 location Data.

Statistic	GPS1	GPS2	GPS3	GPS4	GPS5	After IRNN-DNN Application
Count	18032	18032	18032	55024	33534	NA
Mean	57.56 m	35.65 m	53.13 m	70.44 m	58.16 m	2.868 m
Std	3.77 m	3.97 m	2.96 m	13.63 m	42.94 m	1.09 m
Min	48.70 m	29.40 m	46.50 m	0.00 m	39.40 m	0.0
25%	55.10 m	32.50 m	50.80 m	60.20 m	42.10 m	-
50% (Med)	56.80 m	35.80 m	52.60 m	69.00 m	45.10 m	-
75%	61.60 m	36.80 m	55.30 m	78.70 m	56.30 m	-
Max	62.50 m	46.20 m	59.00 m	100.40 m	267.00 m	9.1 m

Table B-7. Key Statistics from the Urban-2 location Data.

Statistic	GPS1	GPS2	GPS3	GPS4	GPS5	After IRNN-DNN Application
Count	45458	45458	45458	45458	45458	NA
Mean	44.47 m	26.62 m	44.94 m	44.36 m	42.44 m	2.295 m
Std	15.09 m	14.45 m	15.29 m	15.56 m	18.15 m	0.88 m
Min	0.00 m	0.00 m	0.00 m	0.00 m	0.00 m	0.0 m
25%	34.70 m	16.10 m	44.00 m	36.10 m	45.60 m	-
50% (Med)	41.20 m	25.50 m	45.10 m	50.80 m	46.10 m	-
75%	60.40 m	35.50 m	51.90 m	51.60 m	46.70 m	-
Max	99.70 m	56.80 m	67.10 m	167.30 m	167.30 m	8.5 m

Table B-8. Key Statistics from the Urban-1 location Data.

Statistic	GPS1	GPS2	GPS3	GPS4	GPS5	After IRNN-DNN Application
Count	58474	58474	58464	58464	58464	NA
Mean	76.22 m	63.32 m	85.11 m	91.11 m	83.03 m	1.807 m
Std	7.00 m	38.01 m	7.32 m	7.79 m	6.53 m	0.78 m
Min	0.00 m	0.00 m	0.00 m	0.00 m	0.00 m	0.0 m
25%	69.90 m	35.30 m	78.60 m	88.20 m	77.70 m	-
50% (Med)	73.70 m	54.50 m	84.50 m	91.80 m	81.80 m	-
75%	82.80 m	92.00 m	90.40 m	94.60 m	87.60 m	-
Max	90.90 m	347.00 m	98.20 m	136.60 m	122.30 m	8.4 m